Strain Heterogeneity during Creep of Carrara Marble

by

Alejandra Quintanilla Terminel

Submitted to the Department of Earth, Atmospheric and Planetary Sciences
in partial fulfillment of the requirements for the degree of

Doctor of Philosophy

at the

MASSACHUSETTS INSTITUTE OF TECHNOLOGY

September 2014

Signature redacted

Author .....
Department of Earth, Atmospheric and Planetary Sciences
August 29th, 2014

Signature redacted

Certified by .....
J. Brian Evans
Professor of Geophysics
Thesis Supervisor

Signature redacted

Accepted by .....
Robert D. van der Hilst
Schlumberger Professor of Earth Sciences
Head, Department of Earth, Atmospheric and Planetary Sciences

Strain Heterogeneity during Creep of Carrara Marble

by

Alejandra Quintanilla Terminel
Submitted to the Department of Earth, Atmospheric and Planetary Sciences
on August 29th, 2014, in partial fulfillment of the requirements for the degree of
Doctor of Philosophy

Abstract

Creep processes in calcite have been extensively studied, leading to the establishment of deformation mechanism maps. However, flow laws assuming a steady-state and homogeneous creep deformation cannot describe the strain localization and evolving structure described in numerous experimental and field studies. The micromechanical models need therefore to be revisited, and more experimental work and alternative methods to describe strain evolution are necessary. This work focused on the development of experimental and computational tools to describe strain at a micrometric scale, and their application to creep of Carrara marble. Two experimental series, one varying temperature (T), the other varying strain were performed in compression in a conventional triaxial apparatus (Paterson Instruments) at 300 MPa, T=400-700°C , strain rate of $3\times10^{-5}s^{-1}$ and strains of 0.11, 0.22 and 0.36. Chapters 2 and 3 describe the microfabrication and computation technique developed for mapping deformation at a microscale. Chapter 4 describes the development of strain heterogeneity in the experimental series and Chapter 5 provides a complementary crystallographic analysis and preliminary work regarding modeling of the strain field. The experiments document a progressive transition as temperature increases from 400°C to 700°C , from a regime where twinning is an important mechanism of strain accommodation towards an increasing activity of intracrystalline slip systems. This transition is accompanied by a change in length scale of strain heterogeneity. At low T, strain is localized in bands spanning several grains. At high T, strain is more localized along grain boundaries. Furthermore, the wavelength of heterogeneities decreases to a quarter of the grain size, in parallel with an increase in their amplitude. This evolution is also seen at a grain scale and is accompanied by a greater change in crystallographic preferred orientation with respect to the undeformed natural sample, both at the low T and high T end-members of the series. The wavelengths of heterogeneities decrease with strain, suggesting the microstructure has not reached steady state despite a trend towards a local homogenization. This work provides a quantitative analysis of the evolution of intra- and intergranular strain partition, and gives a first insight into the adequate formulation of the evolving parameters in a constitutive law of creep deformation.

Thesis Supervisor: J. Brian Evans
Title: Professor of Geophysics

Acknowledgments

Although this path has been lonely and isolated at times, looking back I mostly remember the amazing people I had the privilege to meet and collaborate with, the blessing of their friendship and the very essential support of my family and friends. I am immensely grateful to all of them. The time constraints and my literary fluency are unfortunately not enough to do justice to the role played by each of them, but I will keep them all dearly in my heart.

First, I would like to thank my advisor, Brian Evans, for this opportunity and for the freedom and trust he gave me, while always leaving his door open for discussions. I would also like to thank the members of my committee: Dave Mainprice from whom I learned a great deal and who played a critical role for finishing this thesis work, Bill Durham for his always pertinent comments and insights, and for the words of encouragement when I needed them the most, also essential for finishing this work, and Sam Bowring for his very enriching perspective.

Oliver Jagoutz escaped from the final committee, but his advice was extremely helpful along the way, I am particularly grateful for his perfectly timed words of encouragements. Uli Faul's comments and suggestions were of great help, I am happy I was still around for his first months in the lab! I was also very lucky to have been around for Ben Holtzman's short visit to MIT, and I am grateful for very rich discussions, artistic melt perspectives, and in general, for his invaluable friendship. Thanks also to Jock Hirst for sample preparation and for sharing his knowledge to maneuver old lathes and drilling machines.

The EBSD analysis would not have been possible without the patience and skills of Fabrice Barou and Dave Mainprice, it was a true pleasure to work with them in Montpellier. I have to thank the whole Géosciences Montpellier lab for their warm welcome, and in particular Andréa Tommasi, Alain Chauvet and Benoit Ildefonse.

Many thanks to Ricardo Lebensohn for providing me with his VPFFT code and for a very enriching exchange of ideas and perspectives on the experimental work.

My short time at the Kohlstedt lab in Minneapolis considerably brightened my experience with the Paterson apparatus, and was essential for finishing my thesis work. I am very grateful for the generosity of everybody in the lab, and to Mark Zimmerman and David Kohlstedt for welcoming me there. I would have never thought I would look forward to moving somewhere colder than Boston!

My experience at MTL was always very pleasant, even when spending days trying new processing techniques under a yellow light. I am very grateful to Kurt Broderick and Dennis Ward, for their patience, help and never-ending curiosity. Not only did they not send me away when I intended to enter a clean room with a piece of marble, but thanks to their contagious enthusiasm and curiosity I always came out of MTL with more energy and ideas for improvements.

I was also fortunate to have been involved in other projects at EAPS, and I am grateful to Dan Rothman's group for insightful group meetings that brought me to think very differently about modeling complex systems, and to Dale Morgan for his different and enriching perspective on geophysics.

Brenda Carbone deserves a distinctive place here, for her constant good mood, her invaluable help for all administrative tasks and for taking care of my plants so many times. Kerin Willis, Carol Sprague, Jacqui Taylor and Vicki McKenna were also very helpful, always with a smile.

I learned a great deal from the students and post-docs in the EAPS department. I am very grateful for their support, advice and great conversations along the way. It will be hard to name them all and do them justice, but I will remember them dearly. Special thanks to Fred Pearce for his endless curiosity, support, patience, and great time spent together. Thanks also to Sudhish Bakku for greats insights about life and a constant good mood. This last year I truly missed Yodit Tewelde's cheerful presence in the office, unbeatable rhythm and wise advice; as well as Alex Evans' intense scientific discussions, great laugh and jokes (even if they were often on me... just a little peak!). I am grateful to both of them for their help when I decided to take the idiom literally and broke a leg hoping for better fortune. I am also grateful to the 7th floor inhabitants, to the Paleomagnetism lab for keeping the floor alive on late nights and weekends; and to Nathaniel Dixon, my officemate for most of my time here, for sharing happiness and miseries, along with a coveted river view.

I am grateful to T.S. Ramakrishnan's group at Schlumberger-Doll Research, and to Laura and Anais Espinal for pointing my wondering soul into graduate school. I was very fortunate to have an amazing local support in Cambridge; it will be a hard task to properly name everybody who helped me keep some of my sanity along this journey. Thanks to Albert Perez for his great humor and to Catherine Graciano and Anthony Barrs for their great company and support. Thanks also to my friends in Mexico and France, strangely in tune after years or even a decade of being away, specially to Jess Cortese and Mathieu Capelot who provided me with a constant supply of chocolate, essential fuel for my thinking.

My family played an essential support role. I know it was hard to understand why on Earth I was still a student after all this time and change of countries, and how could it possibly be so stressful, but they always had the right words to say for the worst moments. I am very grateful to my parents, José and Blanca, for their constant support regardless of the project, and for giving me a strong base from which I always felt safe to explore unknown territories. My brothers Gerardo and Sebastian always gave me the wisest advice while remaining my dearest little brothers, and their words of encouragements meant the most for keeping my head up along this journey. I am looking forward to seeing where their curiosity and dedication takes them. Queridos Canutos, muchísimas gracias por todo, aún en español no tengo las palabras precisas para agradecerles y expresarles lo orgullosa que estoy de ustedes.

And finally, thanks to the new member of my family, Matěj, for jumping continents, for his endless patience, generosity, support... and for that smile that summarizes it all!

Contents

1 Introduction: Overview and background, creep deformation of Carbonate Rocks **17**

1.1 Introduction 17

1.2 Correlation between mechanical history and microstructure 19

1.3 Overview of this dissertation 20

1.4 Background on creep deformation in Carrara marble 22

1.4.1 Flow laws of creep deformation for calcite rocks 22

1.4.2 Deformation mechanisms in calcite 22

2 Methodology for the Microscale Strain Mapping technique **27**

2.1 Introduction 28

2.2 Split Cylinder set-up 28

2.2.1 Preparation of the half cylinder composites 28

2.2.2 Gas apparatus triaxial deformation tests 30

2.3 The photolithography technique 33

2.3.1 Principles of photolithography 33

2.3.2 Grid design 34

2.3.3 Protocol followed at MTL (Microsystems Technology Laboratories) at MIT 36

2.3.4 Additional technical developments 40

2.4 Characterization techniques 41

2.4.1 Optical imaging 41

2.4.2 Electron Back Scattered Diffraction 41

2.5 Summary 42

3 Microscale Strain Mapping Technique **55**

3.1 Motivation 56

3.2 Strain mapping technique on split cylinder assembly 57

3.2.1 Patterned split cylinder 57

3.2.2 Macroscopical mechanical behavior in Paterson apparatus . . 58

3.2.3 Characterization of the surface before and after deformation . 59

3.3 Methodology: strain mapping algorithm 61

3.3.1 Work flow for strain analysis 61

3.3.2 Strain probe: n point averaging technique 63

3.3.3 Computation of $\overline{\overline{F}}$ in 2D and 3D 64

3.3.4 Computation of strain from the deformation gradient tensor $\overline{\overline{F}}$ in finite strain theory 65

3.3.5 Representation of strain 66

3.4 Evaluation of the strain mapping technique 67

3.4.1 Error analysis 67

3.4.2 State of facing surfaces after deformation 69

3.5 Summary 70

4 Strain Heterogeneities during Creep of Carrara marble **89**

4.1 Motivation 90

4.2 Deformation field across different length scales 92

4.2.1 Macroscopic mechanical behavior 92

4.2.2 Macroscopic strain 93

4.2.3 Microscopic strain field 94

4.2.4 Hypothesis of isochoric deformation and axial symmetry . . . 95

4.2.5 Von Mises strain 97

4.3 Characterization of the strain fields 117

4.3.1 Strain distribution 117

4.3.2 Spectral analysis of the strain field 118

4.4 Partition of strain in the polycrystalline material 128
4.4.1 Observed deformation mechanisms 128
4.4.2 Grain and twin area analysis 129
4.4.3 Strain along grain boundaries 131
4.4.4 Intragranular strain 132
4.5 Summary 134

5 Crystallographic Analysis **149**
5.1 Introduction 150
5.2 Methods 150
5.2.1 Representation of crystallographic orientation 151
5.2.2 Electron Backscattered Diffraction (EBSD) method 152
5.2.3 Characterization of the texture 154
5.2.4 Relating texture to strain: Schmid factor 155
5.3 Texture Development 156
5.3.1 Starting material 156
5.3.2 Texture evolution 156
5.4 Twinning 159
5.4.1 e-twinning in calcite 159
5.4.2 Twin statistics and morphology analysis 160
5.4.3 Twin Schmid factor 162
5.5 Modeling polycrystalline plasticity 164
5.5.1 The VPFFT model applied to calcite 165
5.5.2 First comparisons 167
5.5.3 Source of differences: assumptions in experiments and model . 167
5.6 Summary 168

6 Concluding Remarks **191**
6.1 Concluding remarks 192
6.2 Suggested future directions 194

A Optical microscope images of studied samples **196**

B Additional experiments **206**

B.0.1 Description of the experiments 206

B.0.2 Zero strain experiment for first grid design 207

B.0.3 Strain maps 207

C Microfabrication Process **215**

References **217**

List of Figures

2-1 Paterson apparatus 44

2-2 Sample assembly in Paterson apparatus 45

2-3 Stress-strain curves obtained with Paterson apparatuses PI5 and PI10 46

2-4 Design of grid, version 1 and 2 47

2-5 Mayan inspired numbering 48

2-6 Three different levels of the grid organization: quadrants, domains and elemental markers 49

2-7 Photolithography process steps 50

2-8 AFM characterization of etch pits 51

2-9 Patterning on a curved surface 52

2-10 Etch pits on a patterned sample 53

3-1 Gridded surface of split cylinder 73

3-2 Split cylinder assembly (left) and Paterson rig (right) 74

3-3 Macroscopic strain for split cylinder and full cylinder 75

3-4 Marker location and topography of sample deformed to 0.36 76

3-5 Deformation of a continuum body 77

3-6 Representation of the measured area with the n point technique . . . 78

3-7 Strain tensor directions in experimental reference 79

3-8 Sample representation and triaxial test reference 80

3-9 Aspect of markers as a function of temperature 81

3-10 Zero strain experiment strain field 82

3-11 Zero strain experiment histogram 83

3-12 Optical microscope image and topography of gridded and non gridded half for sample of zero strain experiment (left at 700°C , 300MPa for 2 hours) 84
3-13 Optical microscope image and topography of gridded and non gridded half for sample deformed at 600°C , 300MPa, to 0.10 strain 85
3-14 Optical microscope image topography reconstruction and EBSD map of gridded and non gridded half for sample 86
3-15 Strain field of gridded and non gridded area 87

4-1 Stress-strain curves for experiments of temperature and strain series . 104
4-2 Macroscale strain estimation for the temperature series 105
4-3 Macroscale strain estimation for the strain series 106
4-4 Logarithmic strain for $9n$ average contoured on the undeformed mesh for temperature series 107
4-5 Logarithmic strain for $9n$ average contoured on the deformed mesh for temperature series 108
4-6 Logarithmic strain for $9n$ average contoured on the undeformed mesh for strain series 109
4-7 Logarithmic strain for $9n$ average contoured on the deformed mesh for strain series 110
4-8 Macroscopic Poisson ratio for temperature series as a function of n point average 111
4-9 Macroscopic Poisson ratio for strain series as a function of n point average 112
4-10 Von Mises effective strain for the strain series 113
4-11 Von Mises effective strain and deviation for the temperature series . . 114
4-12 Normalized Von Mises effective strain for strain series 115
4-13 Normalized Von Mises effective strain for temperature series 116
4-14 Strain distribution for the strain series experiments 121
4-15 Strain distribution for the temperature series experiments 122
4-16 Normalized strain distribution for the strain series experiments 123

4-17 Normalized strain distribution for the temperature series experiments 124
4-18 Normalized two-dimensional power spectrum of ϵ_{vm} (temperature series) 125
4-19 Normalized two-dimensional power spectrum of ϵ_{vm} (strain series) . . 126
4-20 Normalized standard deviation of ϵ_{vm} field by its mean for all experiments 127
4-21 AFM step size estimation of "micro twins" 138
4-22 Observed mechanisms in the optical microscope images 139
4-23 Mean area change for both experimental series (in %) 140
4-24 Twin area percentage for both experimental series 141
4-25 Strain partition along grain boundaries and intra granular strain for sample CMhH 142
4-26 Statistical descriptors of strain along grain boundaries (mean, std, normalized std) 143
4-27 Percentage of strain along grain boundaries for different n averages . 144
4-28 Percentage of strain along grain boundaries as a function of temperature and strain 145
4-29 Mean and standard deviation of the intragranular Von Mises strain field for temperature series 146
4-30 Mean and standard deviation of the intragranular Von Mises strain field for strain series ($9n$ point average) 147
4-31 Normalized mean(ϵ_{vm}) per grain and normalized std(ϵ_{vm}) vs area before deformation 148

5-1 Axial compression of a single crystal: elements of Schmid factor calculation 175
5-2 Pole figures for the e-twinning axis and for the c axis for starting material 176
5-3 Pole figures for the e-twinning axis and for the c axis for analyzed area before and after deformation 177
5-4 TI evolution for the strain and temperature series 178
5-5 Texture index for Pole figures a, m and r, before and after deformation 179
5-6 Texture index for Pole figures c, f and e, before and after deformation 180

5-7 Absolute normalized difference of texture indexes for ODF and poles a, m, r, c, f and e 181
5-8 Rose diagrams of the SPO (temperature series) 182
5-9 Rose diagrams of the SPO (strain series) 183
5-10 Stereographic representation of e-twinning planes in calcite 184
5-11 Twin morphology as a function of temperature, from the series deformed to 0.11 185
5-12 Twin morphology as a function of strain, from the series at 600°C . . 186
5-13 Twin morphology for experiment at 200°C , 0.03 strain 187
5-14 Twin Schmid factor for a single crystal 188
5-15 Schmid factor for e-twinning before and after deformation for sample deformed at 400°C 189
5-16 First comparison with VPFFT model 190

A-1 Whole samples after deformation 197
A-2 CMhA before and after deformation 198
A-3 CMhB before and after deformation 199
A-4 CMhG before and after deformation 200
A-5 CMhH before and after deformation 201
A-6 CMhI before and after deformation 202
A-7 CMhF before and after deformation 203
A-8 CMhD before and after deformation 204
A-9 CMhC before and after deformation 205

B-1 Stress-strain curves for first version grid experiments 209
B-2 Microscale strain maps for sample CMetCr14 210
B-3 Microscale strain maps for sample CMetCr11 211
B-4 Microscale strain maps for sample CMetCr05 212
B-5 Microscale strain maps for sample CMhA 213
B-6 Secret project sample 214

List of Tables

1.4.1 Crystal planes in calcite 25

3.5.1 Evaluation of the length error in the n point technique 71

3.5.2 Statistical description of the zero strain measurements 72

4.2.1 Experiments described in this section 98

4.2.2 Average strain from the macro-strain measurements 99

4.2.3 Statistical descriptions of logarithmic strain field ($9n$ point averaging) for temperature series 100

4.2.4 Statistical descriptions of logarithmic strain field ($9n$ point averaging) for strain series 101

4.2.5 Mean Poisson ratio for each temperature and for each averaging technique for the temperature series 102

4.2.6 Mean Poisson ratio for each strain and for each averaging technique for the strain series 103

4.5.1 Grain area measurements by digitalization of the grain boundaries . . 136

4.5.2 Grain strain statistics of effective Von Mises strain 137

5.6.1 Texture Index for areas before and after deformation 170

5.6.2 Texture Index for pole figures for analyzed area before and after deformation 171

5.6.3 Texture index of difference of odf and pf 172

5.6.4 Twinning statistics 173

5.6.5 Relative CRSS in VPFFT model for each temperature mode 174

B.0.1 Summary of experiments etched and deposited with Cr 208
B.0.2 Statistical descriptions of the strain field 208
B.0.3 Statistical descriptions of the zero strain measurements for first generation grid 208

Chapter 1

Introduction: Overview and background, creep deformation of Carbonate Rocks

1.1 Introduction

Understanding tectonic processes requires a precise description of the strength of the materials involved. Such descriptions are rendered more difficult because rocks are complex materials, and because deformation occurs under a broad range of thermodynamic conditions, length scales, and duration.

Observations of rock microstructures suggest natural deformation may occur by more than one physical mechanism, either consecutively or concurrently. Depending on the geologic situation, these mechanisms might include granular flow, cataclasis, and crystal plasticity; additionally, mechanical strain might be accompanied by metamorphic reactions, grain growth, dynamic recrystallization, redistribution of second phases, or fluid transport. Both natural observations and laboratory experiments indicate there is a complex interplay among all these possibilities (Delle Piane, Burlini, & Kunze, 2009; Delle Piane, Wilson, & Burlini, 2009; Herwegh & Evans, 2000; Herwegh & Handy, 1996; Herwegh et al., 2003; Oesterling et al., 2007; Rutter, 1999; Xu

et al., 2009).

First order descriptions of the strength of the lithosphere often involve characterization of deformation mechanics into regimes that identify the dominant mechanism accommodating strain, e.g. friction sliding, brittle fracture, or various mechanisms operating during crystal plasticity [among many examples see Kohlstedt et al. (1995)]. Such models are useful in conceptualizing natural deformation and have the advantage that they are in rough agreement with field structural observations, but it has always been clear that many important details are ignored. For example, it has long been apparent that transitions between the various individual regimes occur over a broad range of pressure, temperature, and pore-fluid conditions (Tullis & Yund, 1977).

In this thesis, I focus on natural deformation styles that occur at temperatures and pressures high enough to suppress cataclastic mechanisms. Rocks with low porosity that deform by mechanisms other than friction sliding or cataclasis are non-dilatant and have strengths that depend strongly on strain rate and temperature. Consequently, such flow may properly be called creep (Orowan, 1953). Under these conditions, mechanical behavior is frequently described by constitutive laws developed from model-based phenomenology (Frost & Ashby, 1982). Owing to the slow rate of strain and the large strains accumulated during natural deformation, strength transients are often considered to be unimportant, and thus, the models suppose that the rocks are deforming under steady-state conditions, and that inelastic strain is spatially homogenous on scales larger than a few grains. One assumption particularly critical in the development of deformation maps is that the strain rate can be expressed as a simple function of thermodynamic variables, which might include temperature, mean stress, differential stress, and grain size. The appropriate function is chosen from a set of models developed to describe creep rates limited by a particular dominant mechanism.

In their consideration of deformation mechanisms, Frost and Ashby (1982) and, subsequently, many others, make a distinction between high-temperature power-law creep and low-temperature plasticity, occurring below 0.3 melting temperature. Note that deformation in both regimes is rate-dependent, and so, strictly speaking, both

are creep mechanisms. As an example of a steady-state flow law, consider the general power-law, possibly grain size sensitive, creep model developed to describe deformation where strain is accommodated by dislocation motions, grain boundary sliding, and/or diffusional flow:

$$\dot{\epsilon} = A\,\sigma^n\,d^{-m}\,\exp\left(-\frac{Q_d}{RT}\right) \tag{1.1}$$

Where $\dot{\epsilon}$ is the strain rate, A is a material and creep process dependent constant, which formulation is dependent on the micro-mechanical models of creep, d is the average grain size, Q_d is the activation energy, σ is the differential stress, T the temperature, and R is the usual gas constant.

Theory and experiments indicate that the values of the sensitivity of strain rate to stress, n, and to grain size, m, are characteristic of a particular deformation mechanism. For example, for Nabarro-Herring creep, $n \cong 1$, $m \cong 2$; for Coble creep, $n \cong 1$, $m \cong 3$; for climb-limited dislocation creep, $n \cong 3-5$, $m \cong 0$; and so on (Frost & Ashby, 1982; J. Poirier, 1985). Likewise, values of A, Q_d have characteristic values for each material and mechanism.

Deformation maps are extremely useful in conceptualizing complex creep behavior over a broad range of conditions, and they are in rough agreement with field structural observations, but they also have limitations. They are commonly constructed for single-phase materials with constant structure, that are deforming in steady-state. Consequently, transient changes in strength or microstructure are not considered.

1.2 Correlation between mechanical history and microstructure

Strain localization is common within crustal orogenic belts, where field studies often conclude that displacements of kilometers were accommodated in shear zones with widths of meters (S. M. Schmid, 1975; Burg et al., 1981; Groshong Jr. et al., 1984; Pfiffner, 1982; Bestmann et al., 2000; Herwegh & Kunze, 2002; Ebert et al., 2007;

Austin et al., 2008). Such zones often occur within carbonate rocks, and their structures suggest that strain is accommodated mainly by crystal plastic flow (i.e., processes other than cataclasis). Localization is typically accompanied by major changes in grain size, crystallographic preferred orientation (CPO), major and accessory phase chemistry, pore geometry, and phase dispersion [e.g. Ebert et al. (2007); Herwegh et al. (2005); Oesterling et al. (2007); Pfiffner (1982); Romeo et al. (2007); Rutter et al. (2007)]. Such field observations, as well as extensive experimental evidence over a broad range of confining pressure (P=0-600 MPa), temperature (T=300-1300 K), and strain-rate ($\dot{\epsilon}$ 10×10^{-3}-10×10^{-7} s^{-1}) indicate that the strength of calcite rocks will undergo transient hardening and softening as dislocation structure, grain size and CPO (crystallographic preferred orientation) evolve during inelastic straining (Barnhoorn et al., 2005; Burg, 1999; Hobbs et al., 1990; Montési & Zuber, 2002; J. P. Poirier, 1980; Rutter, 1999). Despite the existence of extensive mechanical data for calcite rocks [D. J. Barber and Wenk (1979); De Bresser and Spiers (1991); Kohlstedt et al. (1995); Rutter (1995, 1998) and references therein], current constitutive laws do not explicitly include changes in such parameters as solid solutes (Freund et al., 2004; Herwegh et al., 2003; Xu et al., 2009), second-phases (Barnhoorn et al., 2003; Bruhn et al., 1999; Dresen & Evans, 1993; Renner et al., 2007; Rybacki et al., 2003; Walker et al., 1990), dislocation microstructure (De Bresser & Spiers, 1991; De Bresser, 1996; De Bresser et al., 2002; Renner et al., 2002), twinning (Rowe & Rutter, 1990), CPO (Barnhoorn et al., 2004; Pieri, Kunze, et al., 2001; Takeshita et al., 1987; Wenk et al., 1986), grain size (Renner et al., 2002), or porosity (Xiao & Evans, 2003). Thus, one particularly important key in modeling the evolution of strength is to identify the important structure variables and to understand the way that they change (Evans, 2005).

1.3 Overview of this dissertation

One goal of my thesis was to quantify the relative contributions to inelastic strain of twinning, grain boundary sliding and intracrystalline dislocation motion mech-

anisms, while under pressure and at several temperatures. The microscale strain mapping technique described in this thesis also allows one to identify characteristic wavelengths of the strain heterogeneities. In addition, by deforming samples to different total strains, it is possible to see how those parameters evolve during deformation. In so doing, it should be possible to understand more fully the elemental processes contributing to the macroscopical rheology of the rock. In particular, mapping strain at a micrometric scale offers a unique opportunity to measure the partitioning of strain between grain boundaries and intracrystalline regions. Furthermore, it provides a signature of the strain development as opposed to only analyzing the final strained state, and gives a better sense of the accuracy of a steady-state description. Much of my thesis work was spent in the development, of experimental and computational techniques to allow the tracking of strain. I applied this analysis of strain to creep deformation of Carrara marble, but this protocol has the potential to be applied to many other materials in different deformation regimes. In the remainder of this chapter, I review some basic knowledge about creep deformation mechanisms that operate in carbonates. Chapter 2 and 3 describe the experimental and computational techniques in detail. Chapter 4 focuses on results concerning the strain heterogeneities that developed in Carrara marble during creep deformation, their characteristic wavelengths and the partition of strain among grain boundaries and intracrystalline processes. Chapter 4 deals with the crystallographic analysis of the deformation and a first application of an FFT viscoplastic deformation model. Finally, in Chapter 6, I discuss future developments of the technique and suggest possible future applications of the microstrain analysis.

1.4 Background on creep deformation in Carrara marble

1.4.1 Flow laws of creep deformation for calcite rocks

Single crystal calcite and carbonate rocks have been extensively studied, and three major regimes of steady-state creep have been delineated following the model based phenomenology introduced by Ashby (1972).

At high stress and low temperature, flow is best described by an exponential law (power law breakdown regime) where equation 1.1 does not hold. Dislocation glide and mechanical twinning operate (Turner et al., 1954; H. Heard, 1963; H. C. Heard & Raleigh, 1972; S. Schmid, 1976; S. Schmid et al., 1977, 1980). At intermediate stress, flow is often described by the power law in 1.1 that is grain size insensitive, with a stress exponent $n \geq 4$. Deformation is associated to dislocation creep, cross-slip, climb and dynamic recrystallisation by subgrain rotation and grain bulging. Some grain boundary sliding may occur (H. C. Heard & Raleigh, 1972; S. Schmid, 1976; S. Schmid et al., 1977, 1980; Walker et al., 1990; Rutter, 1995; De Bresser & Spiers, 1993). At higher temperature and lower stresses, the observed flow law for calcite depends strongly on grain size and diffusion creep and grain boundary sliding (GBS) are thought to dominate. For fine-grained limestone, creep is described by a power law with $n \leq 2$; and deformation may be accommodated by GBS aided by diffusion creep(S. Schmid, 1976; S. Schmid et al., 1977; Walker et al., 1990). For larger grained rocks like Carrara marble, $n \leq 4$; and dislocation creep , dynamic recrystallization by grain boundary migration are predominant (S. Schmid et al., 1980; Rutter, 1995; Walker et al., 1990).

1.4.2 Deformation mechanisms in calcite

Calcite crystal structure

Calcite has rhombohedral symmetry, with point group $\bar{3}2/m$ and space group $R\bar{3}c$. In the calcite structure the cation Ca^{2+} and the CO_3^{2-} groups form alternate layers

parallel to the basal plane. The CO_3 groups are planar triangles oriented normal to the three-fold inversion axis and rotated 180° about this axis (M. Paterson, 1979). The structure can be described as a face-centered rhombohedron, containing four $CaCO_3$ units and corresponding to a distorted face centered cubic cell like the halite NaCl structure. However, this four $CaCO_3$ is not a true unit cell: the primitive cell contains two $CaCO_3$, a morphological cell is also often used and contains 32 $CaCO_3$ units. The calcite structure can therefore be described by different cells that are either rhombohedral or hexagonal resulting in multiple conventions and ensuring confusion. The primitive unit cell is a steep rhombohedron containing two $CaCO_3$ and having parameters $a_{rh} = 0.6375$ nm, and $\alpha = 46.05°$. The structural unit cell is most commonly used (M. Paterson, 1979) and is described by an hexagonal prism with $a_{hex} = 4.99$ nm and $c_{hex} = 17.06$ nm.

Although much of the literature of deformation has used the morphological cell, the structural cell is required for interpreting diffraction patterns. Any ambiguity is removed when planes and directions are referred by the common letter designations given in table 1.4.1.

Deformation processes in calcite

Intracrystalline plastic deformation in calcite occurs when dislocations glide, climb or cross-slip on crystallographic planes. Material displacements on the glide plane occur in the direction of the dislocation Burgers vector. The critical resolved shear stress (CRSS) is defined as the shear stress on the slip plane resolved in the slip direction which is a minimum necessary stress to produce dislocation motions. The actual resolved shear stress is a function of the applied stress and of the orientation of the crystal to respect to the stress direction. When the actual shear stress exceeds the critical, slip occurs for a given strain rate. Similarly, mechanical twinning will occur when the actual resolved shear stress reaches a critical value on a twinning plane. Twinning results in two connected crystalline regions separated by a twin boundary. The twin and host lattices differ by a fixed simple shear. The amount of shear being fixed and determined by the condition that the lattice in one half-space is

a reflection or a 180° rotation of the lattice in the other space, relatively to the twin plane (Christian & Mahajan, 1995). Dislocation slip involves the sliding of adjacent planes of atoms past one another aided by the movement of dislocations and can, in theory, accommodate an infinite amount of strain, whereas mechanical twinning can only accommodate a fixed maximum shear strain. The classical notation of slip planes and directions is used to describe slip and twinning: $\mathbf{x}^{\pm}\{\mathbf{hkil}\} < \mathbf{uvtw} >$ identifies the symmetrically equivalent slip planes $\mathbf{x}\{\mathbf{hkil}\}$, and $< uvtw >$ the slip directions, the superscript indicates the slip sense.

Historically, calcite has been the subject of pioneering studies of crystal plasticity. Crystal twinning was studied on single crystals by the firm application of a blade across the edge of the cleavage rhomb as early as 1860 (Dove, 1860). Later, the development of more elaborated deformation apparatuses allowed more precise studies on calcite single crystals and rocks. Studies on Yule marble (Griggs et al., 1953; Turner et al., 1956) and single crystals (Turner et al., 1954) provided great insight into the relative importance of twinning on $\mathbf{e}^{+}\{\bar{1}018\} < 40\bar{4}1 >$ and slip on $\mathbf{r}^{\pm}\{10\bar{1}4\} < 20\bar{2}\bar{1} >$ and on $\mathbf{f}^{\pm}\{\bar{1}012\} < 2\bar{2}01 >$. Later, additional slip systems on **a** and **m** were proposed (M. S. Paterson & Turner, 1970; Turner & Heard, 1965; Thomas & Renshaw, 1967). Later studies (De Bresser & Spiers, 1990, 1993, 1997) refined the understanding of calcite crystal plasticity, gave more constraints on the CRSS of each slip system, and proposed an additional basal slip $\mathbf{c}(0001) < 11\bar{2}0 >$ and at higher temperatures (above 700K) the replacement of $\mathbf{f}^{\pm}\{\bar{1}012\} < 2\bar{2}01 >$ by $\mathbf{f}^{\pm}\{\bar{1}012\} < 10\bar{1}1 >$. The addition of these systems considerably improved the prediction of textures at higher temperature (D. Barber et al., 2007). An additional slip system, $\mathbf{r}^{\pm}\{10\bar{1}4\} < \bar{1}2\bar{1}0 >$ has been suggested based on analysis of texture development (Pieri, Kunze, et al., 2001).

Letter symbol	Rhombohedral morphological cell		Structural (X-ray) cell
	Rhombohedral indices h k l	Hexagonal indices h k i l	Hexagonal indices h k i l
a1	$1\bar{1}0$	$2\bar{1}\bar{1}0$	$2\bar{1}\bar{1}0$
a2	$01\bar{1}$	$\bar{1}2\bar{1}0$	$\bar{1}2\bar{1}0$
a3	$\bar{1}01$	$\bar{1}\bar{1}20$	$\bar{1}\bar{1}20$
r1	100	$10\bar{1}0$	$10\bar{1}4$
r2	010	$\bar{1}101$	$\bar{1}104$
r3	001	$0\bar{1}11$	$0\bar{1}14$
e1	011	$\bar{1}012$	$\bar{1}018$
e2	101	$1\bar{1}02$	$1\bar{1}08$
e3	110	$01\bar{1}2$	$01\bar{1}8$
f1	$\bar{1}11$	$\bar{2}021$	$\bar{1}012$
f2	$1\bar{1}1$	$2\bar{2}01$	$1\bar{1}02$
f3	$11\bar{1}$	$02\bar{2}1$	$01\bar{1}2$

Table 1.4.1: Crystal planes in calcite, referred by letters and by indices using the structural (X-ray) cell and the morphological cell

Chapter 2

Methodology for the Microscale Strain Mapping technique

Abstract

A description of the partition of strain among identified deformation mechanisms, their evolution during the deformation, and the variables better describing such evolution are necessary to improve the micromechanical models of creep. The microscale strain mapping technique gives the strain field at a micrometric scale and provides a better description of strain accommodation. The technique consists of a combination of the split cylinder technique (Raleigh, 1965; Spiers, 1979; Xu & Evans, 2010) with microfabrication technology used in the semiconductor industry. A metallic grid with an embedded coordinate system was deposited onto a polished surface of a half cylinder. A lift-off technique was used to pattern the surface with a designed grid containing an embedded coordinate system. The technique uses a photosensible material as a shadow mask and metal plasma to cover the exposed surface. The best metal combination for this application was found to be a double layer of Chromium (20 nm) and Gold (30 nm). The design of the pattern is a key factor for the success of the automated analysis and the current grid version is described in detail. Additional developments of the technique, such as the imprint of a curved surface, were implemented and described for future applications.

2.1 Introduction

This thesis involved the development of a new experimental technique in order to extend the strain marking technique. The split cylinder technique (Raleigh, 1965; Spiers, 1979; Xu & Evans, 2010) was improved with the use of microfabrication techniques. The presented patterning technique does not required the introduction of a metal foil used in the past which considerably improved the recovery and coupling of the surfaces. The designed grid containing an embedded coordinate system facilitates the identification of areas before and after deformation, and facilitates the analysis of larger areas as well as the tracking of strain at several length scales. Considerable time was spent in finding an effective procedure to precisely mark the polished surface of a rock, and in optimizing the pattern design. The protocol will be described in detail in section 2.3 to ensure its reproducibility. The technique is very flexible and could be applied to many other materials. The first part describes the split cylinder set-up and the conventional triaxial tests used to describe the development of strain heterogeneities during creep deformation. The second part describes the photolithography technique and the precise protocol developed to mark the half cylinders, and finally the characterization techniques used.

2.2 Split Cylinder set-up

2.2.1 Preparation of the half cylinder composites

The split cylinder technique (Raleigh, 1965) combining petrographic and metallurgic techniques was devised for the study of slip in crystals in experimentally deformed rocks. Later, Spiers (1979) used this technique to determine the rotation of individual grains leading to an e-maximum fabric during axi-symmetric compression of marble. Because the grain orientation was measured before and after deformation, grain ro-

tation could be related to microstructure development. In Spiers experiments, two half cylinders were assembled together with a 0.125 mm thick platinum spacer and a 50 μm mesh, 10 μm thick copper grid in the middle, and deformed in a fluid medium testing machine at 400° C and 200 MPa. The grid adhered to the Pt spacer but also left an impression in the calcite grains, allowing for micro-analysis of deformation. The technique presented here is a combination of the split cylinder set up and micro-fabrication technology. One face of the split cylinder is imprinted with a specifically designed grid of 10 μm resolution, containing an embedded coordinate system. The design and the photolithography technique will be explained in more detail below.

The samples were cored from a single block (and along the same direction) of Carrara marble, a coarse-grained, nearly pure calcium carbonate rock of Liassic age quarried from the northwestern Alpi Apuane region of the Appenines fold and thrust belt in Italy (Coli, 1989). This marble is composed mainly of calcite (impurities are never more than 5% of the total mass, and are not more than 1% for the sample used here). The particular sample used in this work has a granoblastic microfabric, with roughly equiaxed grains (Molli et al., 2000). Structural field observations and geochemical measurements suggest that this marble has probably been exposed to metamorphic temperatures sufficient to coarsen the grains, under small or no deviatoric stresses (Molli & Heilbronner, 1999). Although marbles with type A fabrics are largely isotropic, there may be a weak preferred orientation inherited from earlier deformation episodes: some of the grain boundaries are mildly undulose, and some contain thin (2 to 3 μm) e-twins. This material is useful as a test material for these experiments, because it has been studied extensively by many investigators, is nearly a single mineral phase, and has large, equi-axed grains.

The samples were cored into 20 mm cylinders long and 15 mm diameter. These were cut in half with a diamond blade of 300 μm thickness. Each half was then polished in different steps (Silica grit, 12, 9, 5, 3, 1 and 0.3 μm aluminum oxide),

finishing with colloidal silica (0.03 μm). The purpose of the polishing is to obtain a surface polished to EBSD standards, and to reduce the relief between grains and optimize the microfabrication process described in 2.3. After the flat surfaces were polished, the outer diameter of the cylinders was ground down to a diameter of 10 mm. The final sample is therefore an assembly of two polished half cylinders, 20 mm long with a radius of curvature of 5 mm.

2.2.2 Gas apparatus triaxial deformation tests

Paterson apparatus

The experiments were performed in two Paterson-type gas-medium high-pressure high-temperature triaxial deformation apparatuses, PI-5 at MIT and PI-10 at the University of Minnesota (Figure 3-2 a and b). A detailed description of the apparatuses can be found in M. S. Paterson (1990). Both apparatuses have the same components (Figure 3-2 c), the main difference between them is that PI-10 is equipped for torsion experiments, but in this work only triaxial compression experiments were performed.

In both rigs, argon gas is used as a pressure medium and a three-zone furnace provides a hot-zone about 3 cm long. Calibrations prior to the experiments with a moving thermocouple assure a constant temperature profile with fluctuations of $\pm 2°C$ or better over the length of the hot-zone. The temperature is monitored with a k- or s-type thermocouple located 3 mm away from the top of the sample during a deformation experiment. The pressure is first increased to 100 MPa in 10 to 20 MPa increments with the gas booster, then the furnace is turned on and the temperature is increased at a rate of 1 °C /s together with the confining pressure. The target pressure-temperature (P-T) conditions (P = 300 MPa, T = 400 to 800°C) were reached typically within one hour. Pressure was maintained constant within ± 5 MPa or better over the duration of the experiment. The P-T conditions were maintained

constant for 30 minutes before the actuator was advanced so that the temperature profile has time to settle. The actuator is advanced at a constant displacement rate and its position is monitored internally in PI-10 and externally to the pressure vessel in PI-5. Piston displacement rates of 0.2 μm.s^{-1} to 2 μm.s^{-1} were applied, corresponding to strain rates of 1×10^{-4} to 1×10^{-5} s^{-1} in the 20 mm long samples. All the experiments presented in Chapter 3 were performed at 3×10^{-5} s^{-1} (displacement of 0.6 μm.s^{-1}).

The load recorded by the internal load cell, together with the piston position (corrected for apparatus stiffness in PI-5, recorded internally in PI-10) are used to derive stress-strain curves. To calculate the average stress on the sample, constant volume deformation is assumed (i.e. cross sectional area increases with increasing strain). After reaching the desired amount of strain (up to 0.36 strain in coaxial compression) the experiments were quenched by turning off the power to the furnace, cooling from 800°C to 300°C occurs typically at cooling rates of 0.6°C s^{-1}. Simultaneously with the temperature decrease, the confining pressure is decreased and the actuator is retracted to remove load from the sample. More information concerning these triaxial tests are given in Renner et al. (2002).

Split cylinder assembly

After the surface was patterned with a grid, the half cylinders were rejoined and loaded into a copper jacket. The micro fabrication of the half cylinders will be described in detail in section 2.3, but it is worth noting here that the metal sputtered onto both halves (30 nm on each surface) is enough to ensure the separation of the assembly after deformation: no additional foil is necessary at this step. The two halves were then loaded into copper tubing swaged to the correct dimensions. The final sample assembly was composed of two alumina spacers, two alumina pistons, two zirconia pistons, and the split cylinder sample as described in figure 2-2: the total assembly

is 186 mm long.

After the deformation test, the sample was removed from the outer jacket and then split open along the reference surface. The separation of the half-cylinder assembly was relatively simple to accomplish. Even after deformation at the highest temperature explored (800°C), the separation was an easy step. It only necessitated the gentle help of a razor blade to initiate the opening and then gentle pressure applied with both hands, it is nevertheless important to note that this operation has to be done with extreme care to avoid breaking the sample.

Data treatment

In both Paterson machines, the data are recorded using LabView, various sensors give signals proportional to confining pressure, axial force, displacement, temperature and time. Axial force is measured inside the pressure vessel using an internal capacitance load cell. Displacement is measured by a LVDT (Linear variable differential transformer). At MIT, the LVDT is placed outside of the pressure vessel and the displacement data has to be corrected for the stiffness of the machine, at the University of Minneapolis the LVDT is internal and the stiffness corrections are very small. The data from both rigs are consistent and reproducible, as shown in Figure 2-3, corresponding to experiments done at 600°C , 300 MPa to different final strains at a strain rate of 3×10^{-5}.

The correction for the jacket contribution to the measured force (from which we can infer the strength of the material) is of course, dependent of the material of the jacket. All our experiments were done with copper jackets. For higher temperature, the correction was done using the power-law for creep of copper found in Frost and Ashby (Frost & Ashby, 1982), the thickness of the copper jacket is evaluated from the initial tube (OD 15mm , thickness 0.24 mm).

It is worth noting that there is a certain uncertainty regarding these corrections,

specially for temperatures lower than 500 degrees C. In addition, there may be variations in jacket strength caused by variations in composition and microstructure of the copper at all temperatures, strain rates and pressures (Erik Rybacki, personal communication).

2.3 The photolithography technique

2.3.1 Principles of photolithography

The microscale strain mapping technique relies on calculating the relative displacements of identifiable points in the deformed and undeformed configurations. The samples were patterned using a microfabrication technique (Madou, 2002), with a grid including a coordinate system for easier identification.

High-resolution patterns (with a limit of 3 μm) of very well controlled size, shape and position can be created over an entire surface. Nevertheless, applying it to a highly dissolvable and a multi-grained material was challenging and many parameters usually applied to silicon wafers had to be adjusted. The principles of photolithography are very similar to those of photography in the sense that light is used to transfer a motif from one surface to another. UV light is used to transfer a pattern from a photomask into the photoresist, a light sensitive material that has been used to coat the target material (in our case, the rock sample surface). The photomask is created by laser-drawing the designed pattern into a glass plate covered with chrome and photoresist, and then developing it. The samples are coated with a positive photoresist which becomes soluble to a specific developer after UV exposure. The samples are then exposed to UV through the photomask and developed. The samples are then etched either with a plasma gas or with an acidic solution (a 7% diluted solution of HCl for 1 s gave the most homogeneous result) and sputtered with metal in an AJA international Orion 5 sputterer. Experiments were run for samples treated with 10

nm Chromium but the visibility was poor for higher temperature experiments, these experiments are presented in Appendix B. For the experiments presented in Chapter 2, a double layer of Chromium (Cr: 20 nm) and Gold (Au : 30nm) was used.

Finally, the protective layer of photoresist is removed using (2-2-aminoethoxy)ethanol, N-methyl-2-pyrrolidine. The photolithography technique is very flexible and can be applied to many different materials providing that the parameters of light exposure and metal deposition are changed accordingly. Several metals were tested; the characteristics sought are a low diffusion coefficient to prevent contamination of the calcite, and a high melting temperature. Also, the grid has to be visible before and after the triaxial test. The grid can be sputtered directly onto the sample surface, however it was found that the markers then could slip onto the surface, making much larger the error in strain identification. Moreover, the markers were also much harder to identify after deformation.

2.3.2 Grid design

One of the great advantages of photolithography is that any motif can be transferred into a smooth surface. I used an advanced design software (AutoCAD) to create the pattern layout. As I was working on the automatization of the strain mapping and confronted with the challenge of finding a given area for pre-deformation and post-deformation EBSD mapping, I realized several improvements could be made to the initial design.

Past designs

Through my thesis, several designs were tested, a testimony to the adaptability of the technique. Figure 2-4 shows the two last versions. The first version contained no lines, only markers that were initially triangles. My initial thought was that the triangles could serve not only as strain markers but also as indicators of rotation. The

experiments proved this was not very realistic, and furthermore the triangles were harder to recognize using pattern recognition algorithms. The second version had circles instead of triangles, and the automated location was improved considerably. The last version (and the one used in the analysis presented in Chapter 3) has an improved embedded coordinate system. The elemental markers in all analyzed grids in this thesis are circles of 2 to 3 μm radius with their centers regularly spaced every 10 μm.

The numbering system was inspired by the Mayan numbering system. In the first version, the line number was contained in cartouches placed every 2,350 μm, and the column number was placed every 470 μm. The domains and the numbering system were hard to identify for large deformations.

Current version

The third version of the mask design seen in Figure 2-4 has a more elaborate numbering system in which all information is embedded in each side bar code, and each bar code is easily identified by a cross. The numbering scheme is also used as a grid marker and therefore less "non-gridded" space, where strain cannot be resolved, is left in the sample. Figure 2-5 shows the coding system used in this case. There are different levels of domains in this grid as summarized below and in figure 2-6:

- Ten quadrants defined by the intersection of double lines and identified by a number on the side of the quadrant, the identification on the side is very useful for locating the area of interest in the SEM, particularly for the Electron Backscattered Diffraction technique.

- Each quadrant contains 168 domains (14x12 crosses showing the numbering system), separated by lines or by the numbering code.

- Each domain contains 20 by 24 elemental markers, of which 20 by 20 are circles

and 4 by 20 are the numbering system (also trackable as markers).

I designed similar patterns with lines instead of circular markers, or a combination of both: lines could be better suited for studying crack propagation or grain boundary sliding. The technique is very flexible and grid designs could be adapted to each application.

In total, the polished half contains 806,400 markers spaced every 10 μm, plus marking to signal the top and each quadrant identification number. Each marker therefore has a precise address and can be tracked before and after deformation. In Carrara marble, the grain size is on average 200 μm, corresponding to an average area coverage of 400 markers per grain which ensures a very good estimation of intragranular strain.

The non-gridded half was also sputtered with a thin double layer of metal (10 nm Cr- 20 nm Au). This window helps separate the composite after deformation, while minimizing the perturbation in the out of plane direction. A simple sputtered window was enough to allow separation, even at the highest temperatures (800 ° C).

2.3.3 Protocol followed at MTL (Microsystems Technology Laboratories) at MIT

The following protocol was developed using equipment in the EML (Exploratory Materials Laboratory) laboratory at MTL (Microsystems Technology Laboratory) at MIT, but could be followed in any clean lab with the usual facilities for micro-fabrication (oven, a mask aligner for UV exposure, a thin film deposition plasma sputterer, an acid hood, a hood for polymer development and dissolution, as well as proper disposing mechanisms for acids and organic waste). The photo-lithography technique used here is a lift-off process, a method that allows structures of a target material (a double layer Chromium and Gold in this case) to be deposited on the sur-

face of a substrate (Carrara marble here) using a sacrificial material (here photoresist OCG 825). The process followed at EML is described in more detail in Appendix C.

Prior to the photolithography process itself, a mask has to be created. This is a one time process and a mask can be re-used as long as it doesn't get scratched or damaged. I first worked on the design of the mask using AutoCAD. The design is then imprinted in a glass slide covered with Chrome using a rasterizing laser machine. The mask is then developed in the same ways as the substrate (described below), with the exception that the mask is developed using an etch back process where metal is removed instead of sputtered.

There are six mayor steps of the process illustrated in Figure 2-7: preparation of the substrate and coating with the photoresist, exposure with UV mask through a mask, dissolution of the exposed polymer, thin-layer deposition of the metal (or double layer of metal in this case) and dissolution of the remaining polymer. Each of these steps have been extensively studied on Silicon wafers and have been optimized for the last ten years. Nevertheless, a rock surface represents additional challenges due to its heterogeneity, and the results may vary and may require some experimenting with certain parameters that will be signaled along the way.

The mayor steps in each step of the photolithography are described below, as well as the specifications for unconventional substrates such as Carrara marble:

1. **Substrate preparation.** The substrate is prepared to ensure a reproducible water content and adhesion of the photoresist. The samples were left overnight at 90°C then moved at 130°C for 20 minutes.

2. **Substrate coating.** A spin coater, routine for silicone patterning, could not be used due to the geometry of the sample. Aerosol was tested but did not give adequate results. The substrate was therefore manually painted with a photoresist OCG 825. This step could be improved in order to ensure a reproducible thickness of the coating, as right now it relies on the manual dexterity of the

applicator.

3. **Exposure with UV.** The substrate was placed in a mask aligner which holds the mask under vacuum, and exposed to UV for 20 seconds. The exposure time must be adjusted if the substrate or the coating method is changed as it is dependent of the photoresist thickness. The longer the exposure the easier to dissolve the pattern, but the resist can be over-exposed. On the other hand, under-exposure would result in the absence of exposed substrate rending the following steps meaningless. I should emphasize that, because of how the photoresist is applied, the coating does not have a constant thickness and can result in variation of final results within the sample.

4. **Development: dissolution of exposed polymer.** The exposed photoresist becomes soluble in the developer OCG 934:1:1. The development time is 8 to 10 seconds but that variable must also be adjusted if the substrate or the coating method is changed as it also depends on the thickness of the coating.

5. **Etching of exposed substrate.** The etching step is not necessary to pattern the substrate, nevertheless I found that it dramatically increased the recovery percentage of the grid after deformation and ensured there is no slip of the markers on the substrate during deformation, and the strain is effectively being measured at the surface. Plasma etching was tried but did not give satisfactory results because the polymer was also affected. Thus a wet etch was done. In this case, the lesser the better: a very diluted acid bath, and very short bathing times should be used. The sample was immersed in a solution of 7% diluted HCl solution for one second. The wet etch is highly dependent on the crystallography of the substrate, if the etching time is increased, each grain will have etch pits with noticeable different shape as discussed in 2.3.4. The etch pits were characterized using Atomic Force Microscopy, as seen in Figure 2-10,

the deepest pits in this pattern were about 700 nm.

6. **Target material deposition.** The material deposited is another variable that can be easily adapted to the substrate. Important material criteria are a low diffusion coefficient in calcite, melting temperature higher than the experiments, and visibility after deformation. Titanium, Chromium, platinum, gold were all good candidates and were tried. The best result was obtained with a double layer of Chromium (20 nm) and gold (30 nm). Chromium adhered well on the carbonate surface, and gold has a much higher visibility, therefore a double layer was the optimal choice. It is to be noted that other constraints might be important for other substrates. For example, the effect on O_2 fugacity might be important for an olivine substrate.

7. **Dissolution of the remaining polymer.** The non exposed polymer is dissolved in Microstrip (2-2-aminoethoxy)ethanol, N-methyl-2-pyrrolidine heated in water bath at 90°C , and if necessary, sonicated for short times (about 1s). This step is very delicate and sometimes requires to leave the sample to remain over night in the heated bath.

8. **Patterned substrate.** The result is a patterned substrate: in our case, a gridded half cylinder of Carrara marble.

The reader might find easier to understand the complete process by comparing it to the use of a dark room in photographic development. The photographic paper would be the photoresist, the equivalent of the enlarger using visible light is the aligner using UV, and the negative would be the mask. Note that enlargement is not involved when exposing a photoresist. In both cases, wet chemical treatments are necessary to complete the transformation of the photo sensitive material after being exposed to light. The analogy holds for finding the optimum exposition and developing times:

when changing the substrate it may be necessary to test and experiment with these two variables.

2.3.4 Additional technical developments

Patterning a curved surface

A mask can also be developed on flexible polymers which are basically high resolution transparencies. This mask can then be used to grid curved surfaces. I explored this technique in cylinders of Carrara marble (Figure 2-9). The resolution is lower than the one obtained in flat surfaces (10 μm between objects for the curved surface as opposed to 2 to 5 μm for flat surfaces), nevertheless the same advantages remain: customizable design and metallization process for the strain markers and possibility of etching the pattern to improve the recoverability percentage. An additional challenge in the marking of cylinders is the recovery of the markers after jacketing the sample. This could be improved by changing the etching times and using metals that do not alloy with the jacket material.

Patterning olivine (Fo50)

The photolithography technique was successfully applied to Fo50, the exposure time had to be shortened to half the exposure for Carrara marble, and the target material was Platinum. It is possible to use any specific metal alloy machined to discs of about 3 cm diameter and 1 cm thickness, so the composition of the metal sputtered can be precisely controlled to control the chemical interactions with the substrate.

Etch pits as an indicator of the crystallographic orientation?

During the technique development, different etching processes were investigated. The wet-etch proved to be the most efficient, nevertheless it brings an additional feature that has both advantages and disadvantages. The shape of the etch pits depend

on crystal orientation owing to the anisotropy of the calcite structure (Figure 2-10). Consequently, the detection algorithm is less efficient. However, the shape anisotropy might be exploited to infer information about the crystallographic orientation of the substrate. More advanced pattern recognition algorithms were investigated and this may be an interesting avenue to explore further.

2.4 Characterization techniques

2.4.1 Optical imaging

A Hirox KH-7700 digital microscope was used to study the surface developed during deformation of the originally planar surface. The microscope takes images from a succession of different focal points, spaced by 0.14 μm in height, and merges them into one 2D gray-scale image. The upper and lower limits of focal points are defined manually. The images analyzed in Chapter 3 and 4 were obtained at a magnification of x1400 using reflected light with crossed polarizers. We analyzed both the 2D gray-scale images, a synthesis of the through-focus series of micrographs of the surface, as well as topographic information obtained from such series.

2.4.2 Electron Back Scattered Diffraction

Grain orientation data was obtained using the Electron Backscattered Diffraction (EBSD) method. The EBSD method is based on the formation of Kikuchi lines. When an electron beam is focused on the tilted sample inside the SEM, some radiation is scattered diffusely and diffraction occurs. This diffuse scattering takes place in all directions. The condition for the constructive interference from diffracted electrons from a set of parallel lattice planes is governed by Bragg law:

$$n\lambda = 2d\sin\theta \tag{2.1}$$

where λ is the wavelength, d is the spacing of reflecting planes, θ is the angle of incidence and reflection and n is the order of diffraction. The scattering occurs in all directions, forming a cone normal to the reflecting plane. A flat phosphor screen is placed near the sample and Kikuchi lines are seen where the scattering cone intersects the screen. Two Kikuchi lines form a Kikichu band, and a collection of Kikuchi bands a Kikuchi pattern.

For this work, the samples were prepared for EBSD analysis by polishing as described above up to colloidal silica. The analysis was done after the patterning process, before deformation, and again after deformation, on the deformed surface without re-polishing. Samples were not coated in either case so low vacuum conditions were necessary to prevent charging. Patterns analyses were conducted using a CamScan X500FE CrystalProbe equipped with an Oxford HKL EBSD system at Géosciences, Montpellier, France. The CamScan is an environmental, field emission electron scanning microscope equipped with an Oxford HKL EBSD system. It is particularly adapted to EBSD analysis because the electron gun is tilted at 70°, which allows the Kikuchi patterns to be generated without having to tilt the sample. The operating conditions were a voltage of 15kV, a current of 3-4 nA and a working distance of 25 mm at low-vacuum conditions (2 Pa of gaseous nitrogen). Data was acquired and treated using CHANNEL5 software. Further processing was done with the MTEX open source Matlab toolbox (R. Hielscher, 2008; Bachmann et al., 2010; Mainprice et al., 2011) and will be described in Chapter 5.

2.5 Summary

The micro-fabrication technology was used to extend the split cylinder technique and develop further a microscale strain mapping technique. The application of micro-fabrication to the patterning of the rock surface improved the resolution, the ability

to locate particular areas, and the recovery rate of previous studies. For Carrara marble, the best recovery of the grid was obtained when sputtering a double layer of Chromium (20 nm) and Gold (30 nm). The samples were characterized before and after deformation with a confocal digital optical microscope and Electron Back Scattered mapping. A custom design grid composed of 806,400 markers with an individual trackable address allows one to describe deformation at a micrometric scale and across different length scales.

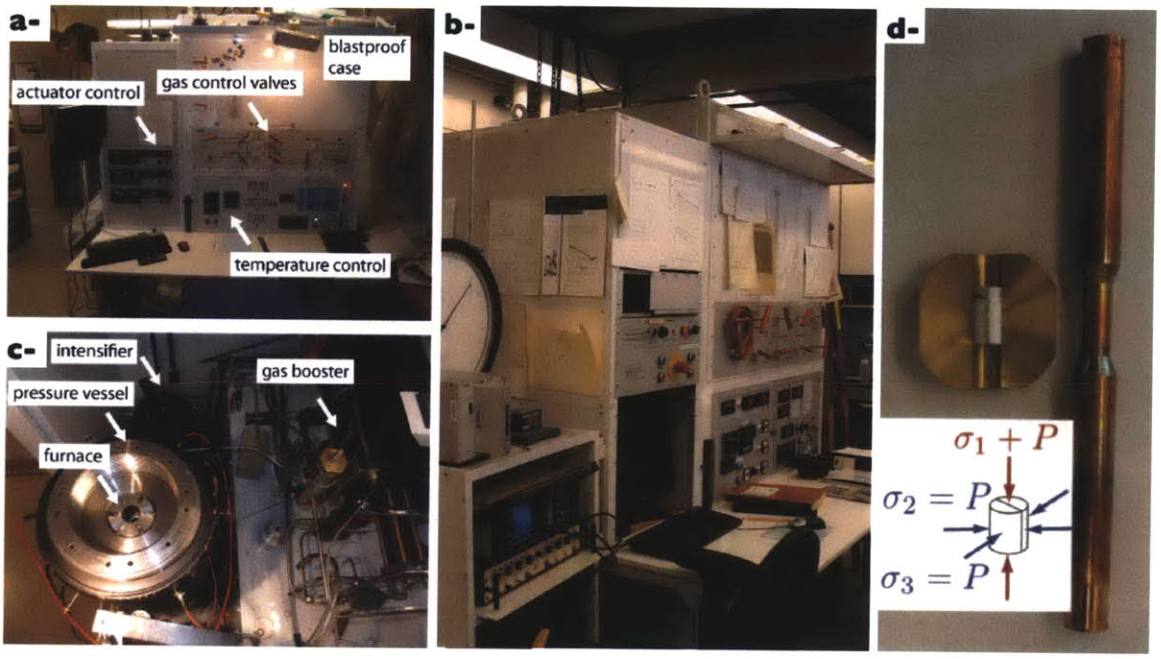

Figure 2-1: Paterson apparatus at UMN (a) and at MIT (b) and their components: three part furnace inside a stainless-steel pressure vessel and gas booster and intensifier to reach the experimental pressure of 300MPa

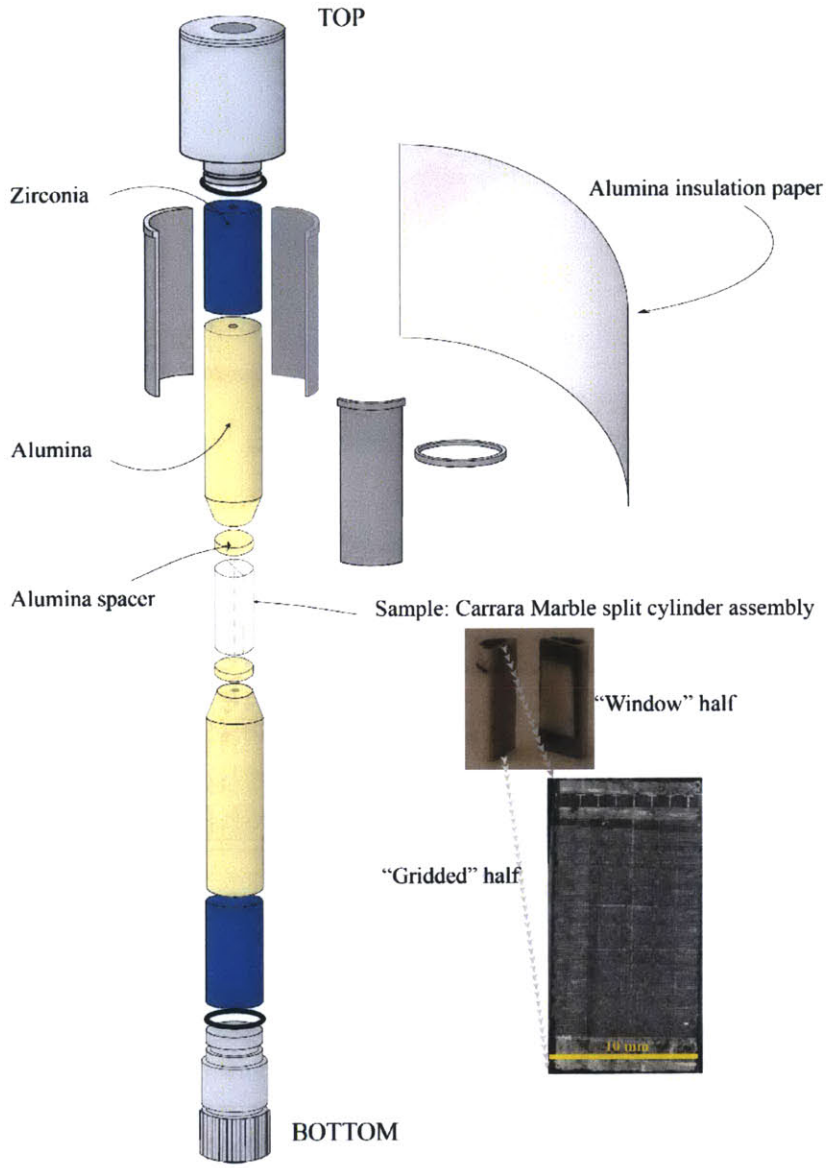

Figure 2-2: Sample assembly in the Paterson apparatus: the copper tubing is first machined to size, the bottom zirconia (30mm) and alumina pistons (50mm) are then introduced, followed by an alumina spacer (3mm), the split cylinder assembly (20mm) and again a spacer (3mm) and an alumina (50mm) and zirconia piston (30mm): the total assembly is 186 mm long

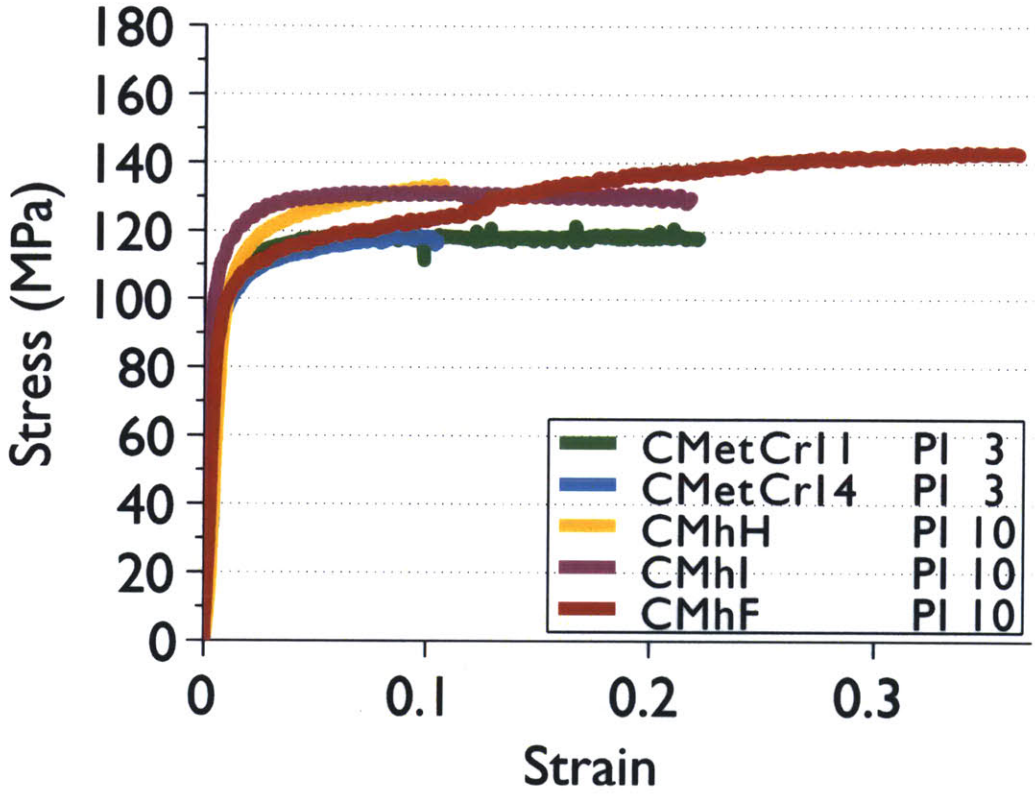

Figure 2-3: Stress strain curves obtained with Paterson apparatuses PI 5(MIT) and PI 10 (UMN), after correction for the stiffness of the rig (for PI5) and for the jacket strength (for both). All experiments were done at 300MPa, 600°C and a strain rate of $3\times10^{-5}s^{-1}$. There is a good reproducibility, even when using different apparatuses.

(a) Version 1: one cartouche for lines every 5 columns

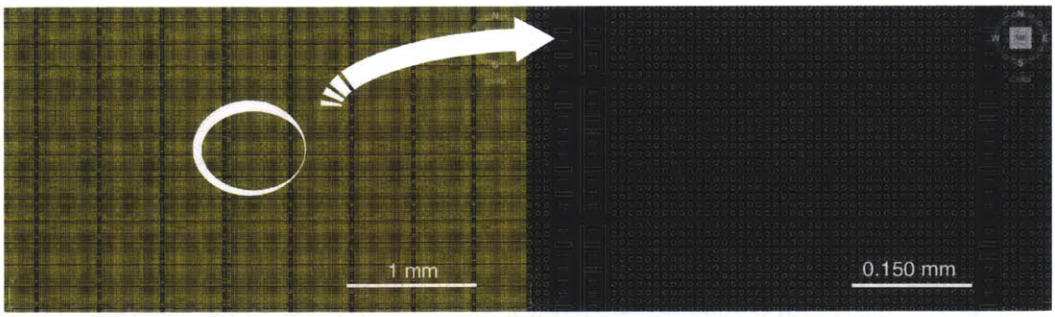

(b) Version 2: both line and column contained in number

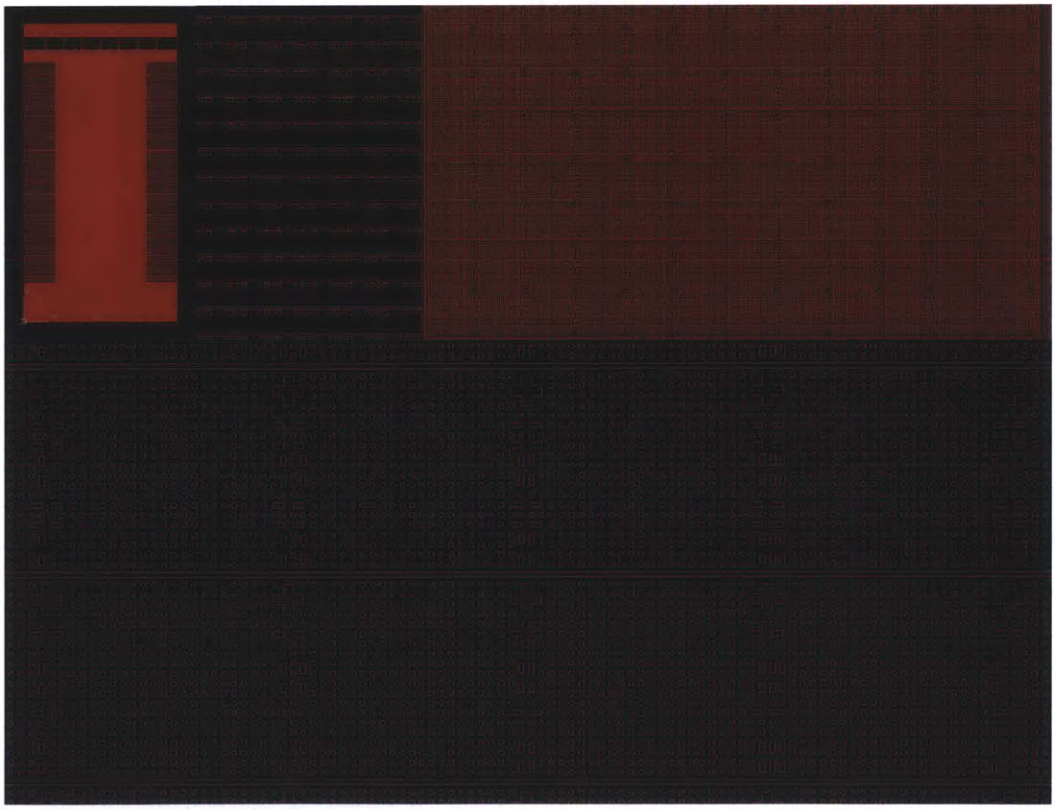

Figure 2-4: Design of grid, version 1 and 2: second design had an improved embedded coordinate system to simplify the automated algorithm

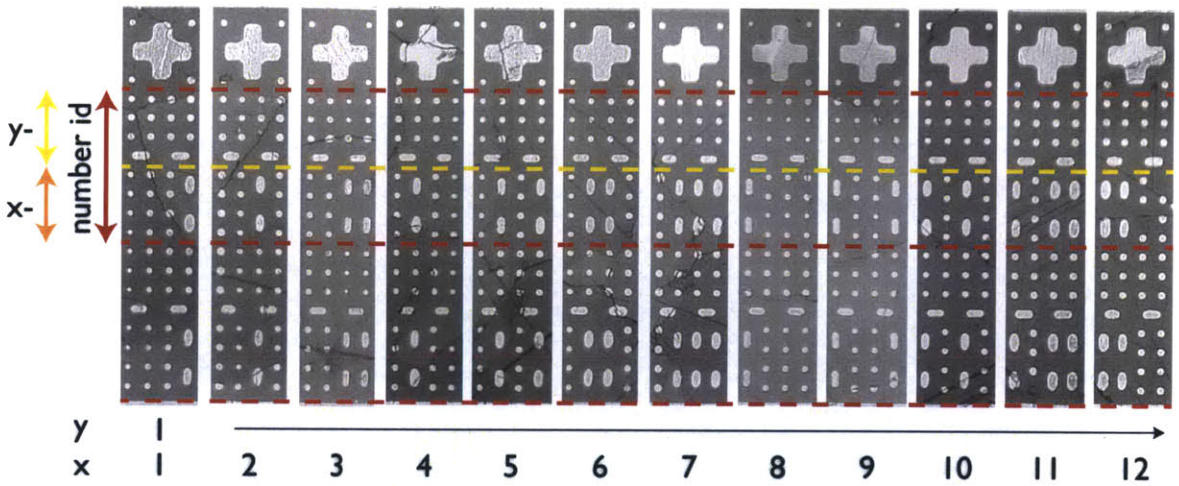

Figure 2-5: The Mayan inspired binary code use to identify each marker precisely: the information is marked twice in case an area is damaged and both coordinates x and y are marked on the side, using the same coding. The image shows the marking for x from 1 to 12, while y is constant. In each quadrant y varies from 1 to 14.

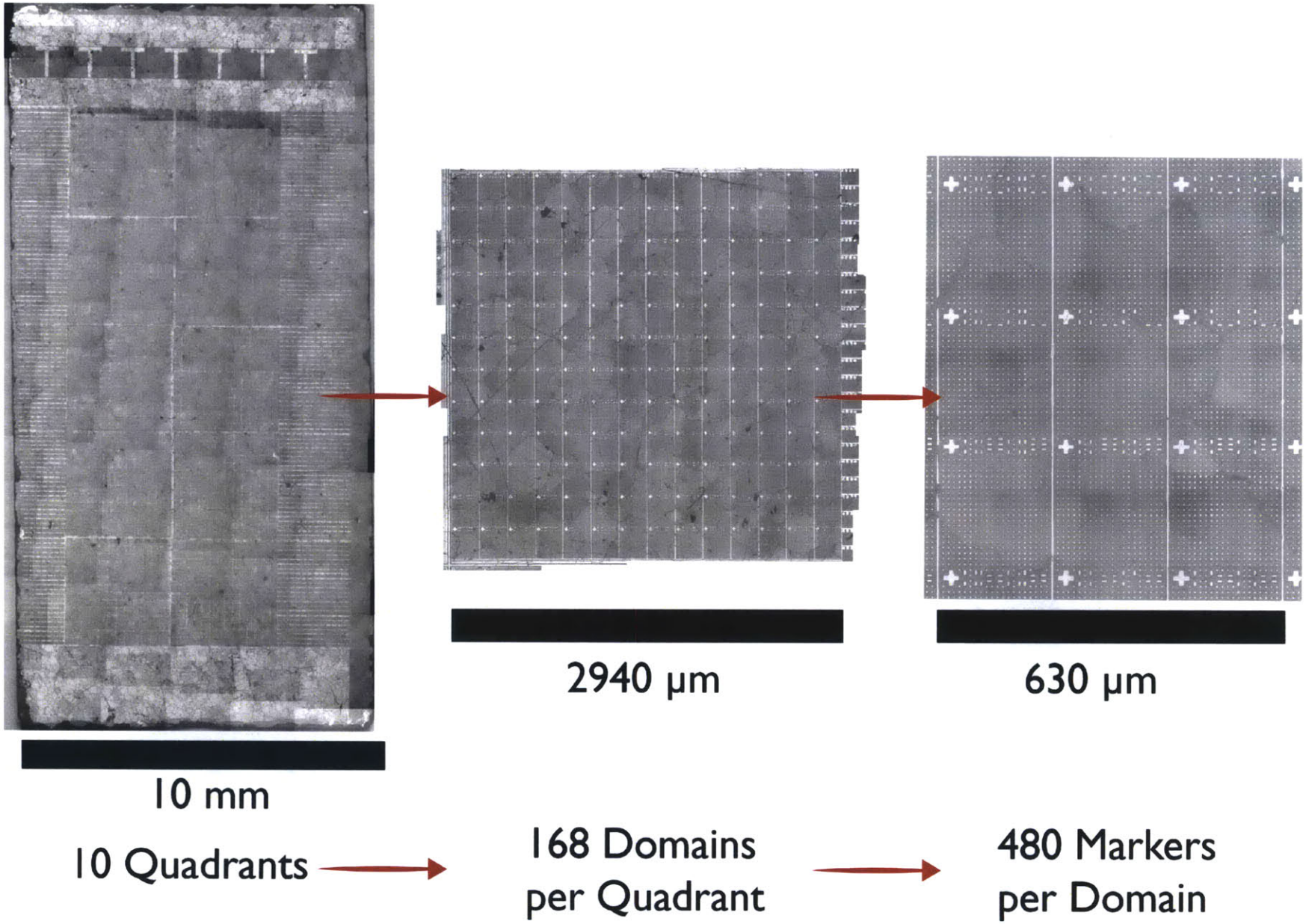

Figure 2-6: Three different levels of the grid organization: quadrants, domains and elemental markers. The sample is 10 mm by 20 mm, contains in total 806, 400 markers spaced every 10 μm and is divided in 10 quadrants of 2,940 μm by 2,880 μm containing each 168 domains of 210 μm by 240 μm containing 480 markers

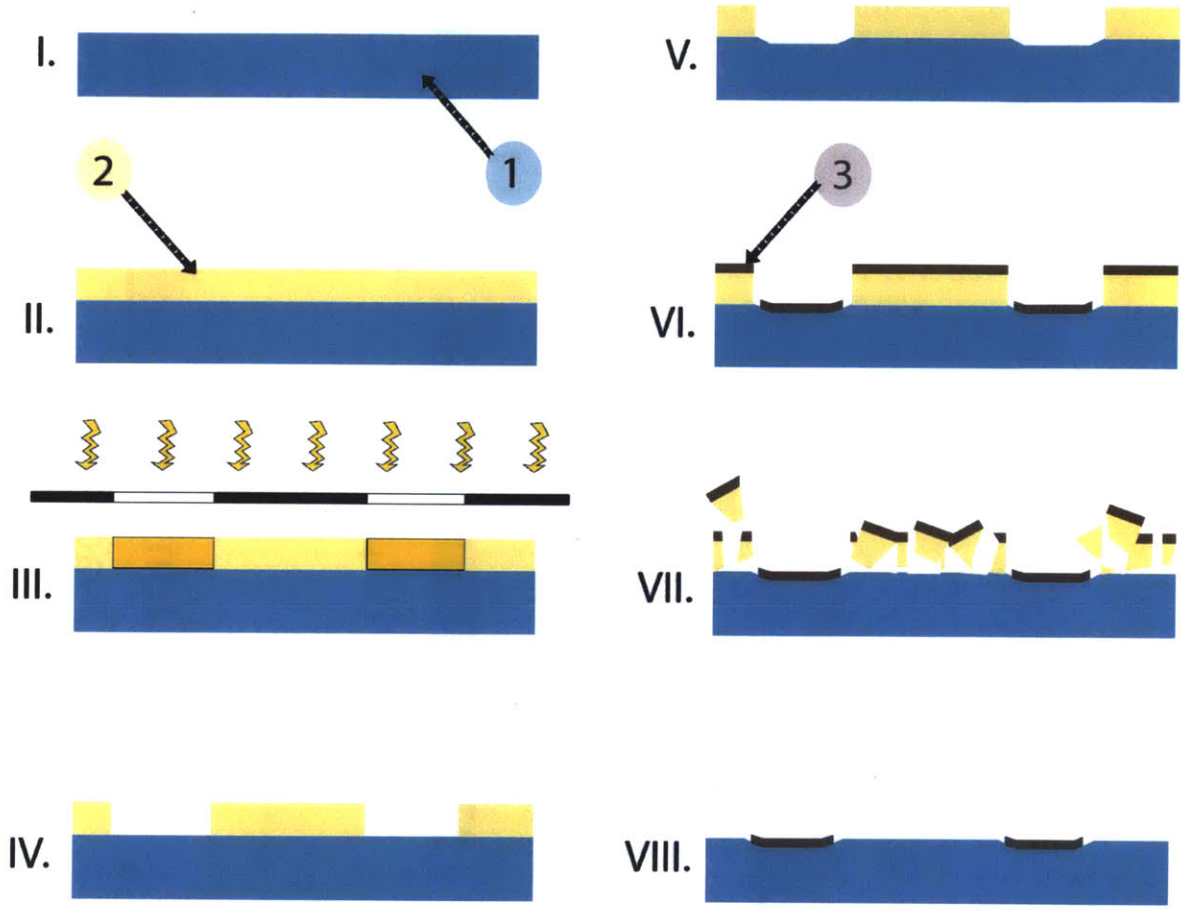

Figure 2-7: Photolithography process steps, 1 represents the substrate (Carrara marble), 2 the photoresist (OCG 825), and 3 the target material (double layer Cr+Au). The described steps are I. substrate preparation, II. substrate coating, III. exposure to UV, IV. Development, V. Etching, VI. Target material deposition, VII. Dissolution of remaining polymer and VIII. Patterned substrate. See text for description of each step.

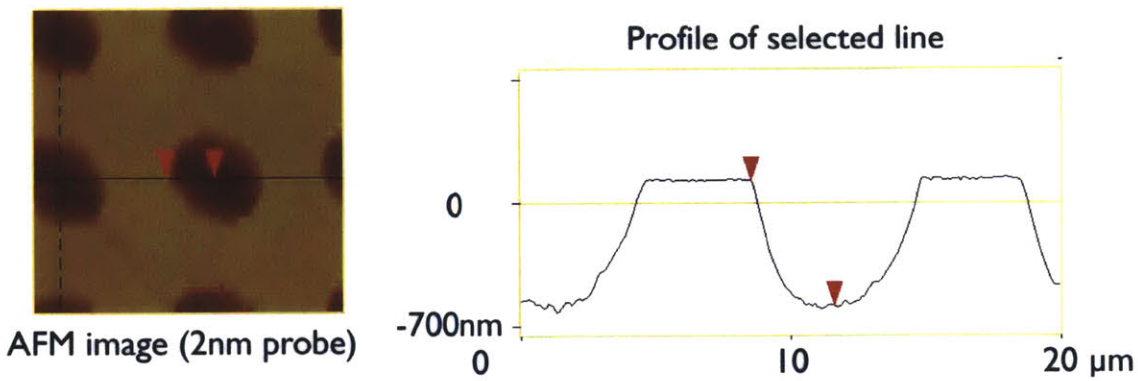

Figure 2-8: Atomic Force Microscopy characterization of etch pits with a 2nm probe: the deepest features are 700 nm deep. The samples were wet-etched, and the depth and shape of each marker is highly dependent of the crystallographic orientation of the grain

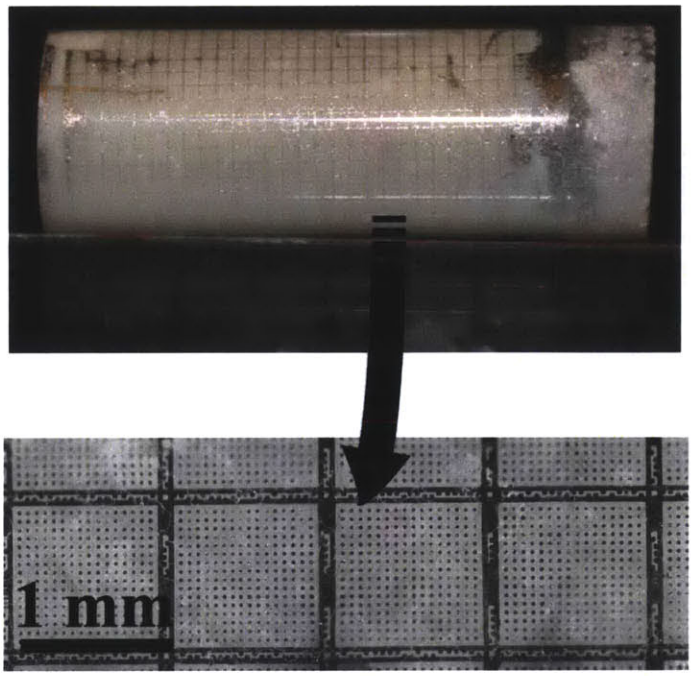

Figure 2-9: Patterning on a curved cylinder: note that the resolution is lower resolution compared to what can be achieved with a chromium mask on a flat surface

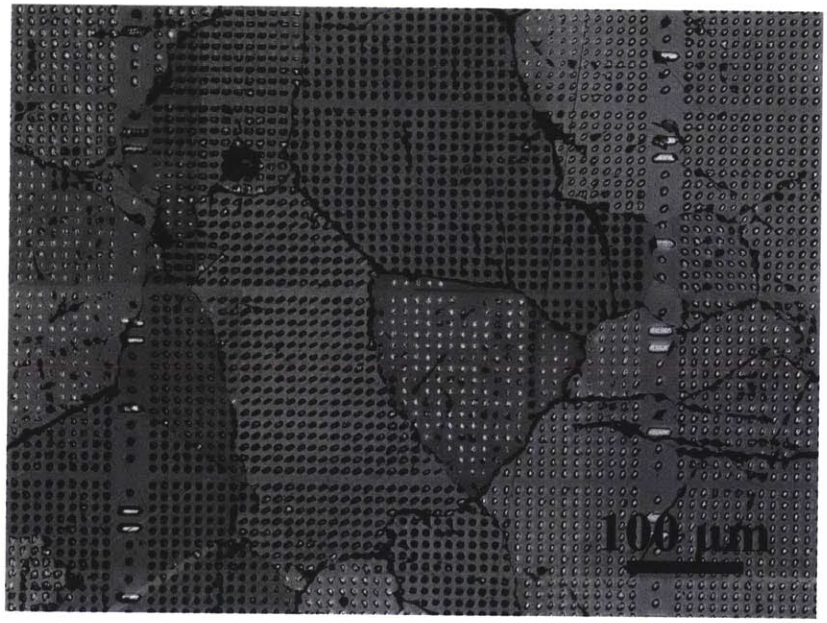

Figure 2-10: Etch pits on sample CMetCr14, note the shape of each etch pit is different for each grain (dependent on the crystallographic orientation of the grain)

Chapter 3

Microscale Strain Mapping Technique

Abstract

The finite strain is computed after characterization of the surface before and after deformation. The markers patterned on the surface of the half cylinder are located with a Hough transform algorithm and their position is tracked before and after deformation using their coordinate address. The best least square fit deformation gradient tensor $\overline{\overline{F}}$ is then found for a moving area defined by n points. The logarithmic finite strain tensor, as well as the effective Von Mises strain, are computed and used as descriptors of the microscopic strain state of the polycrystalline aggregate. The general observations of the mircroscale strain mapping confirm that this technique provides an accurate description of the strain state of the deformed material. First, the split cylinder technique does not have an effect on the macroscopic strain of the assembly. Secondly, a zero strain experiment shows an average strain of zero and a standard deviation of the measurement that depends on n but gives an error estimation of 0.001 strain for an averaging technique of $9n$ points. Furthermore, there is a perfect coupling of strain across surfaces and the deformation mechanisms in one surface induce strain in the opposite half and activate different deformation processes.

3.1 Motivation

The understanding of strain localization is necessary for a correct interpretation of current geological structures as well as for an accurate projection of future deformations. The visco-plastic deformation of Earth Materials is often considered to be homogeneous, as opposed to cataclastic and brittle deformation that is clearly heterogeneous. Nevertheless, strain heterogeneities are commonly observed during viscous deformation processes. At an atomistic level, viscous creep is the rearrangement of areas of local crystalline disorder: a heterogeneous strain field can therefore be expected even at microscopical scales.

A theoretical understanding of strain localization has been long viewed as a required step in the establishment of heterogenous flow laws in industry applications (Steif et al., 1982); it is also a required step for a better understanding of the rheology of the crust. A better description of the elementary processes involved is therefore necessary. Ideally, we would have an in-situ monitoring of the deformation processes during creep and thus document the precise evolution across temporal and spatial scales of each mechanism. To reproduce the conditions leading to crustal strain localization is challenging. We can monitor certain macroscopic behaviors, such as the strength of the material and link them to detailed microscopical observations. We are then left with a forensic case regarding the microstructural evolution during deformation.

The present chapter describes an experimental technique involving a careful characterization of the material before and after deformation, as well as precise tracking of the material deformation at conditions well beyond room pressure and temperature. A micrometric description of the strain field will provide insight not only into the characteristic wavelengths of heterogeneities but also on the evolution of microstructures during inelastic straining.

This work is focused on the development of strain heterogeneities in Carrara mar-

ble during creep deformation. As seen in the previous chapter, Carrara marble is a nearly monomineralic rock, and the core we used is composed of a minimum of 99 % calcite, making it a good natural model for this work. Furthermore, geological strains are often accommodated within shear zones in carbonate rocks, for recent examples see Austin et al. (2008). Owing to extensive laboratory and field studies, there is a comprehensive data base to compare the results to. This chapter provides a description of the split cylinder assembly and of the algorithm used to inverse from displacements to strain. The first results confirming the technique provides an accurate description of the microscopic strain state are also described here. Note that all along this study, unless noted otherwise, strain is dimensionless (and not in %) and that the geological convention is adopted: shortening strain is positive.

3.2 Strain mapping technique on split cylinder assembly

This section focuses on the experimental procedure involved in the microscale strain mapping technique. The conventional triaxial test of a split cylinder assembly is described, followed by the strain mapping algorithm, the strain analysis and finally the error analysis of the technique.

3.2.1 Patterned split cylinder

In my experiments I combined a split cylinder technique used in the past to follow the crystallographic evolution of a population of grains (Raleigh, 1965; Spiers, 1979; Xu & Evans, 2010) and a photolithography technology used extensively in the semiconductor industry (Madou, 2002). The final sample is an assembly of two polished half cylinders, 20 mm long with a radius of curvature of 5 mm, one half is microfabricated while the facing half is only sputtered with a window mask allowing the

separation after deformation, see Chapter 2 for details on the sample preparation and the microfabrication technique.

The strain mapping technique relies on the calculation of the relative displacements of identifiable points in the deformed and undeformed configurations. I designed the grid with the aim of enabling an automated detection and computation of the finite strain field. The grid design features an embedded coordinate system inspired by the Mayan numbering system that assigns a unique address to each marker, allowing for a precise location before and after deformation. Each sample contains 806,400 markers that are divided into quadrants composed of lines and columns; all coordinate information is embedded in the grid. Figure 3-1 shows the split cylinder assembly and the grid at different magnifications.

3.2.2 Macroscopical mechanical behavior in Paterson apparatus

The assembled composite, composed of the two matching half-cylinders, was then jacketed in copper tubing, pressurized to about 230 MPa and heated to the final temperature (from 200°C to 800 °C) at a rate of 25 °C /min in a Paterson deformation apparatus (M. S. Paterson, 1990), as seen in figure 3-2 . The final confining pressure was 300 MPa for all experiments.

First, it was tested whether the split cylinder set-up had any effect on the macroscopical mechanical behavior. The stress strain curves for full cylinders and split cylinders at 600°C (Figure 3-3) indicate that the macroscopic mechanical behavior of split cylinder samples is the same as the one for full cylinders, and both are in agreement with former studies (S. Schmid et al., 1980; Covey-Crump, 1998; De Bresser, 2002). It was verified that split cylinder and full cylinder have the same macroscopic mechanical behavior at temperatures as low as 200°C , closer to cataclastic behavior.

3.2.3 Characterization of the surface before and after deformation

The strain mapping technique relies on an accurate identification of all markers before and after deformation. The samples were imaged using a digital optical microscope (Hirox KH7700), both before and after deformation at x1400 magnification. After deformation, the marked surface is no longer planar, the deviation from planarity being more pronounced as inelastic strain increases. Imaging the deformed plane required the superposition of several images taken at different focal points (every 0.14 μm for the x1400 magnification). The images, between 60 and 70 for the areas presented in this study, are tiled together using the 2D tiling macro on the image analysis software Fiji (Preibisch et al., 2009). The choice of the area to be analyzed was random and was done before deformation, when EBSD data were acquired. The choice is therefore completely independent of the state after deformation and no bias was introduced. Once all the markers centers were identified during the automated image analyses, the markers were ordered via a closer neighbor algorithm into a matrix containing their address and position.

The gridded surface was initially plane, with variations in height less than 0.03 μm. After deformation, the surface was no longer flat owing to deformation out of the plane. Information about the 3D component (i.e. the relief of the deformed surface) can be obtained from the series of images taken with varying focal distances. The Hirox microscope synthesizes this information and outputs a matrix with height information for each pixel. In order to get a similar coverage as the 2D mosaic, the height matrices were stitched together following the stitching done in 2D and the height was referenced to a common 3D origin point for all of them. It is important to note that measurements in the out of plane dimension are not as precise as those in the 2D measurement. It was established by Xu and Evans (2010) that the height

resolution is no better than 0.5 μm, roughly 4 times poorer than the resolution in 2D (0.142 μm per pixel). To summarize, the acquisition of the 3D information involves:

1. Acquisition of multiple images at different focal points for each .

2. Output of height information into *.csv* files

3. Stitching of height matrices using Matlab:

    - Importing the file output by the image analysis software Fiji containing stitching information in 2D (Preibisch et al., 2009).

    - For each height matrix, calculation of the reference offset with respect to surrounding images.

    - Positioning of height information using Fiji output.

Figure 3-4 shows the identified markers and height information for an area studied for sample CMhF (deformed to 0.36 at 600 °C and 300 MPa). Note that, over length scales of 2 mm, absolute height variations are large indicating that the sample was deformed heterogeneously and was bent. Locally, the variations among the 9 closer points are not larger than 2 μ m in average. In surface analysis methods such as profilometry or atomic force microscopy, software corrections regarding the tilt are often applied. These corrections were not applied here as they are not very explicit and would introduce an unquantifiable source of error. The inversion uses the displacements of identified markers versus a moving centroid described in the following section, and so detrending at larger wavelengths is not necessary. However, it is noted that such displacement fields indicate that the actual stress state was more complicated than the standard conventional triaxial conditions assumed.

3.3 Methodology: strain mapping algorithm

The methodologies to measure the displacement field at a micrometrical scale have improved considerably these last years, thanks to an improvement both in characterization and in image analysis techniques. All methods are based on the identification of a material point before and after deformation. A grid deposited on the studied material provides an initial periodic reference and the markers can be identified before and after deformation: among many studies, one could refer to ? (?); Biery et al. (2001); Wu et al. (2006); Grédiac and Hild (2011). Digital image correlation (DIC) (M. Sutton et al., 1983; Pan et al., 2009; M. A. Sutton et al., 2009) does not require the presence of a regular grid, but it relies on the resemblance of the material before and after deformation and is therefore better suited for applications where very small deformations are applied between each correlation (Bornert et al., 2010; Grennerat et al., 2012).

The technique described here relies on the identification of the markers before and after deformation performed at high pressure and temperatures. Indeed, the material can only be characterized before and after deformation under conditions (high T and P), and this renders the image correlation difficult.

In this section, the finite strain terminology will be explained in more detail. Tensors, 2D and 3D, are signaled with a double bar and vectors with a single bar: for example the deformation gradient tensor $\overline{\overline{F}}$ and a material line $d\bar{X}$.

3.3.1 Work flow for strain analysis

After images were tiled, all image processing was done in Matlab. The markers were located via a Hough transform identifying circles of a specific radius. The algorithm works flawlessly for the undeformed sample. After deformation, markers' shape were modified. Some manual correction was required, particularly for samples deformed

at higher temperature. Figure 3-9 shows the aspect of markers after deformation for 400°C to 700°C , and it can be appreciated how the deviation from a circular shape becomes more and more pronounced. Distortion was severe for samples deformed at 800°C , not included in this study. The work flow was as follows:

1. **Before deformation:** acquisition of low and high magnification images. The whole sample was imaged at x140, selected quadrants at x700 and sections for which EBSD data was obtained before deformation were imaged at x1400. At this point, surface is flat with a 0.03 μm height variation (polished to EBSD standards up to colloidal silica).

2. **Conventional triaxial test:** compression in Paterson apparatus as described previously.

3. **After deformation:** Acquisition of 3D images at different magnifications. Strain analysis was done on images acquired at x1400 magnification. At this point, the surface is no longer planar and the images are synthesized from a series taken at several focal points (every 0.14 μm in height). The number of images required for one image depends on the difference between the lower and higher focal points but typically was around 25 (for a height difference of 3.5 μm).

4. Stitching of images using the 2D tiling macro on Fiji (Preibisch et al., 2009).

5. Pattern recognition algorithm.

   (a) Creation of structure to analyze smaller images

   (b) Application of high-pass filter to eliminate noise and Hough transform to detect circles

   (c) Correction of identified markers based on total number of circles

(d) Organization of markers in matrix with each marker address by finding closest neighbor

(e) Computation of 2D deformation gradient tensor $\overline{\overline{F}}$ from n point analysis using the strain probe technique (P-Y Robin)

3.3.2 Strain probe: n point averaging technique

The 2D local strain is calculated using an n-point strain analysis developed by P-Y Robin (pers. comm.), see also Xu and Evans (2010) for a brief description. The analysis inverts the local deformation gradient tensor $\overline{\overline{F}}$ from the relative displacement field of any number of grid markers ($n > 3$).

This least-square fitting produces the deformation gradient tensor $\overline{\overline{F}}$. $\overline{\overline{F}}$ is a 2-D second rank tensor that relates the material line $\overline{dX}$ before deformation to the same material line after deformation $\overline{dx}$ (Figure 3-5).

$$\overline{dx} = \overline{\overline{F}} \cdot \overline{dX} \tag{3.1}$$

In order to consider the local strain and eliminate rigid-body translation, the displacement is calculated relative to a moving centroid, calculated for every set of n points, both in the initial C and the final state c. The computation of the 2-D strain field operates therefore on the material lines, before $d\bar{X}_i$ and after deformation $d\bar{x}_i$.

$$d\bar{X}_i = X_i - C = X_i - \frac{\sum_{i=1}^{n} X_i}{n} \tag{3.2}$$

$$d\bar{x}_i = x_i - C = x_i - \frac{\sum_{i=1}^{n} x_i}{n} \tag{3.3}$$

For a set of n points, the technique finds the deformation gradient tensor $\overline{\overline{F}}$ that provides the best fit of the transformation of $d\bar{X}_i$ into $d\bar{x}_i$. $\overline{\overline{F}}$ can be interpreted as an

affine transformation , transforming a unit square into a parallelogram and describing the deformation in that area. In a homogeneously deformed material, equation 3.1 would have a unique solution no matter which material line is being considered. In a heterogeneous deformation, the system of equations for 3 material lines as defined in 3.1 can be analytically calculated for three points. If more than three points are taken into account, the system is over-determined, and, strictly speaking, may not have a solution.

The least square fit consists of finding $\overline{\overline{F}}$ as the best compromise for all material lines considered. The modeled displacement is given by: $\bar{dx}^* = \overline{\overline{F}} \cdot \bar{dX}$: $\overline{\overline{F}}$ is found by minimizing the sum of the square of the difference between the modeled material lines and the measured ones $\bar{dx}^* - \bar{dx}$. Conceptually, this is equivalent to searching for an homogeneous deformation that best describes the transformation of the area defined by n points. Figure 3-6 shows the area arrangement for n equal to 3, 4, 5, 9 and 25. The fewer points taken into account, the better the idea of the heterogeneity of the deformation; but when more data points are used the influence of inaccurate locations is reduced.

3.3.3 Computation of $\overline{\overline{F}}$ in 2D and 3D

The computation of $\overline{\overline{F}}$ in 2D follows the derivation explained in the strain probe by P-Y. Robin and implemented by Xu and Evans (2010). It solves for the best coefficients of $\overline{\overline{F}}$ by minimizing χ^2, the sum of the square of the difference between the modeled distance and the measured one.

$$\chi^2 = \sum_{i=1}^{n} \|d\overline{x}^* - d\overline{x}\|^2 = \sum_{i=1}^{n} \left\| (d\overline{x}^\top - d\overline{X}^\top \overline{\overline{F}}^\top)(d\overline{x} - \overline{\overline{F}} d\overline{X}) \right\| \tag{3.4}$$

This quadratic expression in $\overline{\overline{F}}$ can be minimized by equating its first derivative to 0 and solved using Cramer's rule.

The computation of $\overline{\overline{F}}$ in 3D has added complications. First, the resolution of the height information is about 0.5 μm, the error in distance evaluation is therefore about 1 μm, considerably more than what was evaluated in 2D. Finding the best fitting deformation gradient in this case would therefore give equal weight to information with different resolutions. An inversion technique taking into account should be explored in the future. Based on previous mechanical testing we assume that the deformation is isochoric (constant volume) for Carrara marble at temperatures above 300°C and confining pressure above 200 MPa, and infer the complete 3D strain tensor. The validity of this assumption can be tested as as it is shown in Chapter 4.

3.3.4 Computation of strain from the deformation gradient tensor $\overline{\overline{F}}$ in finite strain theory

A more detailed description of the deformation gradient tensor can be found in continuum mechanics books such as Reddy (2008), Malvern (1969) and Mase et al. (2010). I chose to compute the logarithmic strain or Hencky strain following Martin et al. (2013) and later Martin et al. (2014).

$\overline{\overline{F}}$ is non singular and can be decomposed into a product of two component tensors (known as polar decomposition) shown in equation 3.5, where $\overline{\overline{R}}$ is the orthogonal rotation tensor, and $\overline{\overline{U}}$ and $\overline{\overline{V}}$ are symmetric, positive-definitive tensors called right stretch tensor and left stretch tensor respectively.

$$\overline{\overline{F}} = \overline{\overline{R}} \cdot \overline{\overline{U}} = \overline{\overline{V}} \cdot \overline{\overline{R}} \tag{3.5}$$

A simpler way to think about these transformations is to imagine that the infinitesimal material line is subjected to two sequential transformations: a stretch described by $\overline{\overline{U}}$ then a rigid body rotation described by $\overline{\overline{R}}$, or first a rotation described by $\overline{\overline{R}}$ then a stretch described by $\overline{\overline{V}}$.

From the stretch tensor $\overline{\overline{U}}$ we can infer the principal direction of strain and their magnitudes, and finally infer the logarithmic strain or Hencky tensor. Several description of strain are available but the Hencky strain tensor has a number of advantages that have made it the tensor of choice for finite strain plasticity: symmetry for the inverse transformation, subsequent co-axial strains are additive, separation into volumetric and isochoric components is possible, and the trace of the tensor vanishes for isochoric transformations (Bazant, 1998). For this computation, $\overline{\overline{U}}$ is first diagonalized. This amounts to the computation of the principal directions, contained in $\overline{\overline{Q}}$ and the principal values, contained in the diagonal tensor $\overline{\overline{D}}$, of the stretch tensor $\overline{\overline{U}}$:

$$\overline{\overline{U}} = \overline{\overline{Q}}^{\top} \cdot \overline{\overline{D}} \cdot \overline{\overline{Q}} \tag{3.6}$$

The Hencky strain tensor will be refered as $\overline{\overline{\epsilon}}$ in the future and is defined as:

$$\overline{\overline{\epsilon}} = \overline{\overline{Q}}^{\top} \cdot ln\overline{\overline{D}} \cdot \overline{\overline{Q}} \tag{3.7}$$

3.3.5 Representation of strain

From the inversion technique, we obtain a local strain tensor for each centroid. The diagonal terms of the tensor correspond to the strains along the principal directions of the experiment: 11 along the cylindrical axis and corresponding to the direction of σ_1, 22 and 33 transverse to it. Figure 3-7 shows the experimental reference. The representations of strain in this work always follows this reference: the shortening strain is applied along the 11 direction. Furthermore, in all figures, both optical microscope images and microscale strain maps, the compression direction corresponds to the vertical direction as shown in figure 3-8.

The principal directions of the experiment do not necessarily correspond to the

directions of the principal directions of the local strain ellipsoid. The complete strain ellipsoid can be described by an effective strain such as the Von Mises strain presented in equation 4.6:

$$\epsilon_{eq} = \sqrt{\frac{2}{3}\left(\epsilon_{11}^2 + \epsilon_{22}^2 + \epsilon_{33}^2 + 2\epsilon_{12}^2\right)} \tag{3.8}$$

3.4 Evaluation of the strain mapping technique

This section presents the preliminary results and the experimental evaluation of the split cylinder assembly and the strain mapping algorithm developed. The experimental results for two particular series, one varying temperature, the other varying strain, will be presented in next chapter.

3.4.1 Error analysis

There are two principal sources of error that limit the resolution of the strain in the conventional triaxial test. It is worth noting that the conventional triaxial test has its own limitations, notably at high strains the deviation from a homogeneous deformation within the test due to end effects (barreling and bending), but this sections focuses solely on the sources of error in the microscale strain mapping technique.

The first error is related to a real deformation introduced by the discontinuity of the split cylinder, the second is related to the algorithm and the error in the estimation of the distance. The first source of error cannot be theoretically estimated. We expect it to be very low since the macroscopical results agree with full cylinders experiments, but the analysis of a proper "zero strain" experiment is presented in this section. The resolution on the marker's location decreases with increasing temperature: Figure 3-9 shows how the markers become progressively harder to locate as the temperature is increased. The zero strain experiment was therefore performed at the highest temperature analyzed in this study: 700°C , and is a high-end estimation of the

experimental error.

The marker location error in the algorithm can be very roughly estimated by considering the "pixel error". The location of the markers' center can be made with a two pixel error. At a magnification of x1400, each pixel represents 0.14 μm, both before and after deformation, equivalent to a high-bound estimation of the resolution of 0.56 μm.

The error in estimating displacements is summarized in table 3.5.1. For each averaging technique this table shows the equivalent area taken into account to evaluate the least square fitting deformation gradient tensor $\overline{\overline{F}}$, the equivalent dimension of a square of the same area and the percentage of error in estimating such distance (equivalent to the ratio of the error of the pixel picking divided by the equivalent distance). The error becomes less representative as more markers are taken into account, nevertheless, information about the heterogeneity is also lost. To summarize; the larger the area the less representative the picking error, but the more reduced resolution on the heterogeneity of the strain field. The error in the third dimension as measured optically by changing the focal plane height is based on the evaluation of matching halves in Xu and Evans (2010) and was estimated to 0.5 μm

A split cylinder sample was left under 300 MPa and 700 ° C for two hours. The error evaluation is therefore a higher bound estimate of the error for lower temperatures. Figure 3-10 shows the error evaluation maps for ϵ_{11} (strain along the compression direction), Figure 3-11 the distribution (binned every 0.0005 strain) and table 3.5.2 gives the average and standard deviation for every n point measurement. The mean strain (around 0.0002) remains stable as the measured area is increased, nevertheless the standard deviation decreases. Table 3.5.2 summarizes the strain data for the zero experiment. The variations in the measurement are both real and a consequence of the picking error, it corresponds here to the upper bound of the measurement error as the zero strain experiment was done at the most challenging temperature. As it

is often the case, a compromise has to be made and we chose a 9 point measurement average for the analysis of the experiments. For a $9n$ point average: the mean strain measured is practically 0 (0.0002 along the compression direction) and a standard deviation of 0.001 strain. For error propagation calculations we will use the standard deviation measure. Indeed, it corresponds both to the picking error and the amplitude of the strain field corresponding to the relaxation of the split cylinder assembly.

3.4.2 State of facing surfaces after deformation

The preparation of the split cylinder (metal window on the facing half and controlled the thickness of a double metal layer Cr-Au) allowed for a very easy separation of the split cylinder after deformation, even at temperatures of 800°C . However, the healing of the microporosity introduced by the markers, and a much stronger surface coupling at higher temperature renders the identification of the markers much more difficult for temperatures greater than 700°C . In all tests, even at the zeros experiment as shown in figure 3-12, there was an imprint of the markers from the marked surface onto the non gridded surface. Similarly, both grain boundaries and twin boundaries were imprinted from one face onto the other (figure 3-13).

Figure 3-14 shows the same area reconstructed in 3D topography, the mold like behavior and perfect coupling is clearly seen. Furthermore, the EBSD maps, represented here in Euler coloring, highlight the presence of an e-twin on the gridded half and show that the twinning caused internal misorientations in the matching surface. The EBSD image of the non-gridded half was mirrored and rotated to facilitate comparison. There is clearly continuity of strain accommodation even if different mechanisms are involved.

The strain fields evaluated in both surfaces are equivalent as it is shown in figure 3-15. The markers' position are superposable within the picking error: the surfaces are therefore perfectly coupled, and although there is a discontinuity of grain struc-

ture, there is a continuity of strain. The strain caused by a particular deformation mechanism on one half was not necessarily accommodated by the same one on the other half. The study of the interaction of both surfaces may be of use to understand the interaction between different mechanisms.

3.5 Summary

The microscale strain mapping technique allows us to infer the strain field at an unprecedented level of detail. Several experimental points are worth noting:

1. The split cylinder assembly does not affect the macroscopical behavior of the material.

2. There is undoubtedly continuity of strain across the split surface.

3. The measurement of strain can be done with a precision of 0.001 strain, as estimated by the standard deviation of the zero strain experiment.

4. At temperatures higher than 800°C the location of the markers is no longer automatable and further development in the microfabrication technique would be worth exploring to study higher temperature deformation.

Furthermore, the experimental evaluation of the strain mapping technique brought up some interesting observations regarding strain accommodation. Particularly, the perfect coupling of the facing surfaces illustrates the accommodation of strain by different mechanisms: a stress field caused by twinning activated mechanisms other than twinning on the facing half. This behavior is to be expected in a polycrystalline material where each grain is likely to deform via different mechanisms, and influence the strain on its neighbors.

	3n	4n	5n	9n	25n
averaged area (μm^2)	50	100	200	400	1600
equivalent distance (μ)	7	10	14.1	20	40
0.56 μm error in estimating distance (%)	4	2.8	1.8	1.3	0.7

Table 3.5.1: Evaluation of the length error in the n point technique. The area A defined by the n points is calculated and an effective length defined as $\sqrt{A}$ is used to estimate the percentage of 2 pixel picking error.

	3n	4n	5n	9n	25n
ϵ_{11}	0.0002	0.0003	0.0002	0.0002	0.0003
std	0.007	0.005	0.004	0.001	0.0005
ϵ_{22}	-0.005	-0.005	-0.005	-0.005	-0.005
std	0.006	0.005	0.003	0.003	0.002
ϵ_{12}	0.0002	-3×10^{-5}	-9×10^{-5}	-7×10^{-5}	-9×10^{-5}
std	3×10^{-3}	3×10^{-3}	2×10^{-3}	1×10^{-3}	6×10^{-4}

Table 3.5.2: Statistical descriptions of the zero strain measurements: note that the strain is dimensionless (not in percent), the standard deviation gives a measurement of the spread of the measurements, positives strains correspond to compression. The mean strain is almost zero and consistent for all averaging techniques.

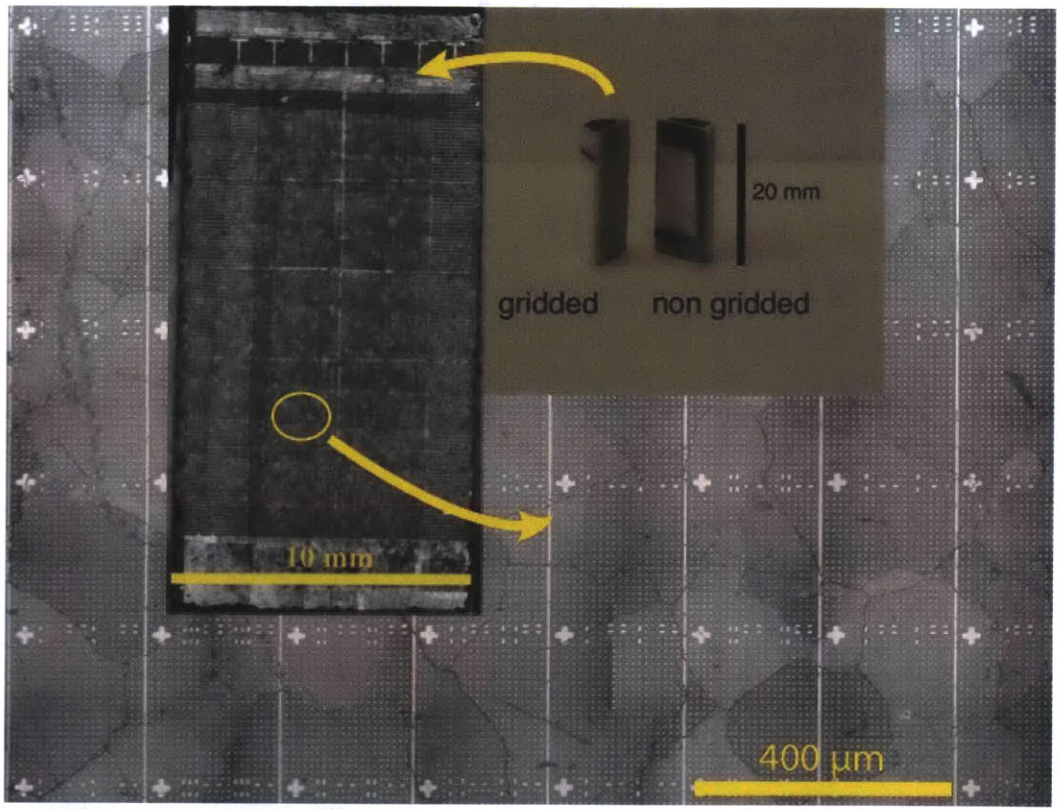

Figure 3-1: Gridded surface of split cylinder: Different scales of the grid are shown here. Only one half is gridded, the other half is sputtered with a thin double layer Cr-Au in window shape to facilitate the separation of the assembly after deformation. The grid is organized in 10 quadrants, containing each 168 domaines of 480 markers each. The markers are spaced every 10 μm

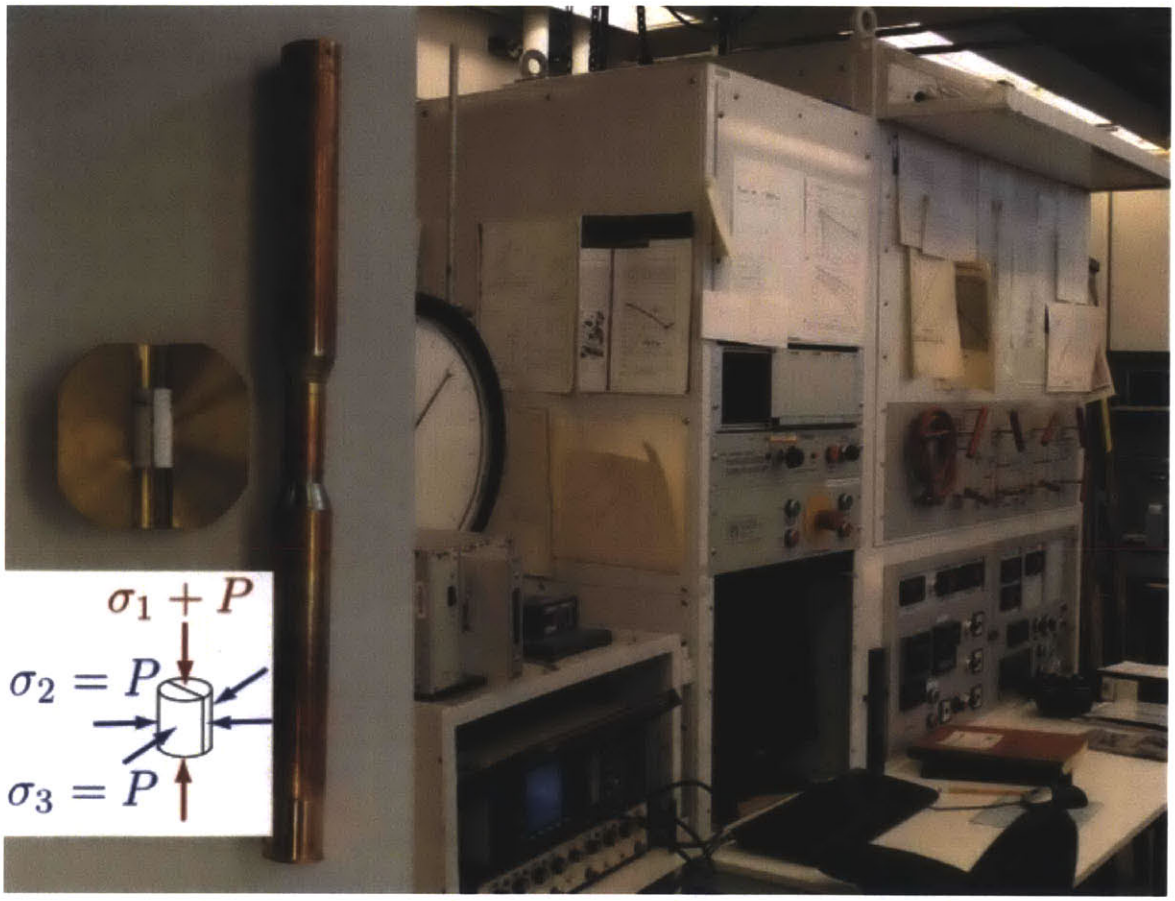

Figure 3-2: Split cylinder assembly (left) and Paterson rig (right). On the left: the sample assembly before introducing it into the apparatus, the sample is inside a copper jacket containing also the alumina and zirconia pistons and alumina spacers. On the right: the paterson apparatus PI-5 at MIT, we can see the controllers, the data acquisition is done via LabView.

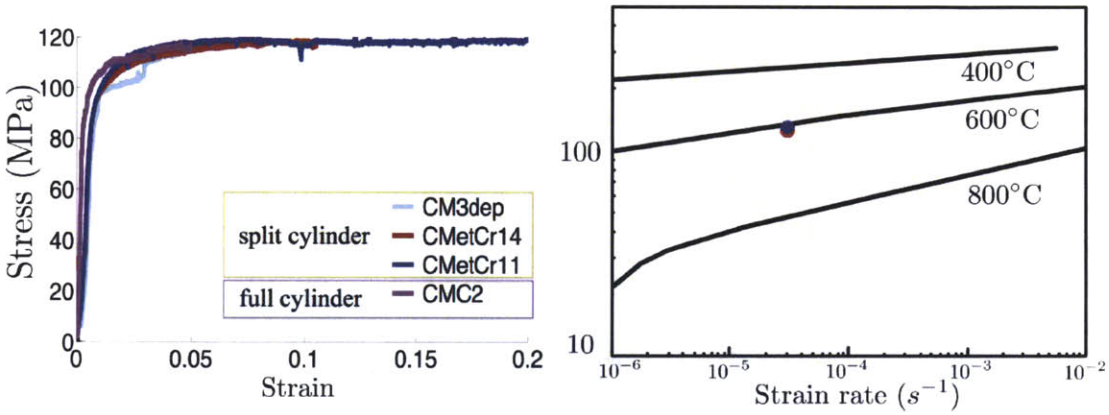

Figure 3-3: Macroscopic strain for split cylinder and full cylinder. Stress-strain curve for experiments realized under the same conditions, 300MPa, 600°C and a strain rate of 3×10^{-5} s^{-1} for full cylinders and split cylinder assemblies. For the split cylinder two patterning techniques are shown here: etched CMetCr14 and CMetCr11 and non etched CM3dep. For all samples the macroscopical mechanical behavior is the same as for a full cylinder, and is in agreement with previous studies (Covey-Crump, 1998; De Bresser, 2002)

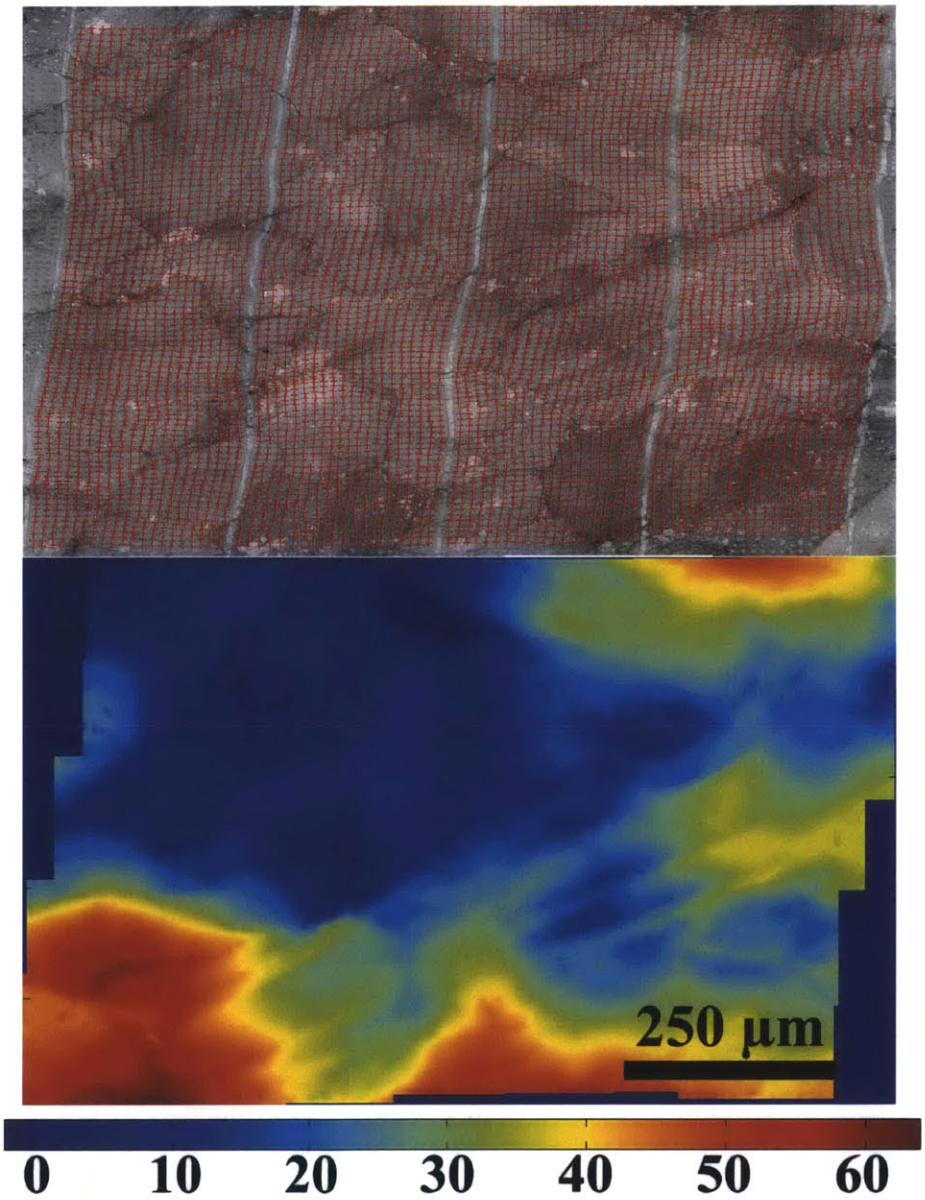

Figure 3-4: Marker location and topography of sample deformed to 0.36. The upper image shows the focus-through image overlaid with the marker detection. The lower image shows the image topography obtained also from the digital microscope by doing a sequence of images at different focal points. This sample is the one with the most dramatic height differences as macroscopic the deformation was the most heterogeneous (barreling and bending occurred).

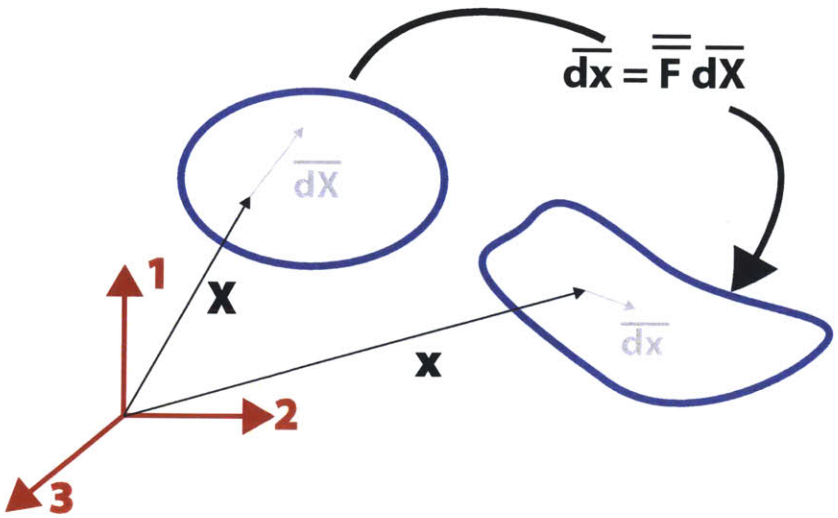

Figure 3-5: Deformation of a continuum body: the deformation gradient tensor $\overline{\overline{F}}$ transforms an undeformed infinitesimal material line $d\bar{X}$ into a deformed $d\bar{x}$

Figure 3-6: Representation of measured area with the n point technique: the n point averaging techniques corresponds to a moving best square fit of the deformation gradient tensor $\overline{\overline{F}}$ describing the deformation of the microscopic are defined by the n markers

$$\overline{\overline{\varepsilon}} = \begin{pmatrix} \varepsilon_{11} & \varepsilon_{12} \\ \varepsilon_{21} & \varepsilon_{22} \end{pmatrix}$$

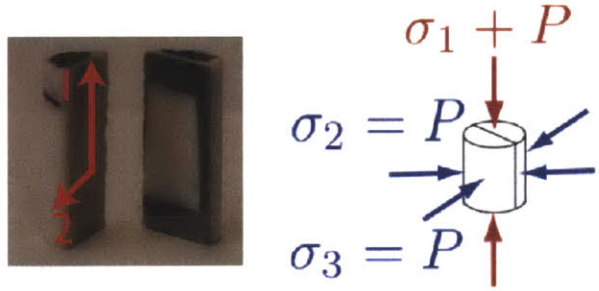

Figure 3-7: Strain tensor components referenced to the principal directions of the experiment: 11 along the cylindrical axis and corresponding to the direction of σ_1, 22 and 33 transverse to it

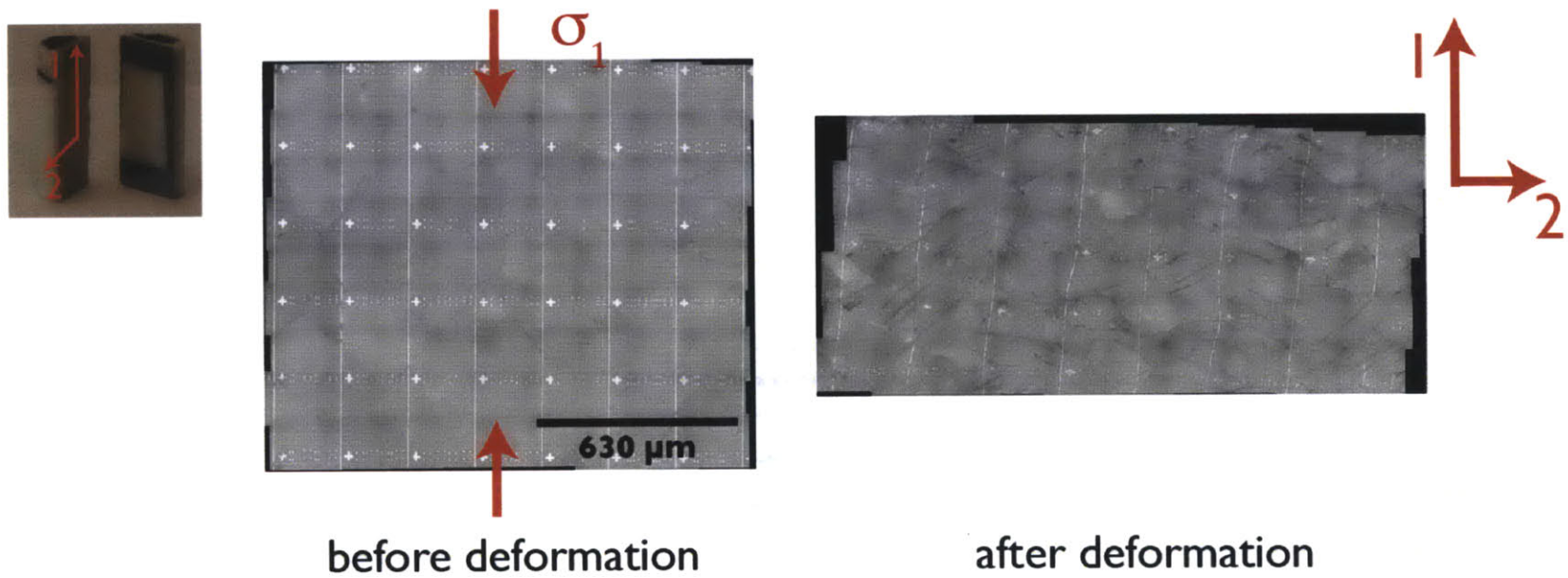

Figure 3-8: Sample representation and triaxial test reference: here, optical microscope images of sample CMhF, shortened 0.2 at 600°C and 300MPa at $3\times10^{-5}s^{-1}$ is shown. Similarly, in all optical microscope images and strain maps, the compression direction is along the vertical direction of the figure.

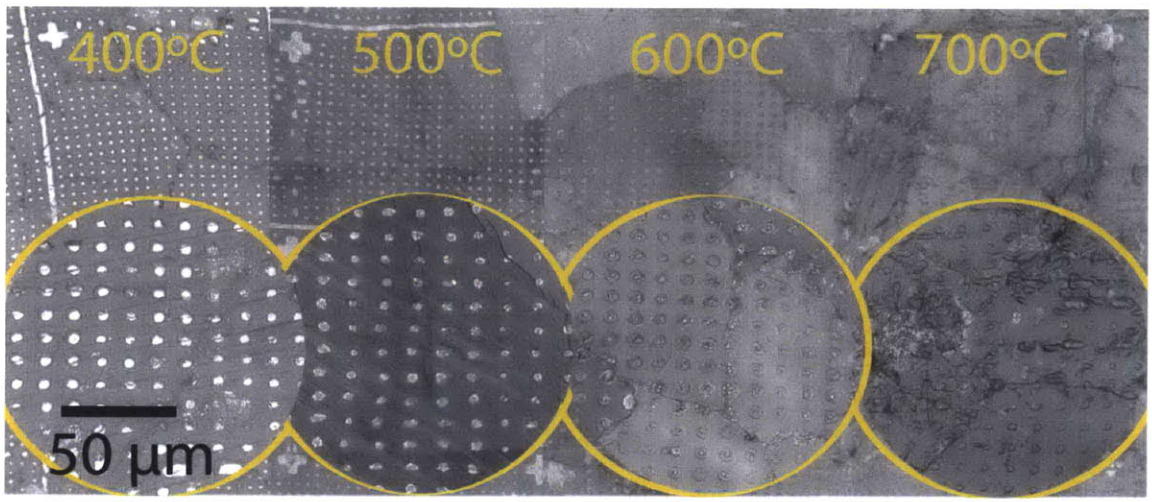

Figure 3-9: Aspect of the markers after a 0.11 axial compression at different temperatures: 400°,500°,600° and 700°: for higher temperatures the markers become harder to identify.

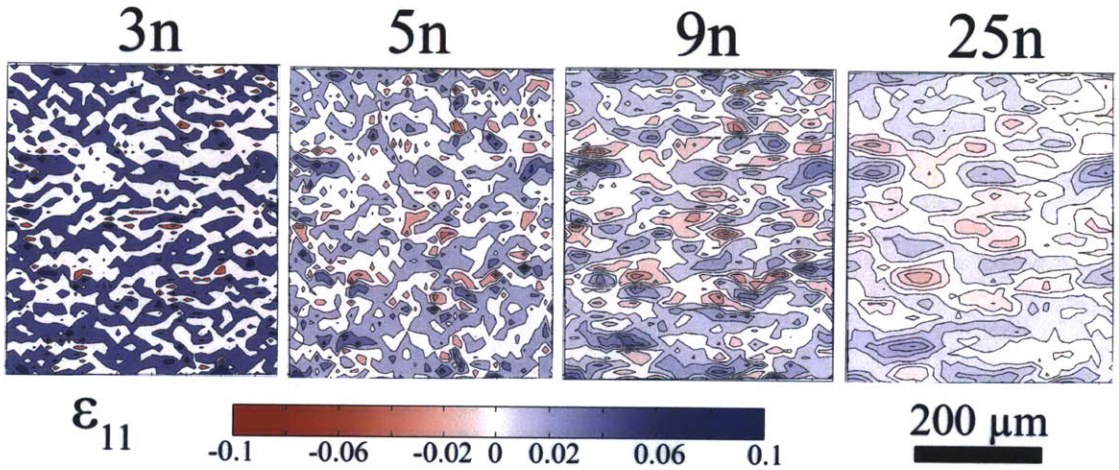

Figure 3-10: Zero strain experiment strain field: the ϵ_{11} component of the analyzed are is shown for four n averaging technique: $3n$, $4n$, $9n$ and $25n$, the compression direction is along the vertical direction of the figure.The larger the averaging are, the lesser the variations but the inversion provides less information on the heterogeneity of the field

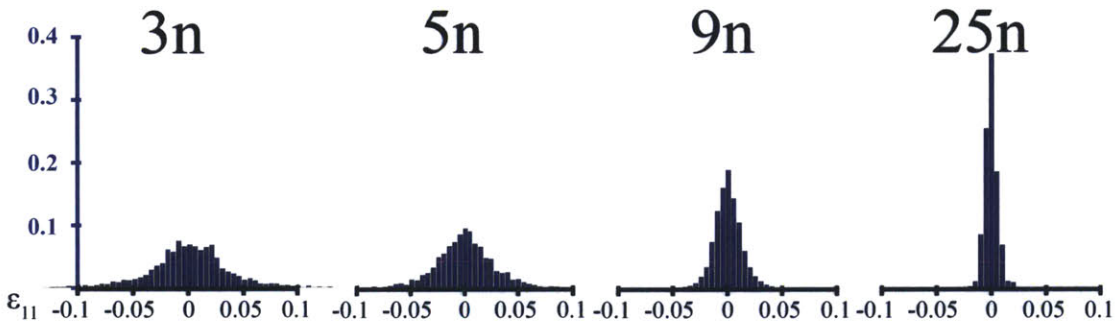

Figure 3-11: Zero strain experiment histogram: the distribution of the ϵ_{11} component of the strain field, binned every 0.0005 strain, is shown here as another way to illustrate the spread of the data for different n point averaging techniques. The average is consistently practically 0, but the standard deviation decreases significantly as n is increased.

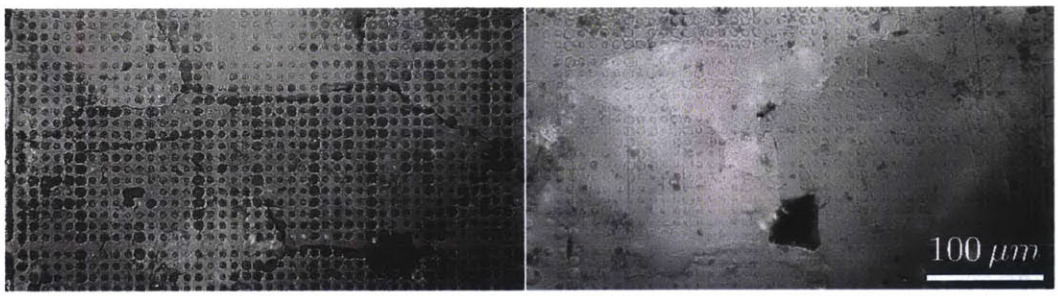

Figure 3-12: Optical microscope image and topography of gridded and non gridded half for sample of zero strain experiment (left at 700°C , 300MPa for 2 hours). The "mold-like" behavior or transfer of topography from one face to the other can be appreciated.

.

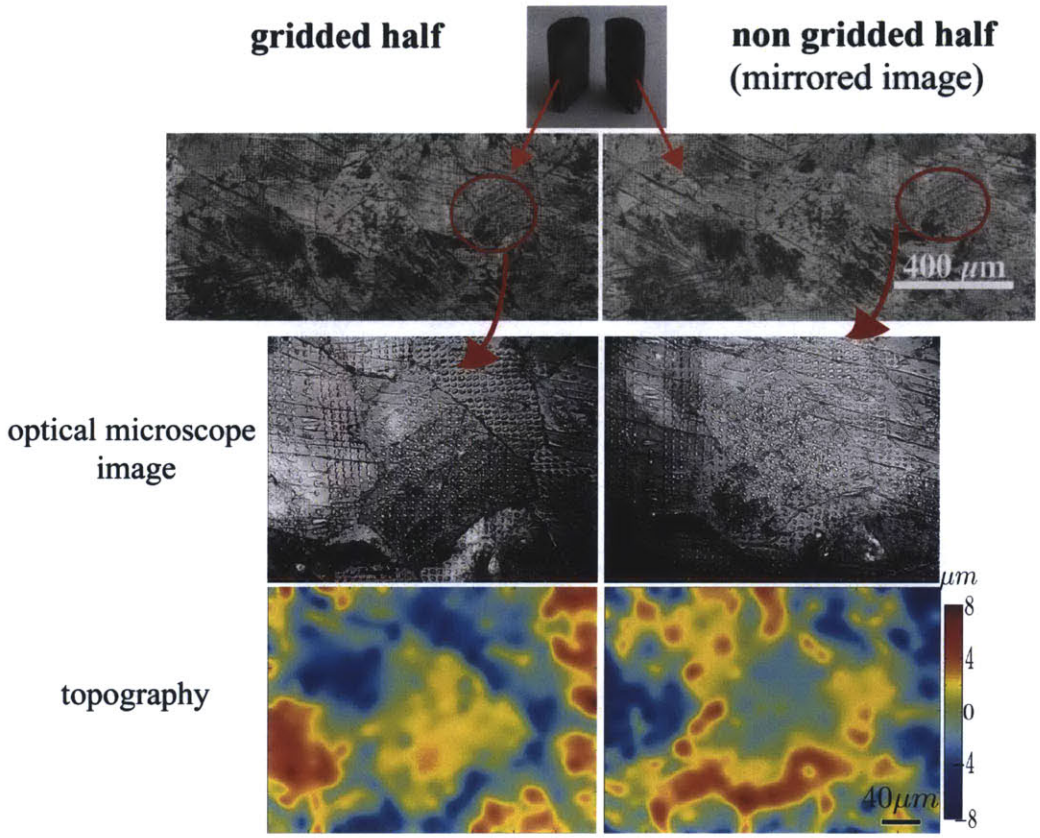

Figure 3-13: Optical microscope image and height information for gridded half (left) and non-gridded half (mirror image, right) for sample deformed at 600°C , 300 MPa to 0.11 strain. Note the transfer not only of markers but also of grain boundaries and twin lines. The topography inferred from the trough-focus series of image is complementary for the gridded and non gridded surface and show that the coupling of the surfaces is done in all dimensions.

.

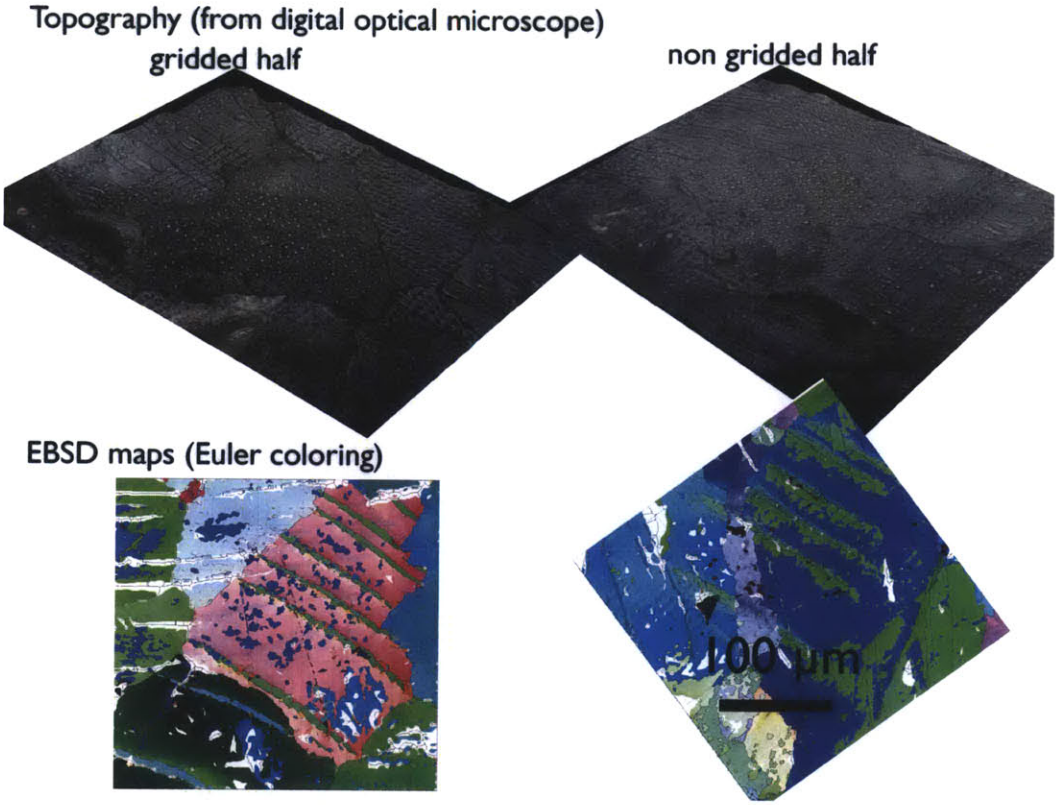

Figure 3-14: Optical microscope image and EBSD map information for gridded half (left) and non-gridded half (mirror image, right) for sample deformed at 600°C , 300 MPa to 0.11 strain. Note that the topography representation is not rotated, whereas the EBSD map was mirrored and rotated to facilitate the comparison. The EBSD map shows that there is a discontinuity on the underlying grain structure, nevertheless the e twinning on the gridded half cause some grain disorientation on the non gridded half.

.

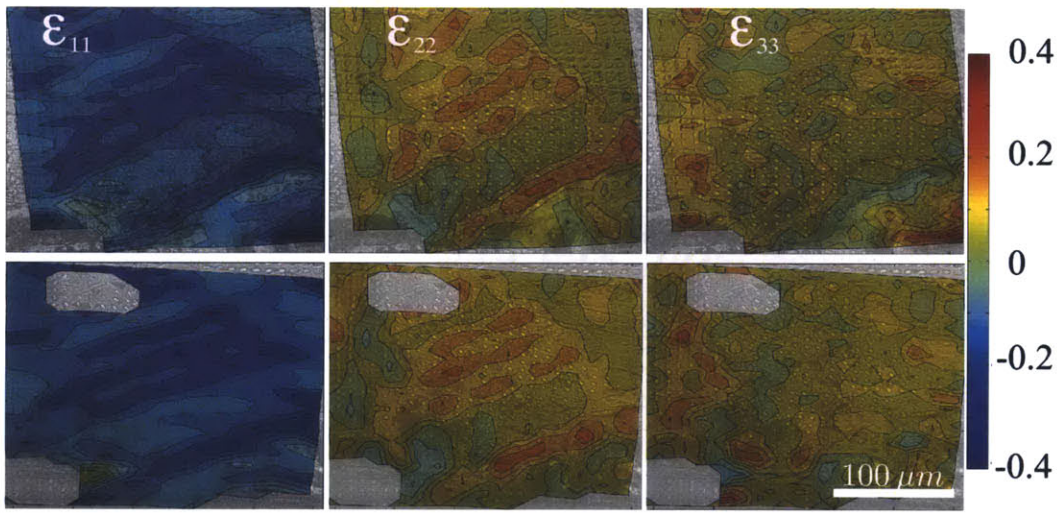

Figure 3-15: Strain field for diagonal values of the logarithmic strain tensor $\bar{\bar{\epsilon}}$ for gridded and non gridded area. Again, there is a very good coupling between both surfaces.

Chapter 4

Strain Heterogeneities during Creep of Carrara marble

Abstract

Two experimental series were performed at a confining pressure of 300 MPa and a strain rate of $3\times10^{-5}\ s^{-1}$. A temperature series explores the effect of temperature at a constant strain, and a strain series explores the effect of strain at a constant temperature. The mean strain inferred from the strain inversion across different length scales is always in excellent agreement with the measured sample strain, but the shape of the distribution of strain in the studied area changes across length scales. Particularly, a bimodal distribution of strain develops for some samples at lower T, which correlates with the localization of strain on structures spanning several grains. The spectral analysis of the strain fields shows that the strain heterogeneities are characterized by smaller wavelengths both with an increase in strain and temperature. However, the distribution of the normalized strain shows that, with respect to the mean strain, the relative amplitude of heterogeneities gets smaller with strain but larger with temperature. The following hypothesis could explain these trends. At higher temperature and lower stresses, more intracrystalline slip systems are activated leading to the development of smaller scales strain heterogeneities, of the order of 50 μm (sub-grain scale). At lower temperature and higher stresses, twinning accommodates an important part of the strain and seemingly is involved in the creation of chains of strained material, responsible for the observed bimodal distribution of strain and larger wavelengths of strain heterogeneities spanning several grains (supra-grain scale). At higher strains for a fixed temperature of 600°C , the polycrystalline aggregate starts accommodating strain along initially stronger systems, leading to a general homogenization relative to the mean strain.

4.1 Motivation

Empirical observations are used to gain insight into the micromechanical processes accommodating deformation. These observations can be used to motivate the development of constitutive equations from a theoretical understanding of the elemental processes. Refining our understanding of deformation requires both approaches, and historically it has necessitated a constant two way flow of acquired knowledge.

Flow laws obtained through the "model based phenomenology" presented by Ashby (1972) are good examples of the power of empirical observations combined with micromechanical models. Nevertheless, it is necessary to refine our theoretical understanding of the elemental processes when the established models do not predict accurately the phenomenon in question. Flow laws often assume that deformation is homogeneous and steady-state. Consequently, they cannot describe strain localization, nor the evolution of the structure leading to the localization.

For Carrara Marble, extensive work has lead to the delineation of three creep regimes (see Chapter 1): two regimes described by a power-law and the power-law breakdown regime best describe by an exponential. It is not always possible to correlate each regime with a specific microstructure or texture (S. M. Schmid et al., 1987), and in the intermediate stress regime, creep does not seem to be well described by a power-law (Renner & Evans, 2002). Moreover, it is not clear that steady-state is indeed reached and that the micro-structural evolution has completed (Covey-Crump, 1998). At laboratory strain rates it is clear that both microstructure and strength continue to evolve until strains of 2 or greater are achieved (Pieri, Burlini, et al., 2001; Pieri, Kunze, et al., 2001; Barnhoorn et al., 2004; Piane & Burlini, 2008). Further, strain is often localized in carbonates shear zones that accommodate large scale displacement of nappes in mountain ranges (S. M. Schmid, 1975; Bestmann et al., 2000; Herwegh & Kunze, 2002; Herwegh et al., 2005; Ebert et al., 2007; Austin et al., 2008). Therefore, it seems necessary to revisit the micromechanical models of creep

in carbonate rocks and establish constitutive laws that include and predict structures that evolve as the deformation takes place (Evans, 2005).

The present study focuses on examining the microstructure evolution of Carrara Marble during creep deformation in order to provide a quantitative insight into several questions. When is steady-state attained? What is the partition of strain among the deformation mechanisms already identified? Does this partition change as deformation progresses?

An approach to answering those questions is to provide a very precise description of the evolution of microstructures and the accommodation of strain at creep conditions. For this purpose, two series of experiments were conducted varying one variable, either temperature or strain, both known to affect the deformation mechanism dominance. The two experimental series presented here are:

- **a temperature series**: samples axially deformed to 0.11 shortening in a conventional triaxial test at 300 MPa, at 400 °C , 500 °C , 600 °C and 700 °C at a strain rate of 3×10^{-5} s^{-1} .

- **a strain series**: samples deformed 0.11, 0.22 and 0.36 shortening in a conventional triaxial test at 300 MPa and 600°C and a strain rate of 3×10^{-5} s^{-1}.

This chapter focuses on the experimental results and data analysis that provides insight into the questions raised above. First, the microscale strain mapping is applied to describe the heterogeneities of the deformation; from the macroscopical stress-strain characterization to the establishment of micrometric strain fields. The strain distribution and spectral signature of the strain fields are then described, and finally the analysis leads to characterization of strain accommodation along intracrystalline and grain boundary processes.

4.2 Deformation field across different length scales

Strain was characterized at different scales. The **sample strain** corresponds to the strain measured in the conventional triaxial test, the **macroscopic strain** corresponds to the strain measured along the 2.94 mm quadrants of the grid, and finally the **microscopic strain** corresponds to the strain measured at a 10 μm scale. The same convention as in previous chapter is used, unless noted otherwise: strain is dimensionless and shortening strain is positive: for instance, 0.11 corresponds to a shortening of 11% of the original length.

4.2.1 Macroscopic mechanical behavior

Summary of the experiments

The assembled composite described in chapter Chapter 3, composed of the two matching half-cylinders, was jacketed in copper tubing, pressurized to about 230 MPa and heated to the final temperature (from 200°C to 800 °C) at a rate of 25 °C /min in a Paterson deformation apparatus (M. S. Paterson, 1990). The final confining pressure was 300 MPa. The tests were performed at a constant displacement rate of 0.036 mm.s^{-1} resulting in a mean strain rate of 3×10^{-5}s^{-1}. Several samples were deformed up to the final strains of 0.11, 0.22 and 0.36 at 600°C . Table 4.2.1 provides a detailed summary of the experimental conditions. More details concerning the conventional triaxial deformation tests are given by Renner et al. (2002). After the deformation test, the sample was removed from the outer jacket and then split open to analyze the deformed gridded surface.

Stress-strain curves

Stress-strain curves of the split cylinders assembly (Figure 4-1) are in agreement with former studies (Covey-Crump, 1998; De Bresser, 2002) . More details of the mechan-

ical data are given in chapter 2. Yielding is followed by hardening for temperatures below 600 °C : a hardening rate h of 0.8 for 400°C , and 0.12 for 500°C . For higher temperatures (700°C and 800°C) the samples slightly weakened (-0.002 and -0.007 respectively). For 600 °C , hardening is dependent of the sample. All three experiments show overall the same strength (around 135 MPa), but the hardening rate differed: for the CMhH and CMhF (deformed to 0.11 and 0.36 respectively) $h \approx 0.12$, whereas h is around 0.04 for CMhI deformed to 0.22. This values are summarized in table 4.2.1.

4.2.2 Macroscopic strain

The deposited metallic grid spans over the entire surface of the half cylinder, thus the strain heterogeneity at different scales can be characterized. A first idea of the partition of strain among the half cylinder is given by inverting for the strain for the corners of all 10 quadrants, i.e. for 18 points. The results presented in figure 4-2 and 4-3 were obtained using the $4n$ averaging technique and give an idea of the **macrostrain** across the sample.

This computation is a measurement of average strain over a large area (2.94 mm length quadrant). The inversion is carried on with 4 points for each quadrant. The purpose of the analysis is to evaluate how homogeneous the axial deformation is across the sample. This macroscale strain analysis raises a couple of important observations regarding the state of strain of the samples. First, mean values of the macroscale strain ϵ_{11} of these measurements (shown in table 4.2.2) are consistent with the sample strain within 0.03. However, the standard deviation increases with strain: the deformation is more heterogeneous, confirmed by the barreling and bending of the samples. The two samples that deviated the most from sample strains were bent and barreled, probably causing the overestimation in this first rough approximation of strain. Secondly, certain samples, particularly CMhG deformed at 500 °C and

CMhD deformed at 700 °C , have a larger variation of strain in the 22 direction, the perpendicular direction to the compression axis. Variations in the sample preparation could be responsible: if the surface was slightly off axis the symmetry of loading could be affected. Appendix A shows the digital macroscopic image for the whole surface for reference: the heterogeneity for sample strains higher than 0.1 is readily apparent.

4.2.3 Microscopic strain field

The following section presents the strain fields obtained experimentally. Microscopic strain was analyzed for areas of 772 800 μm^2. For each sample, the analyzed area was picked randomly among the 10 quadrants situated in the center of the sample (cf. figure 4-2 and figure 4-3), the areas were picked before the compression test, at the moment of the EBSD analysis and therefore no involuntary bias was introduced by picking a "better looking" area after deformation. This section focuses on the description of the strain fields computed for the strain and temperature experimental series, and on the observed deformation mechanisms. The information is mainly conveyed through the strain field maps that will be presented for both experimental series (varying temperature and strain). The strain fields can be plotted on the undeformed grid or on the deformed grid. The first plot represents the projected strain on unstrained grains, the second the accommodated strain by the resulting deformed grains.

Temperature series

All of these samples were deformed axially to 0.11 under conventional triaxial conditions with confining pressure of 300 MPa at temperatures of 400, 500, 600, 700 and 800 °C . Table B.0.2 summarizes the experimental conditions and the mean and standard deviation of the strain field calculated following the strain mapping algorithm and the $9n$ point averaging technique presented in Chapter 3. Figure 4-4

shows the strain fields, ϵ_{11}, ϵ_{12} and ϵ_{22} plotted on the undeformed mesh and figure 4-5 shows the strain fields plotted on the deformed grid. The digitalized grain boundary structure is overlaid. Three qualitative remarks can be made following visual inspection of the fields. First, often there is localized strain along grain boundaries and along twins. Secondly, the spatial scale of the localization features appear to become smaller with increasing temperature. These features are particularly visible along grain boundaries on sample CMhD deformed at 700°C . Finally, there seems to be bands of higher deformation, comprising several grains, particularly within the lower temperature samples, CMhB and CMhG deformed at 400°C and 500 °C respectively.

Strain series

The samples were deformed axially to 0.11 , 0.22 and 0.36 shortening under conventional triaxial conditions with confining pressure of 300 MPa at 600 °C . Table 4.2.4 summarizes the statistics of these experiments, and Figures 4-6 and 4-7 show the results plotted on the undeformed and on the deformed grid. The same localization features along grain boundaries and twins can be observed.

4.2.4 Hypothesis of isochoric deformation and axial symmetry

The Poisson ratio ν is defined as the negative ratio of the transverse to the axial strain in the principal strain axis reference, as defined in equation 4.1.

$$\nu = -\frac{\epsilon_{22}}{\epsilon_{11}} \tag{4.1}$$

For an isochoric deformation, the trace of the the Hencky strain tensor vanishes (Bazant, 1998):

$$\mathrm{Tr}\left(\overline{\overline{\epsilon}}\right) = 0 \tag{4.2}$$

If the deformation is axial symmetric, then:

$$\epsilon_{22} = \epsilon_{33} \tag{4.3}$$

Equations 4.2 and 4.3) give:

$$\nu = -\frac{\epsilon_{22}}{\epsilon_{11}} = \frac{1}{2} \tag{4.4}$$

Figure 4-8 shows the macroscopic poisson ratio for the temperature series, and figure 4-9 for the strain series. On the left is shown the mean and the standard deviation (representing the spread of the data); on the right is shown the mean= with an estimation of the error. The error was estimated using an error propagation analysis based on the error estimated for the zero strain experiment.

$$\text{relative error} = \sqrt{\left(\frac{\text{std}(\epsilon_{11\text{zero strain}})}{<\epsilon_{11-\text{experiment}}>}\right)^2 \cdot \left(\frac{\text{std}(\epsilon_{22\text{zero strain}})}{<\epsilon_{22-\text{experiment}}>}\right)^2} \tag{4.5}$$

Tables 4.2.5 and 4.2.6 summarize the raw data for the macroscopic Poisson ratio and its standard deviation for each averaging technique. Two trends appear: for all experiments the mean macroscopic Poisson ratio tends towards 0.5, but there are undoubtedly some deviations. Note that the sample deformed at the lowest temperature (400°C), and for which there would be more concern of dilation, verifies very well the isochoric/axial symmetry hypothesis. The deviations from the hypothesis do not have any trend related to temperature: indeed, the experiments that deviate the most are the ones at 500°C and 700°C . The deviation is also found at a macroscopic estimation of the strain as seen in the estimation of the strain for the whole sample (see Figure 4-2 and 4-3). It is unlikely that the deviation was caused by dilations but rather by a deviation from an axial symmetry, probably caused by an off-centered deformation. For the strain series, the mean macroscopic Poisson ratio is 0.5 within

the estimated error. The larger averages (100 n and 2500 n) are special cases. The latter corresponding to an area equivalent to the quarter of the whole area, the fit for the deformation gradient $\overline{\overline{F}}$ is in this case is very poor. It is therefore concluded that the hypothesis of isochoric deformation is reasonable, and that the Von Mises strain defined in 4.6 and developed further in the next section is an adequate estimation of the overall magnitude of the 3D strain tensor.

4.2.5 Von Mises strain

The Von Mises strain ϵ_{vm} described in Chapter 3 is used as a descriptor of the strain ellipsoid:

$$\epsilon_{vm} = \sqrt{\frac{2}{3}\left(\epsilon_{11}^2 + \epsilon_{22}^2 + \epsilon_{33}^2 + 2\epsilon_{12}^2\right)} \tag{4.6}$$

The Von Mises strain field gives an estimate of the complete 3D strain ellipsoid as opposed to its projections along the sample reference as presented in Figures 4-5 and 4-7. Figures 4-10 and 4-11 show the Von Mises effective strain for the strain and the temperature series respectively, as well as the normalized deviation from the mean to gives an idea of the relative amplitude of the heterogeneities. Figure 4-13 and figure 4-12 show the Von Mises strain field normalized by its mean value, plotted over the optical microscope image of the analyzed area for the two experimental series varying temperature and strain respectively. The same visually striking features seen in the strain fields for ϵ_{11}, ϵ_{22} and ϵ_{12} emerge. First, the concentration of strain along grain boundaries present is present at all conditions, and twinning is present for all temperatures below 700°C . Secondly, deformation localizes into bands spanning several grains, particularly for samples deformed at lower temperatures CMhB (400 °C) and CMhG (500 °C).

Sample	Pc MPa	T °C	Strain rate s^{-1}	Strain	Strength MPa	h
CMhE	300	700	0	0	0	NA
CMhB	300	400	3.10^{-5}	0.11	223	0.8
CMhG	300	500	3.10^{-5}	0.11	173	0.12
CMhH	300	600	3.10^{-5}	0.11	132	0.12
CMhI	300	600	3.10^{-5}	0.22	133	0.04
CMhF	300	600	3.10^{-5}	0.36	143	0.12
CMhD	300	700	3.10^{-5}	0.11	68	-0.002
CMhC	300	800	3.10^{-5}	0.11	39	-0.007

Table 4.2.1: Experiments on split cylinder described in this chapter: CMhE is the zero experiment. CMhB, CMhG, CMhH, CMhD and CMhC were deformed to 0.11 strain at 400°C , 500°C , 600°C , 700°C and 800°C , and CMhI, and CMhF to 0.22 and 0.36 at 600°C . All experiments were done at 300MPa and a strain rate of 3×10^{-5} s^{-1}. h corresponds to the maximum hardening rate over small strain intervals

	CMhB	CMhG	CMhH	CMhI	CMhF	CMhE	CMhD
Temperature (°C)	400	500	600	600	600	700	700
Sample strain ϵ_{11}	0.11	0.11	0.11	0.22	0.36	0	0.11
ϵ_{11} mean strain	0.11	0.11	0.11	0.24	0.39	0.001	0.11
ϵ_{11} std	0.002	0.002	0.006	0.02	0.007	0.001	1×10^{-5}
ϵ_{22} mean strain	- 0.05	- 0.07	-0.06	-0.13	-0.19	-0.003	- 0.05
ϵ_{22} std	0.002	0.005	7×10^{-5}	0.008	0.005	3×10^{-4}	0.004
ϵ_{12} mean strain	0.007	-0.002	0.005	0.01	0.04	8×10^{-4}	-0.002
ϵ_{12} std	9×10^{-4}	4×10^{-6}	7×10^{-4}	0.002	0.01	9×10^{-4}	7×10^{-4}

Table 4.2.2: Average strain from the strain defined by the quadrant corners ($4n$ point averaging technique). Note that the average is very close to the sample strain, the deviation becomes larger with larger strains, effect that might be caused by the heterogeneity of deformation in the cylinder (barreling and bending occurred for both samples CMhI, deformed to 0.22 and CMhF, deformed to 0.36)

	CMhB	CMhG	CMhH	CMhD
Temperature (°C)	400	500	600	700
sample strain ϵ_{11}	0.11	0.11	0.11	0.11
ϵ_{11} mean stress	0.12	0.12	0.11	0.10
ϵ_{11} std	0.06	0.04	0.05	0.07
ϵ_{22} mean stress	-0.06	-0.07	-0.05	-0.05
ϵ_{22} std	0.06	0.04	0.04	0.05
ϵ_{12} mean stress	0.004	0.007	0	0.004
ϵ_{12} std	0.04	0.02	0.03	0.04
ϵ_{vm} mean stress	0.14	0.13	0.13	0.13
ϵ_{vm} std	0.06	0.04	0.04	0.06

Table 4.2.3: Statistical descriptions of strain field for temperature series: ϵ_{11} (along the compression direction), ϵ_{22} and ϵ_{12} are partial descriptor of the strain ellipsoid and ϵ_{vm} estimates the complete 3D ellipsoid. Note the perfect agreement of macroscopic strain and the average value of the field. The shear strain is close to zero.

	CMhH	CMhI	CMhF
sample strain ϵ_{11}	0.11	0.22	0.36
ϵ_{11} mean strain	0.11	0.24	0. 37
ϵ_{11} std	0.05	0.07	0.1
ϵ_{22} mean strain	-0.05	-0.12	-0.18
ϵ_{22} std	0.04	0.06	0.08
ϵ_{12} mean strain	0	0.03	0.05
ϵ_{12} std	0.02	0.04	0.06
ϵ_{vm} mean strain	0.13	0.26	0.40
ϵ_{vm} std	0.05	0.07	0.12

Table 4.2.4: Statistical descriptions of the studied area for the deformation experiments and a $9n$ point average. The strain is dimensionless (and not in %), and compressional strain is noted positive. For larger strains, shear strain ϵ_{12} becomes larger, a phenomenon to relate to the heterogeneity of the triaxial test for larger strains.

Sample \ n point	3	4	5	9	25	100	2500
CMhB (400°C)	0.46(2.8)	0.50(2.1)	0.50(1.3)	0.49(0.6)	0.48(0.3)	0.48(0.2)	0.49(0.1)
CMhG (500°C)	0.66(1.6)	0.63(1.2)	0.64(0.7)	0.63(0.2)	0.62(0.2)	0.62(0.17)	0.59(0.07)
CMhH (600°C)	0.46(3.7)	0.53(2.8)	0.50(1.8)	0.50 (0.9)	0.47(0.2)	0.46(0.16)	0.44(0.05)
CMhD (700°C)	0.33(4.5)	0.45(4.2)	0.48(3.3)	0.63 (2.6)	0.63(1.2)	0.56(0.17)	0.54(0.03)

Table 4.2.5: Mean Poisson ratio $\nu = -\frac{\epsilon_{22}}{\epsilon_{11}}$ for each temperature condition tested and for different n point averaging techniques: the standard deviation is given in parenthesis and gives an idea of the spread of the data

Sample \ n point	3	4	5	9	25	100	2500
CMhH (0.11)	0.46(3.7)	0.53(2.8)	0.50(1.8)	0.50 (0.9)	0.47(0.2)	0.46(0.16)	0.44(0.05)
CMhI (0.22)	0.50(0.83)	0.50(0.64)	0.49(0.26)	0.49(0.20)	0.48(0.17)	0.48(0.15)	0.48(0.05)
CMhF (0.36)	0.46(1.5)	0.53(1.14)	0.50(0.44)	0.50 (0.24)	0.47(0.19)	0.46(0.16)	0.44(0.04)

Table 4.2.6: Mean Poisson ratio $\nu = -\frac{\epsilon_{22}}{\epsilon_{11}}$ for each strain condition tested and for different n point averaging techniques: the standard deviation is given in parenthesis and gives an idea of the spread of the data

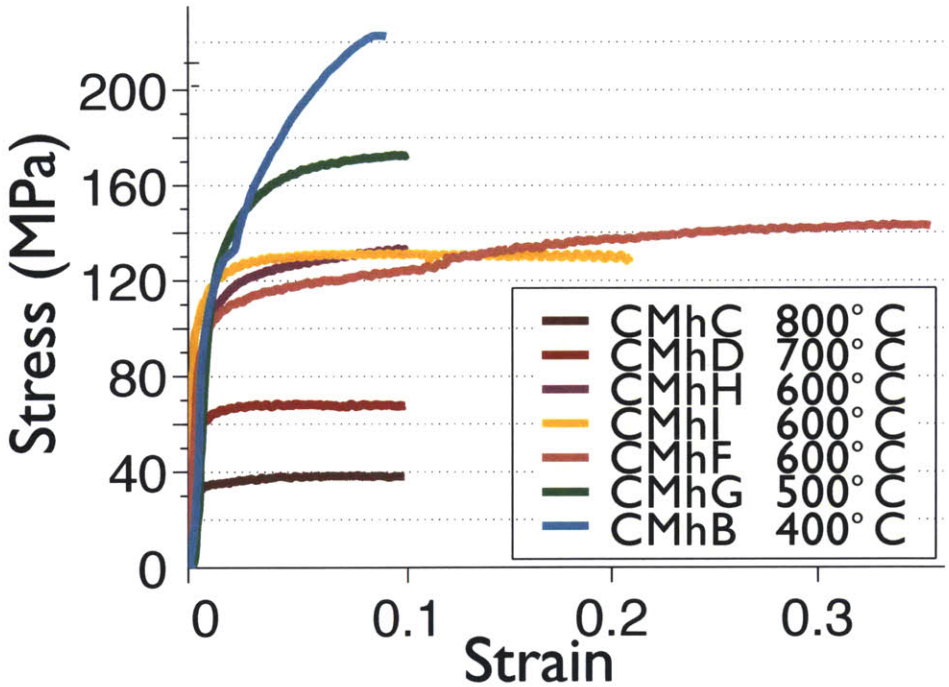

Figure 4-1: Stress-strain curves. Experiments in the temperature series were performed at 300 MPa and 400°C , 500°C , 600°C ,700°C and 800°C to a shortening strain of 0.11 at at 3×10^{-5} s^{-1}. Experiments in the strain series were performed at 300 MPa and 600°C , to shortening strains of 0.11, 0.22 and 0.36 at 3×10^{-5} s^{-1}.

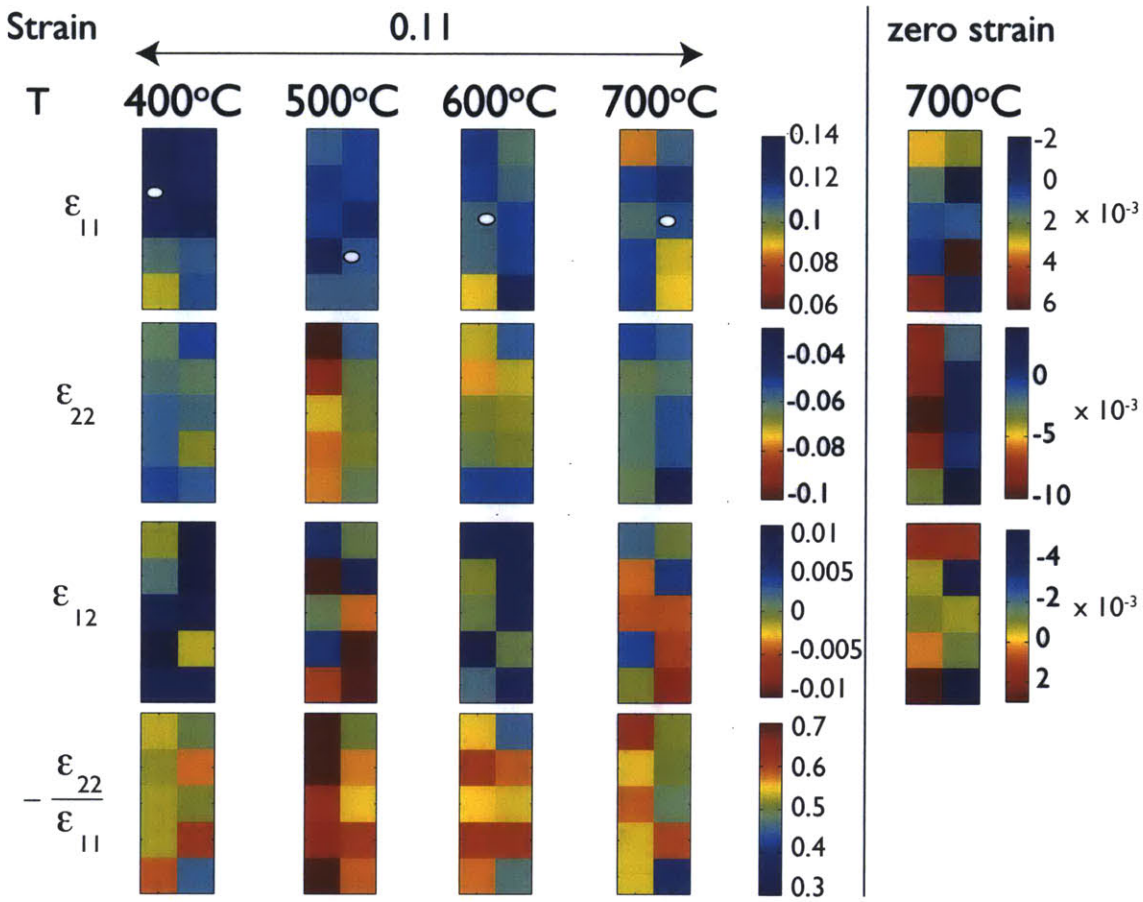

Figure 4-2: Macroscale strain estimation for temperature series. All samples were deformed at a confining pressure of 300MPa to 0.11 strain, at a strain rate of $3\times10^{-5}\ s^{-1}$ at 400°C , 500°C , 600°C and 700°C . The control experiment was left under confining pressure at 700°C without incurring deformation. The strain is computed for each quadrant using the 4 corners and the value of the components of the strain tensor is color coded according to the color scale. Strain is dimensionless and shortening strain is positive. ϵ_{11} corresponds to the compression direction, ϵ_{22} to the perpendicular to the compression, ϵ_{12} to the shear strain and the ratio $-\epsilon_{22}/\epsilon_{11}$ is the Poisson ratio. The same color scale is used for all samples deformed to 0.11 strain in compression , a different color scale is used for the zero strain experiment. The deformation along the split cylinder is heterogeneous, but the average is consistent with the sample strain. White ellipses indicate regions mapped at higher resolution.

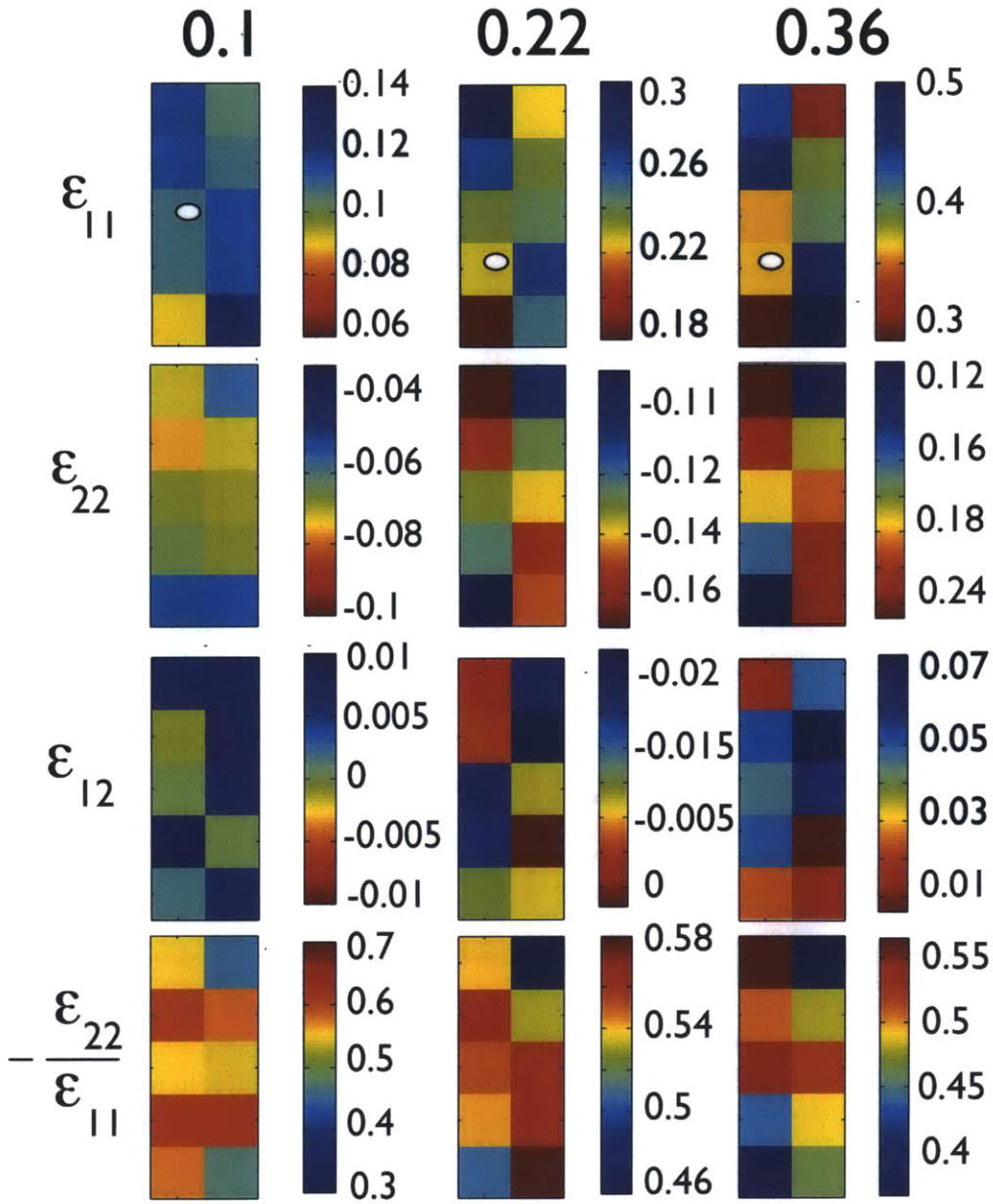

Figure 4-3: Macroscale strain estimation for the strain series, all samples were deformed at 600°C , confining pressure of 300 MPa and a strain rate of 3×10^{-5} s^{-1} to strains of 0.11, 0.22 and 0.36 strain in compression. The strain is computed for each quadrant using the 4 corners and the value of the components of the strain tensor is color coded according to the color scale. Strain is dimensionless and shortening strain is positive. ϵ_{11} corresponds to the compression direction, ϵ_{22} to the perpendicular to the compression, ϵ_{12} to the shear strain and the ratio $-\epsilon_{22}/\epsilon_{11}$ is the Poisson ratio. White ellipses indicate regions mapped at higher resolution.

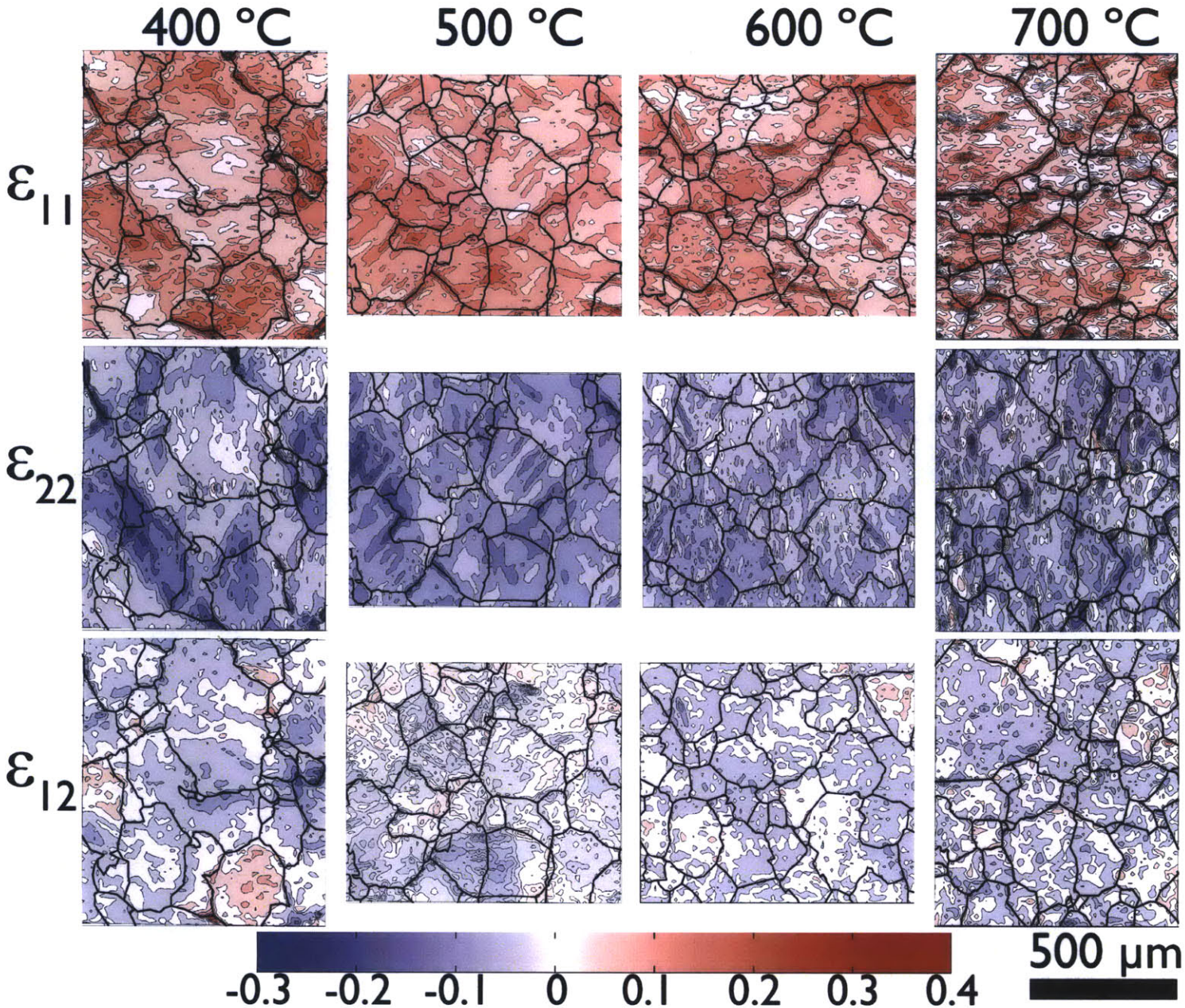

Figure 4-4: Logarithmic strain for $9n$ average contoured on the undeformed mesh with overlay of the undeformed grain structure for temperature series: experiments to 0.11 strain 3×10^{-5} s^{-1} strain rate, 300MPa at 400°C , 500°C , 600°C and 700°C . Strain is dimensionless, and compressive strain is noted positive. The accommodation of strain is seen along grain boundaries and twins, as well as the presence of accommodating structures larger than one grain.

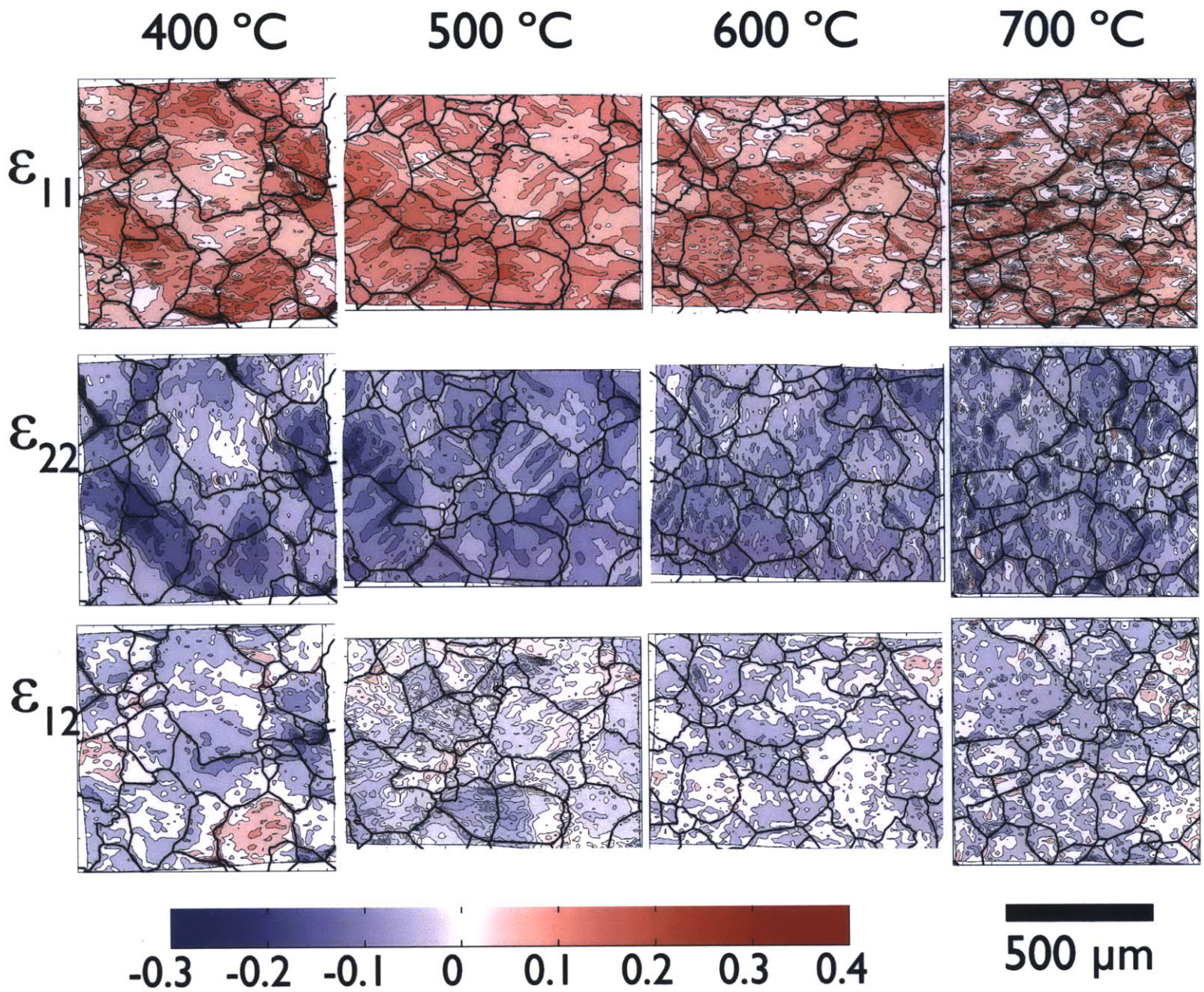

Figure 4-5: Logarithmic strain for $9n$ average contoured on the deformed mesh with overlay of the deformed grain structure for temperature series: experiments to 0.11 strain 3×10^{-5} s^{-1} strain rate, 300MPa at 400°C , 500°C , 600°C and 700°C . Strain is dimensionless, and compressive strain is noted positive. The accommodation of strain is seen along grain boundaries and twins, as well as the presence of accommodating structures larger than one grain.

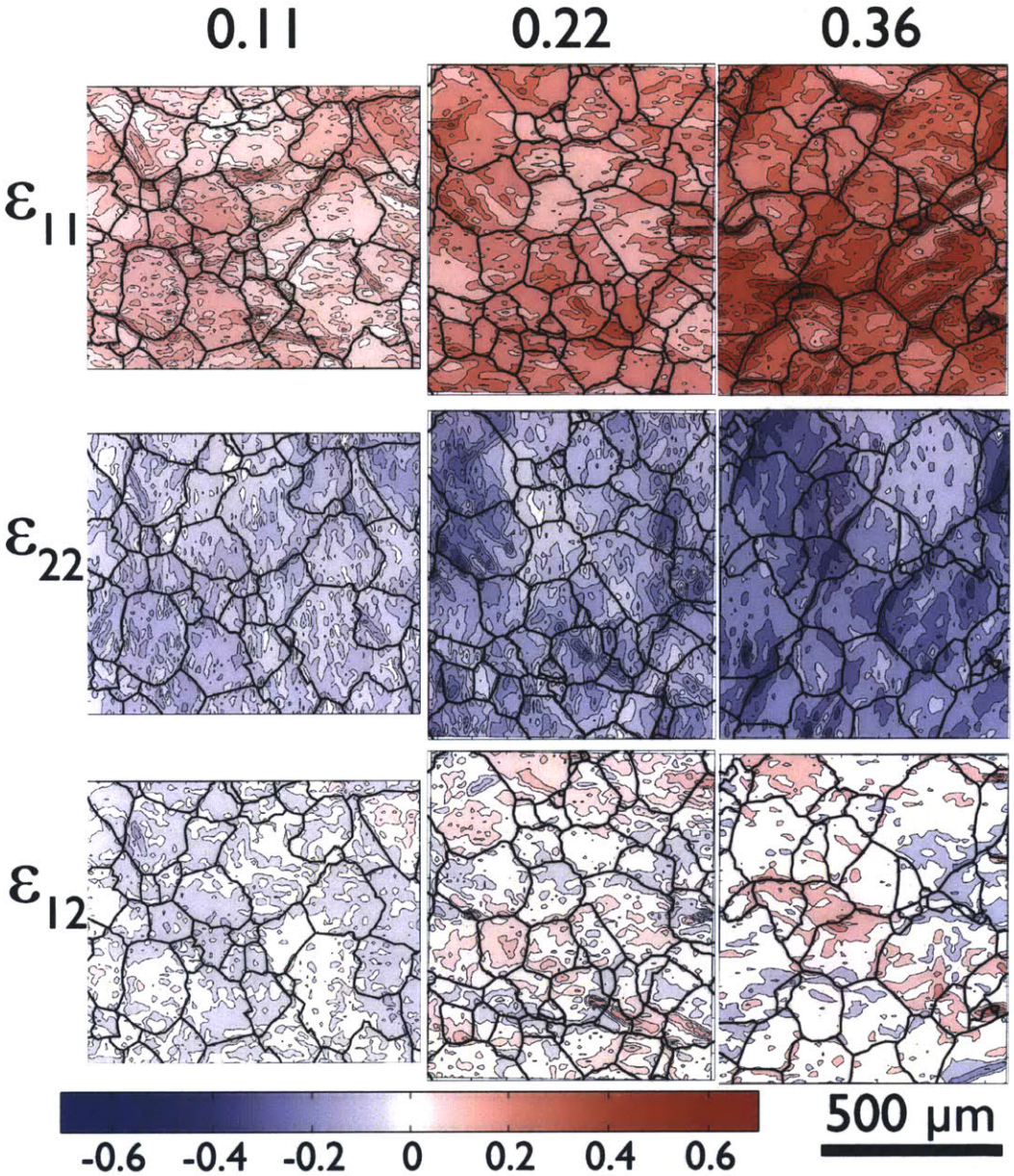

Figure 4-6: Logarithmic strain for $9n$ average contoured on the undeformed mesh with overlay of the undeformed grain structure for strain series: experiments at 600°C , 300 MPa to 0.11, 0.22 and 0.36 strain at 3×10^{-5} s^{-1} strain rate. Strain is dimensionless, and compressive strain is noted positive, the load direction is along the vertical direction of the figure. Note again the accumulation of strain along grain boundaries and twins, as well as the presence of structures larger than one grain, but also that the strain field appears to homogenize with strain

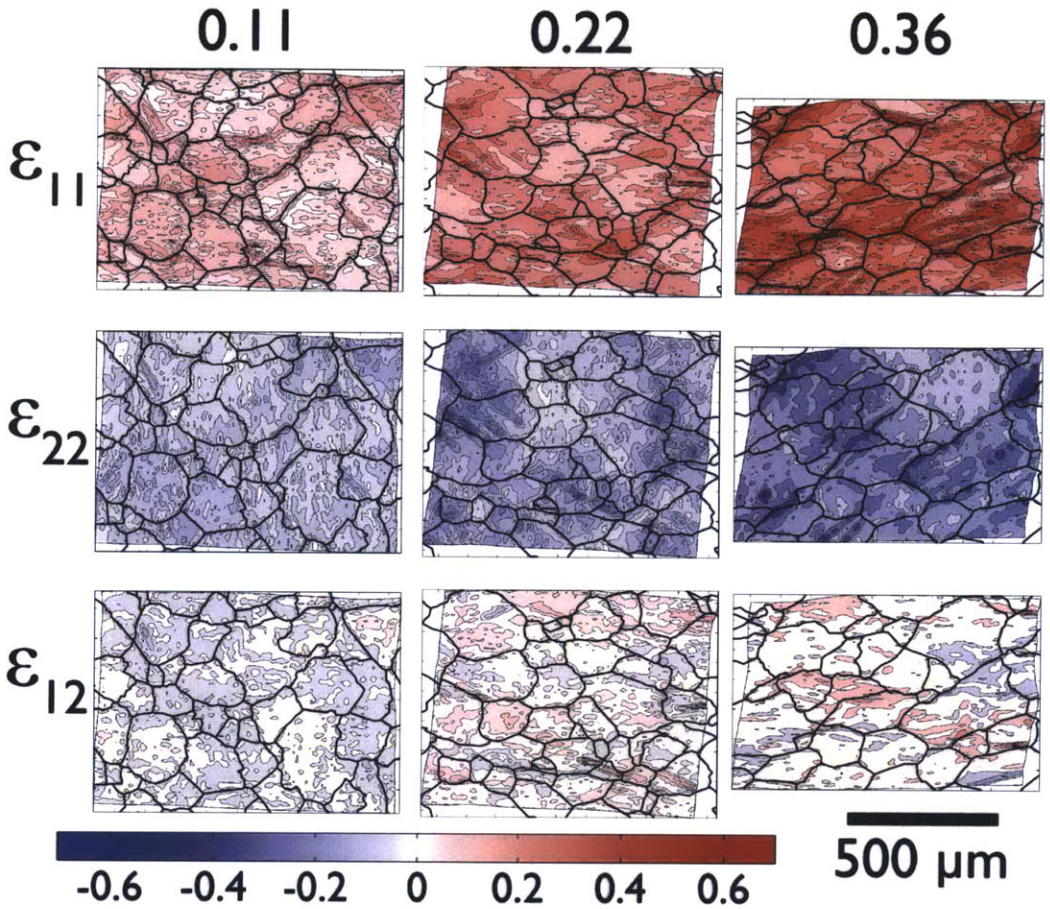

Figure 4-7: Logarithmic strain for $9n$ average contoured on the deformed mesh with overlay of the deformed grain structure for strain series: experiments at 600°C , 300 MPa to 0.11, 0.22 and 0.36 strain at 3×10^{-5} s^{-1} strain rate. Strain is dimensionless, and compressive strain is noted positive, the load direction is along the vertical direction of the figure. Note again the accumulation of strain along grain boundaries and twins, as well as the presence of structures larger than one grain, but also that the strain field appears to homogenize with strain

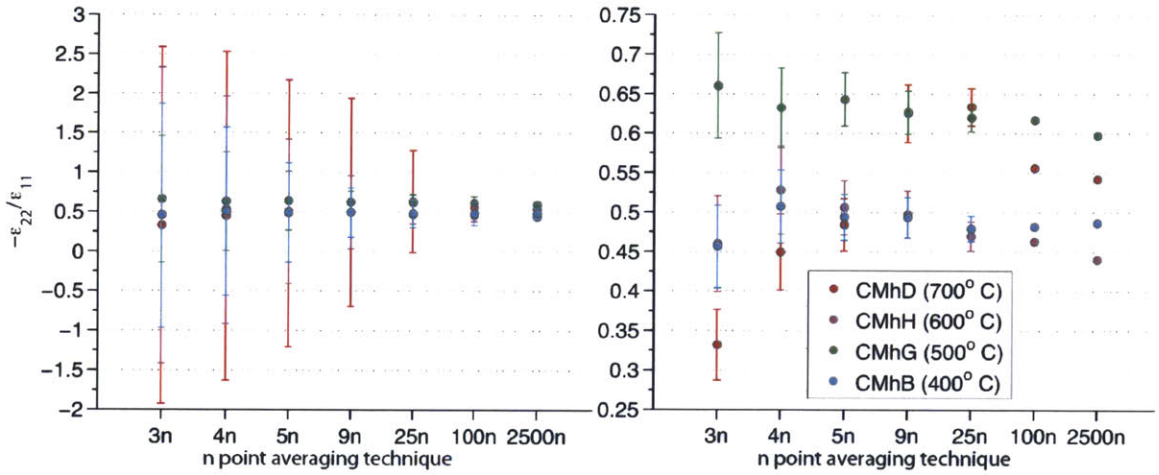

Figure 4-8: Macroscopic poisson ratio for the temperature series as a function of n point average. The figure on the left shows the standard deviation of the data, which is a representation of the spread of the data, the figure on the right shows the error evaluated from the zero strain experiment using an error propagation calculation

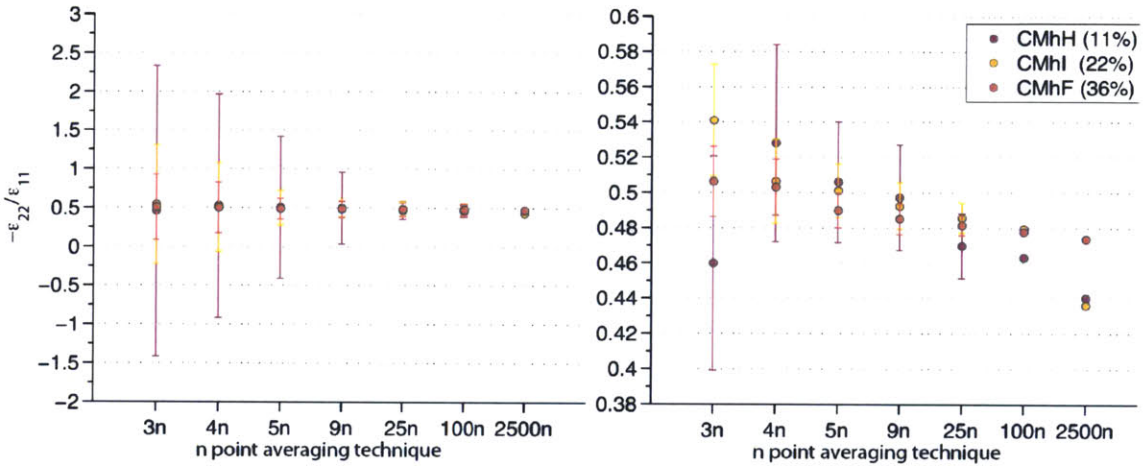

Figure 4-9: Macroscopic poisson ratio for the strain series as a function of n point average. The figure on the left shows the standard deviation of the data, which is a representation of the spread of the data, the figure on the right shows the error evaluated from the zero strain experiment and using an error propagation calculation

.

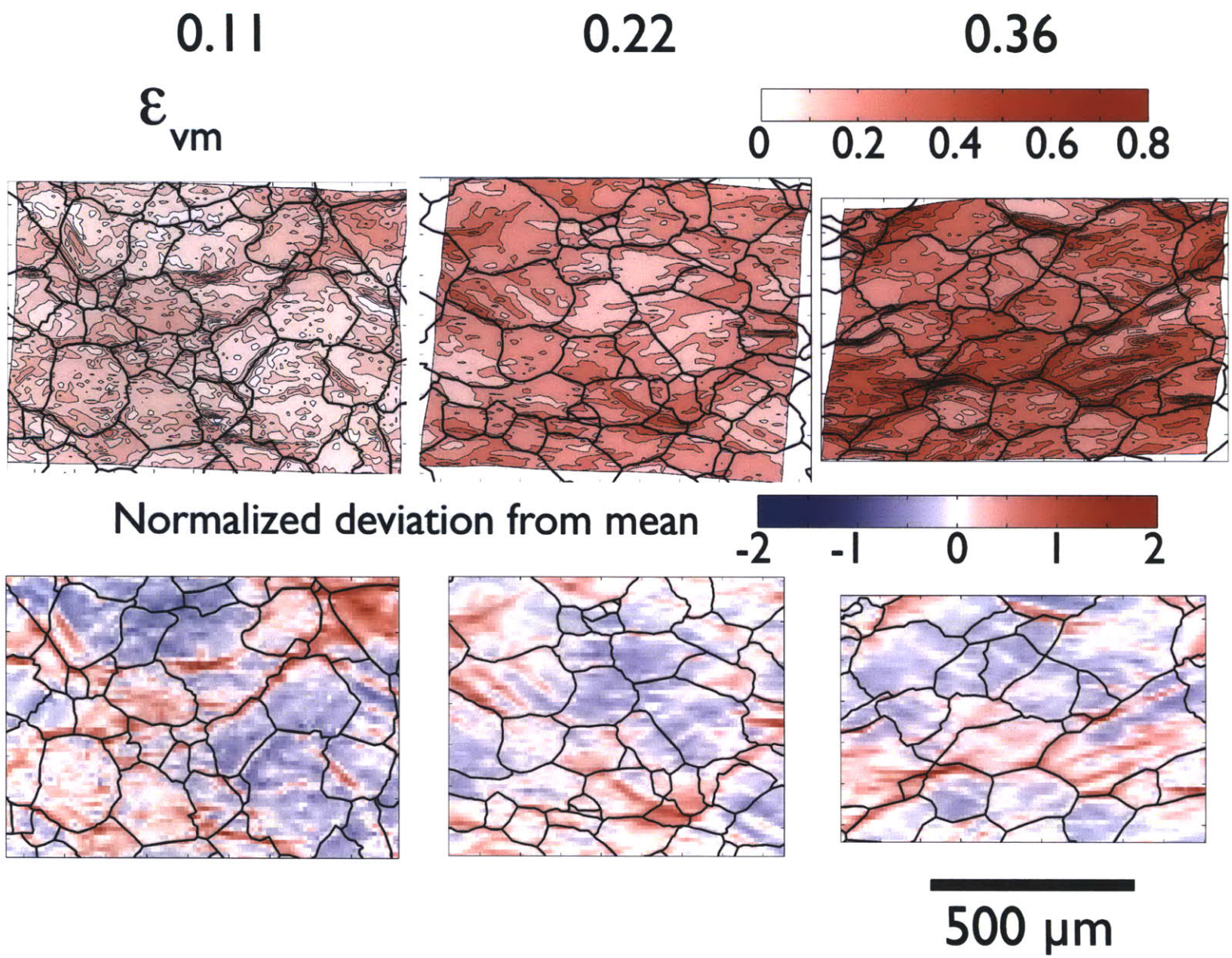

Figure 4-10: Von Mises effective strain for the strain series, as well as the normalized deviation from the mean to gives an idea of the relative amplitude of the heterogeneities. The homogenization with strain is apparent by the lower intensity of the colors.

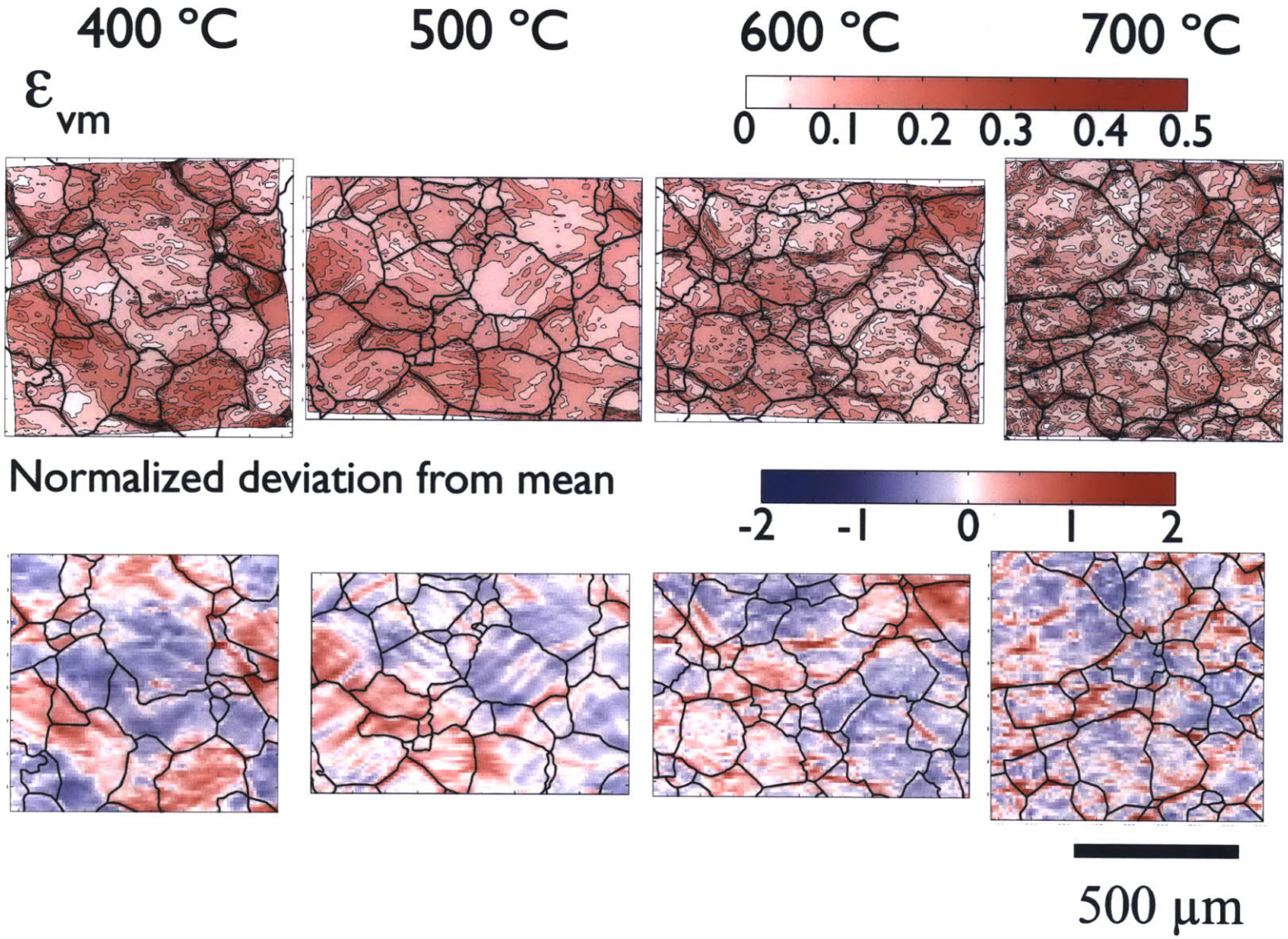

Figure 4-11: Von Mises effective strain for the temperature series, as well as the normalized deviation from the mean to gives an idea of the relative amplitude of the heterogeneities.

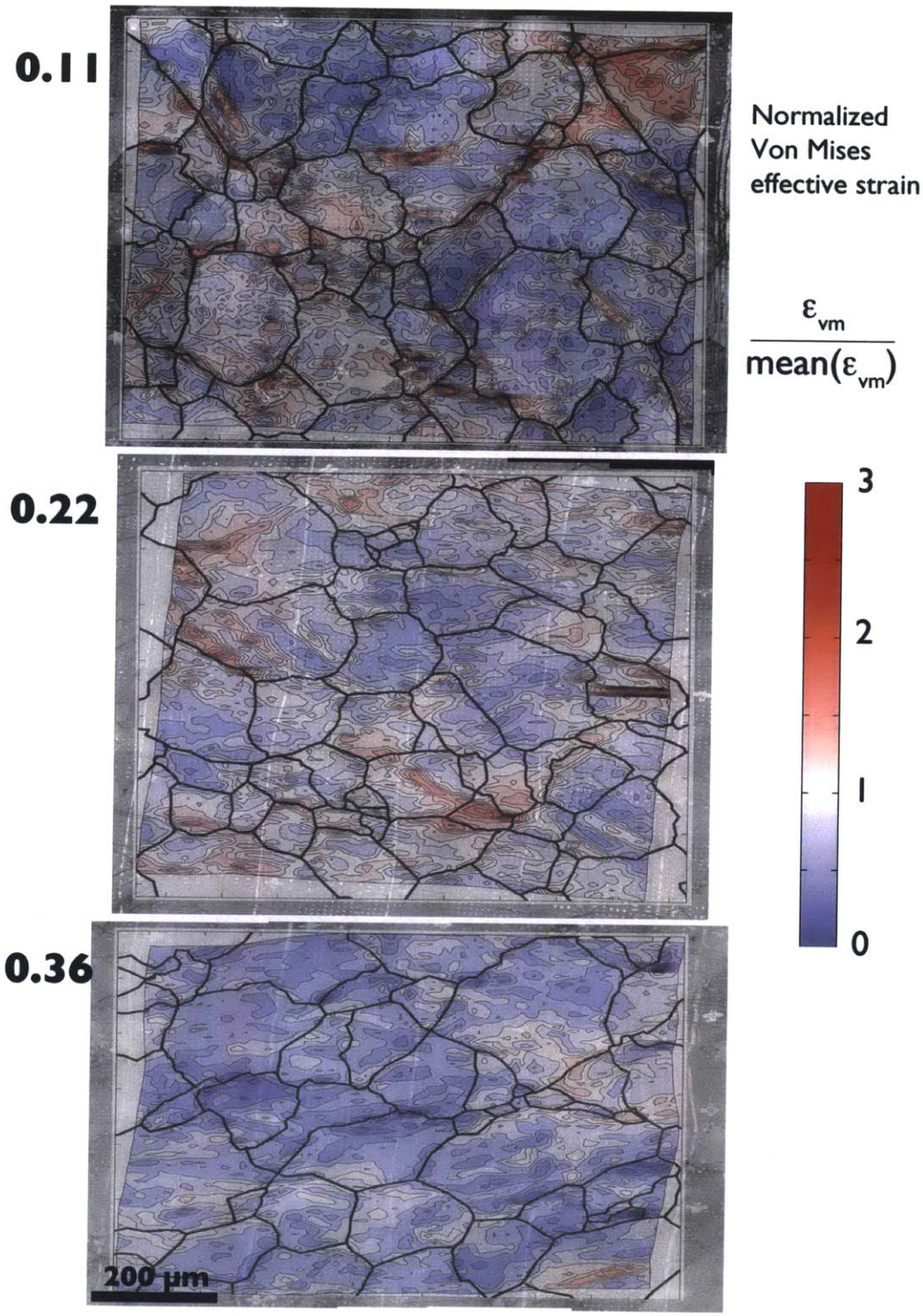

Figure 4-12: Normalized Von Mises effective strain for strain series (0.11, 0.22 and 0.36 at 600°C) contoured on deformed mesh with overlay of deformed grain structure and grain boundaries: a value of 1 means the strain at that particular point is equal to the average strain in the field, lower or higher than 1 means that area accommodates less or more strain that the average respectively

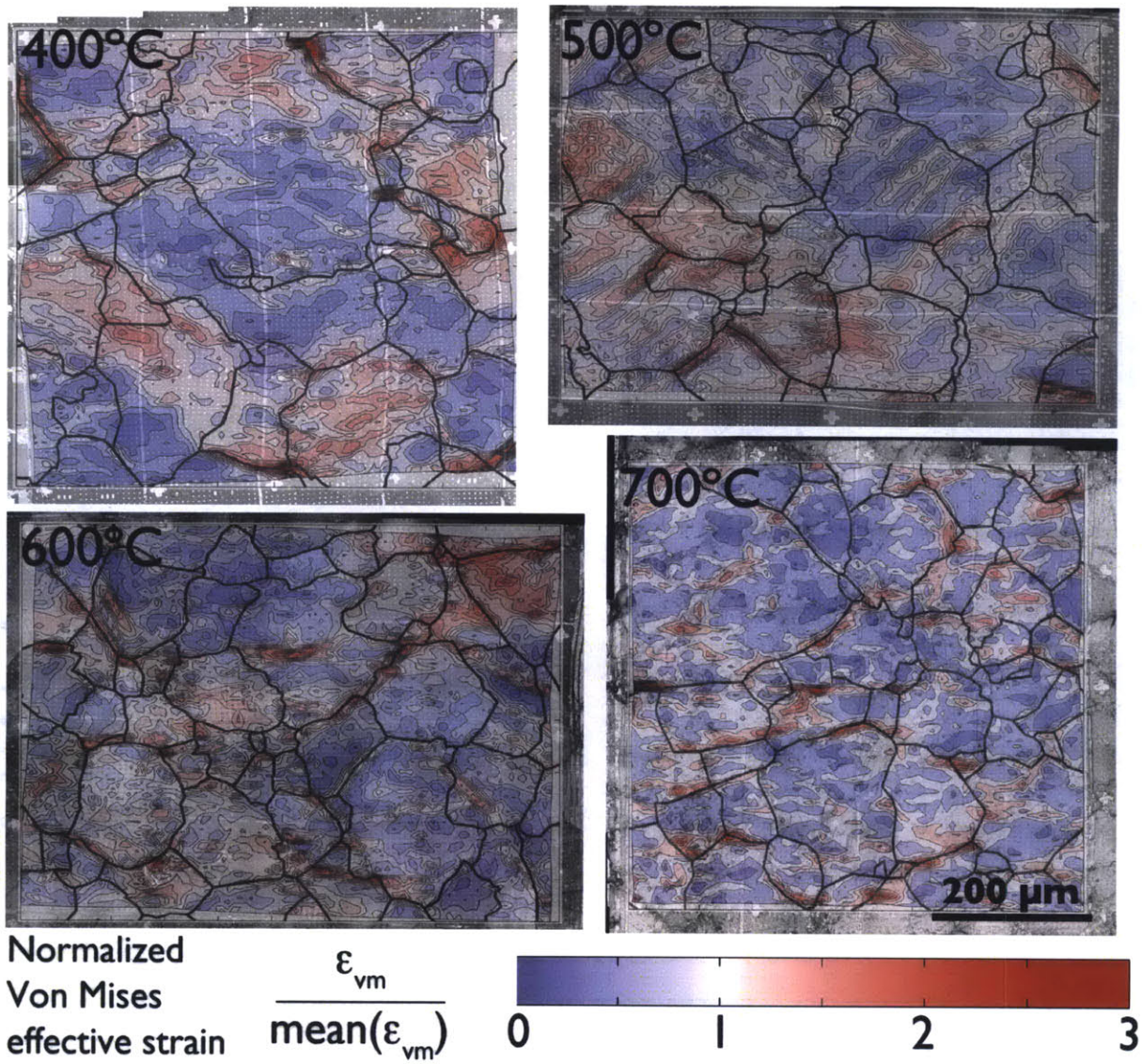

Figure 4-13: Normalized Von Mises effective strain for temperature series (400°C , 500°C , 600°C and 700°C) contoured on the deformed grid with overlay of deformed grain structure and grain boundaries: a value of 1 means the strain at that particular point is equal to the average strain in the field, lower or higher than 1 means that area accommodates less or more strain that the average respectively

4.3 Characterization of the strain fields

To go beyond a visual inspection of the strain fields and their large scale statistics, two additional representations are presented here: the strain distribution and spectral analysis (power density spectra). The distribution of strains for each sample is computed for different n averaging techniques to investigate the strain heterogeneities across different scales. The spectral analysis of the field is a way to access the energy partition (or strain in this case) among different wavelengths and describes the scale of the heterogeneities present the field.

4.3.1 Strain distribution

The distribution of strain can be represented by describing the density of each strain value over the entire analyzed area. The strain values were binned every 0.01 units of strain. As shown in Chapter 3 the spread depends on the number of points n used for the computation of the deformation gradient tensor $\overline{\overline{F}}$. Figure 4-14 and 4-15 show the strain distribution for all samples, for the 11 component, the 22 component and the 12 component and are a good summary of the results of our experiments.

As expected, the distribution is wider when a smaller number of points n is used in the strain analysis algorithm. However, the mean is consistently in excellent agreement with the sample strain. The shape of the distribution is related to the homogeneity of the sample: a homogeneous sample would have a delta peak distribution: all the probed areas would deform at the mean value $< \epsilon_{11} >$. The more heterogeneous the sample is the broader the distribution is. It is interesting to compare the distribution for different n averages because it tells us about the scale of the heterogeneities. Two observations are worth noting. For the sample deformed at 400 °C and at 600 °C , two peaks appear as the local analysis includes more points. At larger scales the distribution becomes bimodal, as suggested by the observation of

bands of strain localization that span several grains. Further analysis, particularly of different areas of the same sample, are necessary to corroborate this hypothesis. Secondly, the general distribution gets broader with temperature and strain.

The distributions were normalized by the mean strain (given in tables B.0.2 and 4.2.4) for each experiment in order to evaluate the heterogeneities as a function of the mean value and to compare samples strained to different values. The normalized distributions for the strain and temperature series are presented in 4-16 and figure 4-17 respectively. The distribution of the normalized strain is also broader for higher temperatures, bur narrower for larger strains.

4.3.2 Spectral analysis of the strain field

The Fourier space gives a good idea of the dominant wavelengths of the given field: a spatial field can be treated just as a temporal signal, and wavelengths and wavenumbers are analogous to time periods and temporal frequencies. The spatial 2D Fast Fourier Transform is computed from the deviation from the mean of the $9n$ Von Mises strain field for all the samples. Figures 4-18 and 4-19 show the two-dimensional power density spectrum of the deviation from the mean of the Von Mises strain field, normalized by the peak of maximum energy. The color scale is related to the energy of a given wavenumber (inverse of a wavelength): warmer colors towards red represent higher energies. The field was normalized by the maximum amplitude: its value and location in wavenumbers (kx,ky) are given in the figure. The maximum values of energy are hard to compare among experiments because the energy is dissipated due to the "leakage" effect caused by the non periodicity of the signal. Nevertheless, the shape and location of the peaks tell us about the dominant wavelengths. For instance, a peak towards the center (smaller wavenumber or larger wavelengths) relates to larger areas strained at similar values, whereas a peak at higher wavenumber corresponds to smaller wavelengths of strain or smaller units of localized strain. The

Nyquist factor, the highest frequency that can be resolved by data with a spacing Δ (here $\Delta = 10\mu m$), is $(2\Delta)^{-1}$, corresponding to a wavenumber of 0.05 μm^{-1} in the horizontal and vertical direction and 0.07 in the diagonal direction (corresponding to wavelengths of 20 μm and 28 μm respectively).

The spectral analysis confirms the trend observed in the strain field maps. For all spectra, a high concentration of wavelengths is present around 200 μm, close to the starting grain length, but there is an evolution regarding smaller wavelengths. At higher temperature, more energy is associated to smaller wavelengths, for the 700°C experiment there is representative population of wavelengths at 100μm in the horizontal direction and 50 μm in the vertical direction. For higher strains, a slight increase on representative wavelengths is also seen, although it is not as important as it is for the temperature increase, and it seems to be limited to the vertical direction for which there is an important population of wavelengths of 100μm. The Fourier spectra also show some directionality. This is harder to interpret as it is strongly influenced by the twinning directionality, which is a function of the grain orientation. Nevertheless, certain directionality along the diagonal does emerge: 45° degree orientation of wavelengths.

A complementary analysis is shown in figure 4-20 where the mean-normalized std of the ϵ_{vm} is plotted for each experiment. The standard deviation gives an idea of the spread of the data, i.e. of the heterogeneity of the field. The standard deviation is normalized by the mean in order to be able compare different experiments. This plot can be related to the normalized distribution of strain seen in figure 4-16 and figure 4-17 where we saw a narrower normalized distribution with increasing strain but a wider normalized distribution with increasing temperature. With the present data, two trends emerge and confirm both the first impression of the strain fields and the spectral analysis. First, the internal local variability of the strain field increases with an increase of temperature. Sample CMhB deformed at 400°C does not follow this

trend, probably because of the high intensity of twinning causing high heterogeneity. Secondly, this analysis suggests a decrease of relative local variability in the strain field for higher strains.

To conclude, the strain field and spectral analysis suggest that:

- From 500°C up to 700°C there is both a decrease of wavelengths (characteristic wavelengths of 50 μm) and an increase of strain heterogeneities amplitudes. For temperatures lower than 500°C the evolution might be controlled by the high activity of e twinning that will also be associated with a decrease of wavelength and increase in amplitude of heterogeneities.

- At 600°C and increasing strains, the strain field shows more directionality as well as a decrease in the wavelength, suggesting an anisotropic deformation of the grain structure. Nevertheless, the strain field becomes relatively more homogeneous as shown by the normalized standard deviation of the field

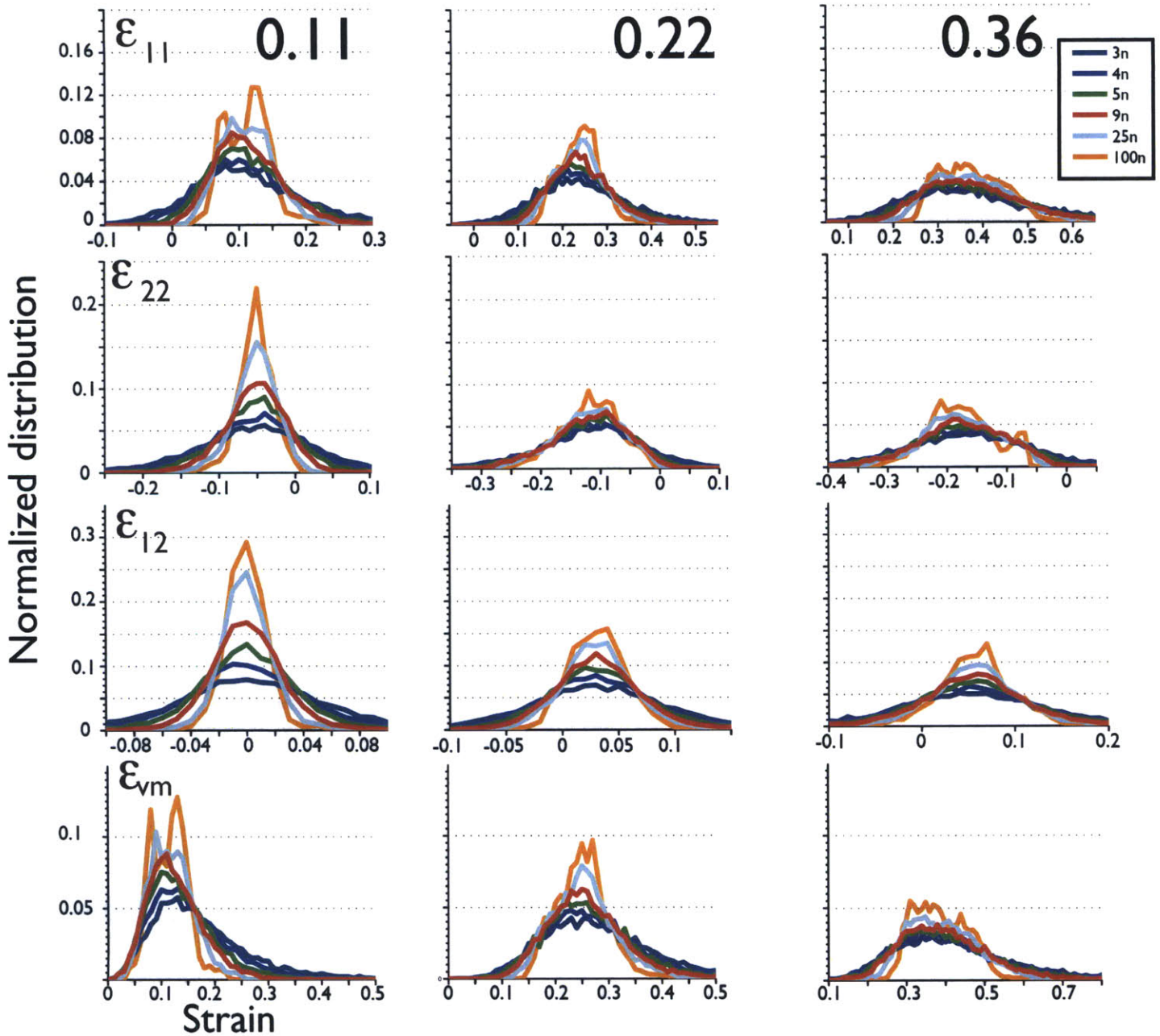

Figure 4-14: Strain distribution for the strain series experiment. The strain was binned every 0.01, compressive strain is negative, and strain is dimensionless.

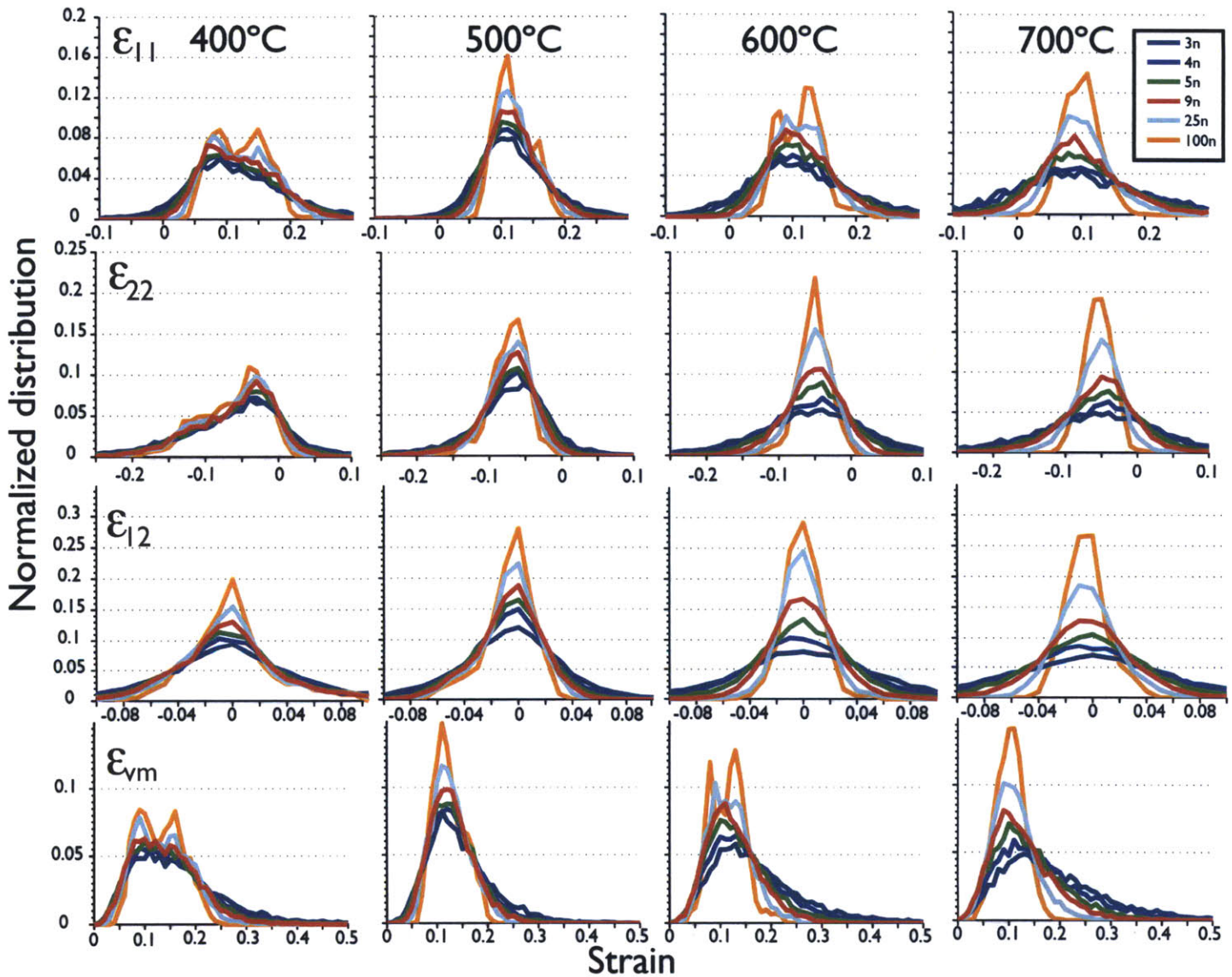

Figure 4-15: Strain distribution for the temperature series experiments. The strain was binned every 0.01, compressive strain is negative, and strain is dimensionless.

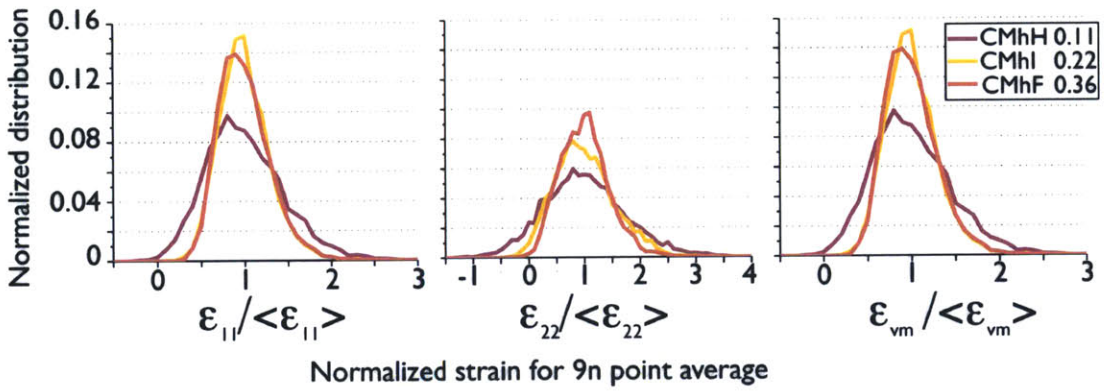

Figure 4-16: Normalized strain distribution for the strain series experiments, normalized by the mean values of the Von Mises effective strain ϵ_{vm}, 0.13, 0.26 and 0.40 for the samples strained to 0.11, 0.22 and 0.36 respectively.

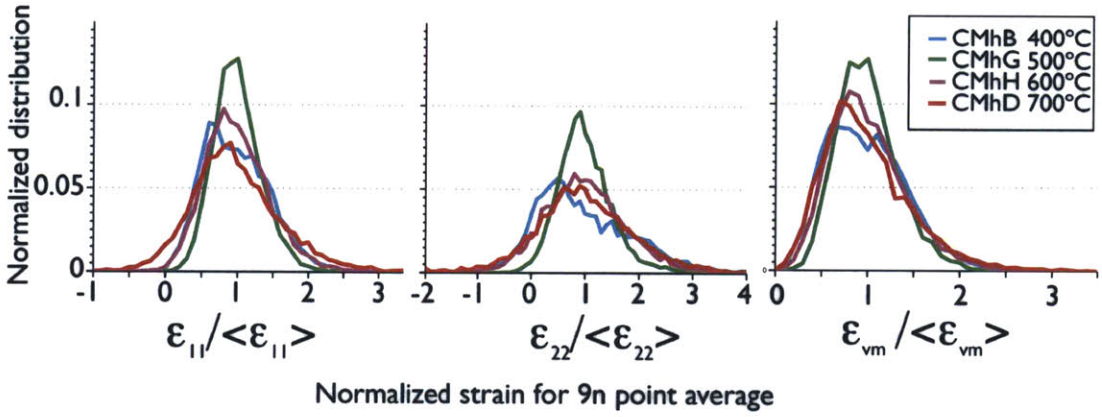

Figure 4-17: Normalized strain distribution for the temperature series experiments, normalized by the mean values of the Von Mises effective strain ϵ_{vm}, 0.14, 0.13, 0.13 and 0.13 for the samples deformed at 400°C , 500°C , 600°C and 700°C respectively

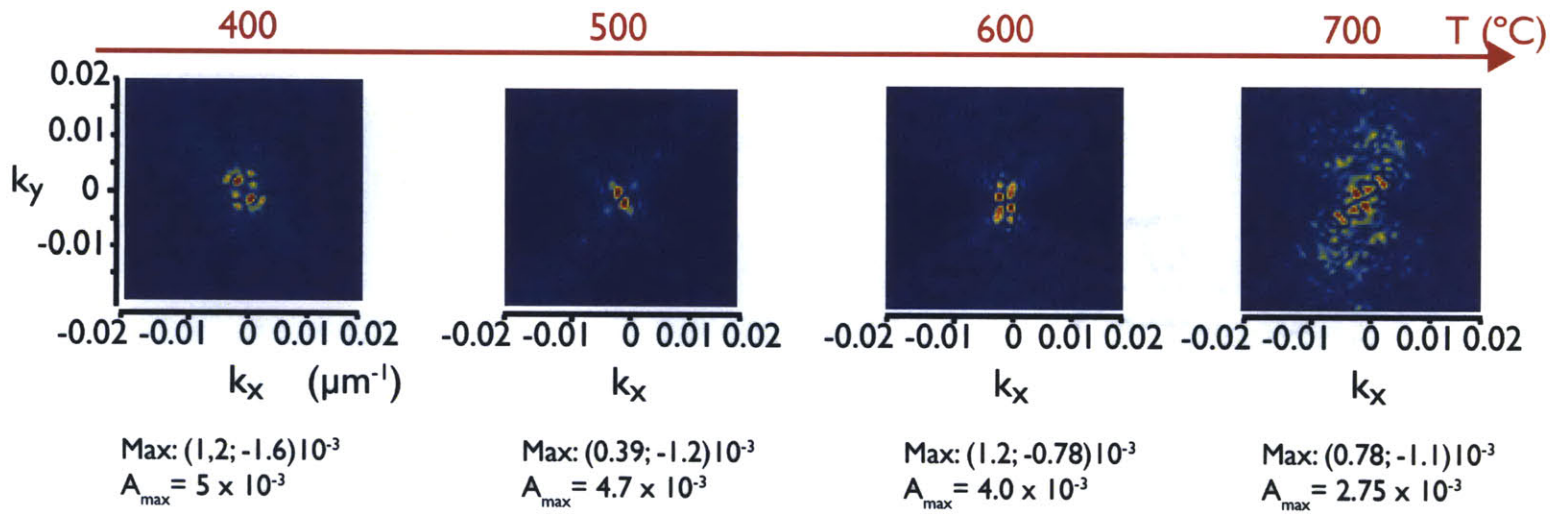

Figure 4-18: Normalized two-dimensional power spectrum of the deviation from the mean of the Von Mises effective strain field for the temperature series (400°C , 500°C , 600°C and 700°C), the field is normalized by the maximum amplitude noted on the figure.

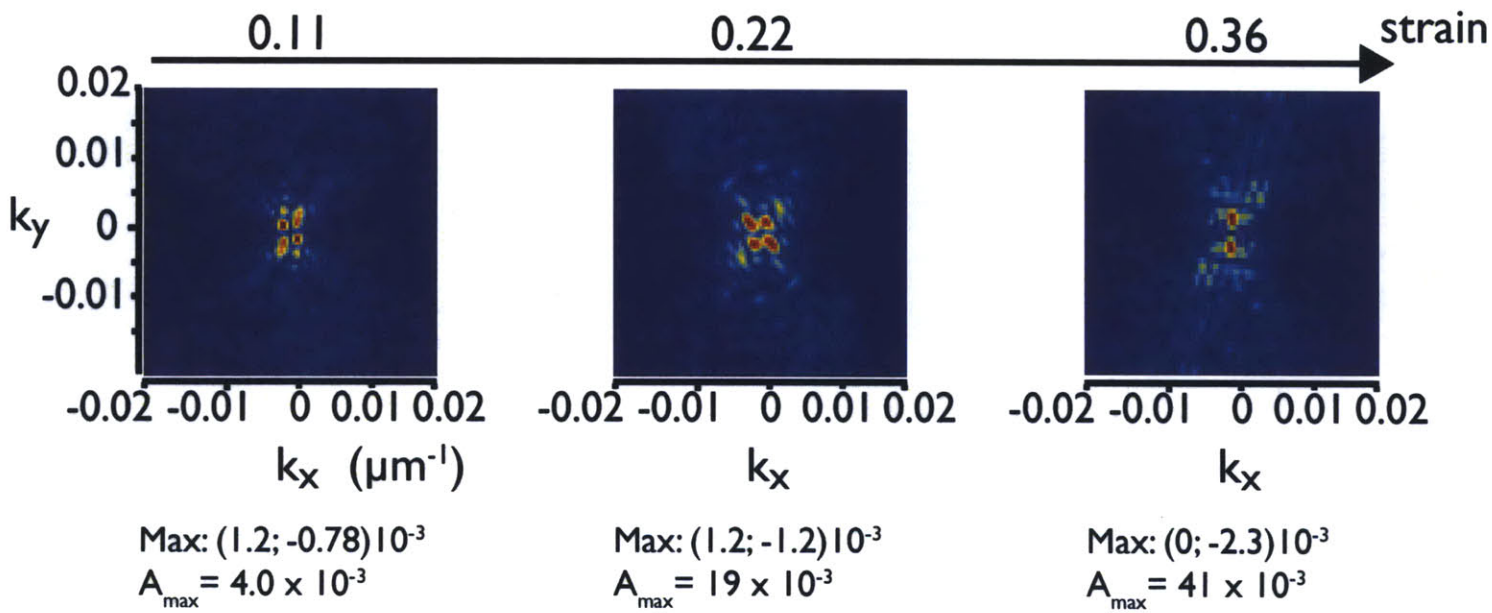

Figure 4-19: Normalized two-dimensional power spectrum of the deviation from the mean of the Von Mises effective strain for the strain series (0.11, 0.22 and 0.36 at 600°C), the field is normalized the maximum amplitude noted on the figure.

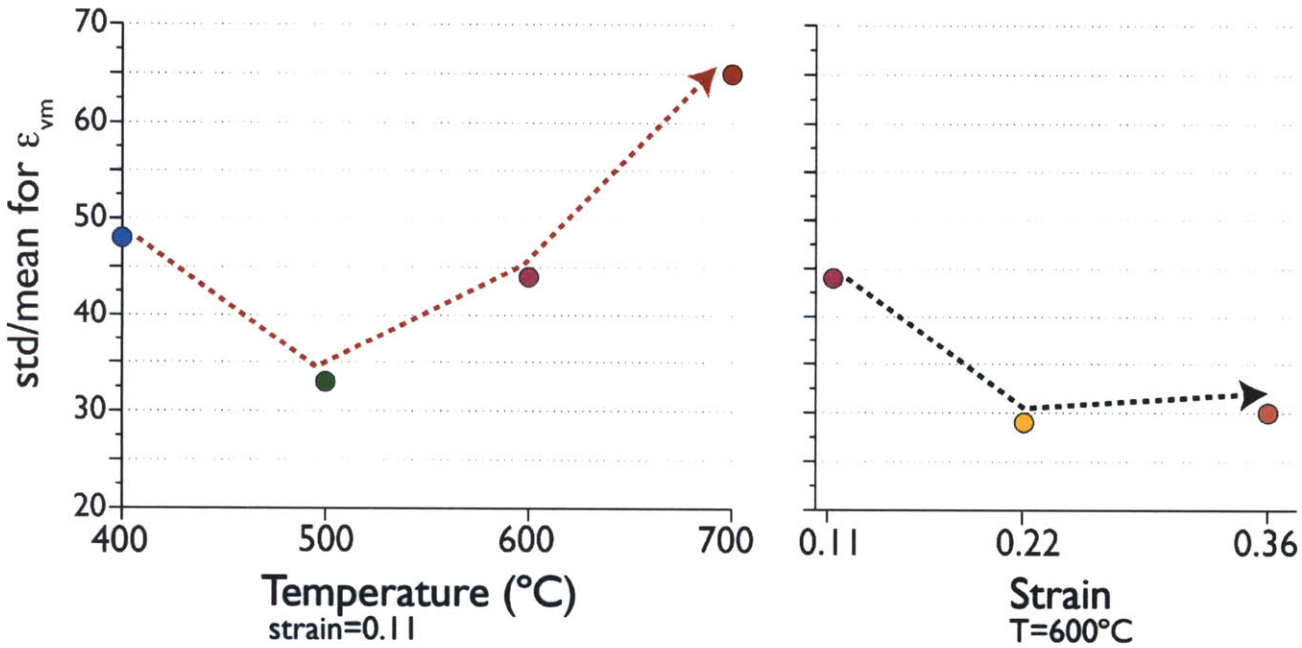

Figure 4-20: Normalized standard deviation of ϵ_{vm} field by its mean for all experiments, the red arrow connects the temperature series (left), the black arrow the strain series (right). The normalized std gives an idea of the spread of the distribution of strain relatively to the mean value and gives an idea of the local heterogeneity. The temperature series documents a transition where the the local variability of the strain field increases with temperature, except for the highly twinned, lower T sample at 400°C . The strain series indicates that the relative heterogeneity of the field decreases with increased strain.

4.4 Partition of strain in the polycrystalline material

4.4.1 Observed deformation mechanisms

Extensive data from previous work shows that calcite deforms by dislocation slip along the **r**,**f**,**c** and **a** systems (Griggs et al., 1953; Turner et al., 1956; M. S. Paterson & Turner, 1970; Turner & Heard, 1965; De Bresser & Spiers, 1990, 1993, 1997), and on the **e**-twinning system (Turner et al., 1954; De Bresser & Spiers, 1997). In addition, grain boundary sliding has been shown to occur at higher temperatures and small grain sizes (S. Schmid et al., 1977). Recrystallization has been documented in larger strain experiments (Pieri, Kunze, et al., 2001; Barnhoorn et al., 2004)

Optical observations of the gridded surface show explicit examples of each of these mechanisms (see Figure 4-22), summarized below:

- **Microtwinning, glide lines**: the sample deformed at 400°C presents very fine lines, parallel to existing twins but too narrow to be mapped with EBSD. These fine lines can be found with less frequency in higher temperature samples, up to 600°C . These striations were already described by Turner et al. (1954). It might correspond to an initial step in the nucleation and growth of a twin, but further studies, particularly a strain sequential experiment with EBSD observations are necessary to explore this hypothesis. An AFM observation of sample CMhH, deformed to 0.11 at 600°C (Figure 4-21), shows that the lines are step-like features of about 100 nm height. Interestingly, they are no longer seen in experiments run at higher temperature (700°C and 800°C)

- **Twinning**: e twinning is very present at 400 °C , 500 °C and 600 °C , it decreases significantly at 700°C . This decrease in the activity of twinning with temperature is consistent with previous studies. Twins tend to become increas-

ingly lensoid-shaped and thicker for higher strains and higher temperature in agreement with Burkhard (1993); Ferrill et al. (2004). There is evidence of "healing": some twins disappear presumably because they are situated in an unfavorable position, particularly at higher temperatures. Twin boundary migration was proposed as a recrystallization mechanism at temperatures above 600 °C by Rutter (1995) but was not observed in the pre-existing twins in this experiments. Twin nucleation appears to be favored over twin boundary migration, but this tendency might be related more to the fact that existing twins are often in an unfavorable orientation than to the difficulty of twin boundary migration.

- **Grain boundary sliding (GBS):** GBS is observed even at lower temperatures (see Figure 4-22 for a clear image of grain boundary sliding at 400°C) but it appears to be more important at higher temperatures. S. Schmid et al. (1980) found no grain boundary sliding at 600°C , and concluded that even at higher temperature (800°C) its contribution to strain was minor. GBS has been proposed as an important grain sensitive, high temperature, strain accommodation mechanism (S. Schmid, 1976; S. M. Schmid & Paterson, 1977), this experiments suggest that it is also found at lower temperatures for larger grain sizes. It is likely that the mechanisms leading to grain boundary shear displacement are different at lower and higher temperatures.

4.4.2 Grain and twin area analysis

The grain boundaries are digitalized from a combination of the EBSD data and the optical microscope images. The boundaries are manually traced on ArcGIS and stored in polygon shape files. The shapefiles are then imported into Matlab using the PolyLX matlab toolbox developed by Ondej Lexa [1]. On average, each analyzed area

[1] http://petrol.natur.cuni.cz/ ondro/polylx:home as seen in April 2014

covers around 50 grains, but not all are complete. Each complete grain was located and identified before and after deformation to follow the area change. Table 4.5.2 shows the number of complete grains analyzed in each area (from 30 to 46) as well as the average area change for each experiment. Figure 4-23 shows the evolution of the average grain area and figure 4-24 the twinned area in each area. For comparison, the area reduction for an isotropic material deforming in an axially symmetric, isochoric compression would be 5.7% for 0.11 strain, 11.7% for 0.22 strain and 20% for 0.36 strain. Only sample CMhD (deformed at 700°C) strongly deviates from this values. Deviations could be caused by the anisotropy of calcite and the size of the sampling, and to errors in the boundary digitalization, and perhaps grain boundary migration. Another phenomenon to consider for higher strains is the "curling microstructure" described in (Wenk et al., 1986), reminiscent of what was identified in metals. W. J. Hosford (1987) explains the curled shape of compressed aluminum specimens by the strong orientation of slip systems causing deformation in plane stain instead of axially symmetric flow.

The twin area was estimated from digitalized optical and EBSD observations. Figure 4-24 shows the fractional twin before and after deformation in all the experiments. Carrara Marble initially contains some twins, which represents a great opportunity to study the evolution of pre-existing twins, but this presence also makes the comparison between samples more delicate. Overall, the twin morphology follows the expected trend documented by an extensive literature on e-twinning in Carrara Marble (see Burkhard (1993); Ferrill et al. (2004) among many). Twins get wider and more lensoid in shape both with temperature and strain. Furthermore, as expected, twin activity decreases with temperature which is manifested by a decrease in twin area. Twin area seems to increase with strain for a fixed temperature of 600°C .

4.4.3 Strain along grain boundaries

Both inter and intragranular strain can be measured. The grain boundaries were digitalized in ArcGIS as explained in subsection 4.4.2. Each grain was then defined as a polygon and the following numerical processing is done in Matlab. All centroids (obtained as described in the strain algorithm description in the previous chapter) belonging to a grain were located and a matrix "mask" was constructed to identify all centroids not belonging to any grain and representative of the strain along grain boundaries. Figure 4-25 illustrates this processing for one sample: CMhH deformed at 600°C , 300 MPa to 0.11 at a strain rate of $3\times10^{-5}s^{-1}$. The figure shows the strain along grain boundaries and inside each grain. We can see the effect of the averaging technique on the identification of the strain along grain boundaries; the boundary strain is larger when larger intra-crystalline volumes are included.

Figure 4-26 shows the mean strain along boundaries, as well as the standard deviation and the normalized standard deviation to allow comparisons between different strains. The calculation depends on the choice of n in the n-point average: for a lower n, the percentage decreases as the area considered "grain boundary" gets smaller. The strain accumulated along grain boundaries average above all grain boundaries is inferior to the intragranular strain. Nevertheless, for most experiments the standard deviation increases with decreasing n meaning that the strain along grain boundaries tends to be localized. Interestingly, the standard deviation decreases with decreasing n for the more strained samples (to 0.22 and 0.36), meaning that for more strained samples, the strain along grain boundaries is less localized. We can observe an interesting evolution with increasing temperature: the averaged strain and standard deviation first decreases with increasing temperature, then increases for temperatures above 600 °C . Furthermore, the two end members of the series present the higher variation of strain along grain boundaries: for the samples deformed at 400°C and 700°C , grain boundaries present more localized strain.

Figure 4-27 shows the percentage of total strain accommodated along grain boundaries for each sample and for each averaging technique, with an estimation of the error from the standard deviation for the zero strain experiment. Figure 4-28 shows a different representation of the data. Here the strain evolution is plotted as a function of temperature or strain for two different n averaging techniques (3 n and 9 n). First, we can see again a decrease of percent of strain along grain boundaries with temperature, and then a larger increase for temperatures above 500 °C . Second, the percent of strain along grain boundaries is constant or decreases with increasing strain. More data is needed to evaluate the evolution with strain.

Both twinning and grain boundary sliding (GBS) would be expected to cause localized strain along boundaries. The described evolution of the percent of strain accommodated along grain boundaries follows closely the expected activity of this two mechanisms. Twinning decreases with temperature and for temperatures above 500 °C , GBS starts being more representative. The strain evolution suggests that grain boundaries accommodates first more strain, and as the sample is more strained other mechanisms have to be activated, in other words, grain boundaries harden with increasing strain. This observation needs to be investigated further. If this grain boundary strain is caused by GBS, it could mean that some grain boundaries are weaker, perhaps due to their orientation. Further analysis, particularly taking into account the crystallographic orientation of the grains showing GBS should extend this observation.

4.4.4 Intragranular strain

In figure 4-29 is shown the mean intragranular strain for the temperature series for a $9n$ point average, as well as the standard deviation of the field. The mean deformation of each grain may vary by a factor of 2 from grain to grain. Furthermore, the standard deviation of local strain within a grain shows an even larger variation. Evidently,

some grains accommodate a much larger strain, and others are more heterogeneous, probably indicating the inter activation of several processes of intracrystalline deformation

Figure 4-30 shows the mean intragranular strain and standard deviation for the strain series for a $9n$ point average. Again, there is a large variability regarding the strain accommodated by each grain, as well as the heterogeneities within a grain. Furthermore, visual inspection of the strain maps suggests that bands of similarly strained grains exist in the samples strained to 0.22 and 0.36 in compression.

In order to investigate the relationship between strain and the geometric parameters of the grain, the data are replotted in a a different form. Figure 4-31 shows the normalized Von Mises strain (i.e. the value of each grain is normalized by the mean value of the intragranular Von Mises strain) versus the equivalent length of the grain before deformation ($\sqrt{\text{Area}}$), as well as the standard deviation of the intragranular ϵ_{vm} normalized by the mean value of that grain. Both values are plotted for a $3n$ and a $9n$ average computation. The first plot gives an idea of the strain accumulated for each grain in comparison to the mean strain. There is no clear correlation with the initial area. The second plot gives an estimation of the heterogeneity of the strain in each grain. This plot shows a separation between samples that corroborates the observations made earlier, particularly regarding the spectral analysis of the fields. Indeed, we can see that the two end members of the temperature series (400 and 700 °C) have more heterogeneous grains, whereas the grains are more homogeneous for intermediate temperature (500°C) and for more strained samples. The large scale evolution of heterogeneities seen in the complete strain field is found again at a grain scale.

4.5 Summary

An unprecedented level of observation on strain accommodation at different length scales can be achieved through the microscale strain mapping technique. Several observations can be made after the optical microscopical analysis and strain computation of the deformed surfaces:

1. The deformation can be characterized as isochoric for temperatures from 400°C to 700°C .

2. Both temperature series and strain series document a progressive transition and all the identified deformation mechanisms are present, but contribute differently to the total strain.

3. There seems to be a transition in the scale of heterogeneity with an increase of T: at low T the strain is localized in larger bands, spanning several grains, whereas at high T the strain field is locally more heterogeneous and the strain localization is limited to wavelengths inferior to the grain size.

4. The experimental series show that the e twinning activity decreases with an increase of temperature. Furthermore, the twinned grains seem to be organized into larger structures (wavelength signature larger than a grain size). This is probably to relate to the mechanisms of nucleation of twins and the role of grain boundaries (Christian & Mahajan, 1995).

5. The wavelength of strain heterogeneities decreases with increased strain suggesting the evolution of the structure is on-going.

6. The strain accommodated along grain boundaries is not only representative of GBS, but of all processes creating strain at the grain boundary level. The twinning contribution is more important at lower temperature and there is an increasing contribution of GBS as the temperature is increased.

Regarding the questions raised in the introduction, this analysis suggests that, although no significative hardening or weakening is really present in the stress-strain curves at T> 600°C , the microstructure has not reached steady-state. For the strain series, the wavelength of heterogeneities actually gets smaller, despite a relative homogenization of the field, suggesting that different strain accommodating mechanisms are being activated and that the structure keeps evolving. Furthermore, the observation of bands of highly strained grains indicate that the evolution towards steady-state is highly dependent on temperature. As expected, the strain partition among different deformation mechanisms does depend on the deformation conditions, but also on strain. It is therefore to be expected that the path towards steady-state will also differ with temperature, pressure and strain-rate. The intracrystalline processes have to be investigated further via a complementary analysis on the crystallographic evolution of the deformed surface. Chapter 4 deals with the texture development of the analyzed areas.

	CMhB	CMhG	CMhH	CMhI	CMhF	CMhD
Temperature (°C)	400	500	600	600	600	700
Sample strain	0.11	0.11	0. 11	0.22	0.36	0.11
Number of complete grains	30	35	43	46	30	40
Area change (%)	-3.4	-2.6	-5	-12.2	-17.3	2.8
twinned area before deformation (e twin) (%)	1.6	0.90	0.24	0.42	0.63	0.62
twinned area after deformation (%)	6.2	4.7	1.4	4.7	2.2	1.2

Table 4.5.1: Grain area measurements by digitalization of the grain boundaries: the number of complete grains analyzed as well as the average area change and twinned area percentage before and after deformation is summarized.

	CMhB	CMhG	CMhH	CMhI	CMhF	CMhD
Temperature (°C)	400	500	600	600	600	700
Sample strain	0.11	0.11	0. 11	0.22	0.36	0.11
Number of complete grains	30	35	43	46	30	40
mean strain along grain boundaries ($9n$)	0.04	0.04	0.05	0.09	0.14	0.05
std strain along grain boundaries ($9n$)	0.08	0.07	0.07	0.13	0.21	0.08
% ϵ_{vm} strain along grain boundaries ($9n$)	32	31	37	36	34	37
mean granular ϵ_{vm} ($9n$)	0.14	0.13	0.12	0.25	0.39	0.11
std granular ϵ_{vm} ($9n$)	0.04	0.03	0.03	0.05	0.09	0.03
mean strain along grain boundaries ($3n$)	0.03	0.02	0.03	0.04	0.05	0.04
std strain along grain boundaries ($3n$)	0.1	0.07	0.09	0.12	0.2	0.11
% ϵ_{vm} strain along grain boundaries ($3n$)	18	16	19	17	18	19
mean granular ϵ_{vm} ($3n$)	0.17	0.14	0.17	0.28	0.42	0.18
std granular ϵ_{vm} ($3n$)	0.06	0.03	0.03	0.05	0.09	0.06

Table 4.5.2: Grain strain statistics of Von Mises strain: mean and standard deviation of strain partition along grain boundaries and intragranular strain for two averaging techniques, $3n$ and $9n$, and percentage of strain along grain boundaries in each case.

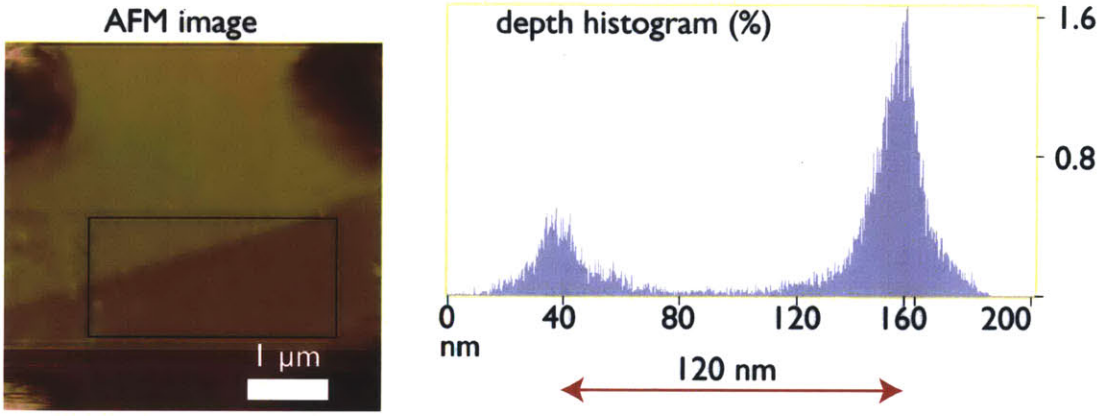

Figure 4-21: AFM step size estimation of "micro twins", on the right the AFM image obtained with a 10nm line raster and the height estimation of the step-like feature: 120 nm. The x-y plot gives the density of each height in the topography

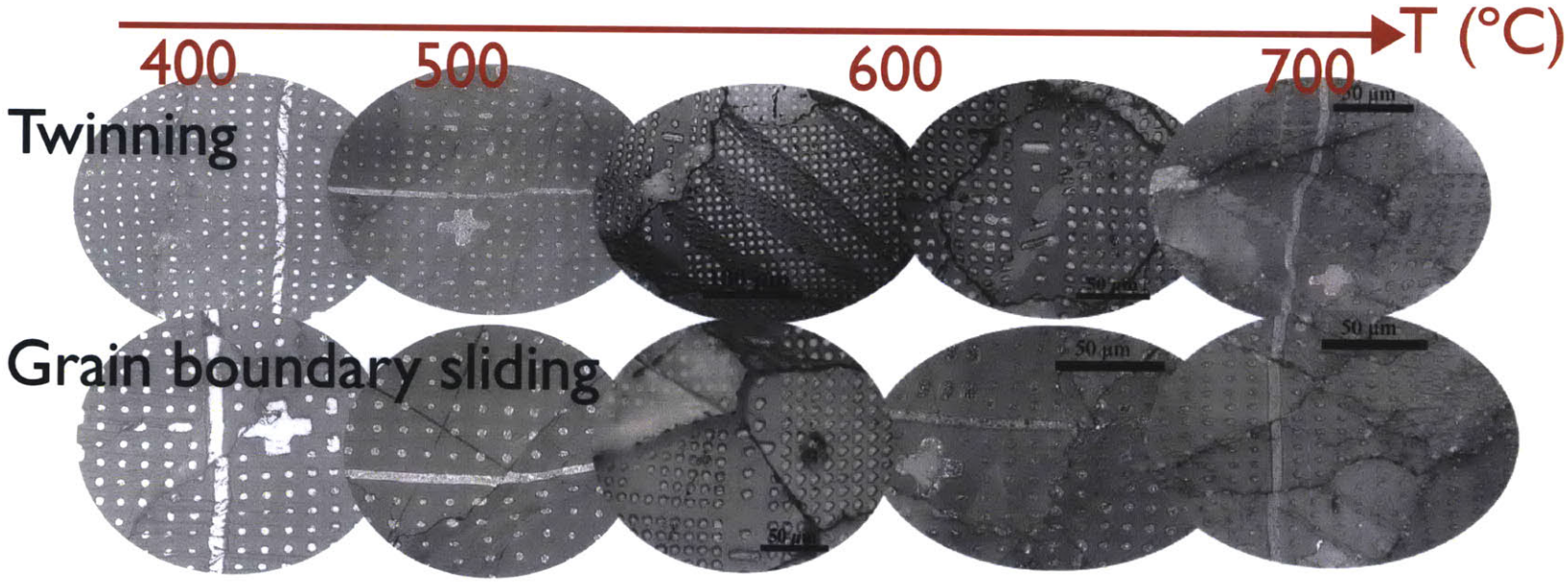

Figure 4-22: Observed mechanisms in the optical microscope images: twinning and grain boundary sliding are seen in all experiments. Particularly, grain boundary sliding is present at lower temperatures (400°C). Twinning has a change of morphology as temperature and strain increase, twins evolve towards a more lensoid shape both with increased temperature and strain in agreement with former studies (Burkhard (1993) among others)

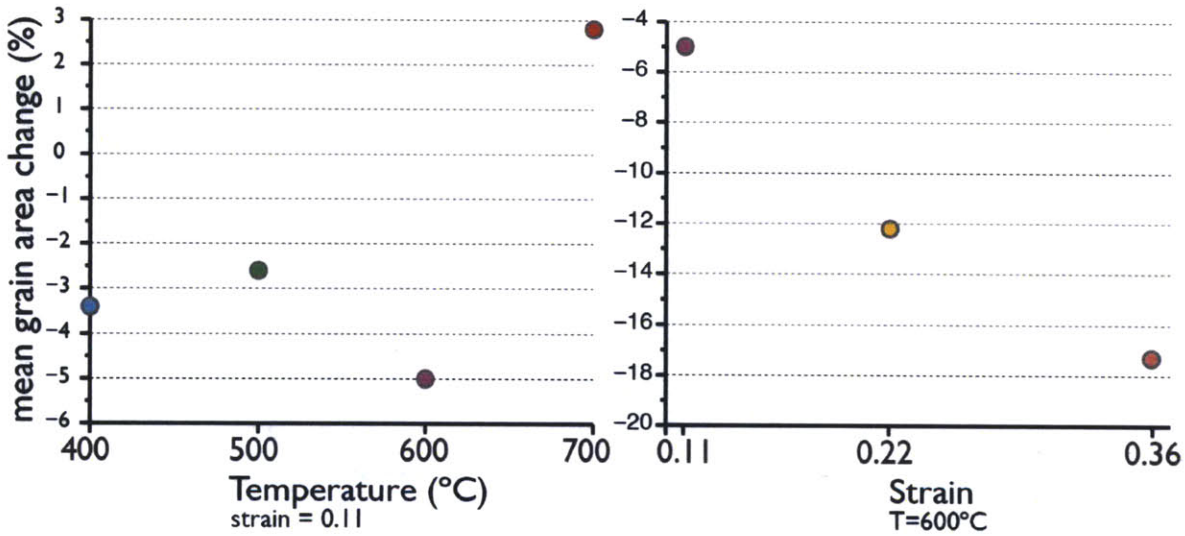

Figure 4-23: Mean area change for both experimental series (in %), for the temperature series on the left (strain of 0.11, T from 400°C to 700°C) and the strain series (T=600°C , strain of 0.11, 0.22 and 0.36), all experiments performed at a constant displacement rate of 3×10^{-5} s^{-1}. For comparison, the area reduction for an isotropic material deforming in an axially symmetric, isochoric compression would be 5.7% for 0.11 strain, 11.7% for 0.22 strain and 20% for 0.36 strain.

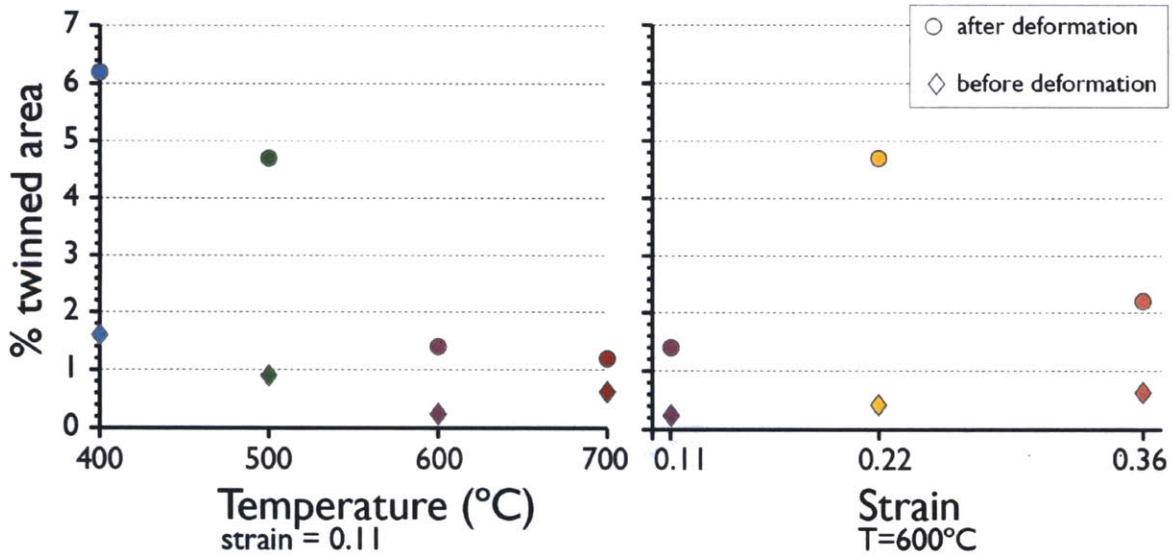

Figure 4-24: Twin area percentage for both experimental series, for the temperature series on the left (strain of 0.11, T from 400°C to 700°C) and the strain series (T=600°C , strain of 0.11, 0.22 and 0.36), all experiments performed at a constant displacement rate of 3×10^{-5} s^{-1}. The diamond markers represent the fraction of twin before deformation, the circles the fraction after deformation. Carrara Marble contains thin, straight twins (no larger than 3 μm), the twin volume increased in all experiments, but the evolution is strongly dependent on temperature.

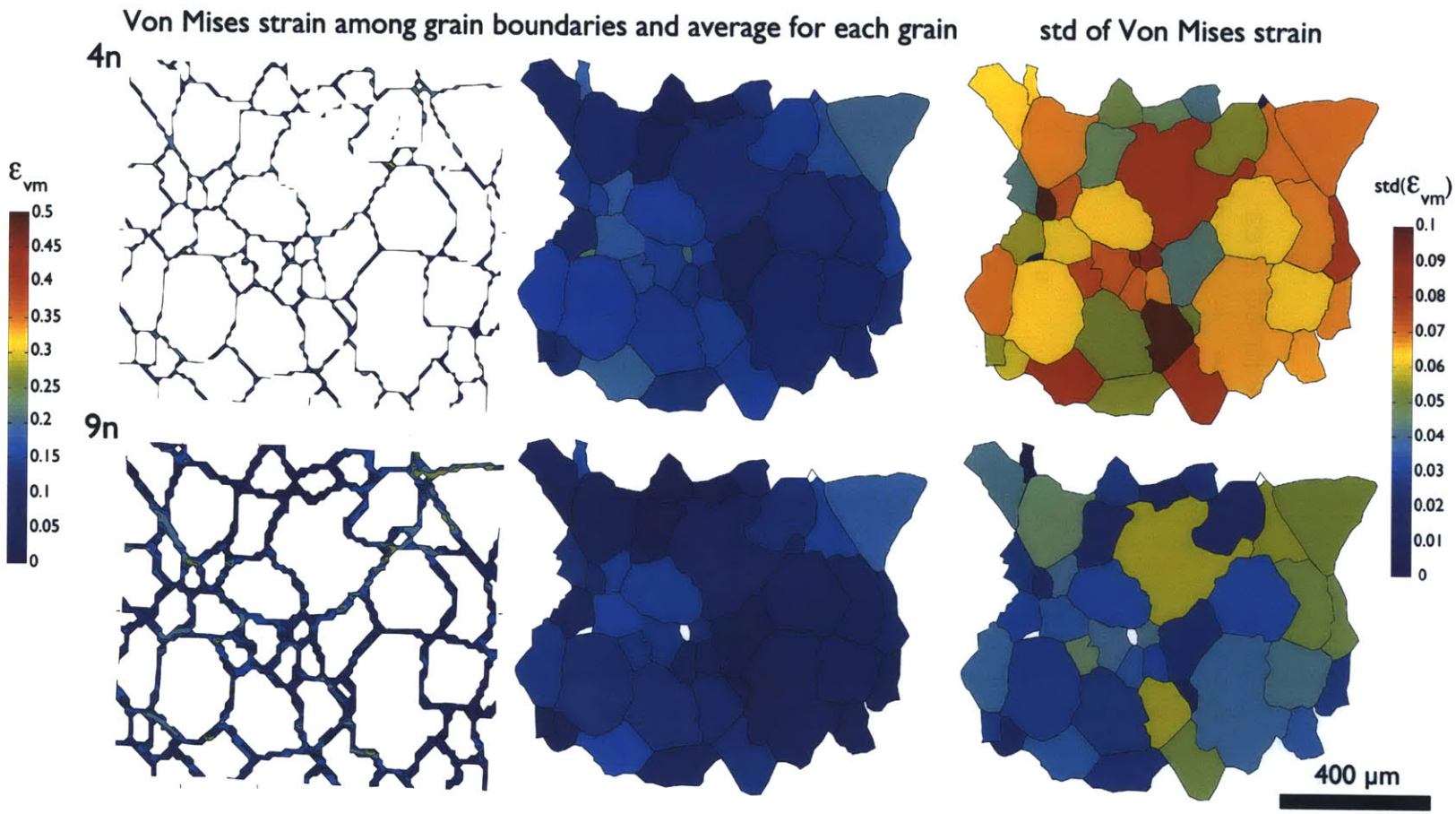

Figure 4-25: Strain partition along grain boundaries and intra granular strain for sample CMhH for averaging techniques of $4n$ and $9n$ points. The effect of the averaging technique can be seen. The mean strain for each grain is close to the overall strain, but the standard deviation varies a lot for each grain

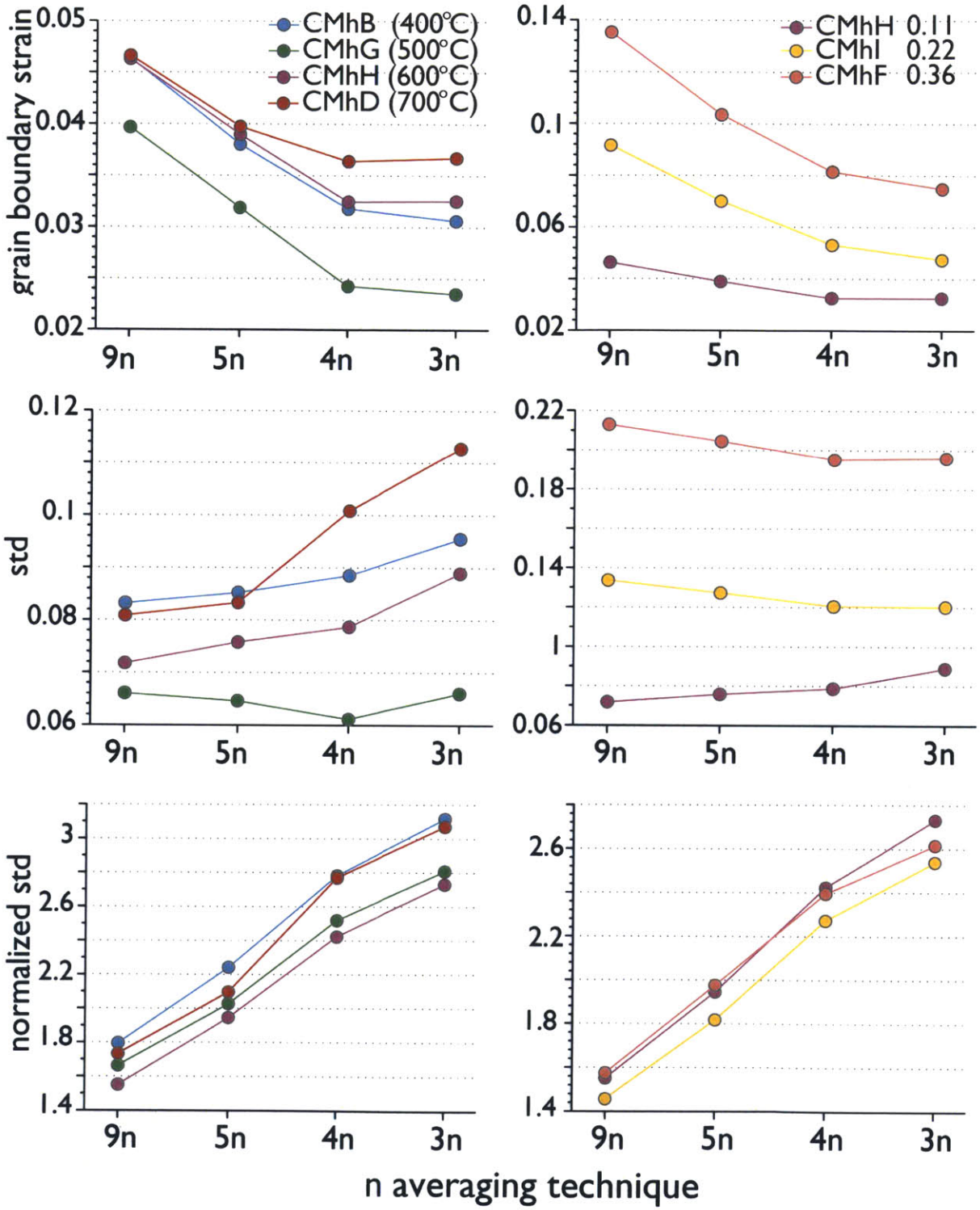

Figure 4-26: Statistical descriptors of strain along grain boundaries (mean, std, normalized std), for $9n$,$5n$,$4n$ and $3n$ average for the temperature (left) and strain series (right). The mean of the strain accommodated along grain boundaries, its std and its normalized std (normalized by the corresponding mean in order to allow comparisons of amplitudes of heterogeneities)

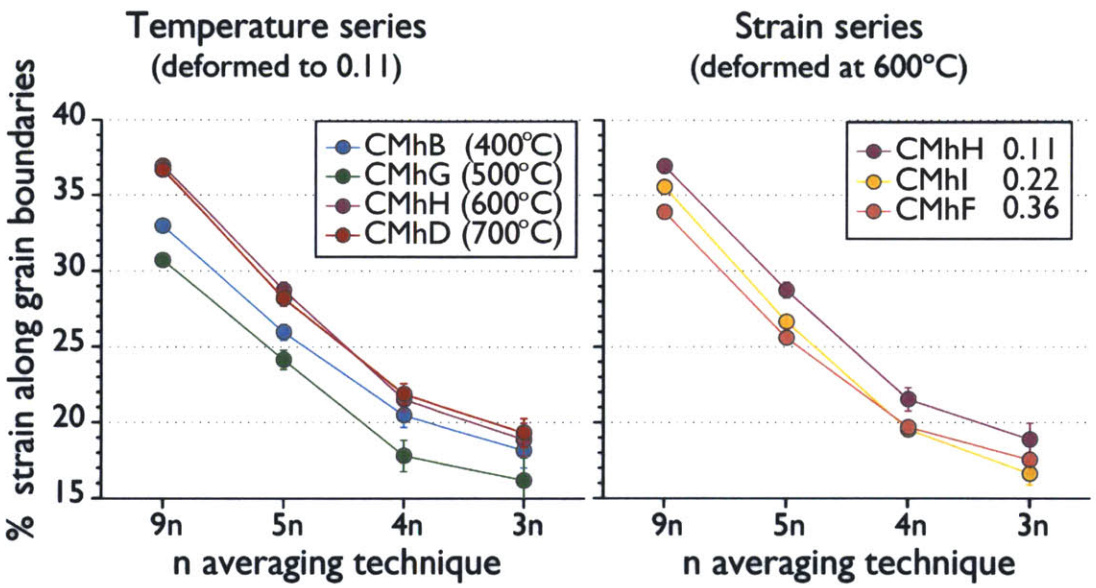

Figure 4-27: Percentage of strain along grain boundaries for $9n$,$5n$,$4n$ and $3n$ average for the temperature (left) and strain series (right). The error bar was calculated using the standard deviation of the zero strain experiment, it is masked by the markers size for $n = 9$.

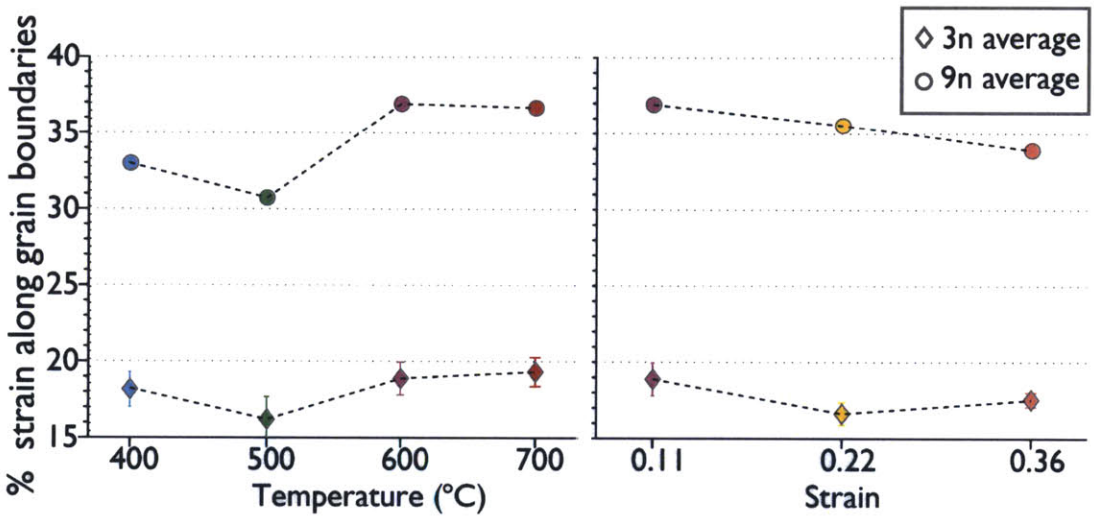

Figure 4-28: Percentage of strain along grain boundaries as a function of temperature and strain, for two n averages: $3n$ and $9n$. This plot is a different representation of the previous one, giving a better idea of the evolution of the strain with increasing temperature and strain. The error bar was calculated using the standard deviation of the zero strain experiment, it is masked by the markers size for $n = 9$.

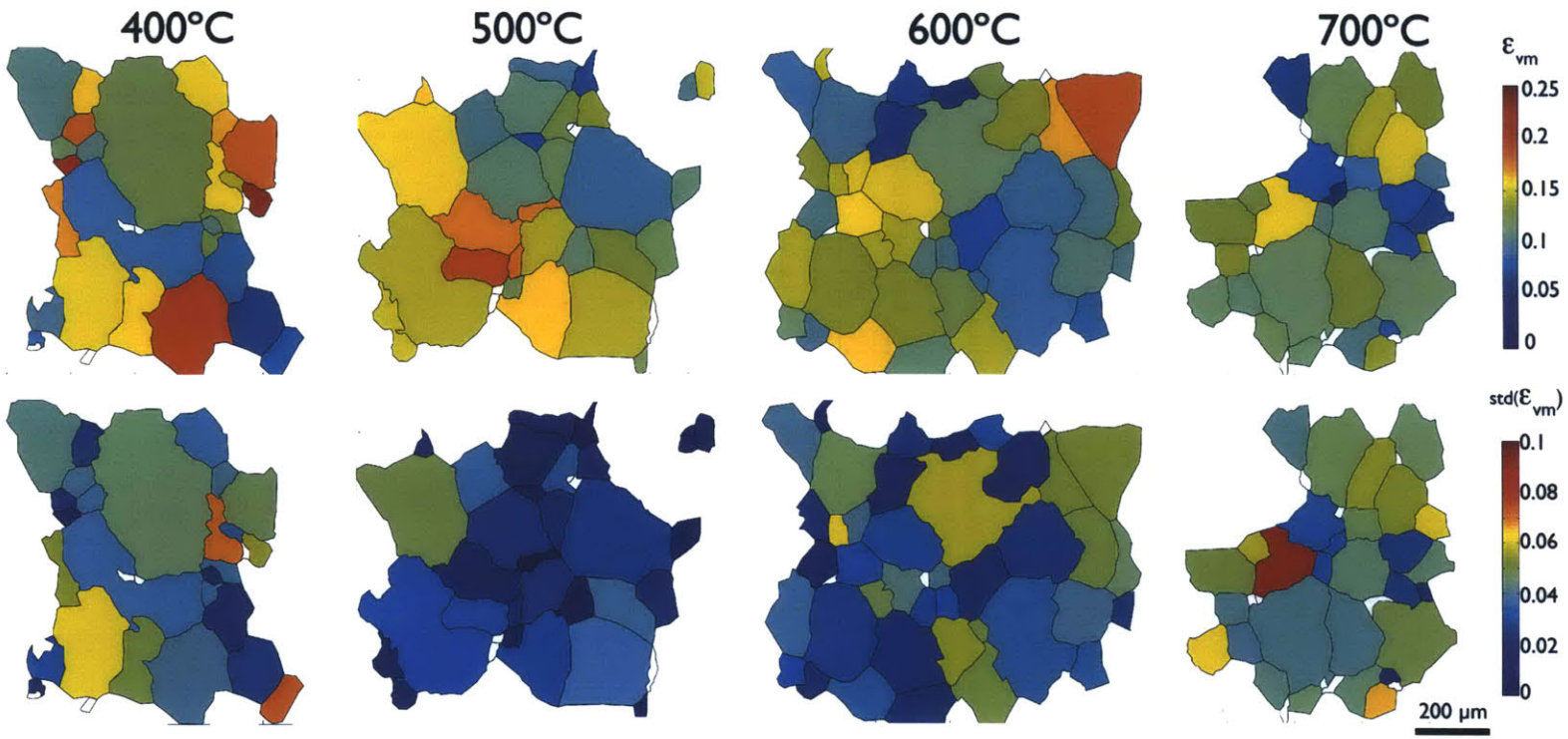

Figure 4-29: Mean and standard deviation of the intragranular Von Mises strain field for the strain series

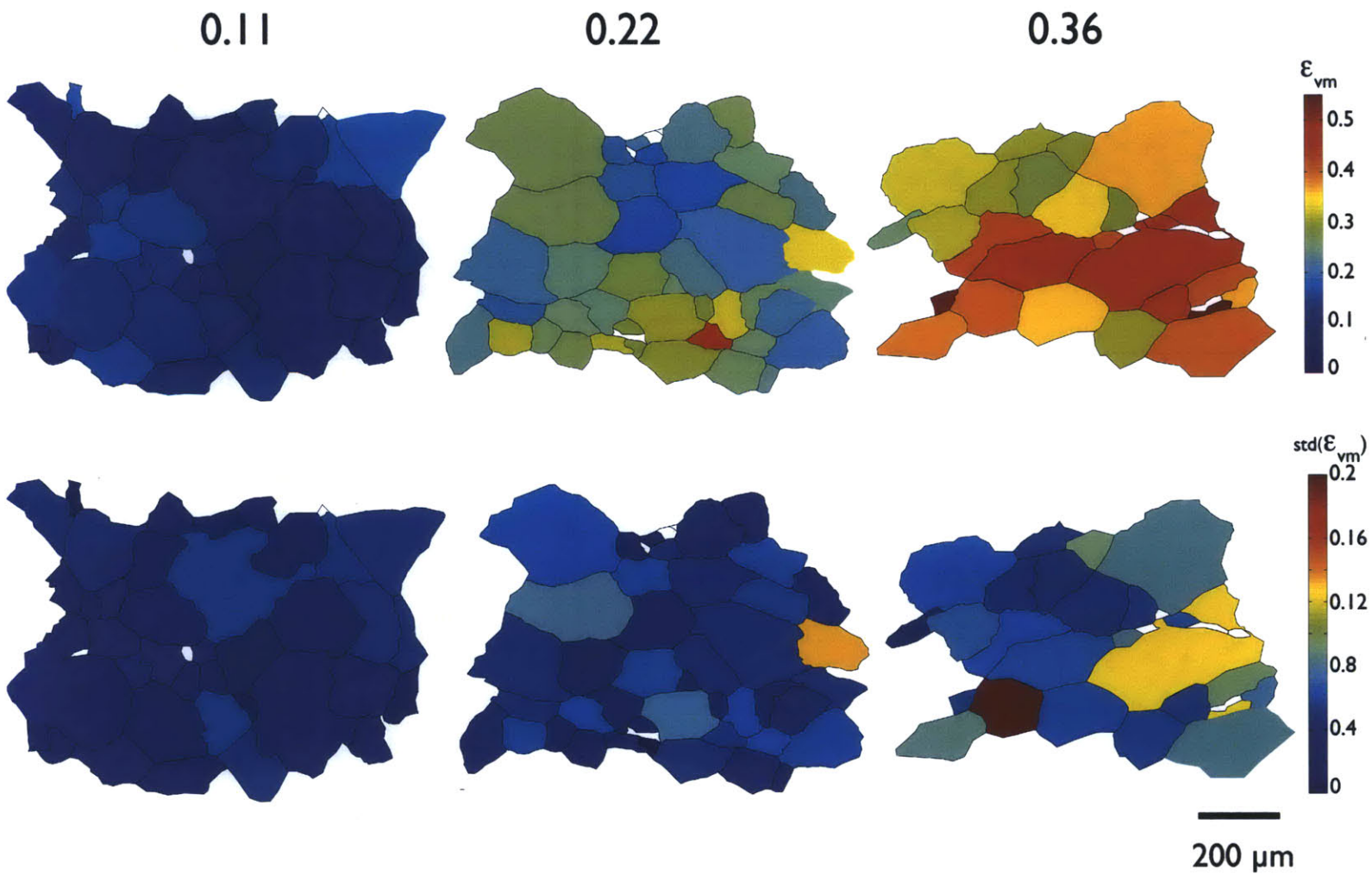

Figure 4-30: Mean and standard deviation of the intragranular Von Mises strain field for the strain series ($9n$ point average)

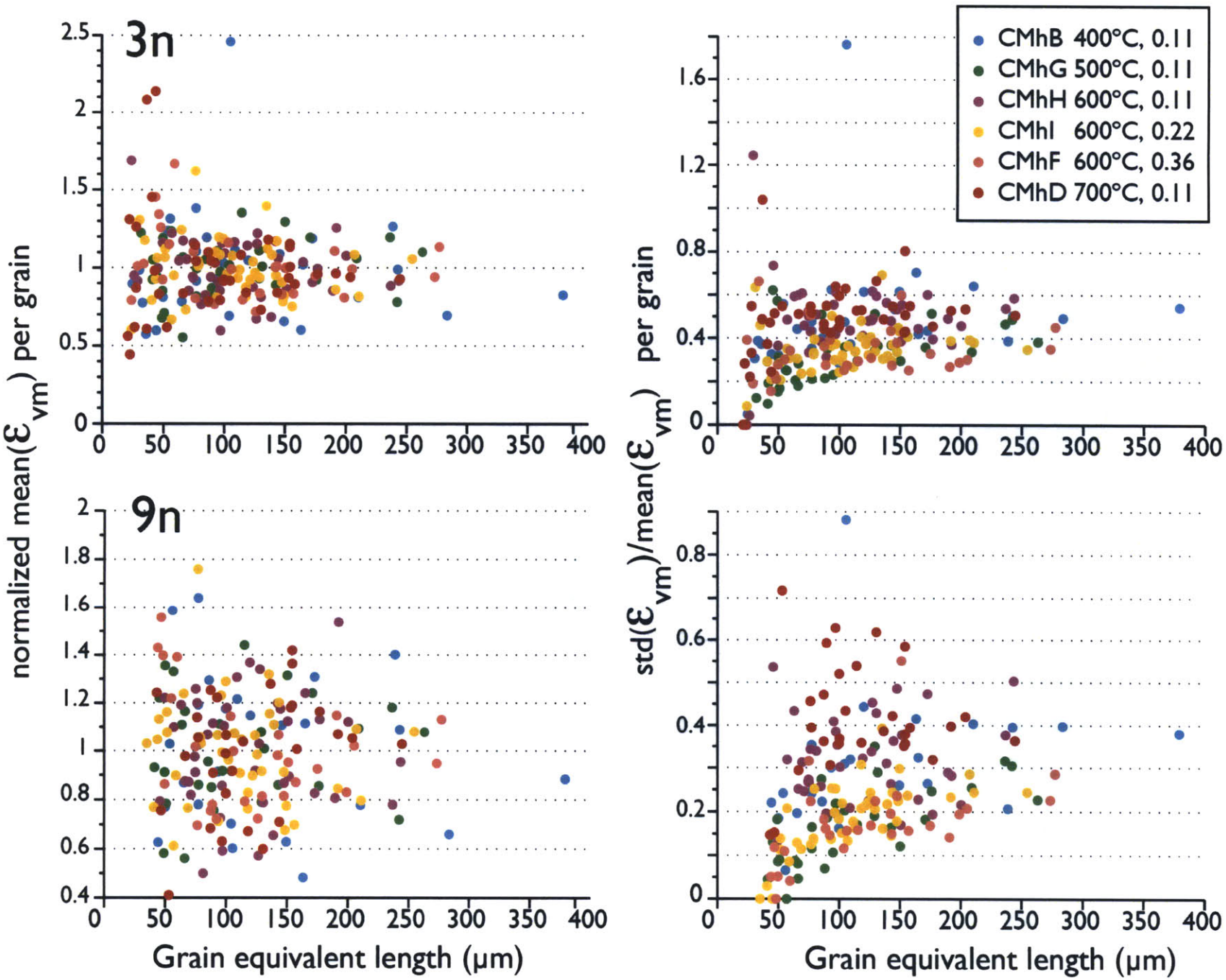

Figure 4-31: Normalized mean(ϵ_{vm}) per grain and normalized std(ϵ_{vm}) vs area before deformation

Chapter 5

Crystallographic Analysis

Abstract

Electron Back Scattered Diffraction (EBSD) data was acquired before and after deformation. The crystallographic evolution analysis complements the microscale strain mapping. Texture production depends on the partitioning of strain among twinning, glide, and boundary sliding. The detailed characterization of the area before and after deformation is a strength to this study. Indeed, averaged over large areas natural Carrara marble has a very weak texture, but the initial texture of smaller areas may vary significantly from the average. For all of the areas where the strain was measured, the texture index (TI) decreased after deformation. However, the path of the evolution differed as the temperature of deformation changed. Samples deformed at the lowest and highest temperatures, 400°C , and 700°C , showed the greatest reductions in TI. The sample deformed at 400°C had a high c-axis pole density, as expected when twinning is important. In general, the c-axis pole density mirrored the twin volume. Over a strain increment of 0.11, the decrease of c-axis density decreased as temperature increased. Both c-axis density and twin volume increased with strain at 600°C . At laboratory strain rates and 500-600°C , there is a transition in the importance of intracrystalline deformation mechanisms, from a regime dominated by twinning towards a regime dominated by intracrystalline slip. We used a Fast Fourier Transform based viscoplastic full-field formulation (VPFFT) to compute the strain field using dislocation slip models given in the literature. The model predictions have much larger wavelengths of strain heterogeneities that the observed microstructures. Among several possible reasons for the discrepancy are the 2-D boundary conditions in the model and the way that twin straining is calculated. The results are preliminary, and more thought should be given to improving models for the activity of each slip systems and to improving the measurement of strain partitioning.

5.1 Introduction

The development of texture is a critical element in understanding the evolution of its macroscopic physical properties of polycrystalline materials as they are deformed. Thus, this chapter focuses on the crystalline structure of the samples before and after deformation. This study has the advantage of having a very precise characterization of the crystallographic orientation of all grains before and after deformation: it is therefore possible to follow the evolution of crystallographic preferred orientation (CPO). The analyses of texture development and of strain at a microscale are complementary, because the strain analysis allows one to measure the partitioning of strain amongst the various inter- or intra-granular mechanisms. Immediately below, an introduction to some of the methods of texture analysis are described. Next, the texture evolution of the deformed samples is described. Then the activity of e-twinning, one of the observed deformation mechanisms is studied, and finally, preliminary work using an n-site viscoplastic FFT based model (VPFFT) is compared to the measured strain.

5.2 Methods

The crystallographic preferred orientation (CPO) of a polycrystalline material is defined by the distribution of orientations of all the individual crystals (i.e. grains) measured relative to some reference lattice system. (For the sake of brevity, CPO and texture will be used synonymously.) A material is said to have a texture if some specific crystallographic orientations have a statistical tendency to be approximately aligned. A polycrystalline has no (or random) texture if the distribution of crystal axes is uniform. This section describes, briefly, the mathematical tools used for texture representation, as well as the experimental methods used to measure CPO.

5.2.1 Representation of crystallographic orientation

The Rotation (Orientation) Matrix and the Misorientation matrix

The orientation of a particular crystal can be defined by describing the angular relations between the crystal coordinate system and the specimen (or reference) coordinate system using a linear tensor transformation:

$$\mathbf{C_c} = \mathbf{g}.\mathbf{C_g} \tag{5.1}$$

Where $\mathbf{C_c}$ and $\mathbf{C_g}$ is the same vector expressed in the crystal and specimen coordinate systems, respectively, and $\mathbf{g}$ is a rotation or orientation matrix, composed of nine direction cosines. The reference coordinate system may be a specimen system or it can be chosen to be the crystallographic system of a neighboring grain. In this case, it is then called misorientation matrix and is calculated from the orientation of both grains:

$$\mathbf{M_{12}} = \mathbf{g_1}^{-1}\mathbf{g_2} \tag{5.2}$$

where $\mathbf{g_1}$ is the rotation matrix for the grain arbitrarily chosen as reference. The rotation and misorientation matrix contain redundant information and can be defined by other mathematical descriptors. Among these are the Euler angles (often used by EBSD systems found in electron microscopes), the axis of rotation and angle representations (often used to define special boundaries between grains), the Rodrigues representation (not usually used in geology), and rotation quaternions, used by the MTEX Matlab toolbox (R. Hielscher, 2008; Bachmann et al., 2010; Mainprice et al., 2011), described in more detail bellow.

Euler angles

The Euler angles refer to three rotations that, when performed in the correct sequence, transform the specimen coordinate system onto the crystal coordinate system. Thus, they are an alternate representation of **g**. Several different conventions for expressing the Euler angles exist, but the most commonly used and those formulated by Bunge (1982). The rotations are as follows: ϕ_1 around the 1 axis, Φ around the rotated 2 axis and ϕ_2 around the rotated 1 axis.

5.2.2 Electron Backscattered Diffraction (EBSD) method

There are several methods to measure the crystallographic orientation distribution: Optical microscopy gives information on the grain orientation by providing information about the orientation of the optical indicatrix. X-ray Diffraction measures the projection of the average texture at a surface (μm penetration), Neutron Diffraction measures the projection of the average texture in bulk (cm penetration). Electron backscattered Diffraction measures the entire (3 angle) local surface texture (nm penetration). The Electron Backscattered Diffraction method (or EBSD), described in more detail in chapter 2, has allowed an incredible advances in the understanding of texture development in geological materials (Mainprice et al., 2004; Prior et al., 2009). Current automated techniques allows one to obtain the crystallographic orientation of crystals with a step sizes as small as tenths of nm, depending on the resolution of the Scanning Electron Microscope and the preparation of the sample.

All analyses presented here were done at Geosciences Montpellier using a CamScan XF500FE CrystalProbe and an Oxford HKL EBSD system described in Chapter 2. The maps were obtained using a voltage of 15kV, a current of 3 to 5 nA and a working distance of 25 mm at low-vacuum conditions (2 Pa of gaseous nitrogen). Data were acquired and treated using CHANNEL5 software. The data acquisition was done with Flamenco for all samples before deformation, and for samples CMhB,

CMhG and CMhH after deformation. Acquisition was done with AZtec for samples CMhI, CMhF and CMhD after deformation. For all samples, two areas, roughly in the middle of the sample were mapped before deformation, one with a step size of 12 μm over about 200 grains; the second area was mapped with a step size of 3 μm over about 50 grains. The smaller area was then found after deformation using the embedded coordinate system and mapped with a reduced step size of 2 μm (or even 1 μm for the most challenging sample, CMhF deformed to 0.36). Additionally, an even smaller map was done at a much higher resolution of 0.5 μm in order to analyze the twin morphology.

The output of the EBSD mapping is a set of three Euler angles at each point. The Euler angles are given with respect to a reference frame related to the SEM sample holder. Experimentally, this means that careful registry of the sample within the holder is necessary for each set of measurements. Thus, the comparison of the orientation of grains before and after deformation incorporates a registry error, which should be reduced in the future, perhaps via the design of an adapted sample holder. Damage produced by deformation presents added complications. We face the challenge of the macroscopic heterogeneity of the triaxial test. Indeed, the definition of the reference for a barrel-shaped, or strongly bent sample is not straight forward. The positioning of the sample is probably quite accurate for samples deformed at 0.11 strain. Errors are estimated to be about 3 to 5 degrees, but are probably much larger for samples deformed to 0.22 and 0.36, where barreling and bending occurred. The rate of successful indexation was, on average 85 % and 74% for the undeformed and deformed samples respectively. The latter rate was a very pleasant surprise, considering the topography and damage that developed during deformation.

EBSD data treatment was done using the MTEX package, a powerful, open-source software toolbox for texture analysis and modeling (R. Hielscher, 2008; Bachmann et al., 2010; Mainprice et al., 2011). MTEX allows for repeatable and controlled orien-

tation data treatment, and even incorporates the calculation of physical properties of polycrystalline aggregates. See Mainprice et al. (2011) for a thorough description of the mathematical tensor capabilities of the MTEX toolbox.

5.2.3 Characterization of the texture

Representing the texture of a polycrystalline material is not straightforward, and several different methods might be necessary depending on the situation. Numerous textbooks such as Kocks (2000); Engler and Randle (2009) describe these representations in more detail. The orientation distribution function (ODF) is a full representation of the texture and is defined as the volume fraction of grains with a specific orientation g, as described in Eq. 1.3. For a uniform (or random) texture, the ODF density is 1 for all orientations. The MTEX toolbox uses radially symmetric kernel density estimation to compute an ODF from EBSD data. For this study, we used the default De la Vallé Poussin kernel with a half-width of 10°.

$$\mathrm{odf}(g) = \frac{1}{V}\frac{dV(g)}{dg} \tag{5.3}$$

Texture can also be represented by plotting pole figures, a partial representation, where a specific crystallographic axis is plotted in a stereographic projection. A pole figure is the angular distribution function of a chosen crystal direction **h** in the specimen coordinates. Although preferred in material science applications, ODF representations are harder to interpret, and pole figures are more typically used by geologists. A quantitative measure of the the strength of the a particular microstructure is given by the texture index (TI), also called J-index Bunge (1982), or F2 by Matthies (Matthies et al., 1988). TI is easily computed with the MTEX toolbox and corresponds to the integral of the norm of the orientation distribution function over the entire angular space of the hemisphere: as defined in equation 5.4:

$$T.I. = \int [f(g)]^2 dg \tag{5.4}$$

TI can be calculated for the entire ODF to give an idea of the general sharpness of the texture: a value of 1 corresponds to a uniform distribution. The TI may also be calculated for a specific pole figure by integrating over the pole angle. Differences between deformed and undeformed TI can be calculated for both ODFs and pole figure (PF) using the function **calcError** in MTEX as follows:

$$\mathrm{RP} = \frac{1}{N} \sum_{i=1}^{i=N} \frac{\left| P_i^{\text{deformed}} - P_i^{\text{inital}} \right|}{P_i^{\text{deformed}}} \tag{5.5}$$

where P is the pole figure density in multiples of a uniform density.

5.2.4 Relating texture to strain: Schmid factor

The notion of the Schmid factor is easy to understand for a single crystal. Dislocation glide occurs on specific slip systems, that are characteristic for each mineral, although they may vary according to the deformation conditions. A particular glide system is defined by the slip plane along which glide occurs, and a Burgers vector that defines the shear displacement along the plane. The critical shear stress required to move dislocation along a specific slip direction and plane in a particular crystal is related to the applied shear stress by :

$$\tau_r = \sigma \cos \Theta \cos \lambda \tag{5.6}$$

where Θ and λ are angles between applied stress and the normal to the slip plane and the slip plane direction, respectively (see Figure 5-1).

5.3 Texture Development

5.3.1 Starting material

Carrara marble has its own history of deformation (Molli & Heilbronner, 1999; Molli et al., 2000). Thus, the starting material for the experiments had some imprinted deformation. It is, therefore important to characterize the starting texture, in order to analyze changes in the texture that are caused by the laboratory deformation. Table 5.6.1 shows the TI of the ODF in each sample for a large area before deformation (about 3.5mm by 3mm,12 μm step size), and for the smaller area that was analyzed following the microscale strain mapping technique (1.5mm by 1mm, 3 μm step size before deformation, 2 μm and 1 μm -for sample CMhF- step size after deformation). Figure 5-2 shows the contoured pole figures of the **c** axis and the pole to the twinning plane **e** for large area maps (comprising around 300 grains) of the starting material. The starting material has a very weak preferred orientation when large areas are considered. However, when smaller areas are averaged, the TI may be larger, between 3 and 4. This is mostly due to reductions in sampling size, from 300 to 50 grains. Smaller areas have also a better characterization of twinned grains. Twinning is a particularly effective way to strengthen texture; it results in a fixed rotation of the **c** axes from host to twin orientation, leading to a phenomenon called volume transfer in the ODF. Because twins initially present in Carrara marble are very thin (no wider than 3μm), the larger step size map may be under-evaluating the twin volume.

5.3.2 Texture evolution

For each experiment, Table 5.6.2 gives the TI for the **c**, **e**, **r**, **f** and **m** poles; the change in the TI after deformation for each pole figure is given in Table 5.6.3. Figure 5-3 shows the pole figures for the **c** axis and the **e** plane pole before and after deformation; and figure 5-4 summarizes the evolution of the TI for the areas analyzed

before and after deformation. Finally, figures 5-5 and 5-6 show the TI for poles **a**, **m** and **r**, and **c**, **f** and **e** respectively. In general, the texture indices decreased after deformation, i.e., deformation weakened the texture. One working hypothesis is that texture weakening occurs because the natural and experimental loading conditions were not geometrically equivalent. Because the initial textures were produced by loading geometry that differed from during the experiments, the initial textures might be expected to weaken as the material is strained in a new direction. Apparently, the strains achieved in these experiments were not large enough to have completely erased the old textures and establish a new one that would increase in intensity with strain.

Although the comparisons from experiment to experiment are more difficult to make because of the differing initial TI, we examined the data for trends in the rate of texture weakening as a function of temperature and strain. Figure 5-7 shows RP, the difference of the texture index for the ODFs and Pfs, calculated in MTEX and defined in 5.5. Notice that these differences correspond to the normalized absolute difference and tell us about the relative change of the textures between the 2 stages. The rate of change was larger at the lowest and highest temperatures, 400 and 700°C , while samples deformed at 500 and 600°C have the lowest rate of change. The rate of change continued to increase with strain at 600°C .

It is interesting to consider the evolution of pole density for the **c**-axes. Many previous experiments indicate that high twinning activity tends to form a small circle girdle pattern at 20 to 30° around the axis of compression, e.g., Spiers (1979); Turner and Weiss (1963). For all the experiments in this study, the rate of change of TI of the **c**-axes correlated with the rate of evolution of the twin area. Both decreased with temperature for strains of 0.11, and both increased with strain at 600°C . These observations could be interpreted as indicating the passage from a deformation regime, which was dominated by twin production and very effective in changing the **c**-axis orientation, to a regime where dislocation slip was dominant. Based on the rate of twin

production, this evolution was progressive with temperatures 500°C and 600°C being transitional. It was also noted that the wavelength of the strain heterogeneities decreased over this temperature range.

The influence of pre-existing strain on both the microstructure and rheological properties is very relevant to the understanding of tectonic processes if rocks are subjected to several strain cycles. Several earlier workers, including Bruijn et al. (2011) and Piane and Burlini (2008) studied the influence of strain history on the strength and microstructure formed in Carrara Marble during torsional loading. These experiments involved reversed torsion cycles with much larger strains that the ones involved in our experiments. Full recrystallization at $\gamma > 5$ produced CPO's without sensitivity to prior shear history. In our experiments, the experimental loading conditions probably did not have any relation to those causing the natural textures, but we can conclude that strains of 0.36 are not able to completely erase the initial CPO.

The microscale strain technique also provides information of the production of shape preferred orientation (SPO) of the grains. Figures 5-8 and 5-9 show rose diagrams obtained with the PolyLX matlab toolbox (function **aparor** applied on the digitalized grain boundaries). The function is based on the projection method described in Panozzo (1983) and the diagram gives the frequency of grains oriented at a given angle. These diagrams describe the shape of a limited number of grains (between 25 and 40), but they do appear to be discernible trends. Before deformation, samples have a weak SPO, inferior to 4% alignment. Deformation to 0.11 does no significant change of SPO. In fact, the SPO produced by deformation at 600°C is reduced. At higher strains, grains tended to be elongated in the direction perpendicular to the compression direction by a measurable amount.

5.4 Twinning

This section focuses on one very visible feature in all experiments: twinning. A similar analysis should be carried out on the identified slip systems on calcite. Linking the activity of different slip systems to the development of strain heterogeneities is a logical expansion of this work.

5.4.1 e-twinning in calcite

Twinning in calcite has been an object of study since the end of the 19th century (Dove, 1860). A calcite crystal can indeed be "manually" twinned via the gentle application of pressure with knife on the intersection of cleavage rhombs. Mechanical twinning in calcite occurs primarily on **e**$\{\bar{1}018\}$ planes in the $< 40\bar{4}1 >$ direction. Twinning has also been observed on **r** $\{10\bar{1}4\} < \bar{1}012 >$ and **f** $\{\bar{1}012\} < 10\bar{1}4 >$ (Borg & Handin, 1967; Weiss & Turner, 1972; M. Paterson, 1979), but these systems appear to be relatively unimportant and were not observed in our experiments. A description of twinning in calcite can be found in D. J. Barber and Wenk (1979), and a review of the earlier literature of calcite mechanical twinning in Klassen-Neklyudova (1964).

For **e** twinning, the shear displacement is in the positive sense in the direction $< 01\bar{1}2 >$. During deformation the **c** axis moves through an angle of 52.5°, and the plane of the carbonate groups, perpendicular to the **c** axis must also be rotated through the same angle. Twinning introduces a very particular discontinuity in the grain: the lattices of the components are always inclined to one another at a definite angle and are rigidly joined at the surface of contact. It is natural to expect a concentration of strain at this zones of contact (Klassen-Neklyudova, 1964). Moreover, twinning introduces a discontinuity, very much like a new grain boundary, and twin boundaries may be a barrier to the movement of dislocations (Serra et al., 2002). Figure 5-10

shows the projection of the twinning elements for the **e** twinning system. Given the symmetry of calcite, three systems ought to be considered: e1($\bar{1}$018)[40$\bar{4}$1], e2 (1$\bar{1}$108)[$\bar{4}$401] and e3 (01$\bar{1}$8)[0$\bar{4}$41], and for each a shear direction [r2:e1], [r3:e2] and [r1:e3].

Because the twin microstructure in natural deformed rocks is visually striking and easily quantifiable, it has been used to infer stress (Jamison & Spang, 1976; Laurent et al., 1981; Rowe & Rutter, 1990; Lacombe & Laurent, 1992; Lacombe, 2007) , strain (Groshong et al., 1984; Gonzlez-Casado et al., 2003), and the temperature of the deformation (Burkhard, 1993; Ferrill et al., 2004). Although it would be very desirable to have a simple relationship between an easily measurable quantity such as twin density, or twin volume, and a single parameter describing the deformation conditions, such as stress or temperature, twinning is likely to be affected by several parameters including strain, temperature, and peak stress (Rybacki et al., 2013).

Many of the studies mentioned above consider twinning to be a mechanism important only at low temperatures. But notice that the twin paleopiezometer established by Rowe and Rutter (1990) was derived from experiments conducted at 400-800°C . All the experiments in this study were performed at the same temperature range as Rowe and Rutter. It is interesting to compare the results of the present study to the work at lower temperatures, particularly because the measurements presented here document the transition from a deformation regime with high twin activity to a deformation accommodated by dislocation creep with little twinning.

5.4.2 Twin statistics and morphology analysis

As in the studies of twin morphology considering deformation at lower temperatures, one can see a distinct change in morphology in our experiments. To span a larger range of temperature, an additional experiment was conducted to a strain of 0.03 at 200°C and a strain rate of $3\times10^{-5}s^{-1}$. Preliminary results are shown in 5.6.4, which

compares the twin area obtained by MTEX analysis of special boundaries to that obtained through visual inspection of EBSD maps followed by digitization of twin boundaries described above. There are two important differences in these estimates: the manual measurements consider only complete grains for which were included in the microscale strain mapping (between 30 and 40 grains), whereas the EBSD area is larger, considering at least 60 grains. However, automatic detection of twin boundaries can be biased by plastic deformation of the twins that will cause deviations from the theoretical geometry for e-twins. Despite these differences, the comparison is quite good overall, with the exception of the samples with larger strains CMhI (deformed to 0.22) and CMhF(deformed to 0.36). This agreement suggests that the smaller areas in the microscale strain mapping analyses may still be representative. Thus, measurements of twin density (twins per mm) were made on a few grains (10). The results are quite preliminary, but they are reported here to compare our experiments with previous studies. Clearly, additional measurement are necessary to make firm conclusions. In agreement with previous work (Burkhard, 1993; Ferrill et al., 2004), the mean twin intensities (twin planes/mm) in our experiments correlated negatively with temperature, and increase with strain, even though our experiments were done at higher temperatures. Rowe and Rutter (1990) relate σ, the stress in MPa to N_L the twin density in number of twins per mm:

$$\sigma = -52.0 + 171.1 \log(N_L) \tag{5.7}$$

This relationship over estimates the stresses of the temperature series samples by 26%, 33%, 57% and 132%, but we are mindful of the authors warning about increasingly large errors at higher temperatures as the twins become more and more lensoid in shape. Similarly, the paleopiezometer from Rybacki et al. (2013) underestimates the stresses found here. That relation was established with microstructures formed at

lower temperatures. In all cases, the stress and twin density data are quite scattered, and error estimates are fairly large.

Twin morphology has been used as a geothermometer, and twins have been described as thin, tabular thick, curved and lensed, and thick patchy (modified by dynamic recrystallization) according to Burkhard (1993) and later Ferrill et al. (2004). Figures 5-11 and 5-12 show the morphological evolution in our samples, based on the EBSD data collected on small areas of the deformed samples with a step size of 0.5 μm. Figure 5-13 shows preliminary results from the experiment performed at 200°C . All twins above 300°C show tabular thick, curved and lensed characteristics as expected for those temperatures (Ferrill et al., 2004). The tendency for twins to thicken continues to temperatures as high as 600°C . At 700°C , twinning is almost limited to the pre-existing twins.

5.4.3 Twin Schmid factor

Figure 5-14 illustrates the value of the Schmid factor (SF) according to the orientation of the crystal relative to the axis of tension or compression (figure by David Mainprice). A negative SF corresponds to activation of twinning by compressive stress, while a positive SF would correspond to activation by tensile stress. In these experiments, local stresses are expected to be compressional. Very large heterogeneities of local stress could cause some grains to be under extension (T), but such stress fields are probably quite unlikely. Grains most likely to twin will have a Schmid factor of -0.5, i.e, with an **f1** axis oriented towards the axis of compression (C) as shown in figure 5-14.

Figure 5-15 shows Schmid factor for all three twinning systems for sample CMhB, deformed to 0.11 at 400°C , as well as a representation of the grain and twin structure for the analyzed area. Each system of twinning is represented by a different color. It can be seen that many of the grains that twinned correspond to grains with a SF

close to -0.5 in one of the systems. However, not all grains with large negative SFś twinned. Moreover, twin nucleation seems to be favored over twin thickening. Another important observation, true in all samples, is that some grains, not particularly favorably oriented, will twin when situated next to a grain that is favorably oriented and has twinned. This observation suggest that strain accommodation caused by twinning in neighbor grains allow the creation of bands of more highly strained grains. Former studies have observed high dislocation densities along twin boundaries, another observation suggesting local stress concentrations can create bands of strain with characteristic distances large than a single grain (Chen et al., 2011; Larsson & Christy, 2008; De Bresser, 1996; D. J. Barber & Wenk, 1979; Rybacki et al., 2013). This high stress concentration and high density of dislocations could explain the creation of chains of twinned grains, accommodating larger strains than the average. Further studies and analysis of the dislocation density for those grains may provide more insight into the mechanism of nucleation of twinning.

A more complete statistical analysis of these samples, following a recent study of deformation in high-purity poly-crystalline zirconium at 77K (Capolungo et al., 2009) might reveal statistical correlations between e-twinning in calcite, and grain size, crystallographic orientation, grain-boundary length, and neighbor misorientation. It would be particularly interesting discover the deformation conditions for which twin nucleation is favored over twin propagation, to understand the effect of grain-grain misorientation, and to twin activity with the strain accommodation and macroscopic hardening. These results suggest that twinning in one grain is very much influenced by surrounding grains. It would be interesting to relate this accommodation to nucleation probability, and to the creation of deformation bands larger than the grain size.

5.5 Modeling polycrystalline plasticity

The ultimate aims of experimental rock deformation are to provide rheological constraints and better methods to interpret microstructural signatures of rocks deformed under natural conditions. Unfortunately, the deformation conditions accessible in the laboratory are limited, both by material constraints and by the life expectancy of the experimentalist; thus, extrapolation over many orders of magnitude time and length are necessary. In addition to recent improvements in the experimental methods, current workers also benefit from enormous advances in numerical methods used to model deformation at geological conditions. Experiments and models must go hand in hand. Meaningful predictions from a numerical model, based on a solid theoretical understanding of the deformation mechanisms, require testing and calibration through experiments. Modeling polycrystalline plastic deformation has been of great interest to material scientist and there is now an extensive body of work on this subject (Reid (1973); W. F. Hosford (1993); Khan and Huang (1995); Kocks (2000); Neto et al. (2008) among many).

Two end-member descriptions of deformation in a polycrystalline material are the Taylor model (Taylor, 1938), which assumes a homogeneous strain (Turner et al., 1954), and the Sachs model, which assumes a uniform stress state (Wagner et al., 1982; Wenk et al., 1986). The Taylor assumption is accurate for materials that are plastically isotropic (i.e. have many slip systems of comparable strength), but for anisotropic materials it leads to prediction of excessively high stresses and incorrect textures. Thus the Taylor model provides an upper bound. With the Sachs approach, only the most favorable oriented slip systems are activated and strains may not be compatible along grain boundaries but the stress is always homogeneous. This model represents a lower bound of strength for the polycrystalline aggregate. The viscoplastic self-consistent model (VPSC) is an intermediate approach (Molinari et al., 1987; R. A. Lebensohn & Tom, 1993), that considers each grain as an inclusion

in a homogeneous, but possibly anisotropic, plastic medium with properties of the aggregate. This model is based on the Eshelby inclusion model (Eshelby, 1957) and relates the local stress and strain rate to the macroscopical stresses and strain rates of the aggregate.

The n-site viscoplastic FFT formulation (or VPFFT model) (R. Lebensohn, 2001) solves the micromechanical fields exactly for a given microstructure because it treats flow at each site separately. The resolution of the model is defined by the resolution of the orientation information (in this case, the EBSD data). As opposed to the VPSC model that gives the average strain-rate inside each grain, the VPFFT model predicts the local strain rate in each site and can therefore model strain heterogeneities within the grain, making it a very interesting model to compare to the microscale strain mapping analysis. This section presents the preliminary comparisons between the experimental microscale strain analysis and the VPFFT predictions of strain distribution among the calcite polycrystalline aggregate.

5.5.1 The VPFFT model applied to calcite

The model presents a solution of the local problem of an inhomogeneous viscoplastic medium undergoing an applied velocity gradient V_{ij}. It assumes the viscoplastic medium is an anisotropic polycrystal deforming by dislocation glide and uses the Green's function method to solve for the equilibrium of stresses and compatibility of deformations. The technique uses an iterative process of convolutions between the Green function and the polarization field. The equations are solved in the Fourier space where these convolutions become multiplications. The model has been reviewed in detail in literature (R. Lebensohn, 2001; R. A. Lebensohn et al., 2008, 2009) and we will discuss a few details pertinent for this work. As described earlier, the input is the EBSD data set and the output is a deformation field with the same resolution (3 μm in this application).

The VPFFT formulation assumes the material deforms by dislocation glide, and the output is a function of the choice of the slip systems and their relative strength, similarly to the viscoplastic self consistent formulation (VPSC). The latter has been used to describe the texture development in calcite and compare it to natural or experimentally deformed samples (R. A. Lebensohn et al., 1998; Wenk et al., 1987; Pieri, Kunze, et al., 2001; D. Barber et al., 2007; Xu & Evans, 2010; Austin et al., 2014). Despite extensive work on dislocations in calcite, uncertainty still exists, particularly related to the CRSS of each slip system and their contribution to strain under different conditions of deformation. Laboratory experiments by De Bresser and Spiers (1990, 1993, 1997) show that dislocation glide in calcite occurs on the $\mathbf{r}^{\pm}\{\mathbf{10\bar{1}4}\} < \mathbf{20\bar{2}\bar{1}} >$, $\mathbf{c}^{\pm}(\mathbf{0001}) < \mathbf{11\bar{2}0} >$ and $\mathbf{f}^{\pm}\{\mathbf{\bar{1}012}\} < \mathbf{10\bar{1}1} >$. Modeling studies use various combinations of these systems with adjustments to their relative CRSS values. Most do not take into account twinning (D. Barber et al., 2007; Pieri, Kunze, et al., 2001; Austin et al., 2014; Xu & Evans, 2010).

The VPFFT code was provided by Dr. Ricardo A. Lebensohn from Los Alamos National Laboratory, and was run with the EBSD data collected at Géosciences Montpellier. The results presented here follow the slip systems and relative strength described in R. A. Lebensohn et al. (1998) but do not account for recrystallization which was not observed. Volume transfer due to twinning (seen in the samples) was not included. The deformations mechanisms considered and their relative CRSS (in arbitrary units) are summarized in table 5.6.5: negative and positive slip on $\mathbf{r}^{-}\{\mathbf{10\bar{1}4}\} < \mathbf{20\bar{2}\bar{1}} >$, $\mathbf{r}^{+}\{\mathbf{10\bar{1}4}\} < \mathbf{\bar{2}021} >$, negative slip on $\mathbf{f}^{-}\{\mathbf{\bar{1}012}\} < \mathbf{2\bar{2}01} >$ and $\mathbf{e}^{+}$ twinning $\{\bar{1}018\} < 40\bar{4}1 >$. Twinning is treated as a pseudo-slip and no volume transfer is considered. Three regimes are considered: low temperature (LT), intermediate temperature (IT) and high temperature (HT), depending on the relative importance of each system.

5.5.2 First comparisons

In figure 5-16 model results from the three temperature modes are compared to the microscale strain mapping technique on sample CMhH, deformed at 600°C to 0.11 strain. The model spans a larger area but both are displayed at the same scale for comparisons. From this preliminary results, it is apparent that the model did not capture the heterogeneity that was experimentally observed. The amplitudes of the strain variations are similar in both, but the length scales are greater in the model. Only one directionality seems to be apparent in the model whereas the experiments show strain localization along several directions. The evolution of strain localization also seems to evolve in the opposite sense of what was experimentally observed. At the high temperature mode, the strain localization in bands comprising several grains is more apparent, a feature observed experimentally at lower temperatures and that disappeared with increase in temperature.

5.5.3 Source of differences: assumptions in experiments and model

Boundary conditions The VPFFT model requires periodicity in all directions, the EBSD grid is therefore repeated in the 2D space. In the third dimension, however, no variation of granular structure is taken into account and the grains are assumed to be infinite columns. This is quite different from the experiments where there is a 3-D grain structure, including a planar interface along the gridded surface. As seen in Chapter 3, despite the discontinuity of grain structure there is a perfect continuity of strain across the split surface, and therefore facing grains interact mechanically. Any strain occurring on the face of one half-cylinder is accommodated by a grain in the facing half. The mechanical constraints of both the experiments and the model differ from conditions of a grain deforming within a 3-D matrix of grains.

Twinning in the model Twinning represents an additional source of reorientation. When a twin is formed, a volume fraction of the host crystal adopts a new crystallographic orientation, related to the host's by reflection or 180° rotation. It is challenging to model this volumetric change because the model must account for the creation of new grains. The implications of twinning in the local strain field must also be substantial. Twin boundaries may hinder the propagation of dislocations within the grain (Christian & Mahajan, 1995) and are related to the strain hardening of the material. In the VPFFT model, twinning is considered as a pseudo-slip system with no consequence for hardening.

Wavelength of strain field The difference in the scale of the heterogeneities needs to be explored further, but it is probably related to either volume transfer or strain hardening, both of which will shorten the mean free path for slip. The considered slip systems do not capture the evolution with temperature described in Chapter 4. Nevertheless, this comparison may be useful for elucidating dominating slip systems.

5.6 Summary

The texture analysis and first comparison of the VPFFT model and experiments poses many new questions, but conclusions may also be drawn. The microscale strain mapping technique documents a transition for a twinning-dominated regime to one controlled primarily by dislocation glide over the temperature range from 400°C to 700°C . A complication arises from the preexisting texture within the marble, but this study presents the advantage of a careful characterization of the texture before and after deformation. Furthermore, twinning seems to be an important mechanism for the creation of bands of more strained grains and the localization of strain in structures larger than the grain size. More strain analyses could be used to elucidate the changes in the relative contribution of the various slip systems. This information

might substantially aid in the construction of the slip models.

Sample	TI ODF large area (%indexed)	TI ODF analyzed area (%indexed)	TI ODF after deformation (%indexed)
CMhB	1.49 (77.2)	3.89 (83.3)	3.39 (52.2)
CMhG	1.32 (85)	2.72 (88.5)	2.42 (81.3)
CMhH	1.28(77.2)	2.49 (76.9)	2.06 (80.5)
CMhI	1.31(87.5)	2.56 (93.1)	2.09 (83.4)
CMhF	1.39 (82.5)	2.99 (87)	2.14 (65.7)
CMhD	1.33 (81.2)	3.14 (88.4)	2.77 (78.5)

Table 5.6.1: Texture Index for starting material and for analyzed area before and after deformation for the temperature series and strain series experiments. The Texture Index is a measure of the sharpness of a texture and corresponds to the second moment of the orientation distribution

	c(0001)		**e**$(01\bar{1}8)$		**r**$(10\bar{1}4)$		**f** $(01\bar{1}2)$		**a** $(2\bar{1}\bar{1}0)$		**m** $(10\bar{1}0)$	
Sample	Jpf bd	Jpf ad	Jpf bd	Jpf ad	Jpf bd	Jpf ad	Jpf bd	Jpf ad	Jpf bd	Jpf ad	Jpf bd	Jpf ad
CMhB	1.6	1.41	1.18	1.13	1.17	1.13	1.19	1.16	1.23	1.20	1.21	1.16
CMhG	1.50	1.46	1.15	1.15	1.12	1.10	1.14	1.11	1.13	1.11	1.13	1.11
CMhH	1.35	1.33	1.12	1.12	1.12	1.10	1.13	1.10	1.11	1.09	1.14	1.09
CMhI	1.43	1.47	1.16	1.22	1.11	1.08	1.11	1.06	1.16	1.13	1.14	1.14
CMhF	1.49	1.44	1.18	1.18	1.14	1.11	1.14	1.07	1.13	1.12	1.13	1.12
CMhD	1.62	1.68	1.21	1.22	1.17	1.12	1.10	1.09	1.16	1.17	1.16	1.17

Table 5.6.2: Texture Index for pole figures for analyzed area before and after deformation for the temperature series and strain series experiments, calculated in a 1 degree grid

Sample	ODF	Poles					
		c(0001)	**e**$(01\bar{1}8)$	**r**$(10\bar{1}4)$	**f** $(01\bar{1}2)$	**a** $(2\bar{1}\bar{1}0)$	**m** $(10\bar{1}0)$
CMhB	0.26	0.09	0.06	0.06	0.09	0.1	0.07
CMhG	0.19	0.08	0.04	0.05	0.05	0.08	0.05
CMhH	0.19	0.06	0.04	0.04	0.05	0.07	0.07
CMhI	0.31	0.09	0.06	0.09	0.13	0.11	0.08
CMhF	0.38	0.15	0.11	0.10	0.17	0.12	0.10
CMhD	0.21	0.05	0.05	0.06	0.09	0.07	0.08

Table 5.6.3: Texture index of **difference** of odf and pf, gives an indication of the magnitude of the difference of texture after deformation

Sample	Twinned area fraction ebsd data		Twinned area fraction (analyzed data)		Twinned grains		Re-twinned grain	Twin intensity (twins/mm)
	bd	ad	bd	ad	bd	ad		
CMhB	0.46	7.3	1.6	6.2	7	13	2	88
CMhG	0.54	5.3	0.9	4.7	8	11	2	44
CMhH	0.09	2.2	0.23	1.4	4	10	1	33
CMhI	2.2	0.6	0.42	4.7	3	9	2	23
CMhF	0.38	5.2	0.63	2.2	3	5	1	23
CMhD	2.6	3.6	0.62	1.2	3	4	0	17

Table 5.6.4: Twinning statistics: twinned area before and after deformation, evaluated with the EBSD data (via identification of special boundaries) and on the analyzed grains (number of grains given in previous chapter), and number of grains where the twin either expanded or the grain continued to twin in the pre-existing twinning system (called here "Re-twinned grains"). All observed twins were e twins.

Mode	LT	IT	HT
$\mathbf{r}^-$ $\{10\bar{1}4\} < 20\bar{2}\bar{1} >$	1	1	1
$\mathbf{r}^+$ $\{10\bar{1}4\} < \bar{2}021 >$	1.6	2	2
$\mathbf{f}^-$ $\{\bar{1}012\} < 0\bar{2}2\bar{1} >$	1.6	1	0.5
$\mathbf{e}^+$ twinning $\{\bar{1}018\} < 40\bar{4}1 >$	0.4	0.8	2

Table 5.6.5: Relative CRSS in VPFFT model for each temperature mode (arbitrary units), from R. A. Lebensohn et al. (1998). For the low temperature mode (LT) and the intermediate temperature mode (IT), $\mathbf{e}^+$ twinning (treated as a pseudo slip) is the weakest slip system, for the high temperature mode (HT) $\mathbf{f}^-$ is the weakest slip

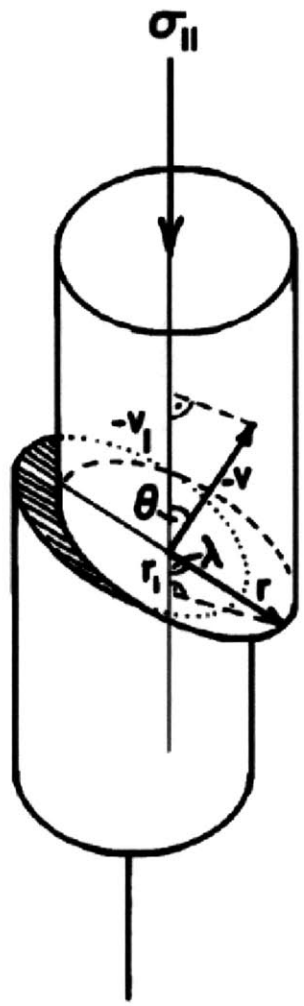

Figure 5-1: Axial compression of a single crystal: elements of Schmid factor calculation, in (Wenk et al., 1986) after Schmid, 1928. Θ and λ are angles between applied stress and the normal to the slip plane and the slip plane direction, respectively.

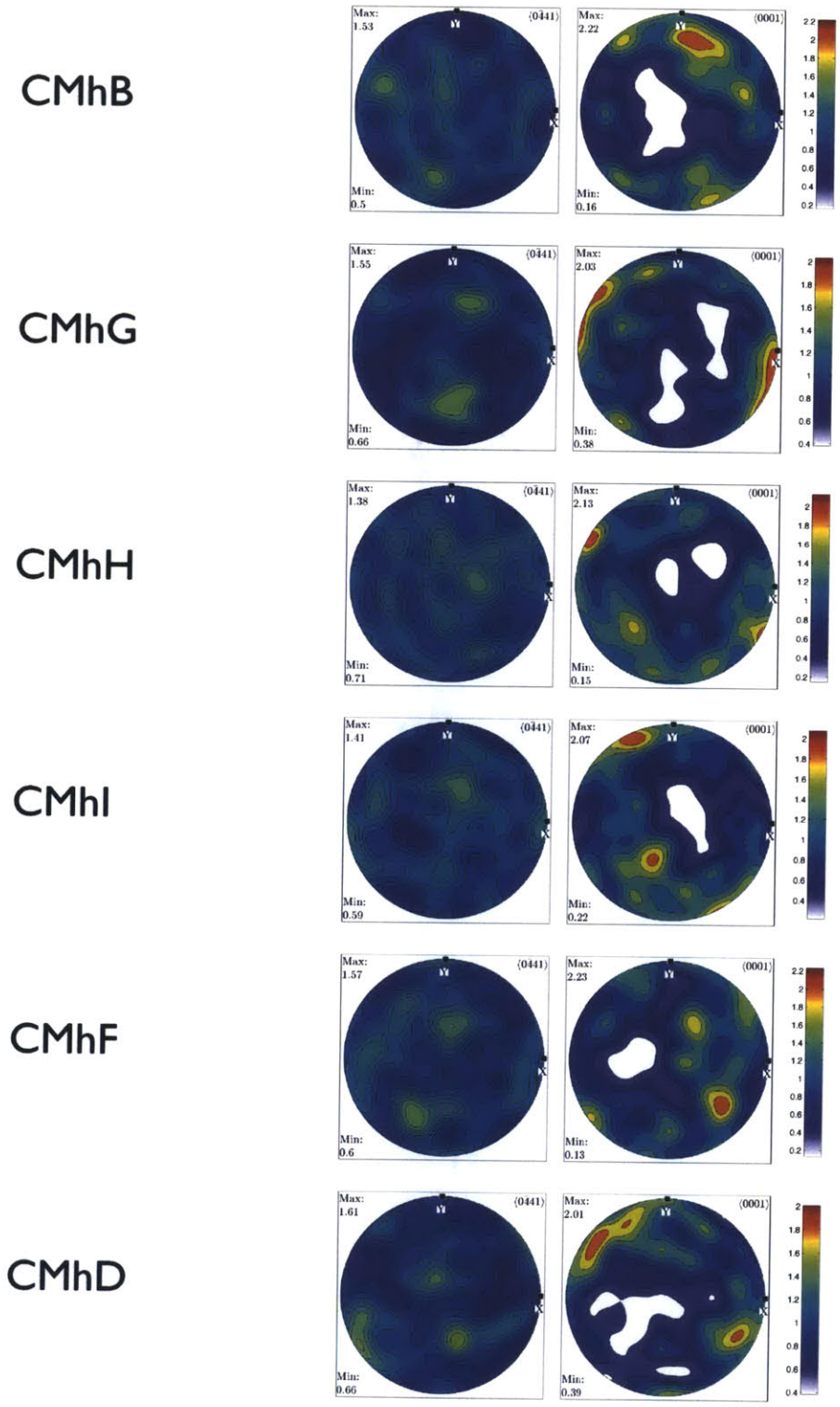

Figure 5-2: Pole figures for c axis and e-twinning axis for starting material. Lower hemisphere, equal area projection, contour given in multiples of uniform distribution. The areas analyzed here are of the order of 3.5mm by 3mm with a step size of 12 μm, containing in average 300 grains and represent a good statistical representation of the starting material. Y is the compression direction σ_1.

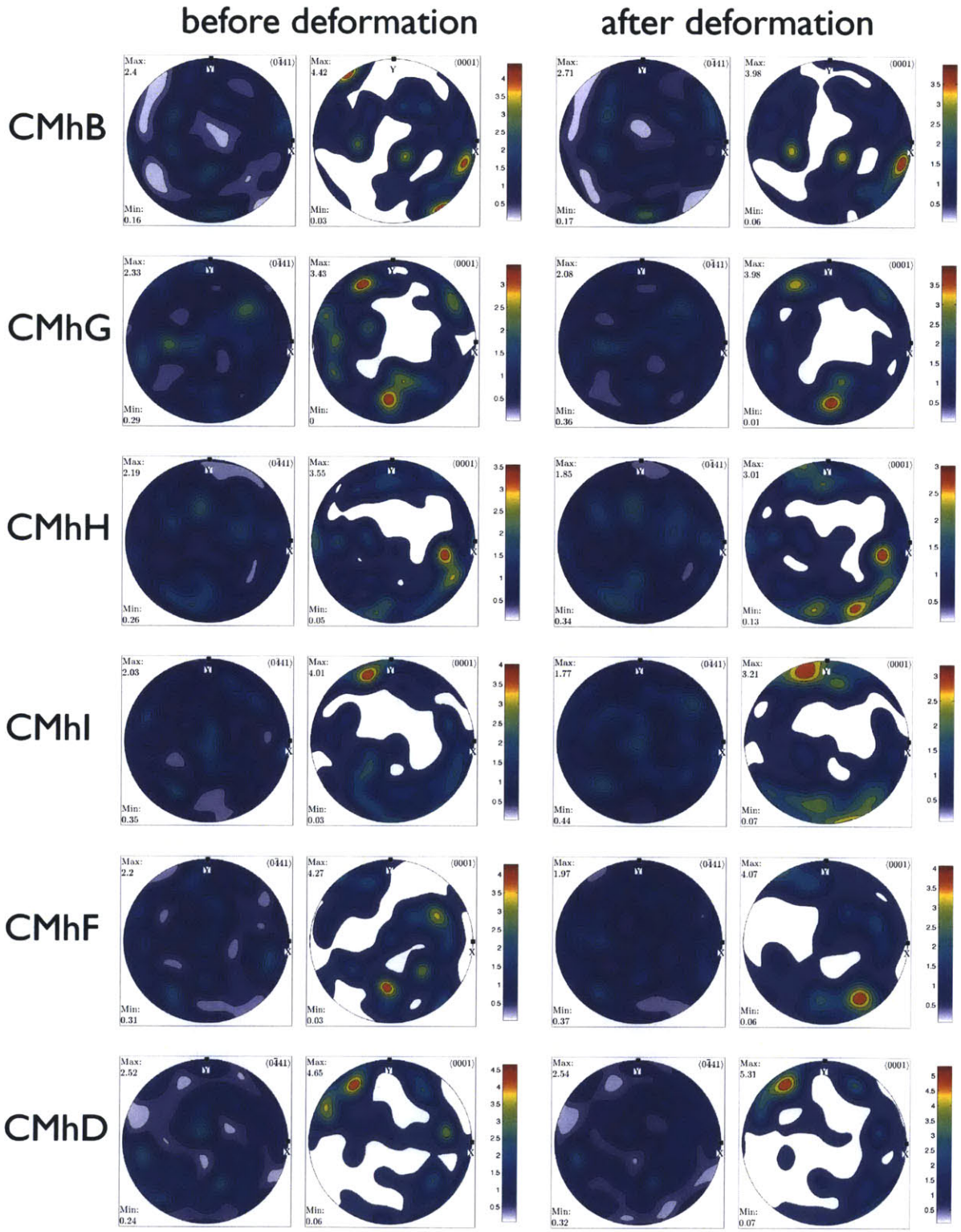

Figure 5-3: Pole figures for c axis and e-twinning axis for analyzed area before and after deformation. Lower hemisphere, equal area projection, contour given in multiples of uniform distribution. The areas analyzed here are of the order of 1mm by 1mm and contain in average 60 to 100 grains. Y is the compression direction σ_1.

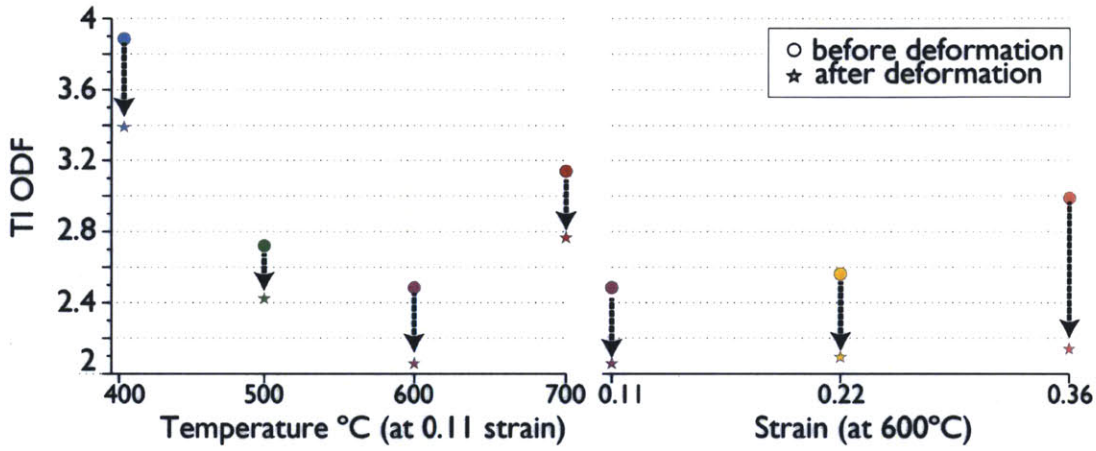

Figure 5-4: TI evolution for the strain and temperature series. The Texture Index is represented for the same area before and after deformation, as a function of temperature (on the right) and strain (on the left). In all cases the initial TI is larger, deformation is "erasing" the CPO initially contained in Carrara Marble, however, this evolution changes with the deformation conditions. Particularly, we can see that for higher strain, the decrease is larger, similarly with the lower (400°C) and higher temperature (700°C).

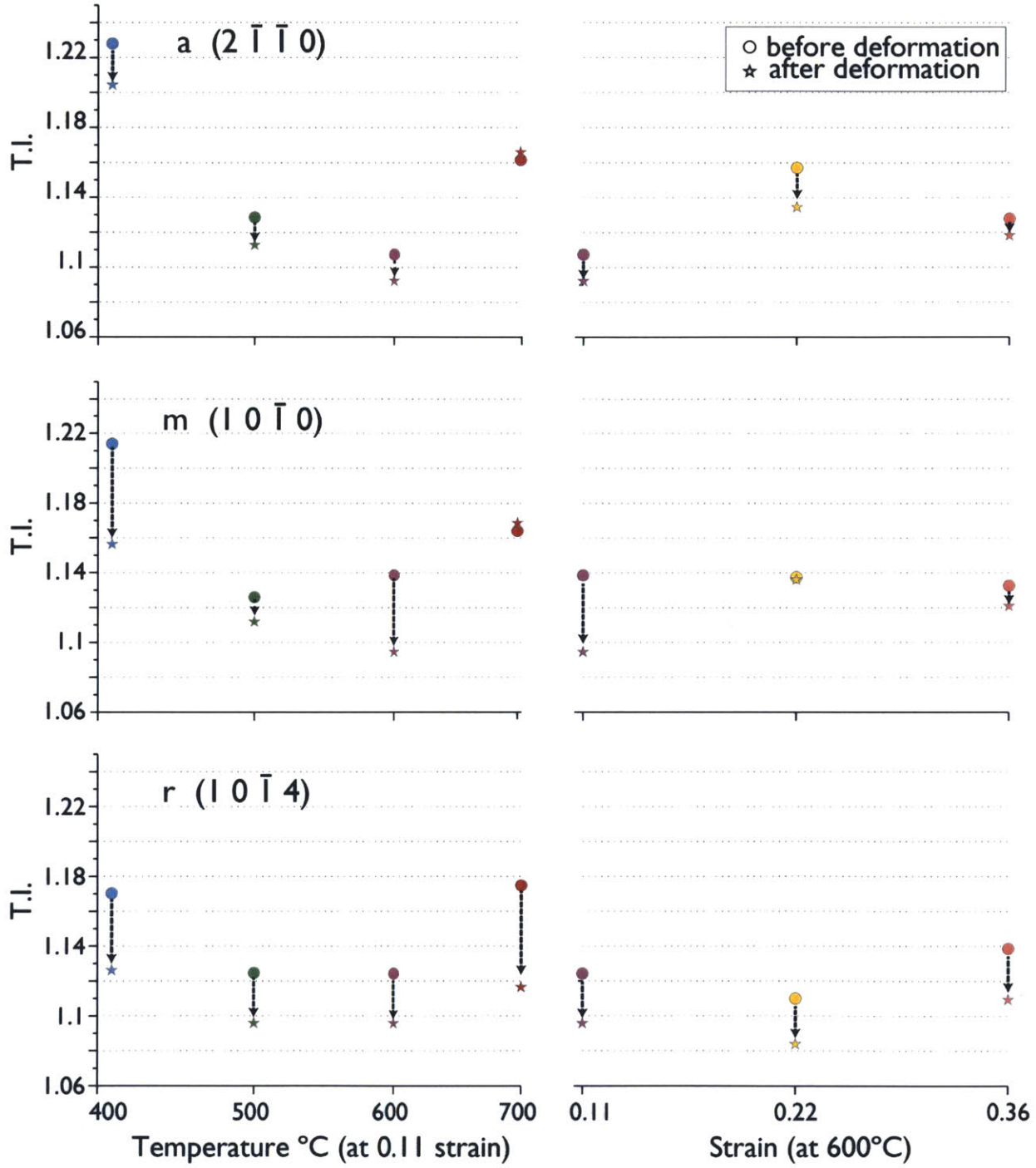

Figure 5-5: Texture Index (TI) for Pole figures a, m and r: all indexes decreased after deformation.

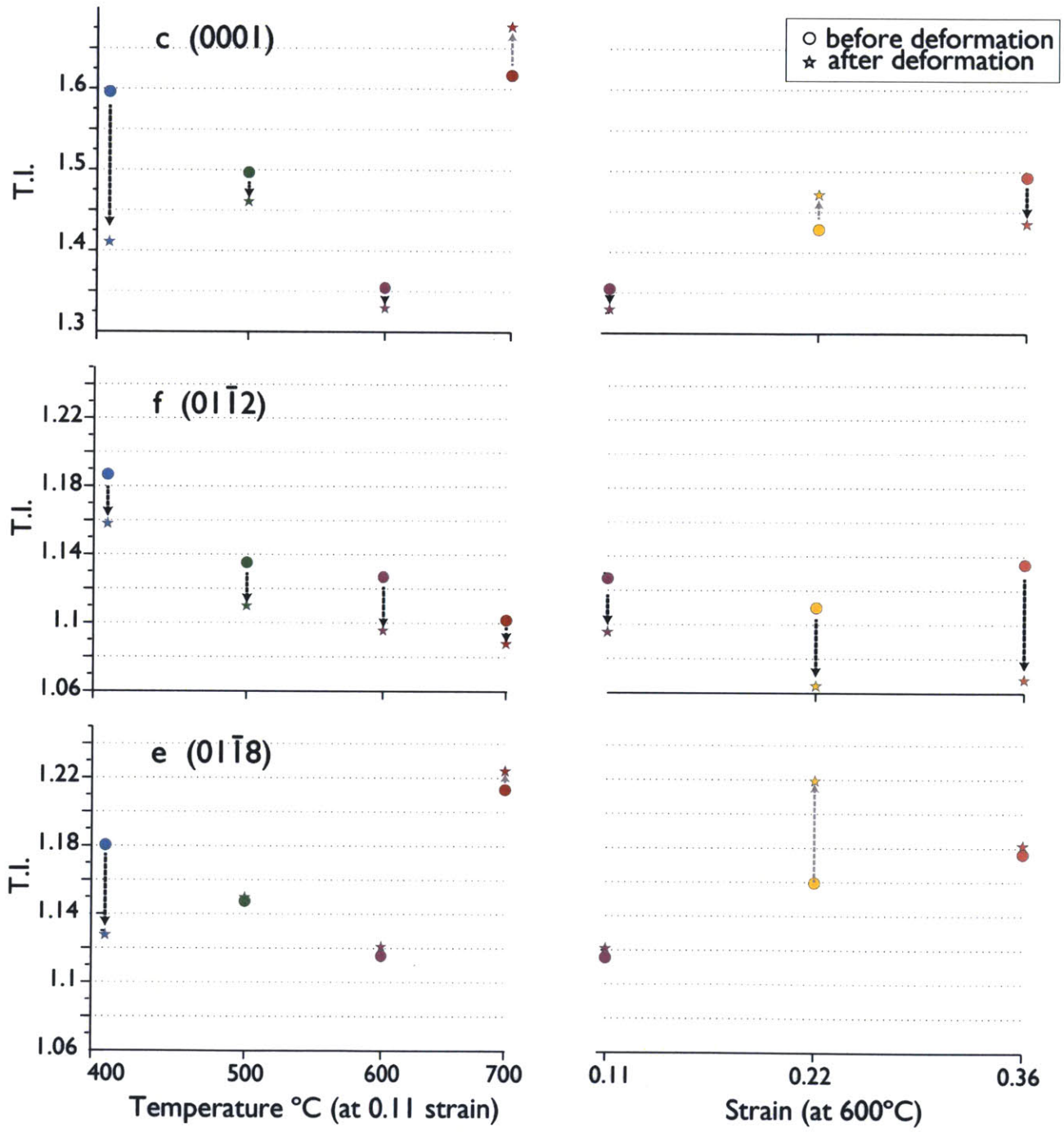

Figure 5-6: Texture index (TI) for Pole figures c, f and e. The change in TI for pole **c** is in agreement with the twin volume. For samples CMhD deformed at 700°C , and CMhI, deformed to 0.22 and 600°C , the TI increased for **c** and **e**

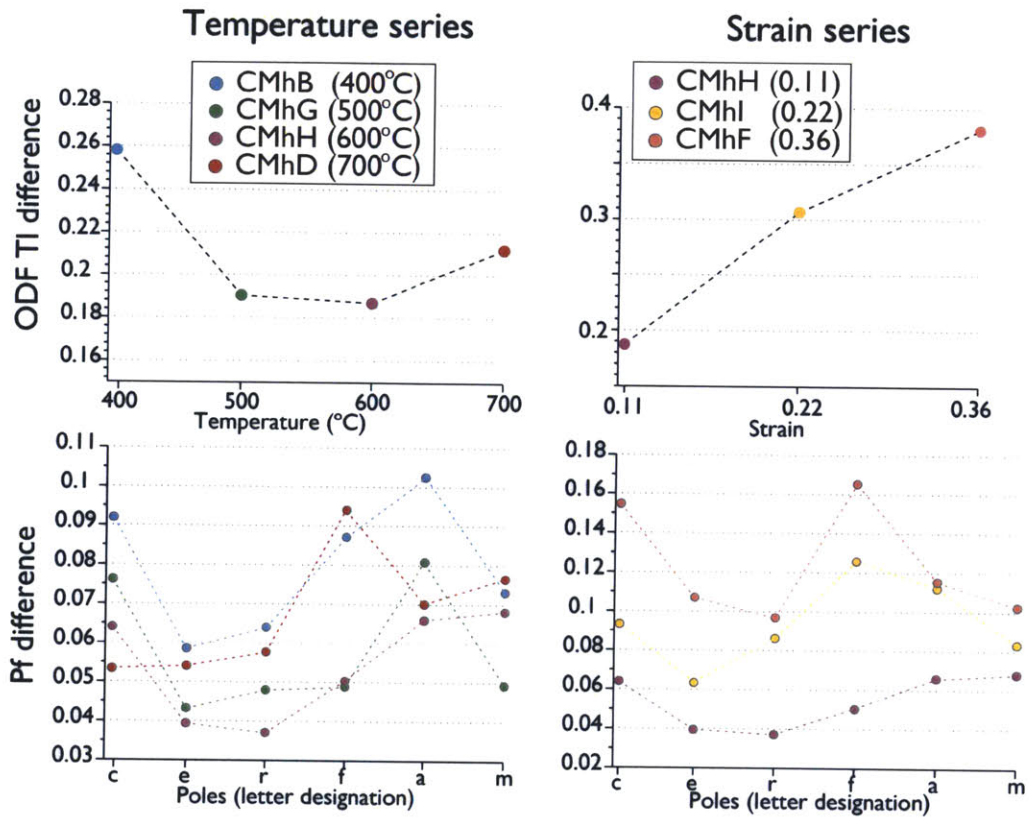

Figure 5-7: Absolute normalized difference of texture indexes for ODF and poles a, m, r, c, f and e. Note that the temperatures 500 and 600°C appear to be transition stages between a twinning dominated regime towards an increased activity of more slip systems.

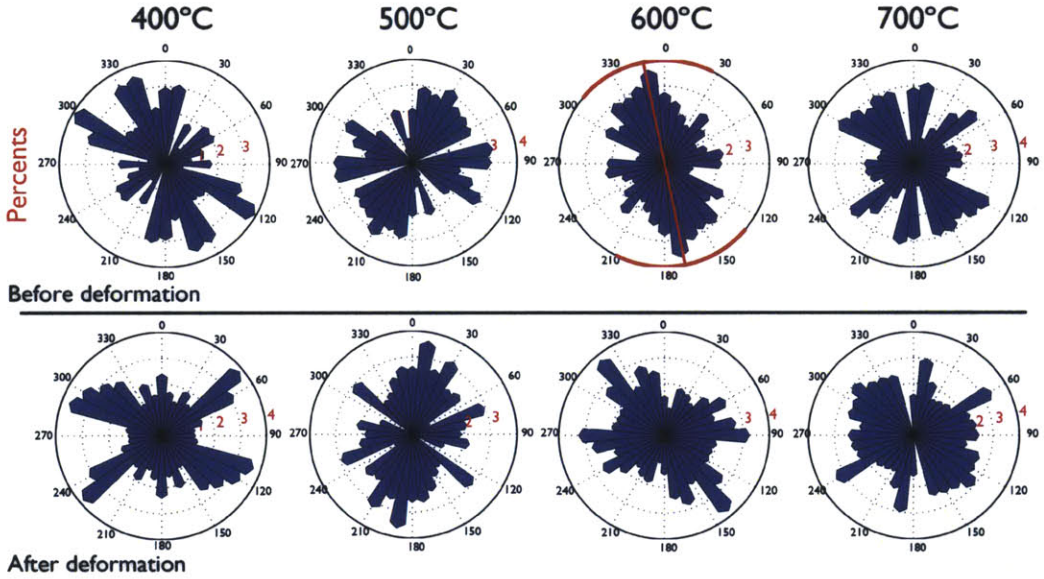

Figure 5-8: Rose diagrams of the SPO (varying temperature series). Diagrams obtained using the functions **aparor** returning particle projection following Panozzo (1983) and **prose** plotting frequency circular histograms and given the percentage of grains alined in a given orientation. In all cases the SPO is very weak (never more than 4% of the grains). The deformation to 0.11 compression does not imprint a SPO, on the opposite it erases a very weak previous one present on the sample deformed at 600°C .

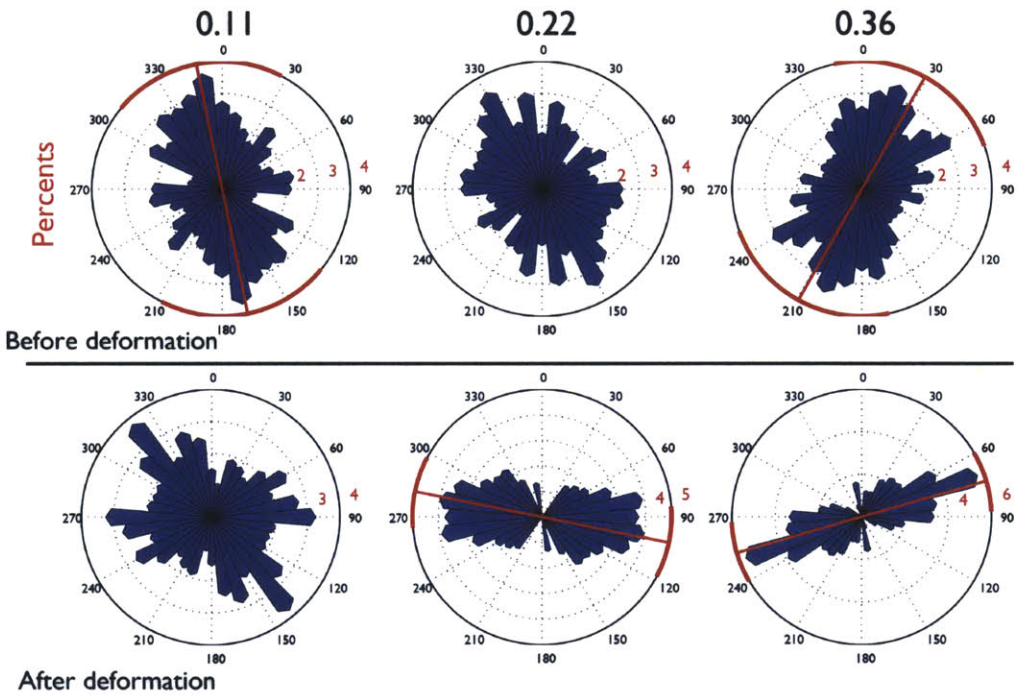

Figure 5-9: Rose diagrams of the SPO (varying temperature series). Diagrams obtained using the functions **aparor** returning particle projection following Panozzo (1983) and **prose** plotting frequency circular histograms and given the percentage of grains alined in a given orientation. The initial SPO is weak (never more than 4%) but higher strains do imprint a more important SPO.

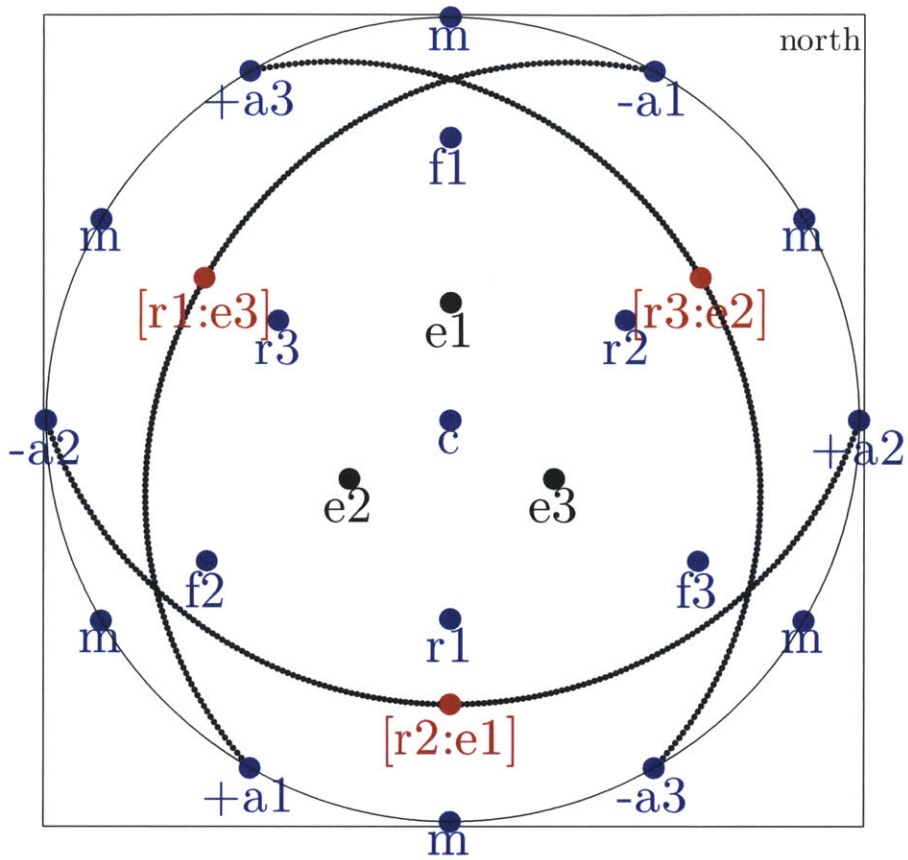

Figure 5-10: Stereographic representation of e-twinning planes in calcite. In the upper hemisphere, e1($\bar{1}018$)[$40\bar{4}1$], e2 ($1\bar{1}108$)[$\bar{4}401$] and e3 ($01\bar{1}8$)[$0\bar{4}41$]. Twin shear sense in e-twin plane is positive, towards the +c axis in the upper hemisphere, -c axis in the lower hemisphere. The stereonet shows the pole and traces of the twin planes (in black) in the upper hemisphere, as well as the shear directions (in red) [r2:e1], [r3:e2] and [r1:e3].

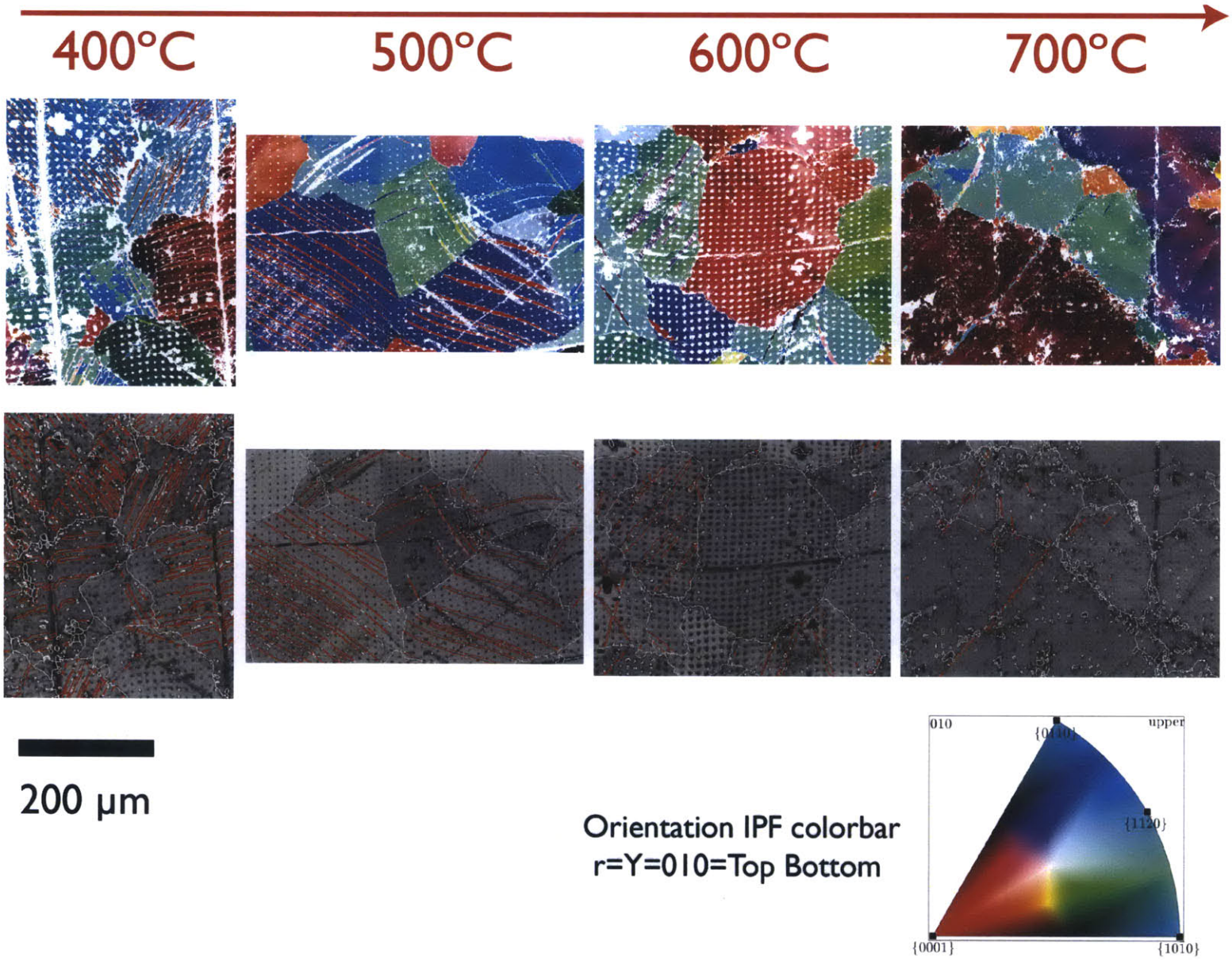

Figure 5-11: Twin morphology as a function of temperature, from the series deformed to 0.11, deformed at 400, 500, 600 and 700 °C . Note the evolution of towards a thicker and more lensoid-shape twins. EBSD maps of 2 μm resolution, IFP color code, and Band contrast image with superposition of grain boundaries (white) and identified twin boundaries (red)

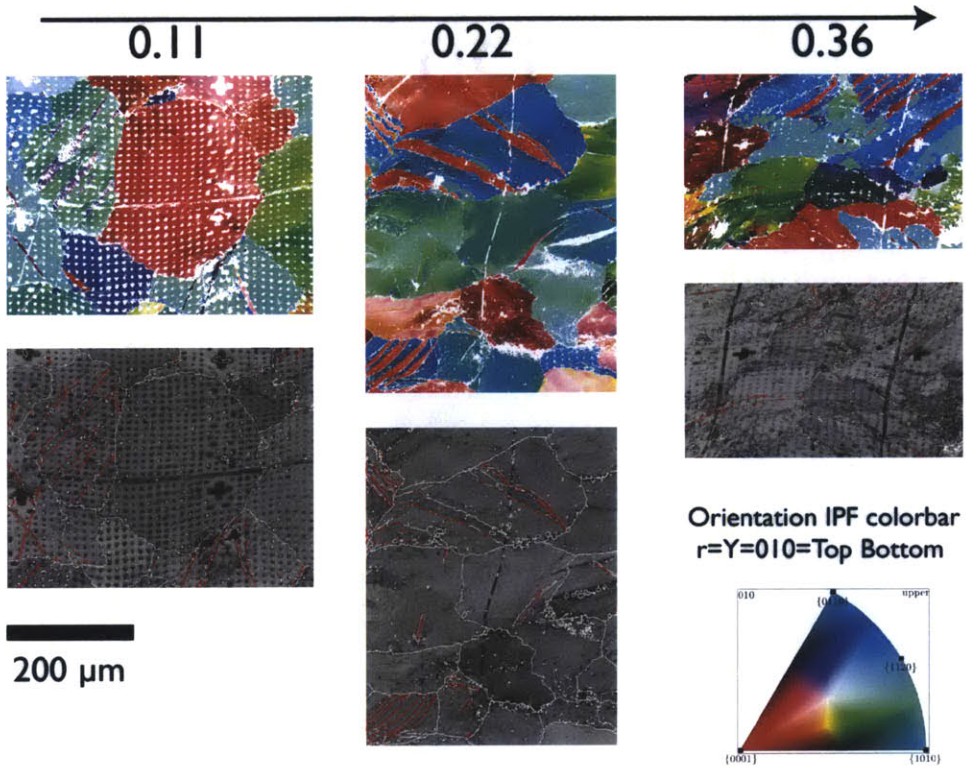

Figure 5-12: Twin morphology as a function of strain, experiments conducted at 600°C , deformed to 0.11, 0.22 and 0.36. Note the evolution towards thicker twins. EBSD maps of 2 μm resolution (1 μm for sample deformed to 0.36), IFP color code, and Band contrast image with superposition of grain boundaries (white) and identified twin boundaries (red)

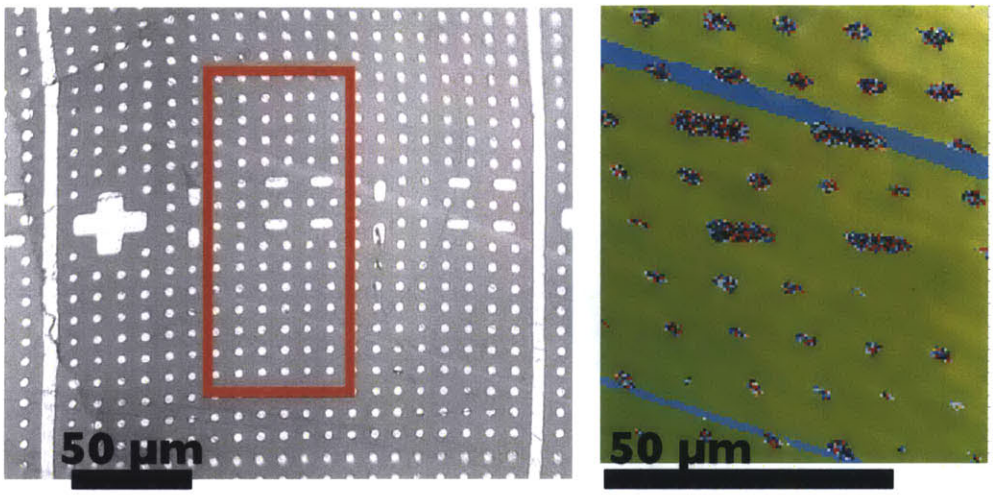

Figure 5-13: Twin morphology for experiment at 200°C , 0.03 strain. Optical image on the left, EBSD map (0.2 μm resolution), Euler color code on the left. Note the presence of fine lines, not resolved in the EBSD map.

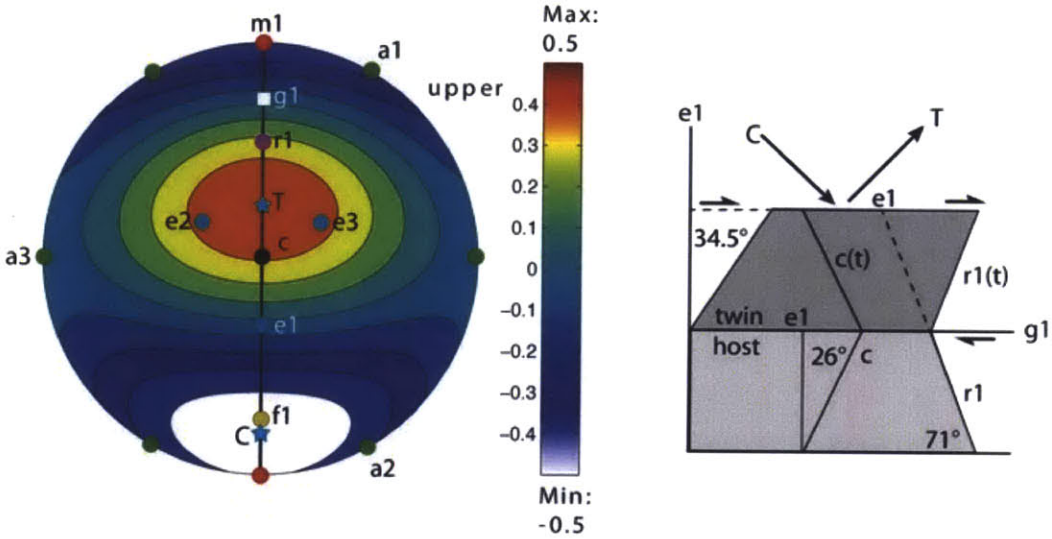

Figure 5-14: Twin Schmid factor for a single crystal as a function of its orientation. Tension and Compression directions are noted by stars. The crystal would be in the most favorable orientation in compression if the pole **f1** is oriented in the direction of the compression as illustrated in the diagram on the right

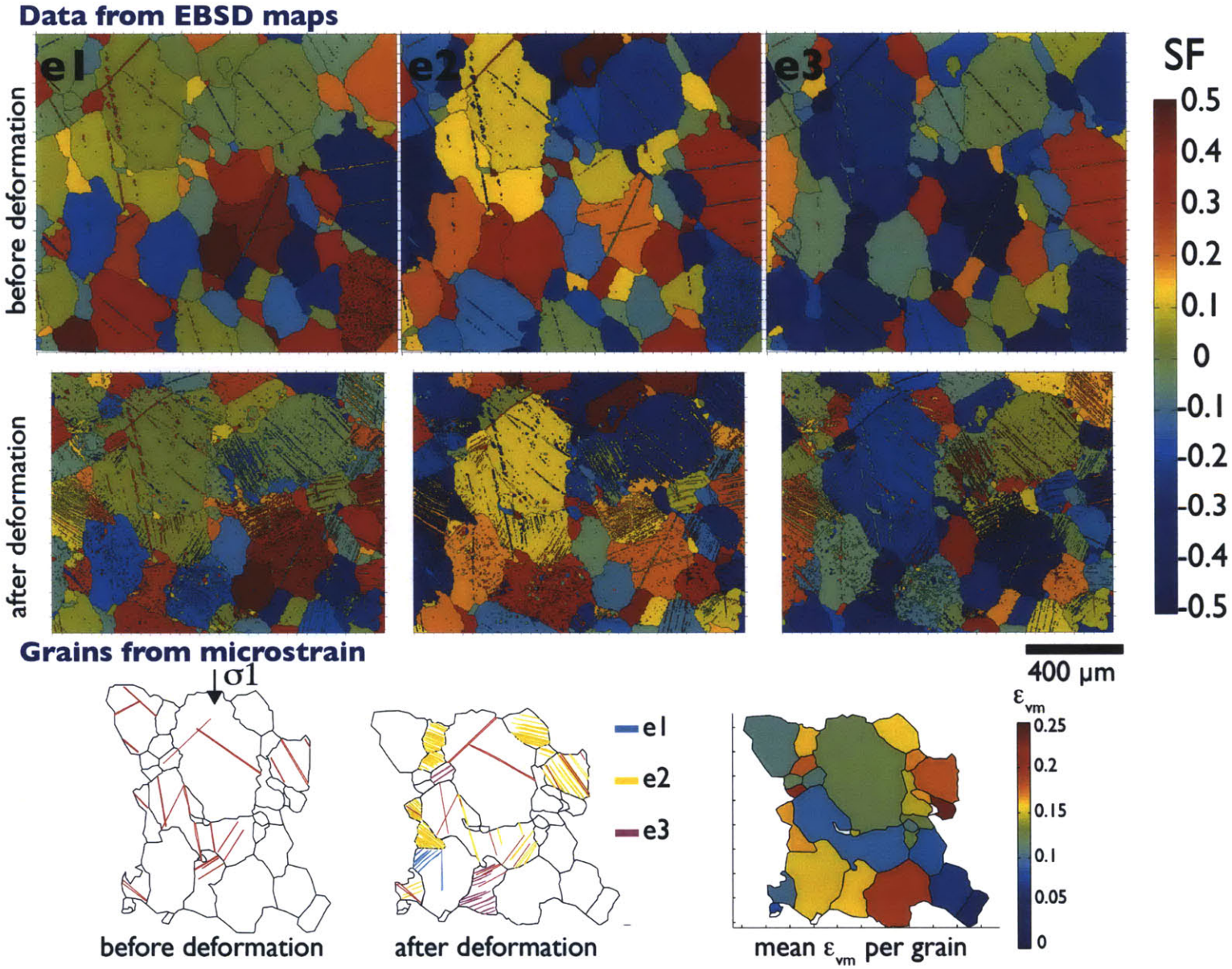

Figure 5-15: Schmid factor (SF) for e-twinning before and after deformation for sample CMhB, deformed at 400°C to 0.11 in compression. The maps show the SF before and after deformation derived from the orientation maps acquired through EBSD. On the bottom the analyzed grains following microscale strain mapping are shown, before and after deformation, as well as the intracrystalline mean ϵ_{vm}. Most of the twinned grains do correspond very well to a SF close to -0.5 in one of the e-twinning systems, however no all grains likely to twin have twins, moreover twinning does not seem to correlate to higher strain accommodation among the grains.

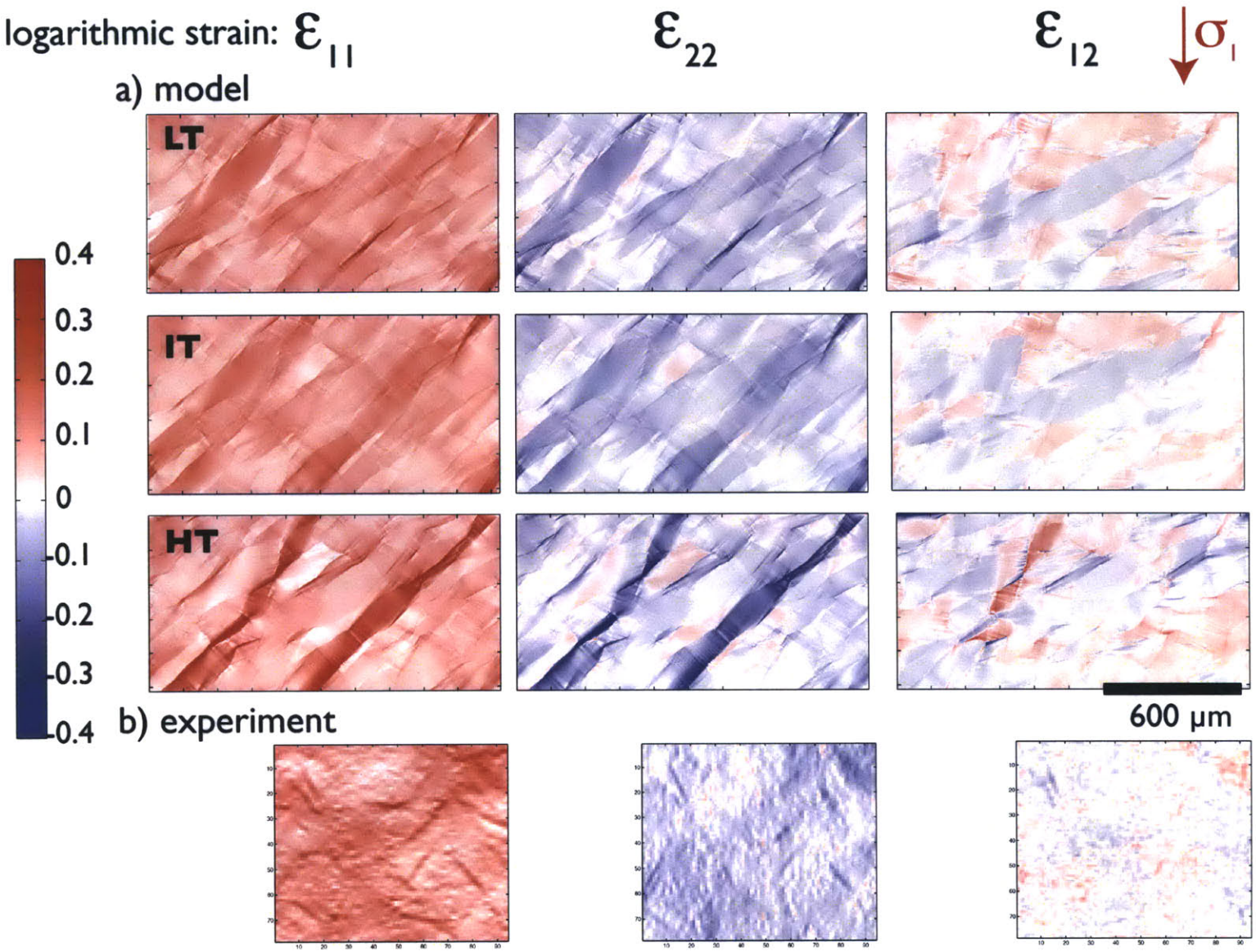

Figure 5-16: First comparison with VPFFT model: ϵ_{11}, ϵ_{22} and ϵ_{12} for model and microscale strain mapping for sample deformed to 0.11 at 3×10^{-5} s^{-1} at 600°C and 300 MPa. The three temperature modes from R. A. Lebensohn et al. (1998) and summarized in 5.6.5 are given for comparison. The loading direction is along the vertical direction of the image.

Chapter 6

Concluding Remarks

The deformation behavior of calcite and carbonate rocks has been the subject of many laboratory and field structural studies. Building on this substantial base, I sought to gain insight into the relative contributions to inelastic strain of the individual deformation mechanisms, including twinning, grain boundary sliding, and intracrystalline dislocation motion mechanisms. To accomplish this task, considerable time and effort was spent developing a technique to characterize strain at length scales smaller than the grain size. The marking technique described here provides quantitative strain measures with spatial resolution of about 10 μm, and so, that effort seems to have been warranted. The current results of this work provide new constraints on strain partitioning; I hope that this work and future extensions of the technique will lead to the development of more accurate micromechanical models of deformation that will give a deeper understanding of creep deformation in the Earth. In addition, an improved knowledge of the development of microscopic state variables should help to provide better tools to interpret the microstructure of naturally deformed rocks

6.1 Concluding remarks

The application of the microscale strain mapping (MSSM) technique to deformation in Carrara Marble led to several general observations, some in agreement with previous work, but with the added advantage that new, quantitative data for strain partitioning are now available. The MSSM measurements also give detailed information about the evolution of the local strain field. Some conclusions are listed below:

1. Several mechanisms (twinning, intracrystalline slip systems and grain boundary associated mechanisms) contributed to the inelastic strain in experiments over the range of 400-700°C , but the relative contribution to strain of each mechanism changed with the conditions of deformation. Localized strain at grain boundaries was observed at temperatures as low as 400°C . Likewise, twin generation, albeit minimal, was still present to temperatures as high as 700°C .

2. Over the temperature range of 400°C to 700°C , the microscale strain mapping technique showed that the contribution of strain from twinning decreased with respect to that from intracrystalline dislocation slip, in agreement with previous works [e.g. S. Schmid et al. (1980); Rutter (1995); Turner et al. (1954); D. J. Barber and Wenk (1979); Burkhard (1993); Ferrill et al. (2004); D. Barber et al. (2007); Rybacki et al. (2013)]. As temperature increased, the decrease in twin activity was accompanied by a decrease in the wavelength of the strain heterogeneities, as well as an increase in their amplitudes

3. The decrease in wavelength may be explained, in part, by the activation of additional slip systems, but the heterogeneity of the local strain field also indicates a change in the way that the sub-grain defect structure evolves during the initial stages of creep. During deformation at 600°C , where both dislocation slip and twinning are active, the strain field becomes more homogeneous with increased

strain. The wavelength of heterogeneities continues to decrease, suggesting that steady-state has not been reached for strains less than 0.36.

4. Under conditions where twinning is active, there is a suggestion that strain could be localized in bands spanning several grains. Because the termination of a twin at a grain boundary will require strain accommodation in the neighboring grain, the stress field in the neighbor grain might be increased. If this load-transfer phenomenon continues as strain increases, it could lead to the development of shear zones at a multi-grain scale.

5. Grain boundary sliding (GBS) is considered to be a high-temperature, low-stress, grain-size-sensitive deformation mechanism in carbonates (S. Schmid, 1976; S. Schmid et al., 1977). S. Schmid et al. (1980) proposed that GBS was a deformation mechanism that contributed only very weakly to strain in Carrara marble at high temperatures, being largely absent below 800°C . However, I observed strain that was localized along grain boundary regions in all experiments, even at 400°C , and GBS was observed at 400°C . The contribution of this boundary localization to the total strain did increase with temperature. Interestingly, at 600°C , there is a suggestion that the grain boundary regions hardened with strain, a phenomenon to be explored further.

6. This thesis work also provides an additional illustration of the potential importance of the strain path in determining rock strength. Even though the local texture of Carrara marble is relatively weak (Molli & Heilbronner, 1999), it was not erased by the imposed axial deformation up to 0.36 axial shortening.

6.2 Suggested future directions

A logical extension of this work is to analyze larger areas to provide a stronger data set and strengthen the conclusions. Furthermore, a statistical analysis relating grain orientation to strain accommodation would provide great insight into the contribution of the intracrystalline slip mechanisms. The data gained could then be used for extended applications of the viscoplastic full-field and mean-field models. Specific suggestions for further studies are given below.

1. The experimental series performed at temperatures from 400°C to 700°C documents the transition from a strong presence of twinning towards an increase in intracrystalline dislocation slip. The strain field produced in the first strain increment of 0.11 suggested that the length scale of the heterogeneities in the local strain field decreased with temperature as well. How does the development of heterogeneity in local strain depend on strain rate? How does this development of microstructure correlate with bulk mechanical properties such as hardening?

2. A different evolution was seen with increasing strain: Both the wavelengths of the heterogeneities and their relative amplitude decreased with increased deformation. It is logical to ask is whether this evolution with strain depends on temperature. If fewer slip systems are activated, or if the relative activity on the various systems changes, one might expect the production of texture to be affected. There might also be increased localization at a grain scale, encouraging the development of a bimodal distribution of grain scale strains. Thus, it is important to perform a set of strain series at lower temperatures.

3. Several aspects of twinning were observed that could be explored further. At lower temperatures we observed the development of fine lines co-zonal with the twin plane, similar to the microtwin features documented by Turner et al. (1954). The exact nature of these features is not known, but they may

be involved in twin nucleation. By conducting additional experiments at low temperatures and small strains and by tracking the topography, strain and development of texture, one might investigate the kinetics of twin nucleation.

4. Another aspect to explore is the apparent connectivity of twinned grains observed at lower temperatures, where a twin in a neighbor appeared to be a favorable influence for twinning. If there is indeed a connectivity, it might be related to the mechanisms of twin nucleation and propagation. Despite extensive studies on twinning, it is not clear what conditions favor propagation over nucleation, or what variables affect the kinetics of twin development (Christian & Mahajan, 1995). The observations should be extensive enough to provide robust statistical information that could relate strain contributions to boundary misorientation and to grain orientation (Capolungo et al., 2009), paying particular attention to the development of strain bands.

5. It was observed that the localization of strain at grain boundaries (implicating several mechanisms, from twinning to GBS) decreased with increasing total strain, suggesting that the grain boundary regions are hardening. If grain boundary sliding is accommodated via dislocation motion, it may be that grain boundaries in a particular orientation are weaker, and slip on those boundaries might be activated first. In any case, grain boundary strain was never found to be larger than 20% of the total strain accommodated. These experiments suggest that the initial shape of the grains might also be a factor to consider when analyzing the intragranular heterogeneities, as suggested by Raj and Ashby (1971) who studied sliding in a coplanar grain boundary. A statistical analysis, relating GBS to grain orientation, shape and strain accommodation would also provide great insight into the parameters controlling GBS.

Appendix A

Optical microscope images of studied samples

This appendix is the compilation of the optical microscope images of the samples analyzed in the thesis before and after deformation. The images were acquired using a Hirox digital optical microscope, and stitched together using Fiji as described in Chapter 2. The samples analyzed in the thesis are the ones belonging to the temperature series: CMhB, CMhG, CMhH and CMhD, deformed to 0.11 shortening at $3\times10^{-5}s^{-1}$, at 300 MPa, and 400°C , 500°C , 600°C and 700°C respectively; and the ones belonging to the strain series, CMhH, CMhI and CMhF deformed to 0.11, 0.22 and 0.36 shortening respectively at $3\times10^{-5}s^{-1}$, at 300 MPa and 600°C . Sample CMhA was deformed to 0.04 at $3\times10^{-5}s^{-1}$, at 300 MPa and 200°C and its analysis is included in Appendix B. Sample CMhC was deformed to 0.11 shortening at $3\times10^{-5}s^{-1}$, at 300 MPa and 800°C but the surface was too damaged to allow for a microscale strain mapping.

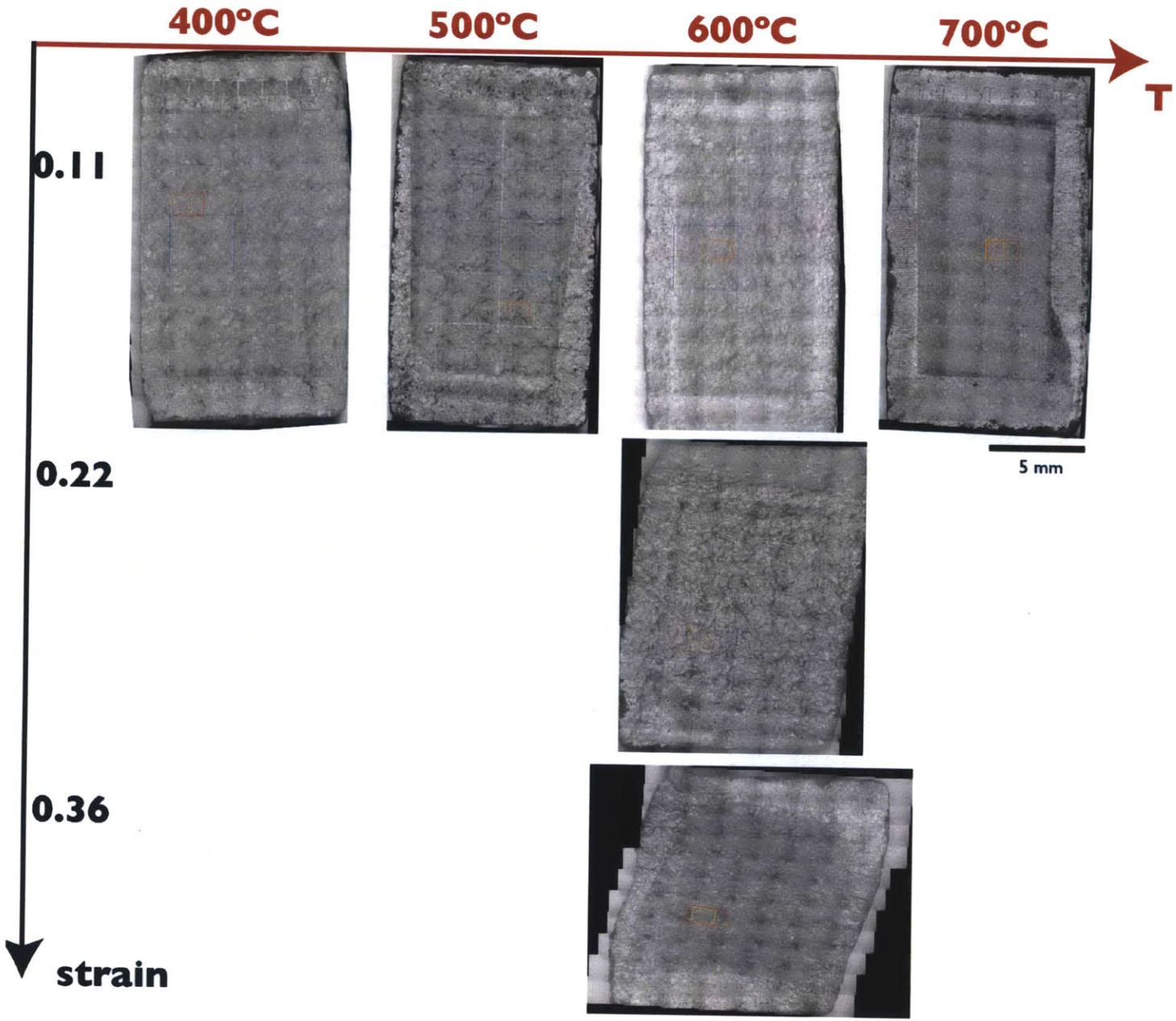

Figure A-1: Whole samples after deformation for experimental series presented in thesis: stitched x140 images of the CMh series: the test heterogeneity is more pronounced with increasing strain. Loading is along the vertical direction of the figure.

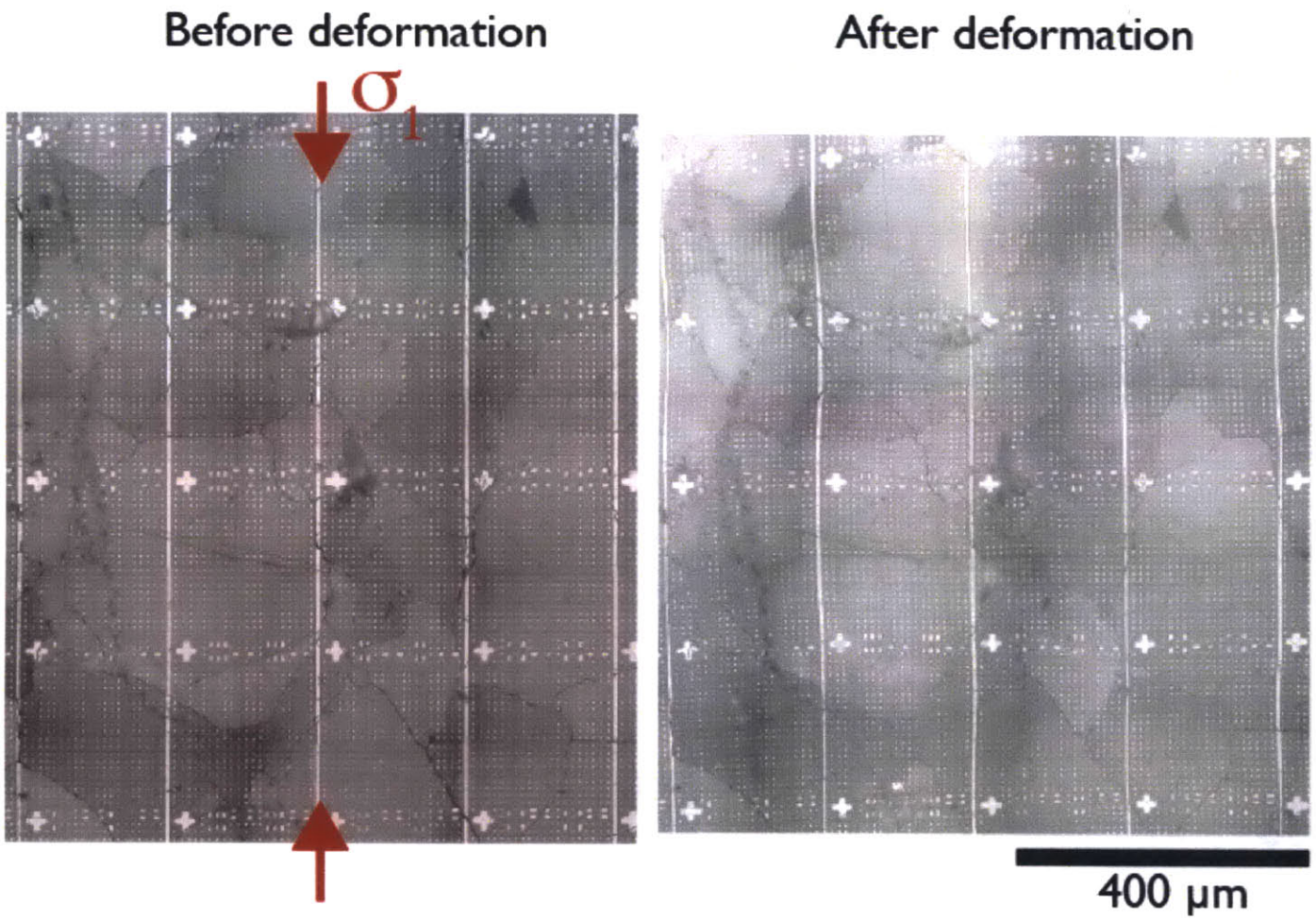

Figure A-2: CMhA before and after deformation. Optical microscope image of CMhA. Sample deformed to 0.04 shortening at $3\times10^{-5}s^{-1}$ at 300 MPa and 200°C (deformation maps in appendix B).

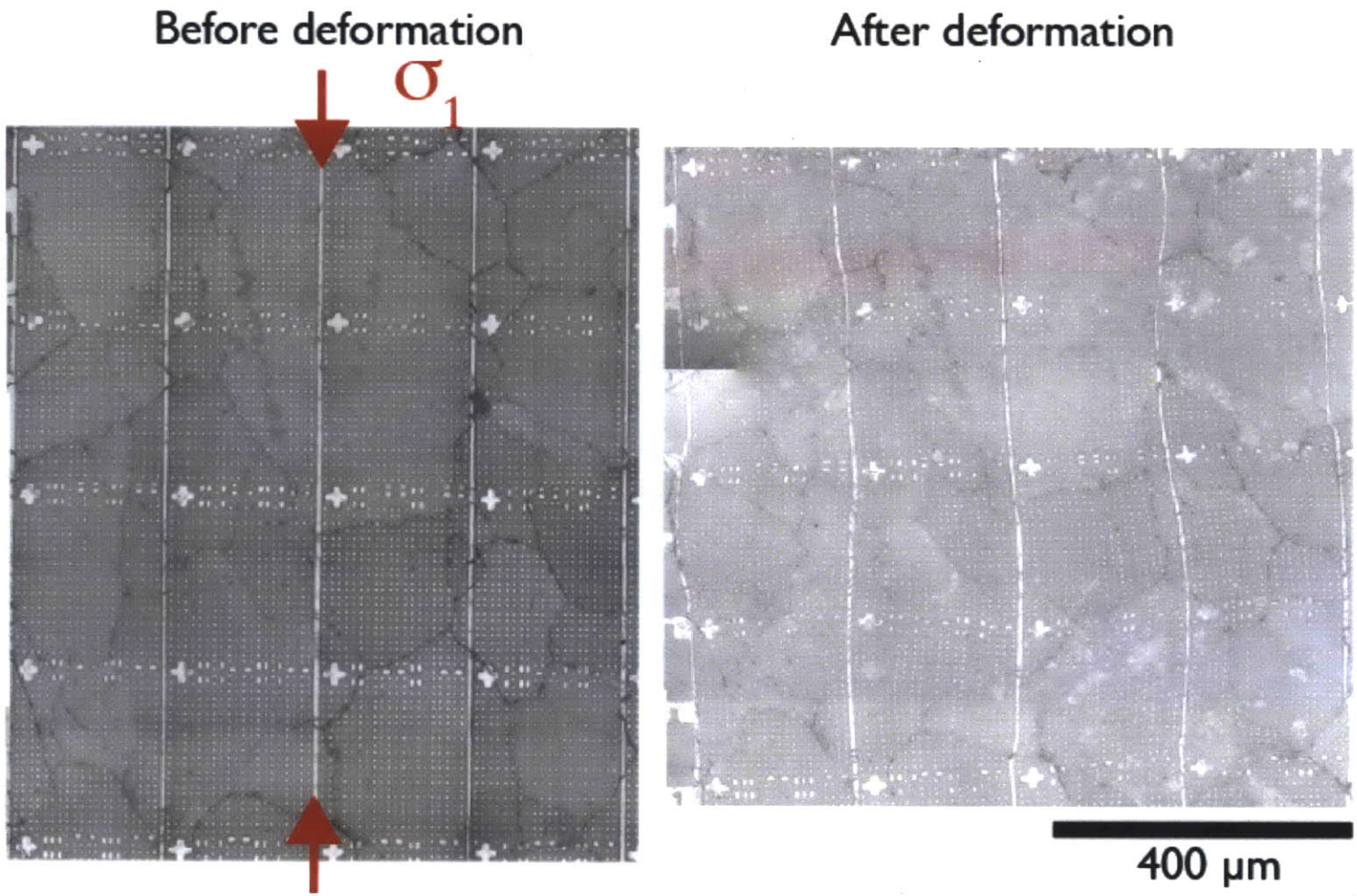

Figure A-3: CMhB before and after deformation. Optical microscope image of CMhB. Sample deformed 0.11 shortening at $3\times10^{-5}s^{-1}$ at 300 MPa and 400°C

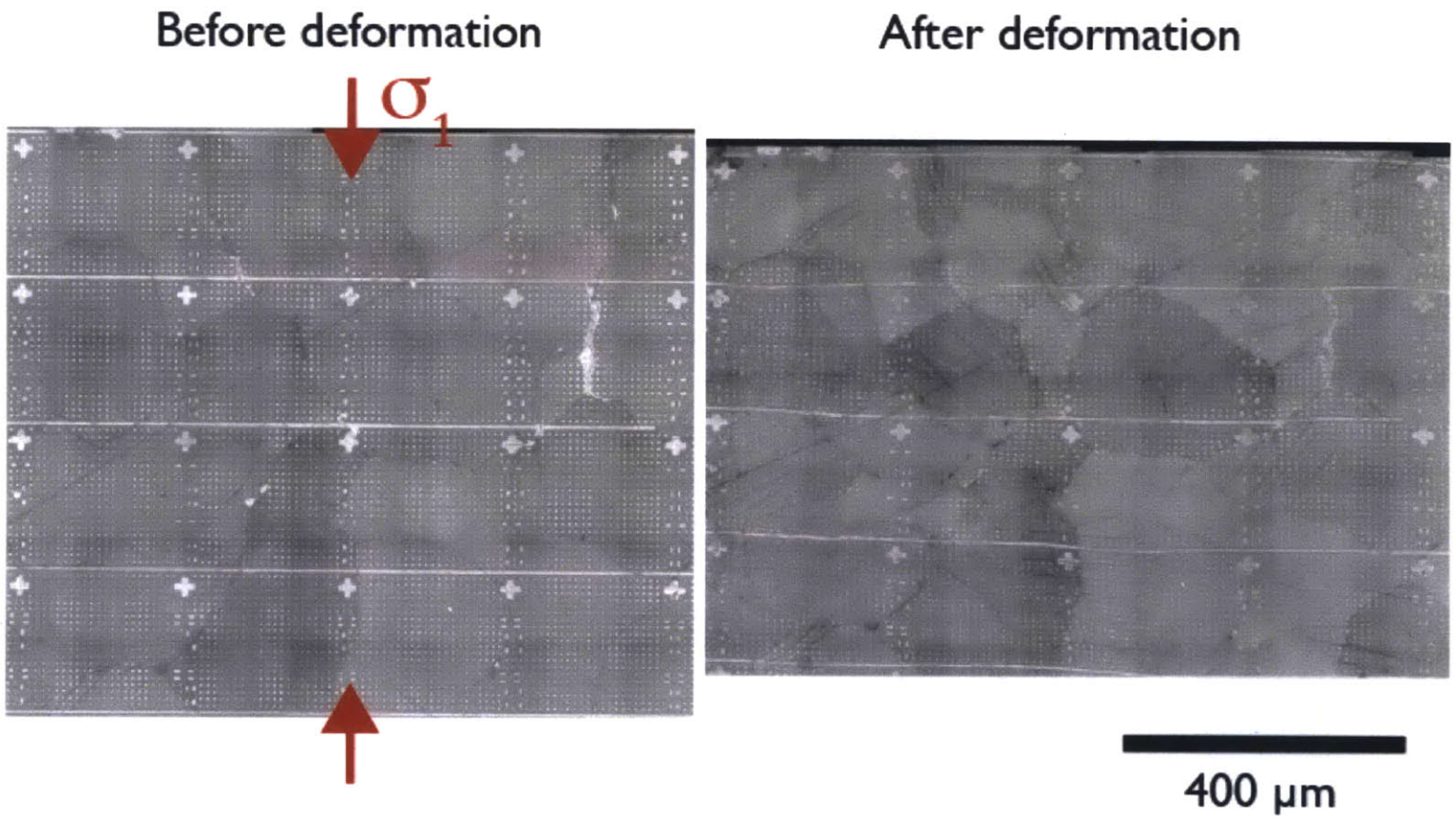

Figure A-4: CMhB before and after deformation. Optical microscope image of CMhG. Sample deformed 0.11 shortening at $3\times10^{-5}s^{-1}$ at 300 MPa and 500°C

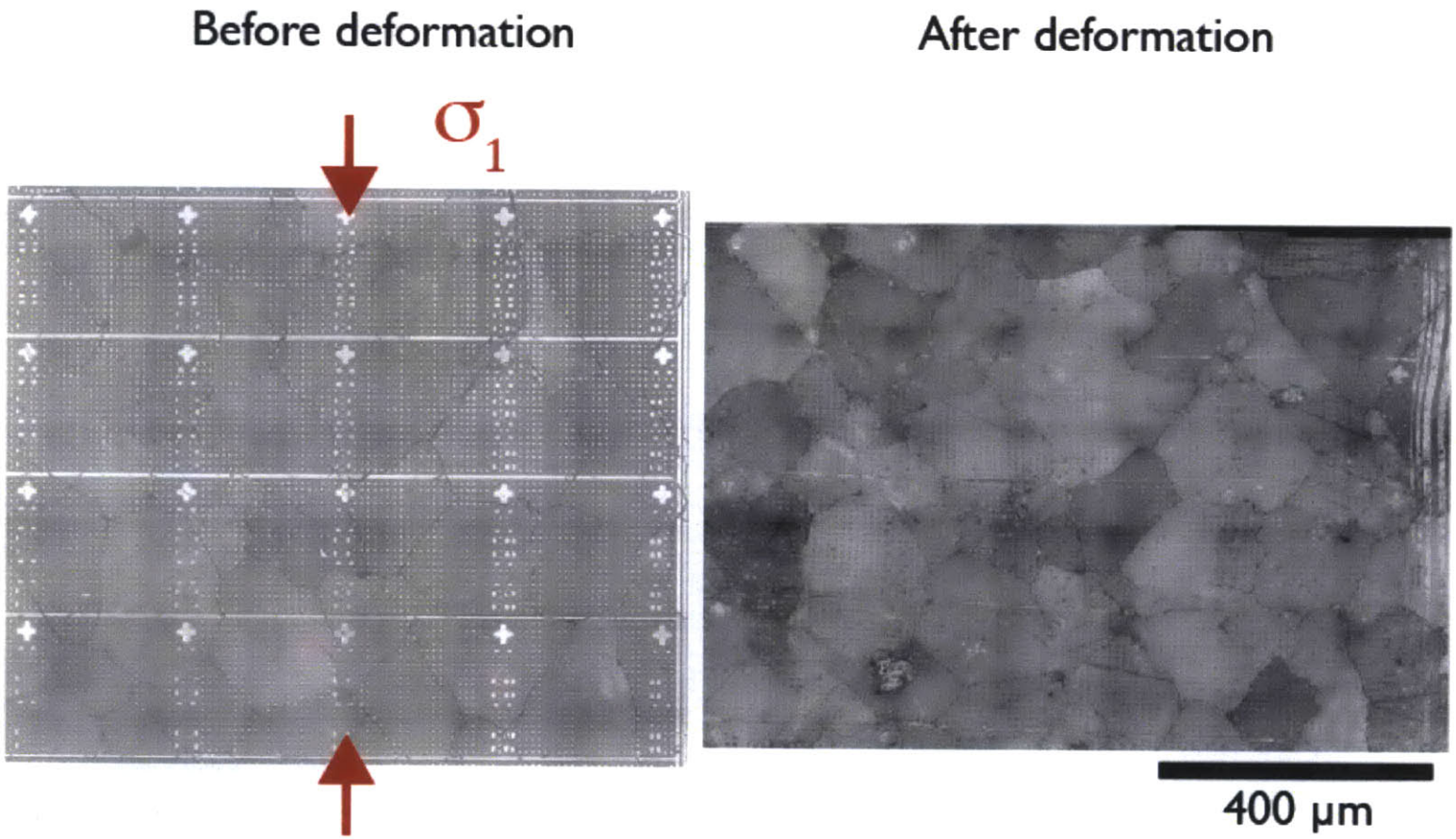

Figure A-5: CMhH before and after deformation. Optical microscope image of CMhH. Sample deformed 0.11 shortening at $3\times10^{-5}s^{-1}$ at 300 MPa and 600°C

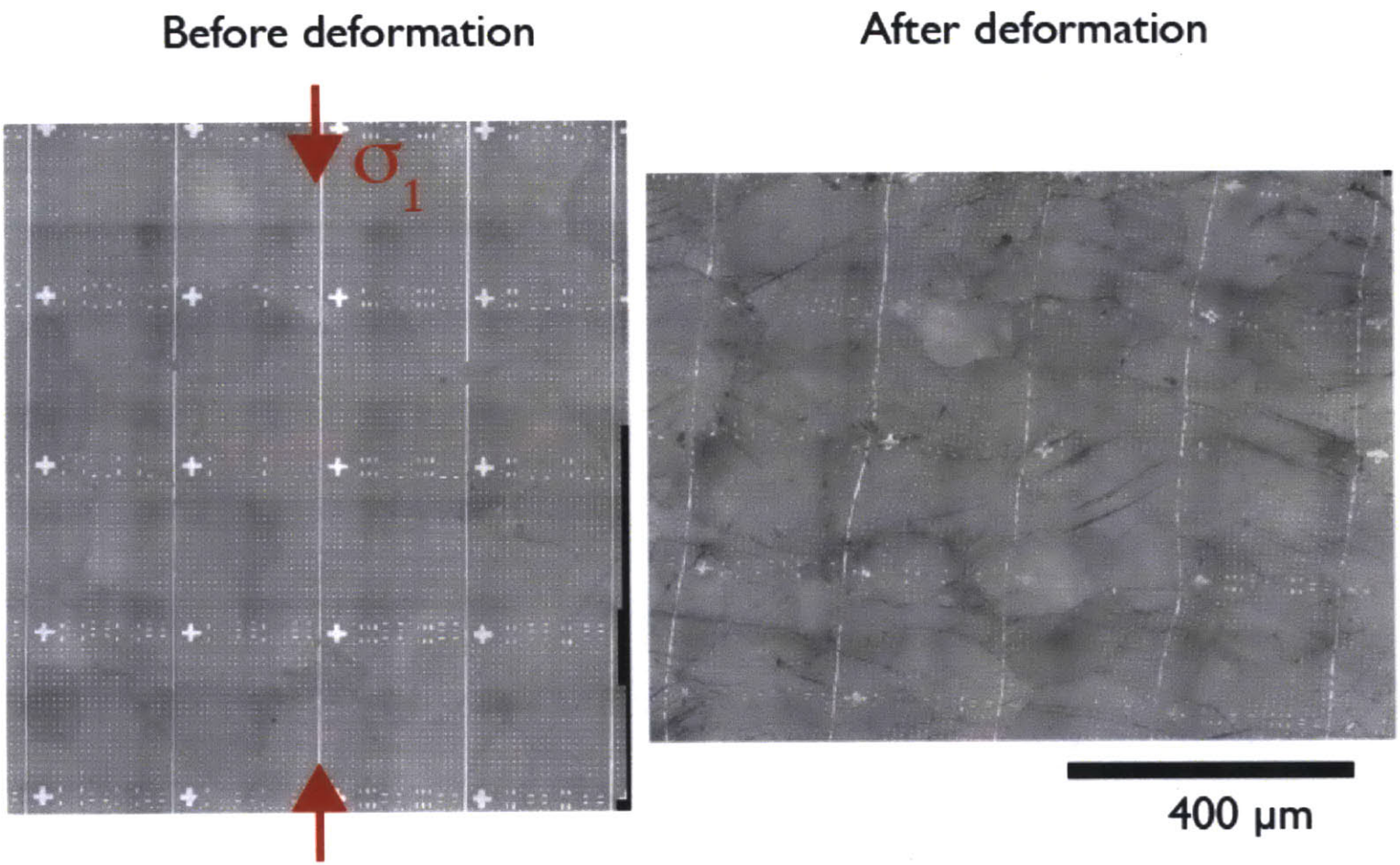

Figure A-6: CMhI before and after deformation. Optical microscope image of CMhI. Sample deformed 0.22 shortening at $3\times10^{-5}s^{-1}$ at 300 MPa and 600°C

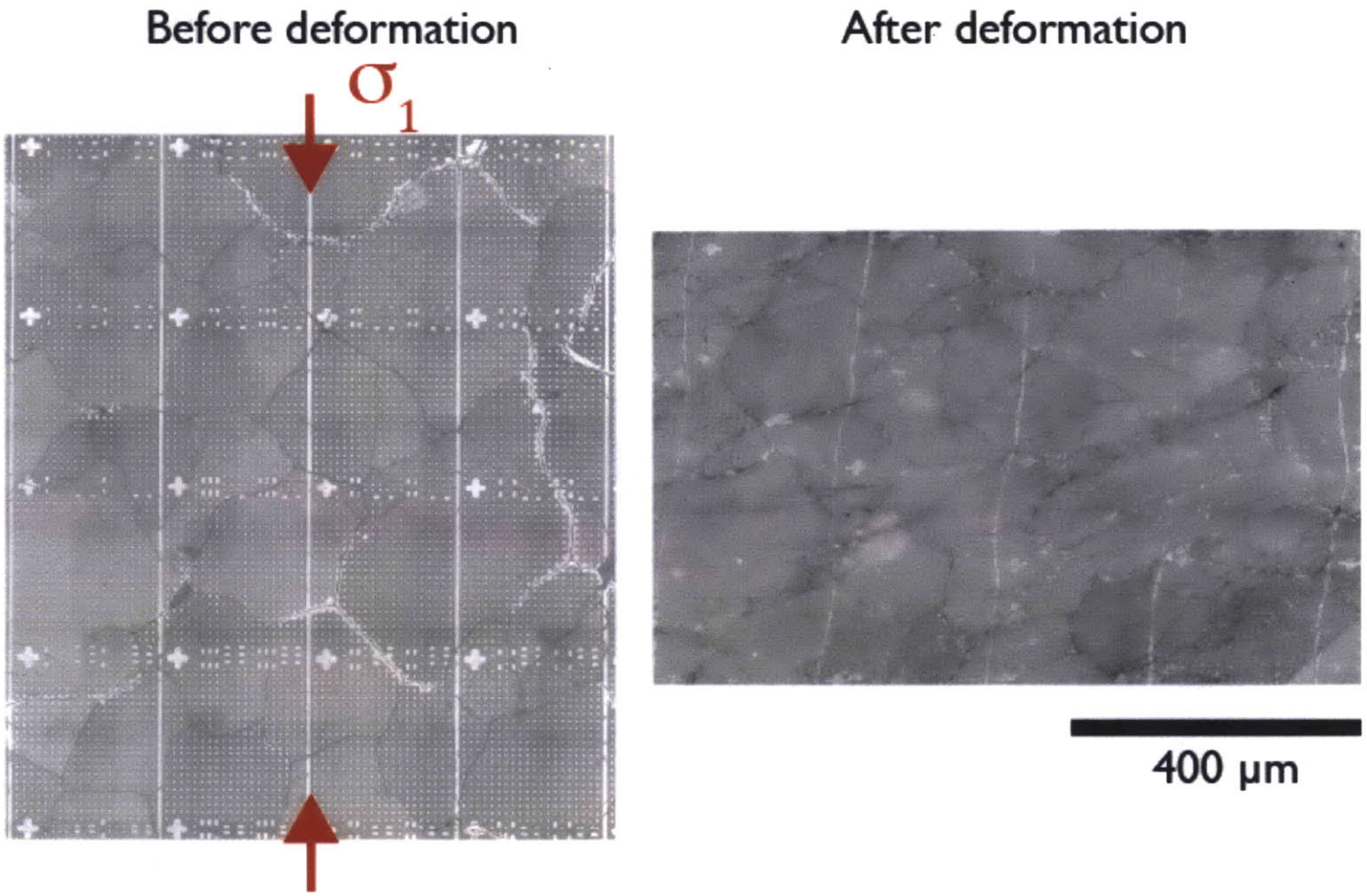

Figure A-7: CMhF before and after deformation. Optical microscope image of CMhF. Sample deformed 0.36 shortening at $3\times10^{-5}s^{-1}$ at 300 MPa and 600°C

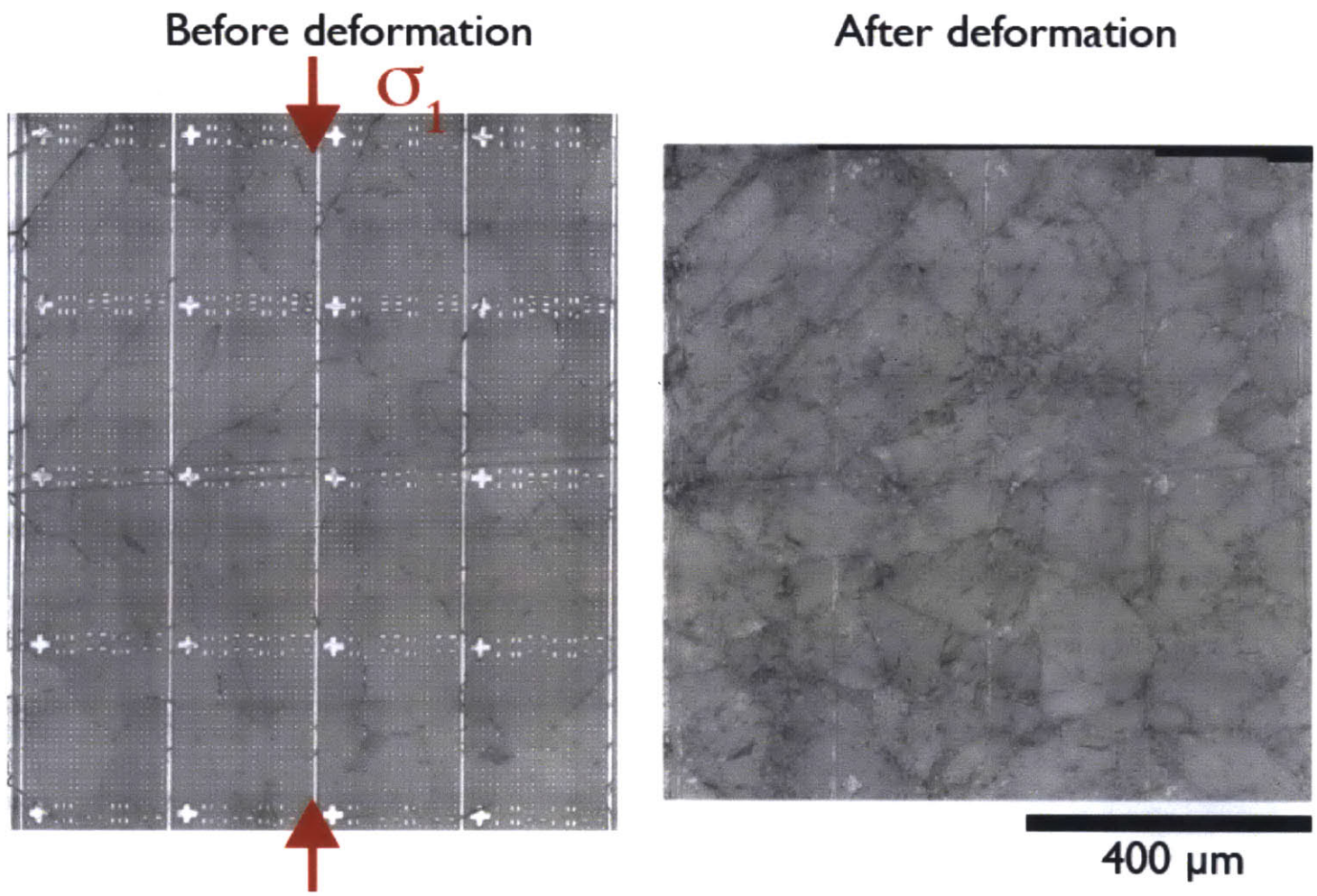

Figure A-8: CMhD before and after deformation. Optical microscope image of CMhD. Sample deformed 0.11 shortening at $3\times10^{-5}s^{-1}$ at 300 MPa and 700°C

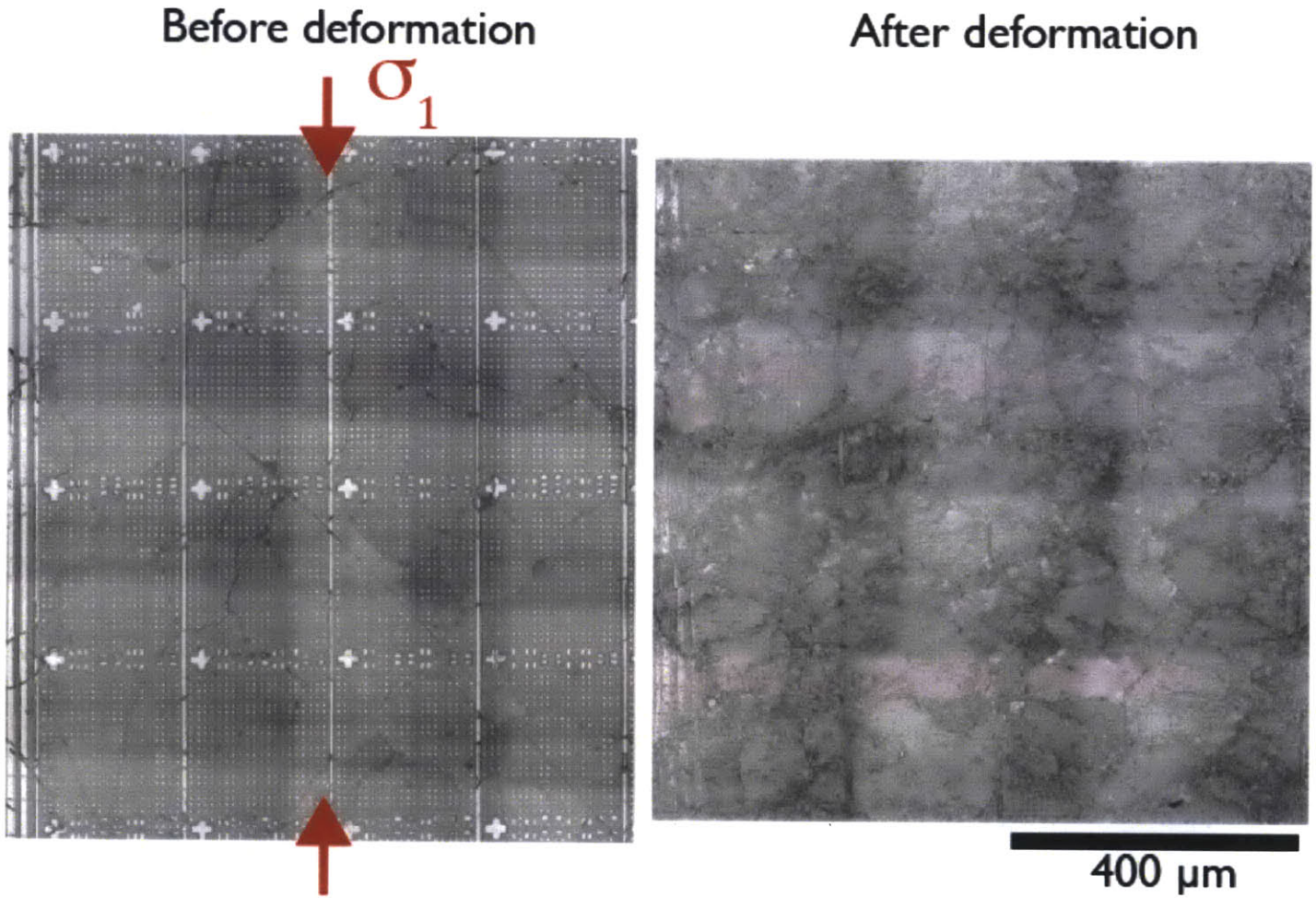

Figure A-9: CMhC before and after deformation. Optical microscope image of CMhC. Sample deformed 0.11 shortening at $3\times10^{-5}s^{-1}$ at 300 MPa and 800°C . This sample was not analyzed following the MSSM technique because the markers could not be recognized with the automated technique.

Appendix B

Additional experiments

The development of the microscale strain measurement technique involved extensive experimental development, particularly when optimizing the grid design for an automated strain analysis. This appendix summarizes the experiments not presented in the main text of this thesis.

B.0.1 Description of the experiments

An experimental series (**CMetCrXX**) was performed on samples marked with the initial grid design and sputtered only with Chromium (10 nm) after a more pronounced acid etch with HCl (etch pits of up to 1 μm). Sample CMhA was prepared the same way as the experimental series presented in the thesis (newest grid design, slight acid etch and double layer Cr + Au) but was shortened to a smaller strain of 0.04 (ie. 4%) to keep a differential stress inferior to the confining pressure and not to fracture the sample (Goetze criterium, Evans and Kohlstedt (1995)).

Table B.0.2 summarizes the strain for a 9n point analysis for all experiments

Figure B-1 shows the mechanical data of this experiments as well as their position with regard to former studies.

B.0.2 Zero strain experiment for first grid design

The zero strain experiment was performed in this case at 600°C : table B.0.3 summarizes the zero strain analysis done for the CMetCr series. It can be seen that the resolution was greatly improved with the new design and micro-patterning technique applied to the experiments presented in the thesis.

B.0.3 Strain maps

Sample	Cp (MPa)	T (°C)	Strain rate	Strain	Strength (MPa)
CMetCr07	300	600	0	0.005 (isostatic)	0
CMetCr14	300	600	3×10^{-5}	0.11	117
CMetCr05	300	630	1×10^{-5}	0.11	81
CMetCr11	300	600	3×10^{-5}	0.20	120
CMhA	300	200	3×10^{-5}	0.04	250

Table B.0.1: Summary of experiments etched and deposited with Cr

	CMetCr14	CMetCr11	CMetCr05	CMhA
sample strain	0.11	0.2	0.11	0.05
ϵ_{11}	0.12	0.25	0.12	0.05
std	0.06	0.09	0.09	0.024
ϵ_{22}	-0.06	-0.14	-0.05	-0.026
std	0.06	0.09	0.09	0.024
ϵ_{12}	0.005	-0.009	-0.007	0.003
std	4.1	5.6	6.2	0.018

Table B.0.2: Statistical descriptions of the strain field

	3n	4n	5n	9n	25n
averaged area (μm^2)	50	100	200	400	1600
equivalent distance (μ)	7	10	14.1	20	40
0.5 μm error (%)	3.5	2.5	1.76	1.25	0.63
ϵ_{11}	-0.0043	-0.0044	-0.0046	-0.0046	-0.44
std	0.048	0.039	0.027	0.02	0.01

Table B.0.3: Statistical descriptions of the zero strain measurements for first generation grid

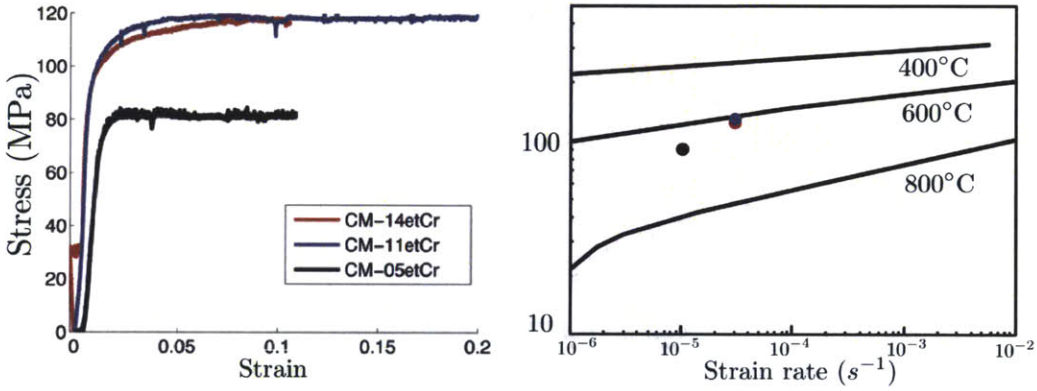

Figure B-1: Stress-strain curves for first version grid experiments, all were performed at 300MPa, CMetCr14 and CMetCr11 at 600°C and $3\times10^{-5}s^{-1}$ to 0.10 and 0.2 shortening strain, and CMetCr05 to 0.1 at 630 °C , $1\times10^{-5}s^{-1}$.

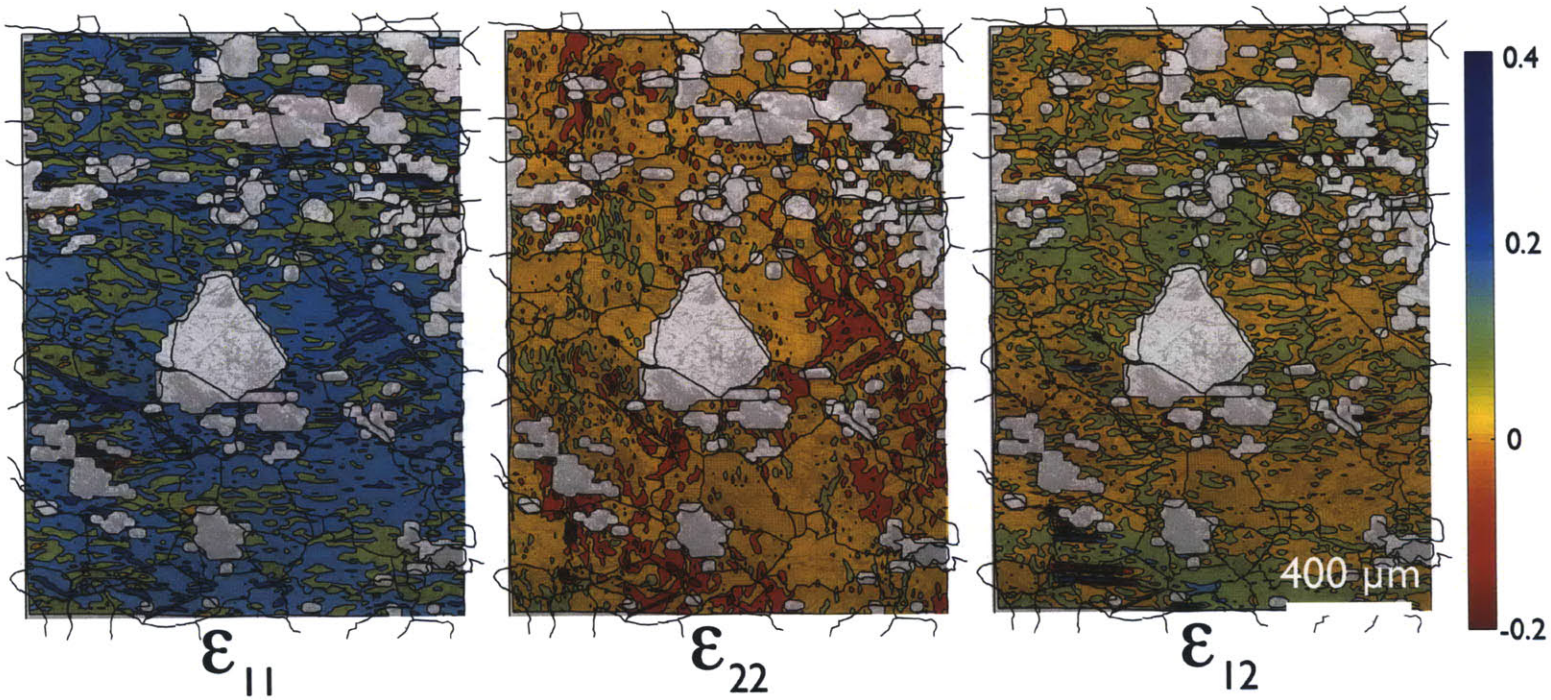

Figure B-2: Microscale strain maps for sample CMetCr14, deformed to 0.11 at 300 MPa, 600°C and 3×10^{-5} s^{-1}. Strain is dimensionless and positive when related to shortening, the strain map is overlaid on top of the optical microscope image. The digitalized traced grain boundaries are plotted in black. The compression direction σ_{11} is along the vertical axis of the figure.

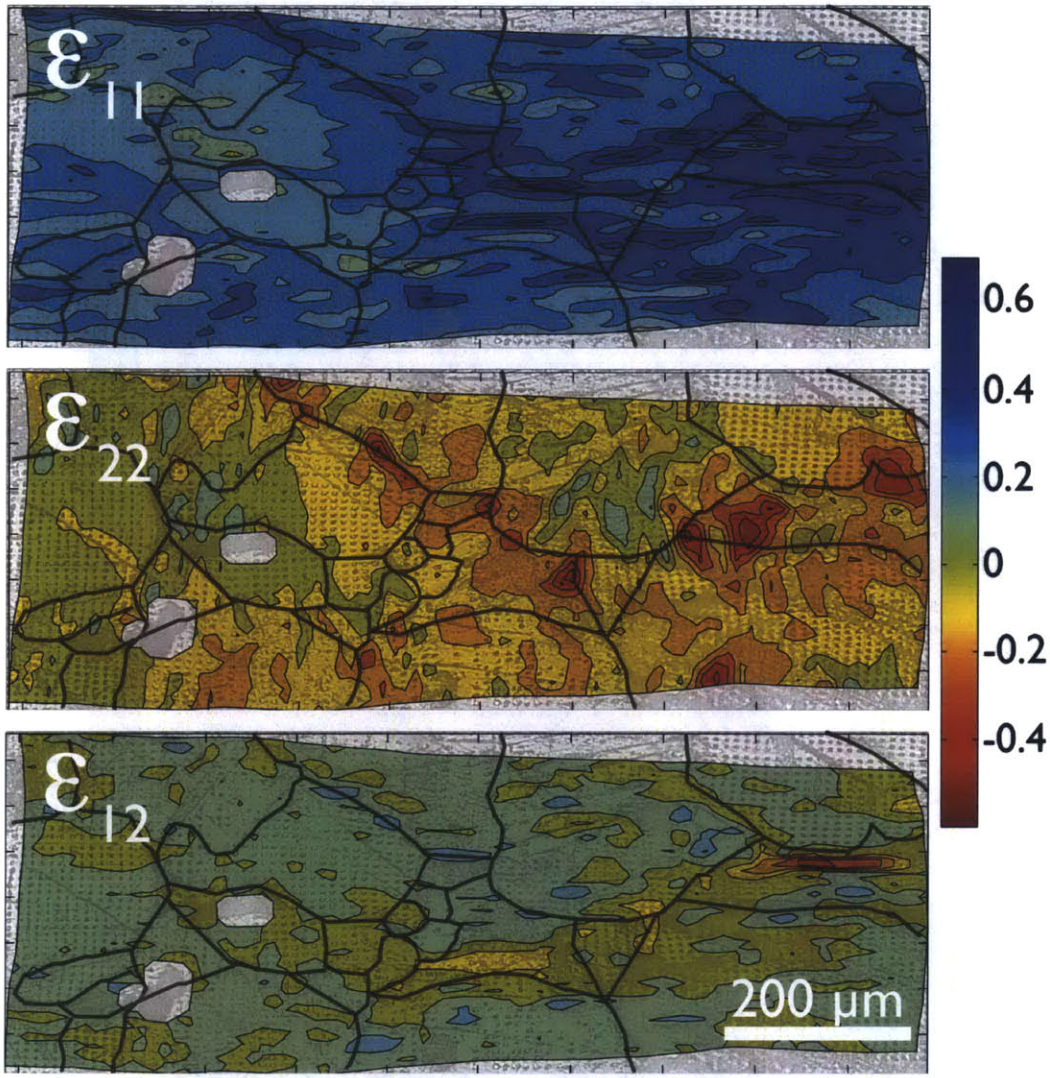

Figure B-3: Microscale strain maps for sample CMetCr11 deformed to 0.2 at 300 MPa, 600°C and 3×10^{-5} s^{-1}. Strain is dimensionless and positive when related to shortening, the strain map is overlaid on top of the optical microscope image. The digitalized traced grain boundaries are plotted in black. The compression direction σ_{11} is along the vertical axis of the figure.

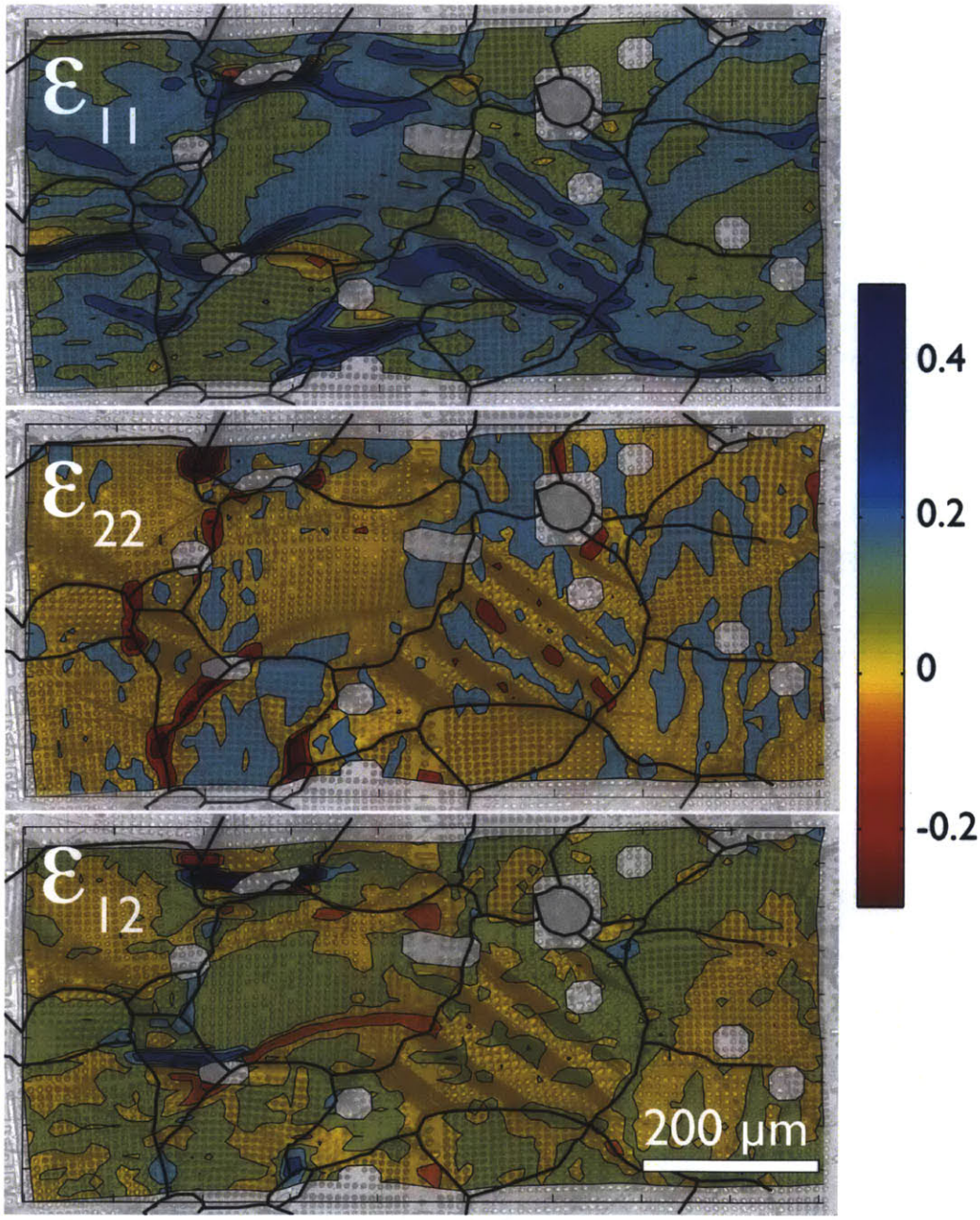

Figure B-4: Microscale strain maps for sample CMetCr05 deformed to 0.11 at 300 MPa, 600°C and 1×10^{-5} s^{-1}. Strain is dimensionless and positive when related to shortening, the strain map is overlaid on top of the optical microscope image. The digitalized traced grain boundaries are plotted in black The compression direction σ_{11} is along the vertical axis of the figure.

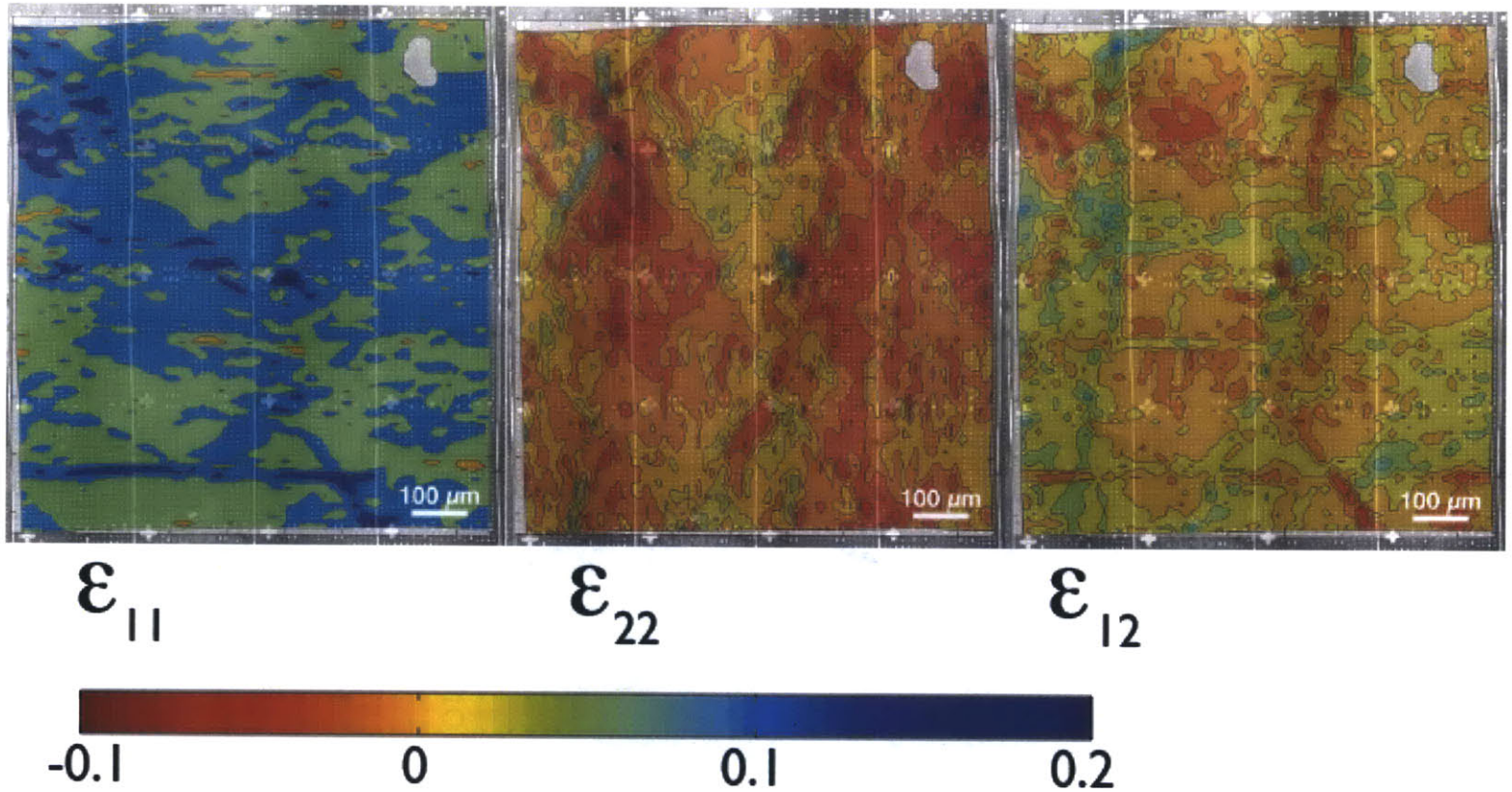

Figure B-5: Microscale strain maps for sample CMhA, deformed to 0.04 at 300 MPa, 600°C and 3×10^{-5} s^{-1}.Strain is dimensionless and positive when related to shortening, the strain map is overlaid on top of the optical microscope image. The compression direction σ_{11} is along the vertical axis of the figure.

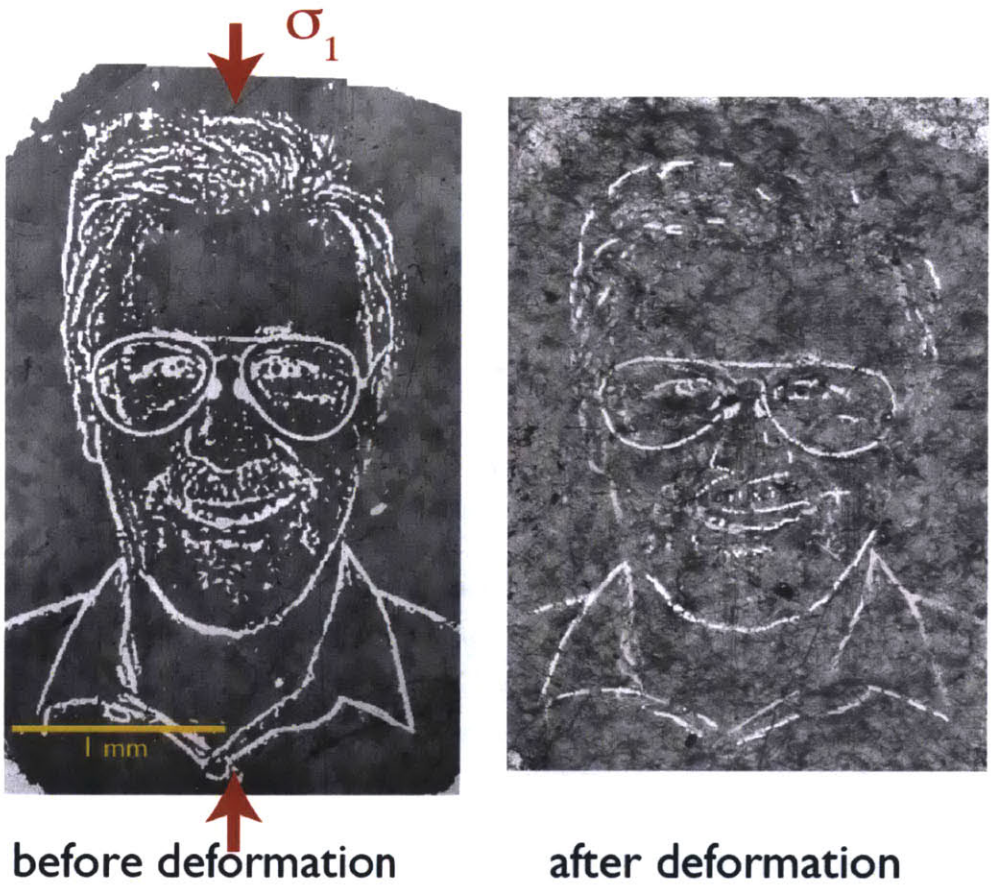

Figure B-6: Secret project sample: experiment serving both as a tribute and as a testimony to the great flexibility of the microfabrication technique. The patterning was done in similar conditions as the experiments presented in this thesis: slight acid etch and double layer Cr + Au. Sample deformed to 0.11 at 300 MPa, 600°C and 3×10^{-5} s^{-1}. and The compression direction σ_{11} is along the vertical axis of the figure.

Appendix C

Microfabrication Process

The microfabrication process performed in the MTL EML lab at MIT is explained here in more detail. The process has to be performed in a clean lab. The samples must be cleaned and ideally left in an oven at 110°C 24h prior to processing to decrease water content. All samples used in this thesis were microfabricated using the photoresist OCG 825-20. It is now obsolete and was removed from the EML lab in April 2014. SPR 700 is used as a replacement. I adapted the protocol to SPR in August 2014, but also give the values that were used with OCG 825-20 for reference.

1. Bake: 20 minutes at 130°C .
2. Polymer deposition: Sample manually "painted" using clean lab brush with photoresist.
3. Pre-bake: 20 minutes (30 minutes for SPR) at 90 °C .
4. UV exposure: Exposure for 20 s for OCG 825, 30s for SFR in aligner MA-4.
5. Development: Development for 10 s in OCG developer (OCG 934:1:1) or 5 s in SPR developer (CD 26).
6. Acid etch: 1s acid etch in 7% diluted HCl.

7. Deposition: Use of AJA sputter, a plasma sputterer with Argon as sputter gas (12 sccm flow rate). Two layers have to be deposited one after the other to increase adhesion of Gold, first 20 nm of Cr, then 30 nm of Au. The plasma is ignited at 30 mT and the deposition is done at 3 mT. The sputtering rate depends on the state of the target and on the gun used and is evaluated using a quartz crystal before each deposition (typical procedure). It typical was on the order of 0.5 Å/s.

8. Dissolution of the remaining polymer: for both OCG 825-20 and SPR 700 the samples are left for one hour (sometimes even over-night) in a heated bath set at 90 °C of microstrip, following all safety requirements. Sonicator should only be used if this gentler step does not remove the polymer, and in such case it should be used 1s at a time.

References

Ashby, M. (1972). A first report on deformation-mechanism maps. *Acta Metallurgica*, *20*(7), 887-8897.

Austin, N., Evans, B., Herwegh, M., & Ebert, A. (2008, September). Strain localization in the morcles nappe (helvetic alps, switzerland). *Swiss Journal of Geosciences*, *101*(2), 341-360.

Austin, N., Evans, B., Rybacki, E., & Dresen, G. (2014). Strength evolution and the development of crystallographic preferred orientation during deformation of two-phase marbles. *Tectonophysics*.

Bachmann, F., Hielscher, R., & Schaeben, H. (2010, February). Texture analysis with MTEX free and open source software toolbox. *Solid State Phenomena*, *160*, 63-68.

Barber, D., Wenk, H.-R., Gomez-Barreiro, J., Rybacki, E., & Dresen, G. (2007, March). Basal slip and texture development in calcite: new results from torsion experiments. *Physics and Chemistry of Minerals*, *34*(2), 73-84.

Barber, D. J., & Wenk, H.-R. (1979, December). Deformation twinning in calcite, dolomite, and other rhombohedral carbonates. *Physics and Chemistry of Minerals*, *5*(2), 141-165.

Barnhoorn, A., Bystricky, M., Burlini, L., & Kunze, K. (2004, May). The role of recrystallisation on the deformation behaviour of calcite rocks: large strain torsion experiments on carrara marble. *Journal of Structural Geology*, *26*(5), 885-903.

Barnhoorn, A., Bystricky, M., Kunze, K., & Burlini, L. (2003, April). High strain deformation of calcite-anhydrite aggregates. In *EGS - AGU - EUG joint assembly* (Vol. -1, p. 7537).

Barnhoorn, A., Bystricky, M., Kunze, K., Burlini, L., & Burg, J.-P. (2005, December). Strain localisation in bimineralic rocks: Experimental deformation of synthetic calcite-anhydrite aggregates. *Earth and Planetary Science Letters*, *240*(3-4), 748-763.

Bazant, Z. P. (1998, April). Easy-to-compute tensors with symmetric inverse approximating hencky finite strain and its rate. *Journal of Engineering Materials and Technology*, *120*(2), 131-136.

Bestmann, M., Kunze, K., & Matthews, A. (2000, November). Evolution of a calcite marble shear zone complex on thassos island, greece: microstructural and textural fabrics and their kinematic significance. *Journal of Structural Geology*, *22*(1112), 1789-1807.

Biery, N. E., De Graef, M., & Pollock, T. M. (2001, December). Influence of microstructure and strain distribution on failure properties in intermetallic TiAl-based alloys. *Materials Science and Engineering: A*, *319-321*, 613-617.

Borg, I., & Handin, J. (1967, January). Torsion of calcite single crystals. *Journal of Geophysical Research*, *72*(2), 641-669.

Bornert, M., Valès, F., Gharbi, H., & Nguyen Minh, D. (2010). Multiscale full-field strain measurements for micromechanical investigations of the hydromechanical behaviour of clayey rocks. *Strain*, *46*(1), 33-46.

Bruhn, D. F., Olgaard, D. L., & Dell'Angelo, L. N. (1999). Evidence for enhanced deformation in two-phase rocks: Experiments on the rheology of calcite-anhydrite aggregates. *Journal of Geophysical Research*, *104*(B1), 707.

Bruijn, R. H. C., Kunze, K., Mainprice, D., & Burlini, L. (2011, April). Mechanical and microstructural development of carrara marble with pre-existing strain variation. *Tectonophysics*, *503*(12), 75-91.

Bunge, H. J. (1982). *Texture analysis in materials science: mathematical methods.* Butterworths.

Burg, J.-P. (1999, August). Ductile structures and instabilities: their implication for variscan tectonics in the ardennes. *Tectonophysics*, *309*(1-4), 1-25.

Burg, J. P., Iglesias, M., Laurent, P., Matte, P., & Ribeiro, A. (1981, October). Variscan intracontinental deformation: The coimbra cordoba shear zone (sw iberian peninsula). *Tectonophysics*, *78*(14), 161-177.

Burkhard, M. (1993, March). Calcite twins, their geometry, appearance and significance as stress-strain markers and indicators of tectonic regime: a review. *Journal of Structural Geology*, *15*(305), 351-368.

Capolungo, L., Marshall, P., McCabe, R., Beyerlein, I., & Tomé, C. (2009, December). Nucleation and growth of twins in zr: A statistical study. *Acta Materialia*, *57*(20), 6047-6056.

Chen, K., Kunz, M., Tamura, N., & Wenk, H.-R. (2011, June). Deformation twinning and residual stress in calcite studied with synchrotron polychromatic x-ray microdiffraction. *Physics and Chemistry of Minerals*, *38*(6), 491-500.

Christian, J. W., & Mahajan, S. (1995). Deformation twinning. *Progress in Materials Science*, *39*(12), 1-157.

Coli, M. (1989). Litho-structural assemblage and deformation history of "carrara marble". *Boll. Soc. Geol. Ital.*, *108*, 581-590.

Covey-Crump, S. J. (1998, December). Evolution of mechanical state in carrara marble during deformation at 400° to 700°c. *Journal of Geophysical Research: Solid Earth*, *103*(B12), 29781-29794.

De Bresser, J. H. P. (1996). Steady state dislocation densities in experimentally deformed calcite materials: Single crystals versus polycrystals. *Journal of Geophysical Research: Solid Earth (19782012)*, *101*(B10), 22189-22201.

De Bresser, J. H. P. (2002). On the mechanism of dislocation creep of calcite at high temperature: inferences from experimentally measured pressure sensitivity and strain rate sensitivity of flow stress. *Journal of Geophysical Research: Solid Earth (19782012)*, *107*(B12), ECV-4.

De Bresser, J. H. P., Evans, B., & Renner, J. (2002). On estimating the strength of calcite rocks under natural conditions. *Geological Society, London, Special Publications*, *200*(1), 309-329.

De Bresser, J. H. P., & Spiers, C. J. (1990, January). High-temperature deformation of calcite single crystals by r+ and f+ slip. *Geological Society, London, Special Publications*, *54*(1), 285-298.

De Bresser, J. H. P., & Spiers, C. J. (1991). Intracrystalline deformation of calcite. *Geologica ultraiectina, Utrecht University.*

De Bresser, J. H. P., & Spiers, C. J. (1993, April). Slip systems in calcite single crystals deformed at 300 and 800°c. *Journal of Geophysical Research: Solid Earth*, *98*(B4).

De Bresser, J. H. P., & Spiers, C. J. (1997). Strength characteristics of the r, f, and c slip systems in calcite. *Tectonophysics*, *272*(1), 123.

Delle Piane, C., Burlini, L., & Kunze, K. (2009, March). The influence of dolomite on the plastic flow of calcite: Rheological, microstructural and chemical evolution during large strain torsion experiments. *Tectonophysics*, *467*(14), 145-166.

Delle Piane, C., Wilson, C. J. L., & Burlini, L. (2009, October). Dilatant plasticity in high-strain experiments on calcite-muscovite aggregates. *Journal of Structural Geology*, *31*(10), 1084-1099.

Dove, H. (1860). Optische notizen. *Ann Phys*, *110*(9), 286-290.

Dresen, G., & Evans, B. (1993, July). Brittle and semibrittle deformation of synthetic marbles composed of two phases. *Journal of Geophysical Research: Solid Earth*, *98*(B7), 11921-11933.

Ebert, A., Herwegh, M., Evans, B., Pfiffner, A., Austin, N., & Vennemann, T. (2007, November). Microfabrics in carbonate mylonites along a large-scale shear zone (helvetic alps). *Tectonophysics*, *444*(14), 1-26.

Engler, O., & Randle, V. (2009). (2edition ed.). Boca Raton: CRC Press.

Eshelby, J. D. (1957). The determination of the elastic field of an ellipsoidal inclusion, and related problems. *Proceedings of the Royal Society of London. Series A. Mathematical and Physical Sciences*, *241*(1226), 376-396.

Evans, B. (2005, January). Creep constitutive laws for rocks with evolving structure. *Geological Society, London, Special Publications*, *245*(1), 329 -346.

Evans, B., & Kohlstedt, D. L. (1995). Rheology of rocks. In T. J. Ahrens (Ed.), *Rock physics & phase relations* (p. 148-165). American Geophysical Union.

Ferrill, D. A., Morris, A. P., Evans, M. A., Burkhard, M., Groshong, R. H., & Onasch, C. M. (2004, August). Calcite twin morphology: a low-temperature deformation geothermometer. *Journal of Structural Geology*, *26*(8), 1521-1529.

Freund, D., Wang, Z., Rybacki, E., & Dresen, G. (2004, October). High-temperature creep of synthetic calcite aggregates: influence of mn-content. *Earth and Planetary Science Letters*, *226*(34), 433-448.

Frost, H. J., & Ashby, M. F. (1982). *Deformation-mechanism maps: the plasticity and creep of metals and ceramics.* Pergamon Press.

Gonzlez-Casado, J. M., Jiménez-Berrocoso, ., García-Cuevas, C., & Elorza, J. (2003, November). Strain determinations using inoceramid shells as strain markers: a

comparison of the calcite strain gauge technique and the fry method. *Journal of Structural Geology*, *25*(11), 1773-1778.

Grédiac, M., & Hild, F. (2011). *Mesures de champs et identification en mécanique des solides.* Lavoisier.

Grennerat, F., Montagnat, M., Castelnau, O., Vacher, P., Moulinec, H., Suquet, P., & Duval, P. (2012, May). Experimental characterization of the intragranular strain field in columnar ice during transient creep. *Acta Materialia*, *60*(8), 3655–3666.

Griggs, D., Turner, F. J., Borg, I., & Sosoka, J. (1953, December). Deformation of yule marble: Part v at 300°c. *Geological Society of America Bulletin*, *64*(12), 1327-1342.

Groshong, R. H., Teufel, L. W., & Gasteiger, C. (1984, March). Precision and accuracy of the calcite strain-gage technique. *Geological Society of America Bulletin*, *95*(3), 357-363.

Groshong Jr., R. H., Pfiffner, O. A., & Pringle, L. R. (1984). Strain partitioning in the helvetic thrust belt of eastern switzerland from the leading edge to the internal zone. *Journal of Structural Geology*, *6*(1-2), 5-18.

Heard, H. (1963). Effects of large changes in strain rate in the experimental deformation of yule marble. *Journal of Geology*, *71*, 162-195.

Heard, H. C., & Raleigh, C. B. (1972, April). Steady-state flow in marble at 500°c to 800°c. *Geological Society of America Bulletin*, *83*(4), 935-956.

Herwegh, M., De Bresser, J. H. P., & Ter Heege, J. H. (2005). Combining natural microstructures with composite flow laws: an improved approach for the extrapolation of lab data to nature. *Journal of Structural Geology*, *27*(3), 503-521.

Herwegh, M., & Evans, B. (2000). Grain growth and chemical exchange in polyphase rocks: Inferences from calcite-dolomite HIP experiments. *EOS Trans. AGU*, *81 (48)*, TI2F-07.

Herwegh, M., & Handy, M. R. (1996, May). The evolution of high-temperature mylonitic microfabrics: evidence from simple shearing of a quartz analogue (norcamphor). *Journal of Structural Geology*, *18*(5), 689-710.

Herwegh, M., & Kunze, K. (2002, September). The influence of nano-scale second-phase particles on deformation of fine grained calcite mylonites. *Journal of Structural Geology*, *24*(9), 1463-1478.

Herwegh, M., Xiao, X., & Evans, B. (2003, July). The effect of dissolved magnesium on diffusion creep in calcite. *Earth and Planetary Science Letters*, *212*(34), 457-470.

Hobbs, B. E., Moehlhaus, H.-B., & Ord, A. (1990, January). Instability, softening and localization of deformation. *Geological Society, London, Special Publications*, *54*(1), 143-165.

Hosford, W. F. (1993). *The mechanics of crystals and textured polycrystals.* New York: Oxford University Press.

Hosford, W. J. (1987). Microstructural changes during deformation of [011] fiber-textured metals. *Transactions of the metallurgical society of AIME*, *230*, 12-15.

Jamison, W. R., & Spang, J. H. (1976, June). Use of calcite twin lamellae to infer differential stress. *Geological Society of America Bulletin*, *87*(6), 868-872.

Khan, A. S., & Huang, S. (1995). *Continuum theory of plasticity* (1edition ed.). New York: Wiley-Interscience.

Klassen-Neklyudova, M. V. (1964, January). Twinning during plastic deformation and fracture of crystals. In *Mechanical twinning of crystals* (p. 101-104). Springer US.

Kocks, U. F. (2000). *Texture and anisotropy: Preferred orientations in polycrystals and their effect on materials properties.* Cambridge University Press.

Kohlstedt, D. L., Evans, B., & Mackwell, S. J. (1995, September). Strength of the lithosphere: Constraints imposed by laboratory experiments. *Journal of Geophysical Research: Solid Earth*, *100*(B9), 17587-17602.

Lacombe, O. (2007, January). Comparison of paleostress magnitudes from calcite twins with contemporary stress magnitudes and frictional sliding criteria in the continental crust: Mechanical implications. *Journal of Structural Geology*, *29*(1), 86-99.

Lacombe, O., & Laurent, P. (1992, February). Determination of principal stress magnitudes using calcite twins and rock mechanics data. *Tectonophysics*, *202*(1), 83-93.

Larsson, A.-K., & Christy, A. G. (2008, January). On twinning and microstructures in calcite and dolomite. *American Mineralogist*, *93*(1), 103-113.

Laurent, P., Bernard, P., Vasseur, G., & Etchecopar, A. (1981, October). Stress tensor determination from the study of e twins in calcite: A linear programming method. *Tectonophysics*, *78*(14), 651-660.

Lebensohn, R. (2001). N-site modeling of a 3D viscoplastic polycrystal using fast fourier transform. *Acta Materialia*, *49*(14), 2723 to 2737.

Lebensohn, R. A., Brenner, R., Castelnau, O., & Rollett, A. D. (2008, September). Orientation image-based micromechanical modelling of subgrain texture evolution in polycrystalline copper. *Acta Materialia*, *56*(15), 3914-3926.

Lebensohn, R. A., Montagnat, M., Mansuy, P., Duval, P., Meysonnier, J., & Philip, A. (2009, March). Modeling viscoplastic behavior and heterogeneous intracrystalline deformation of columnar ice polycrystals. *Acta Materialia*, *57*(5), 1405-1415.

Lebensohn, R. A., & Tom, C. N. (1993, September). A self-consistent anisotropic approach for the simulation of plastic deformation and texture development of polycrystals: Application to zirconium alloys. *Acta Metallurgica et Materialia*, *41*(9), 2611-2624.

Lebensohn, R. A., Wenk, H. R., & Tome, C. (1998). Modelling deformation and recrystallization textures in calcite. *Acta muter. Vol*, *46*(8), 2683-2693.

Madou, M. J. (2002). *Fundamentals of microfabrication: the science of miniaturization.* CRC Press.

Mainprice, D., Bascou, J., Cordier, P., & Tommasi, A. (2004, November). Crystal preferred orientations of garnet: comparison between numerical simulations and electron back-scattered diffraction (EBSD) measurements in naturally deformed eclogites. *Journal of Structural Geology*, *26*(11), 2089-2102.

Mainprice, D., Hielscher, R., & Schaeben, H. (2011, January). Calculating anisotropic physical properties from texture data using the MTEX open-source package.

Geological Society, London, Special Publications, *360*(1), 175-192.

Malvern, L. E. (1969). *Introduction to the mechanics of a continuous medium.* Prentice-Hall.

Martin, G., Caldemaison, D., Bornert, M., Pinna, C., Brachet, Y., Vairon, M., ... Pardoen, T. (2013, February). Characterization of the high temperature strain partitioning in duplex steels. *Experimental Mechanics*, *53*(2), 205-215.

Martin, G., Sinclair, C. W., & Lebensohn, R. A. (2014, May). Microscale plastic strain heterogeneity in slip dominated deformation of magnesium alloy containing rare earth. *Materials Science and Engineering: A*, *603*, 37-51.

Mase, G. T., Smelser, R. M., & G. E., Mase. (2010). *Continuum mechanics for engineers.* Boca Raton: CRC Press.

Matthies, S., Wenk, H., & Vinel, G. (1988). Some basic concepts of texture analysis and comparison of three methods to calculate orientation distributions from pole figures. *J. Appl. Cryst.*, *21*, 285-304.

Molinari, A., Canova, G. R., & Ahzi, S. (1987, December). A self consistent approach of the large deformation polycrystal viscoplasticity. *Acta Metallurgica*, *35*(12), 2983-2994.

Molli, G., Conti, P., Giorgetti, G., Meccheri, M., & Oesterling, N. (2000, November). Microfabric study on the deformational and thermal history of the alpi apuane marbles (carrara marbles), italy. *Journal of Structural Geology*, *22*(11-12), 1809-1825.

Molli, G., & Heilbronner, R. (1999, March). Microstructures associated with static and dynamic recrystallization of carrara marble (alpi apuane, NW tuscany, italy). *Geologie en Mijnbouw*, *78*(1), 119-126.

Montési, L. G. J., & Zuber, M. T. (2002, March). A unified description of localization for application to large-scale tectonics. *Journal of Geophysical Research: Solid Earth*, *107*(B3), ECV 1-1.

Neto, E. A. d. S., Peric, D., & Owen, D. R. J. (2008). *Computational methods for plasticity: Theory and applications* (1edition ed.). Chichester, West Sussex, UK: Wiley.

Oesterling, N., Heilbronner, R., Stunitz, H., Barnhoorn, A., & Molli, G. (2007, April). Strain dependent variation of microstructure and texture in naturally deformed carrara marble. *Journal of Structural Geology*, *29*(4), 681-696.

Orowan, E. (1953). Creep in metallic and non metallic materials. *Proceedings of the First National Congress of Applied mechanics*, 453.

Pan, B., Qian, K., Xie, H., & Asundi, A. (2009, June). Two-dimensional digital image correlation for in-plane displacement and strain measurement: a review. *Measurement Science and Technology*, *20*(6), 062001.

Panozzo, R. H. (1983, June). Two-dimensional analysis of shape-fabric using projections of digitized lines in a plane. *Tectonophysics*, *95*(34), 279-294.

Paterson, M. (1979). Deformation mechanisms in carbonate crystals. *Physics of Materials, A Festschrift for Dr. Walter Boas*, 199-208.

Paterson, M. S. (1990). Rock deformation experimentation. In A. G. Duba, W. B. Durham, J. W. Handin, & H. F. Wang (Eds.), *The brittle-ductile transition in rocks* (p. 187-194). American Geophysical Union.

Paterson, M. S., & Turner, F. J. (1970, January). Experimental deformation of constrained crystals of calcite in extension. In P. D. P. Paulitsch (Ed.), *Experimental and natural rock deformation / experimentelle und nataoerliche gesteinsverformung* (p. 109-141). Springer Berlin Heidelberg.

Pfiffner, A. O. (1982). Deformation mechanisms and flow regimes in limestones from the helvetic zone of the swiss alps. *Journal of Structural Geology*, *4*(4), 429-442.

Piane, C. D., & Burlini, L. (2008, September). Influence of strain history on the mechanical and micro-fabric evolution of calcite rocks: insights from torsion experiments. *Swiss Journal of Geosciences*, *101*(2), 361-375.

Pieri, M., Burlini, L., Kunze, K., Stretton, I., & Olgaard, D. L. (2001, September). Rheological and microstructural evolution of carrara marble with high shear strain: results from high temperature torsion experiments. *Journal of Structural Geology*, *23*(9), 1393-1413.

Pieri, M., Kunze, K., Burlini, L., Stretton, I., Olgaard, D. L., Burg, J. P., & Wenk, H. R. (2001, January). Texture development of calcite by deformation and dynamic recrystallization at 1000 k during torsion experiments of marble to large strains. *Tectonophysics*, *330*(1-2), 119-140.

Poirier, J. (1985). *Creep of crystals: High-temperature deformation processes in metals, ceramics and minerals.* Cambridge University Press.

Poirier, J. P. (1980). Shear localization and shear instability in materials in the ductile field. *Journal of Structural Geology*, *2*(12), 135-142.

Preibisch, S., Saalfeld, S., & Tomancak, P. (2009, June). Globally optimal stitching of tiled 3D microscopic image acquisitions. *Bioinformatics*, *25*(11), 1463-1465.

Prior, D. J., Mariani, E., & Wheeler, J. (2009, January). EBSD in the earth sciences: Applications, common practice, and challenges. In A. J. Schwartz, M. Kumar, B. L. Adams, & D. P. Field (Eds.), *Electron backscatter diffraction in materials science* (p. 345-360). Springer US.

Raj, R., & Ashby, M. F. (1971, April). On grain boundary sliding and diffusional creep. *Metallurgical Transactions*, *2*(4), 1113-1127.

Raleigh, C. B. (1965). Glide mechanisms in experimentally deformed minerals. *Science*, *150*, 739-741.

Reddy, J. N. (2008). *An introduction to continuum mechanics.* Cambridge University Press.

Reid, C. N. (1973). *Deformation geometry for materials scientists.* Pergamon Press.

Renner, J., & Evans, B. (2002, January). Do calcite rocks obey the power-law creep equation? *Geological Society, London, Special Publications*, *200*(1), 293-307.

Renner, J., Evans, B., & Siddiqi, G. (2002, December). Dislocation creep of calcite. *Journal of Geophysical Research: Solid Earth*, *107*(B12), 2364.

Renner, J., Siddiqi, G., & Evans, B. (2007, July). Plastic flow of two-phase marbles. *Journal of Geophysical Research: Solid Earth*, *112*(B7), B07203.

R. Hielscher, H. S. (2008). A novel pole figure inversion method: specification of the MTEX algorithm. *Journal of Applied Crystallography - J APPL CRYST*, *41*(6), 1024-1037.

Romeo, I., Capote, R., & Lunar, R. (2007, August). Crystallographic preferred orientations and microstructure of a variscan marble mylonite in the ossa-morena

zone (SW iberia). *Journal of Structural Geology*, *29*(8), 1353-1368.

Rowe, K., & Rutter, E. (1990, January). Paleostress estimation using calcite twinning: experimental calibration and application to nature. *Journal of Structural Geology*, *12*(1), 1-17.

Rutter, E. H. (1995). Experimental study of the influence of stress, temperature, and strain on the dynamic recrystallization of carrara marble. *Journal of Geophysical Research*, *100*(B12), PP. 24,651-24,663.

Rutter, E. H. (1998). Use of extension testing to investigate the influence of finite strain on the rheological behaviour of marble. *J. Struct. Geol.*, *20*(2-3), 243-254.

Rutter, E. H. (1999, March). On the relationship between the formation of shear zones and the form of the flow law for rocks undergoing dynamic recrystallization. *Tectonophysics*, *303*(14), 147-158.

Rutter, E. H., Faulkner, D. R., Brodie, K. H., Phillips, R. J., & Searle, M. P. (2007, August). Rock deformation processes in the karakoram fault zone, eastern karakoram, ladakh, NW india. *Journal of Structural Geology*, *29*(8), 1315-1326.

Rybacki, E., Evans, B., Janssen, C., Wirth, R., & Dresen, G. (2013, August). Influence of stress, temperature, and strain on calcite twins constrained by deformation experiments. *Tectonophysics*, *601*, 20-36.

Rybacki, E., Paterson, M. S., Wirth, R., & Dresen, G. (2003, February). Rheology of calcite-quartz aggregates deformed to large strain in torsion. *Journal of Geophysical Research: Solid Earth*, *108*(B2), 2089.

Schmid, S. (1976, March). Rheological evidence for changes in the deformation mechanism of solenhofen limestone towards low stresses. *Tectonophysics*, *31*(1-2), T21-T28.

Schmid, S., Boland, J., & Paterson, M. (1977, December). Superplastic flow in finegrained limestone. *Tectonophysics*, *43*(3-4), 257-291.

Schmid, S., Paterson, M., & Boland, J. (1980, June). High temperature flow and dynamic recrystallization in carrara marble. *Tectonophysics*, *65*(3-4), 245-280.

Schmid, S. M. (1975). *The glarus overthrust: field evidence and mechanical model.* Birkhuser.

Schmid, S. M., Panozzo, R., & Bauer, S. (1987). Simple shear experiments on calcite rocks: rheology and microfabric. *Journal of Structural Geology*, *9*(56), 747-778.

Schmid, S. M., & Paterson, M. S. (1977, January). Strain analysis in an experimentally deformed oolitic limestone. In S. K. Saxena, S. Bhattacharji, H. Annersten, & O. Stephansson (Eds.), *Energetics of geological processes* (p. 67-93). Springer Berlin Heidelberg.

Serra, A., Bacon, D. J., & Pond, R. C. (2002, March). Twins as barriers to basal slip in hexagonal-close-packed metals. *Metallurgical and Materials Transactions A*, *33*(3), 809-812.

Spiers, C. (1979). Fabric development in calcite polycrystals deformed at 400C. *Bull. Mineral.*, *102*, 282-289.

Steif, P. S., Spaepen, F., & Hutchinson, J. W. (1982, February). Strain localization in amorphous metals. *Acta Metallurgica*, *30*(2), 447-455.

Sutton, M., Wolters, W., Peters, W., Ranson, W., & McNeill, S. (1983, August). Determination of displacements using an improved digital correlation method. *Image and Vision Computing*, *1*(3), 133-139.

Sutton, M. A., Orteu, J. J., & Schreier, H. (2009). *Image correlation for shape, motion and deformation measurements: Basic concepts,theory and applications* (2009edition ed.). New York, N.Y: Springer.

Takeshita, T., Tom, C., Wenk, H.-R., & Kocks, U. F. (1987, November). Single-crystal yield surface for trigonal lattices: Application to texture transitions in calcite polycrystals. *Journal of Geophysical Research: Solid Earth*, *92*(B12), 12917-12930.

Taylor, S. G. I. (1938). *Plastic strain in metals.*

Thomas, J. M., & Renshaw, G. D. (1967, January). Influence of dislocations on the thermal decomposition of calcium carbonate. *Journal of the Chemical Society A: Inorganic, Physical, Theoretical*(0), 2058-2061.

Tullis, J., & Yund, R. A. (1977, December). Experimental deformation of dry westerly granite. *Journal of Geophysical Research*, *82*(36), 5705-5718.

Turner, F. J., Griggs, D. T., Clark, R. H., & Dixon, R. H. (1956, September). Deformation of yule marble. part vii: Development of oriented fabrics at 300° to 500°. *Geological Society of America Bulletin*, *67*(9), 1259-1294.

Turner, F. J., Griggs, D. T., & Heard, H. (1954). Experimental deformation of calcite crystals. *Geological Society of America Bulletin*, *65*(9), 883.

Turner, F. J., & Heard, H. C. (1965). Deformation in calcite crystals at different strain rates. *Univ. Calif. Publ. Geol. Sci.*, *46*, 883-934.

Turner, F. J., & Weiss, L. E. (1963). *Structural analysis of metamorphic tectonites.* McGraw-Hill.

Wagner, F., Wenk, H.-R., Kern, H., Houtte, P. V., & Esling, C. (1982, September). Development of preferred orientation in plane strain deformed limestone: Experiment and theory. *Contributions to Mineralogy and Petrology*, *80*(2), 132-139.

Walker, A. N., Rutter, E. H., & Brodie, K. H. (1990, January). Experimental study of grain-size sensitive flow of synthetic, hot-pressed calcite rocks. *Geological Society, London, Special Publications*, *54*(1), 259-284.

Weiss, L. E., & Turner, F. J. (1972). Some observations on translation gliding and kinking in experimentally deformed calcite and dolomite. In H. C. Heard, I. Y. Borg, N. L. Carter, & C. B. Raleigh (Eds.), *Flow and fracture of rocks.* American Geophysical Union.

Wenk, H. R., Takeshita, T., Bechler, E., Erskine, B. G., & Matthies, S. (1987). Pure shear and simple shear calcite textures. comparison of experimental, theoretical and natural data. *Journal of Structural Geology*, *9*(56), 731-745.

Wenk, H. R., Takeshita, T., Van Houtte, P., & Wagner, F. (1986, March). Plastic anisotropy and texture development in calcite polycrystals. *Journal of Geophysical Research: Solid Earth*, *91*(B3), 3861-3869.

Wu, A., De Graef, M., & Pollock, T. (2006). Grain-scale strain mapping for analysis of slip activity in polycrystalline b2 rual. *Philosophical Magazine*, *86*(25-26), 3995-4008.

Xiao, X., & Evans, B. (2003, December). Shear-enhanced compaction during non-linear viscous creep of porous calcite-quartz aggregates. *Earth and Planetary Science Letters*, *216*(4), 725-740.

Xu, L., & Evans, B. (2010). Strain heterogeneity in deformed carrara marble using a microscale strain mapping technique. *Journal of Geophysical Research*, *115*, 18 PP.

Xu, L., Renner, J., Herwegh, M., & Evans, B. (2009, March). The effect of dissolved magnesium on creep of calcite II: transition from diffusion creep to dislocation creep. *Contributions to Mineralogy and Petrology*, *157*(3), 339-358.